

Material and structural modelling in collision research

9th Technical Meeting, 1995
München, Germany

Crash tests of thin sheet aluminium boxes by means of a Large Hopkinson Bar device.

C. Albertini, E. Cadoni, P. Francocci, K. Labibes and A. Petrangeli

European Commission - Joint Research Centre. Institute for Safety Technology,
21020 Ispra (Varese), Italy

*- Discussion sur l'analyse des signaux.
propagation des ondes (en pratique liées
reverse cage)
influence du buzzer.*

Abstract: The Large Hopkinson's bar method allows an accurate measurement of load and displacement values obtained by deforming thin sheet metal structures at high strain rates and therefore of their deformation energy. These experimental tests were carried out at different impact velocities on thin sheet aluminium boxes used as crash absorbers for the vehicles safety. This study allowed to give a better understanding of thin sheet aluminium mechanical behavior a impact by the fact of the absence of noise on the obtained strain gauge records.

1. INTRODUCTION

During the last decade the road safety has become an important social problem; this is due to the high number of deaths, only in Europe 50000 every year. As a consequence, an increase of public opinion's interest has cooperated to initiate the solution of this problem. So, the automotive industries have addressed a lot of efforts to safety-measures, as it is possible to note watching their advertising campaigns.

It is possible to divide the safety-measures in two ways: the measures concerning the road condition, the drivers education etc. (active safety), and those that directly interest the automotive body behaviour at impact (passive safety).

The survival of car passengers in case of an accident is mainly dependent on the synergetic intervention of many safety measures which are effective if the cabin remains free from intrusion and is not deformed. The task of keeping the cabin undeformed is conferred by the designer to the transformation of the cars kinetic energy in deformation energy of some structures of the car body which must deform in a controlled mode without intrusion in the cabin. These structures are named crash absorbers. In case of car collision they absorb energy limiting the damage to the passenger compartment, leading the folding and fracture propagation along selected paths.

In the frame of the Human Capital and Mobility Programme of the European Commission, a project called "Calibration of Impact Rigs for Dynamic Component Crash Testing" has been developed with the participation of thirteen Laboratories. This project consists of thin sheet aluminium boxes crash-characteristics comparison (used as collision car-safety devices) measured by different impact rigs (drop hammer, horizontal sledge etc.) and by the Large Dynamic Test Facility (LDTF) of JRC-ISPRA Site.

The aim of this comparison is the study of a calibration procedure of impact rigs which might take into account the effects of stress wave propagation; this feature should be allowed by the performances of LDTF which is a large Hopkinson bar (LHB) device whose measurement of forces and displacements during the specimen process deformation is based on the well established uniaxial elastic plane stress wave propagation theory [1]. The current measurement methods (based on drop weight

towers or sledge/barriers equipment) introduce considerable uncertainties due to the inertia effects, to the vibration characteristics of all the masses involved and to the uncontrolled wave propagation phenomena [2]. In the present paper the experimental results regarding tests on thin sheet aluminium boxes carried out at JRC-ISPRA are shown.

2. LDTF CONFIGURATION FOR CRASH TESTS OF THIN SHEET METAL BOXES

The classical split Hopkinson's bar equipment has mainly been used for compression tests at high strain rate of small metal specimens [1,3].

The modified Hopkinson's bar of our laboratory [4] consists of a high-strength steel cable, 100 m long, used as a prestressed bar. The strain rate is determined by the amplitude of the elastic prestress stored in the cable. By exploding a blocking bolt the elastic potential energy stored in the cable is released. A nearly rectangular tension pulse of 40 ms is then generated and propagates along the incident bar, loads the specimen and propagates along the transmission bar. Note that the deformation speed remains constant during the whole test.

By using a rather long incident and transmission bar it is possible to generate tensile pulses of long duration allowing large deformation of the specimen up to failure while disallowing the superposition of the waves with those reflected from the bar ends.

The application of the uniaxial propagation theory of elastic stress waves along bars having small transverse dimensions with respect to the wavelength of the applied stress pulse [1,3,5] (whatever the gauge length of the specimen) allows the calculation of:

- a) The history and amplitude $P(t)$ of the loading pulse generated by the pretensioned bar and propagated to the specimen along the incident (input) bar.

$$P(t) = A_I \cdot E \cdot \varepsilon_I(t) \quad [1]$$

where: t = time; A_I = input bar cross section area; E = elastic modulus of the input bar.

- b) History and amplitude of response loading $R(t)$ at both ends, connected to the specimen, of the incident and transmission bars.

$$R_{INPUT}(t) = E A_I [\varepsilon_I(t) + \varepsilon_R(t)] \quad [2]$$

$$R_{OUTPUT}(t) = E A_O \varepsilon_T(t) \quad [3]$$

where A_O = output bar cross section area.

- c) Displacement history and amplitude $S(t)$ at both ends, connected to the specimen, of the incident and transmission bars.

$$S_{INPUT} = c_0 \int_0^t [\varepsilon_I(t) - \varepsilon_R(t)] dt \quad [4]$$

$$S_{OUTPUT} = c_0 \int_0^t [\varepsilon_T(t)] dt \quad [5]$$

These test conditions were obtained by using the LDTF modified to a large Hopkinson bar system as shown in Figure 1 for testing under compression.

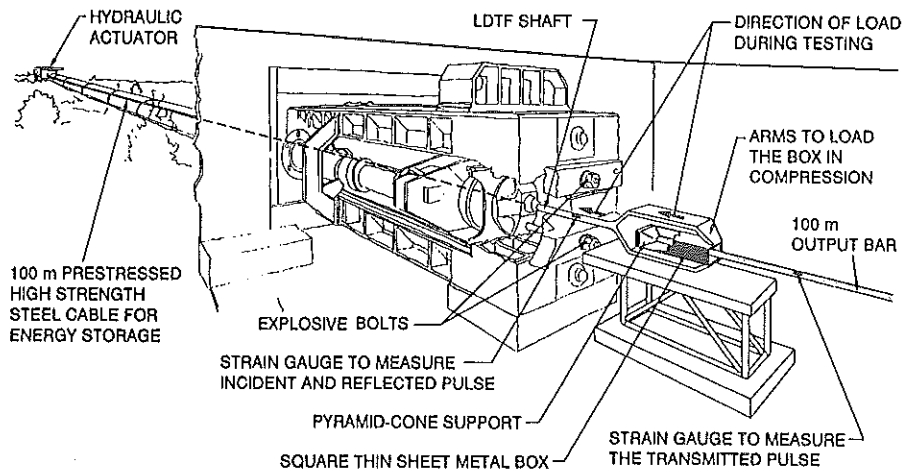


Figure 1 Layout to crash tests of thin sheet aluminium boxes by LHB device

3. TESTING PROGRAM

The experimental tests were carried out at impact velocities ranging from 0 to 50 km/h. The specimens have square section (60*60mm) and 3.4 - 1.7 mm thin. They have been triggered to avoid the effect of scattering among the load-displacement characteristics shown in precedent impact studies of not treated boxes however a comparison between triggered and no-triggered specimen tests results has been carried out. An high speed camera (which can reach 10000 frames/s) has been used to obtain tests films in order to analyze the behaviour of the specimens, with special regard to the observation of the folds and to the calculation of the boxes shortening speed. Five strain gauges are glued at different positions on the specimen to better understand its deformation characteristics (Figure 2).

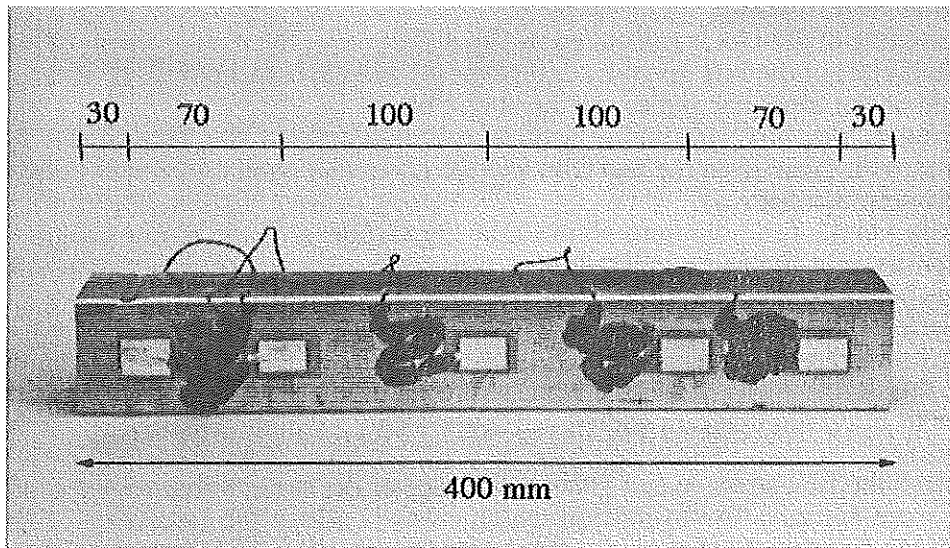


Figure 2 Aluminium box specimen with strain gauges position

4. EXPERIMENTAL RESULTS

During each test the incident pulse ϵ_I , the reflected pulse ϵ_R and the transmission pulse ϵ_T are measured at the strain-gauge stations placed on the incident and transmission bar.

A typical test record is shown in Figure 3; here the pulses are seen without any filtering process, showing that the Hopkinson bar system allows a good resolution of loading and response waves.

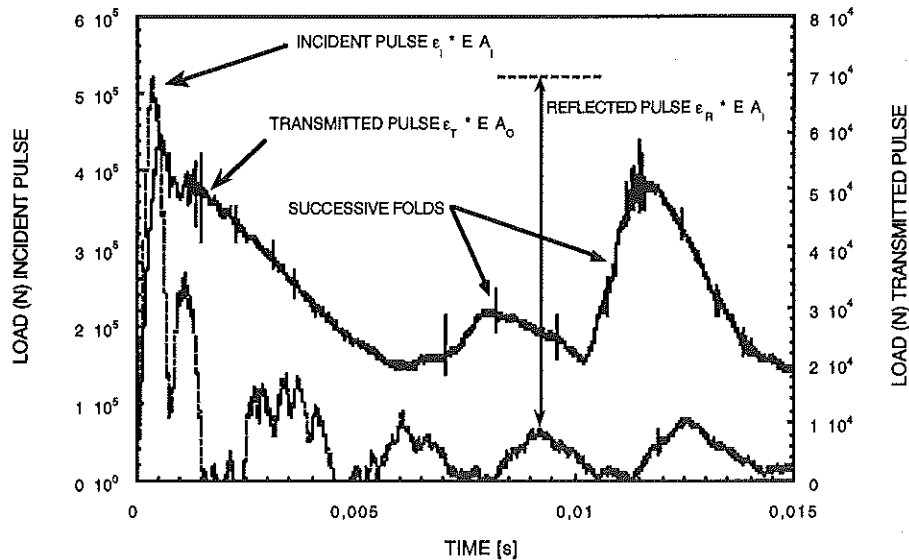


Figure 3 Record from input and output gauges

The records of ϵ_I , ϵ_R , ϵ_T are free from any spurious reflections from the bar ends for a time of 20 ms because the output bar has a length of 50 m; this clean recording time will reach 40 ms by increasing the length of the output bar up to 100 m as permitted by the supporting civil structure.

The shortening of the box is calculated by the difference of the displacement of the input and output ends of the box given by equations (4) and (5) respectively; ϵ_I and ϵ_R being measured on the input bar and ϵ_T on the output bar.

Furthermore, the box shortening values calculated from the Hopkinson bar are compared with those from the fast film and we observe a good agreement between the two measurement methods.

The strain versus time diagram shows that the response of the strain gauges on the specimen has got the same behaviour as the strain response of the transmission bar since the peaks correspond to the folds forming. The first strain gauge shows a higher strain with respect to the others because it is positioned at the point where the first fold appears with a plastic deformation.

Taking the deformation values of each strain gauge at different times position it is possible to build the diagram shown in Figure 4 and 5 which gives the strain state on the specimen.

In Figure 5 the first strain gauge gives a decrease of the strain value versus time and a change from compression to tension which corresponds to the formation of the first fold. In the same scale of time the strain remains nearly constant on the other strain gauge locations.

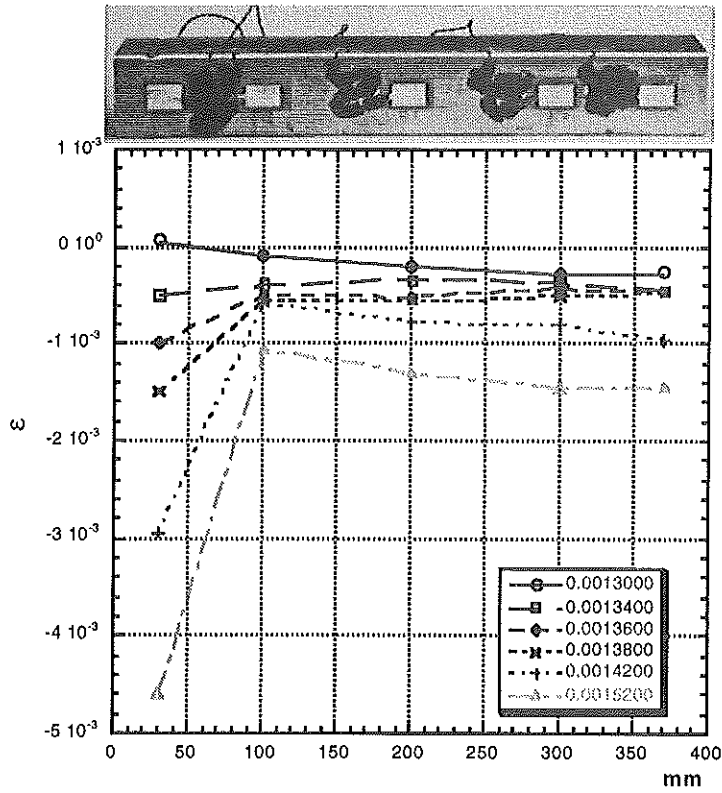


Figure 4 Strain distribution on specimen before the first fold formation

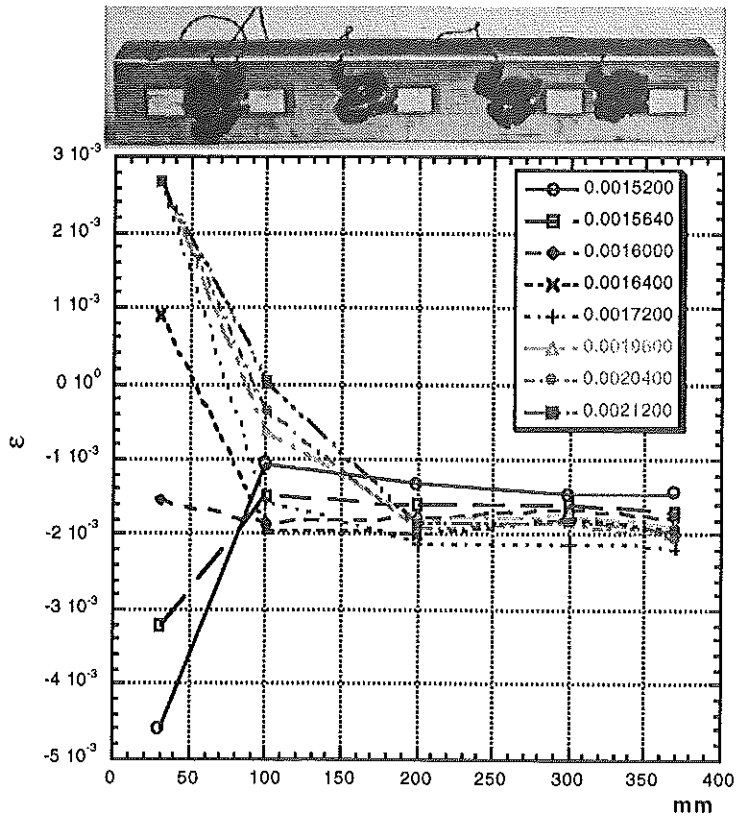


Figure 5 Strain distribution on specimen during the first fold formation

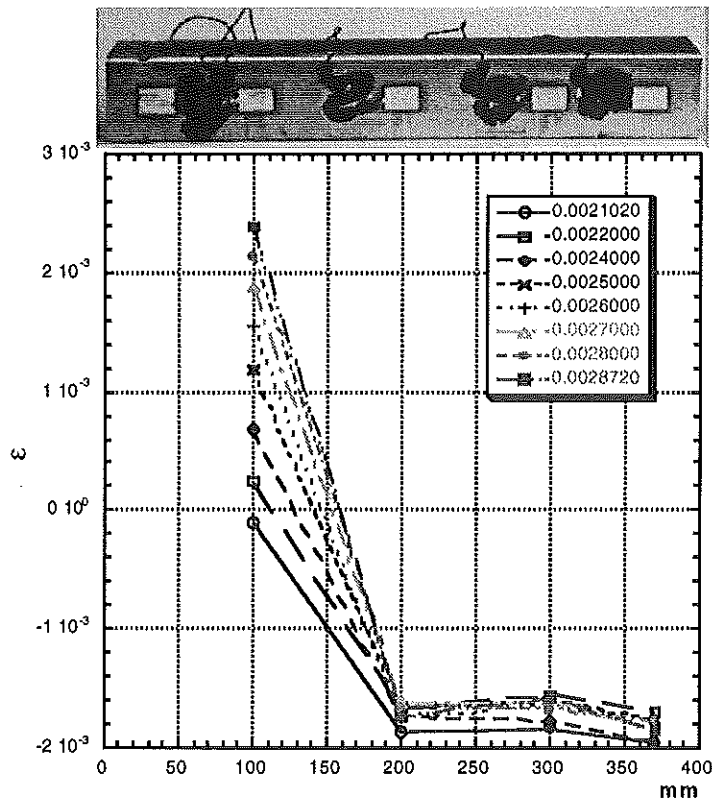


Figure 6 Strain distribution on specimen after the first fold formation

After the first fold formation the same strain history is obtained for the second strain gauge (Figure 6) : the strain value decreases and the compression is inverted in tension. At the same time the other three strain gauges have an approximately constant strain value. Thus, it is possible to obtain the local strains on the specimen by means of strain gauges response. However the stress can be given only during the first microseconds when the material is still in the elastic state.

Another important parameter for the analysis which can be obtained from the specimen - strain - gauge records is the local strain rate. From Figure 4 we have calculated that the strain rate in the folding region is $\sim 25 \text{ s}^{-1}$.

The comparison among the curves load-time and the frames obtained by the film has shown that the fold formation on the specimen corresponds to an increase of the load reaching a peak and then a decrease of the load values corresponding to the plastic deformation.

In Figure 7 and in Figure 8 are shown the load-time curve for a triggered and a non-triggered specimen respectively.

In Figure 9 and in Figure 10 are reported the load-shortening curves obtained from triggered and non-triggered specimen respectively.

For the non triggered specimens the first peak load is greater than the successive and it was also found in this case that the absorbed energy is more important than the value obtained for triggered specimens; that means that the triggering governs not only the formation of the first fold but also of the successive folds.

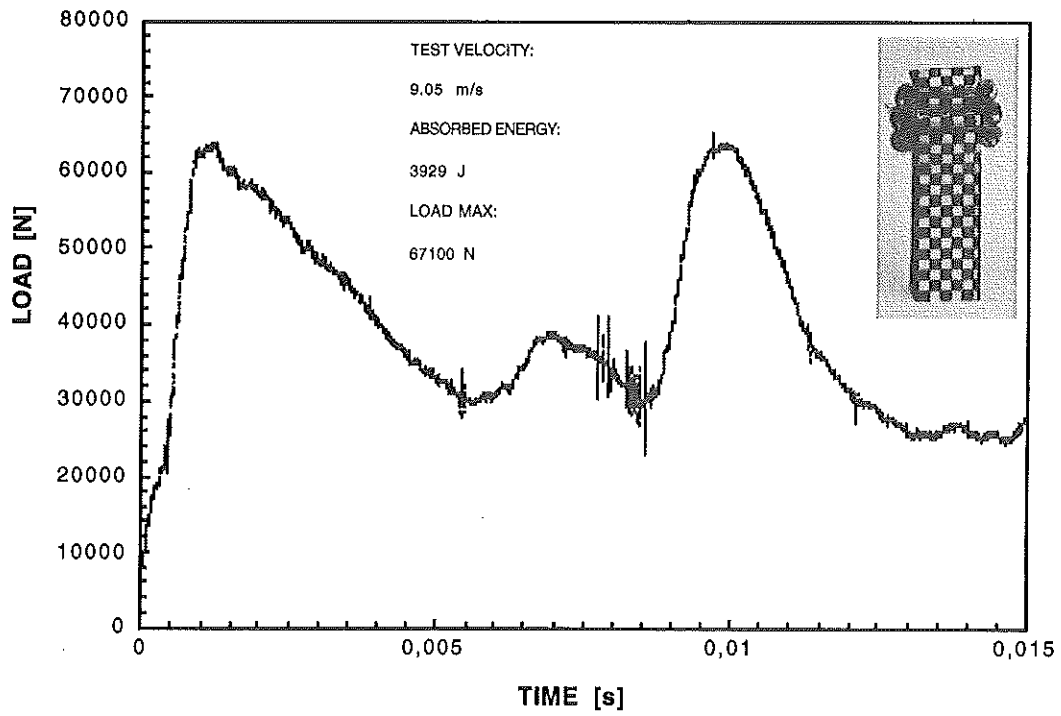


Figure 7 Load-time curve of triggered specimen

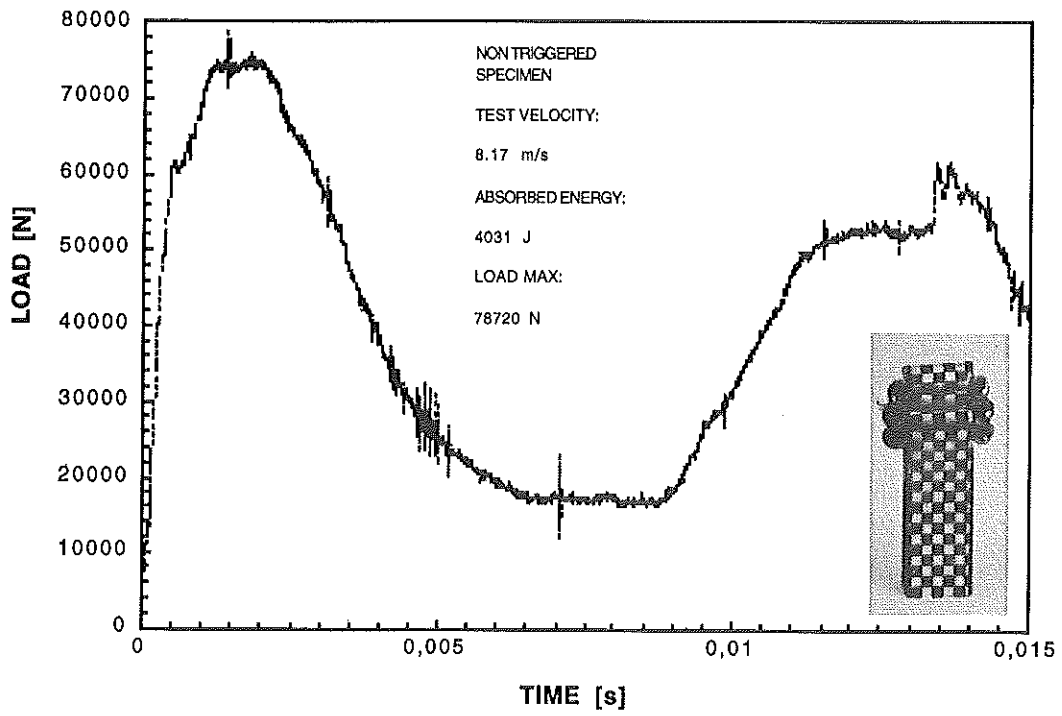


Figure 8 Load-time curve of non-triggered specimen

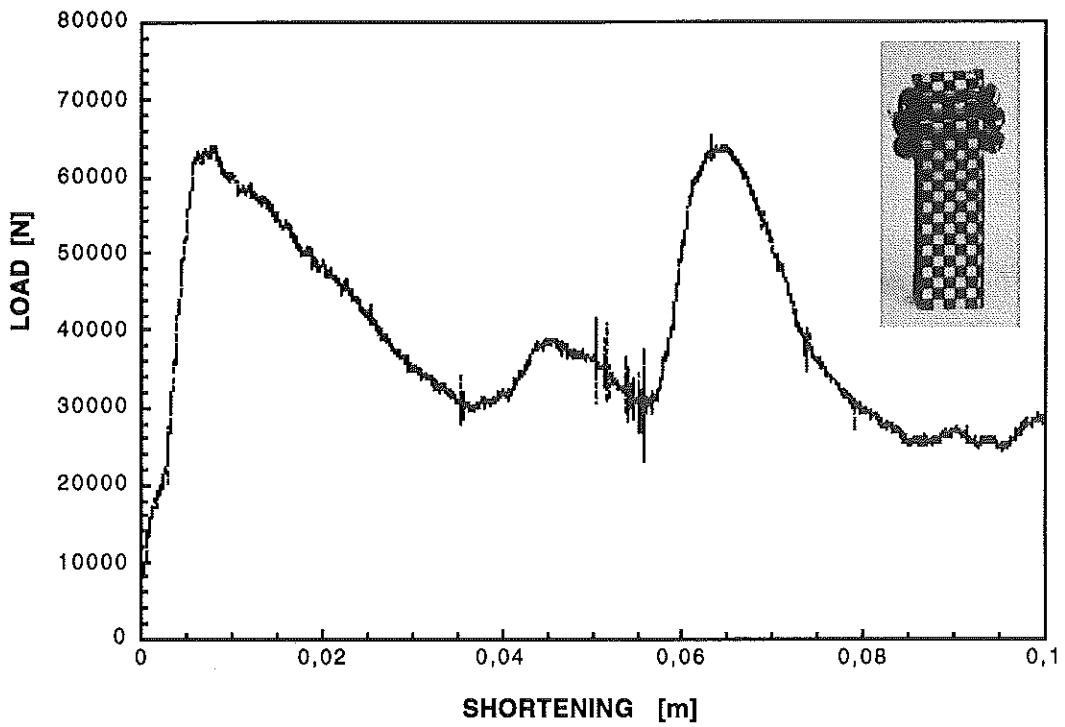


Figure 9 Load-shortening curve of triggered specimen

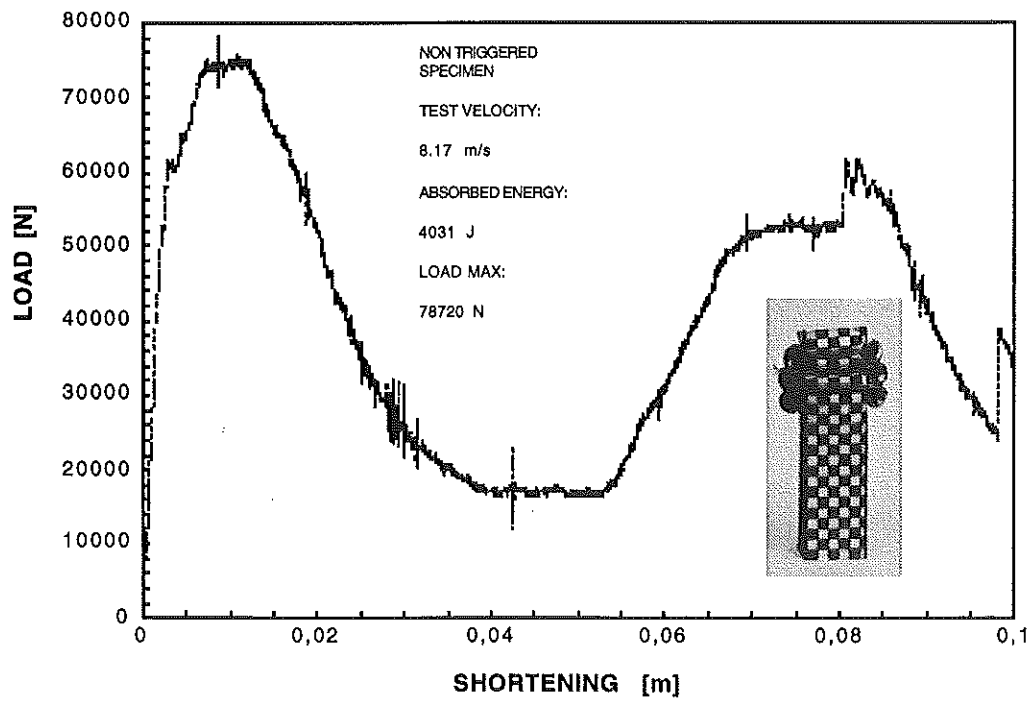


Figure 10 Load-shortening curve of non-triggered specimen

In Table 1 we have collected the energy corresponding to output load-shortening characteristic for a shortening of 100 mm, the peak output load for all the test. Also the static tests are collected.

DYNAMIC TESTS

test #	impact velocity	energy absorbed	Max. output load	Note
	[m/s]	at 100 mm short. [J]	[N]	
1	7.48	2985	59200	Batch 1, Triggered
2	8.17	4031	78720	Batch 1, Non Trig.
3	9.05	3929	67100	Batch 2, Trig.
4	10.87	3871	66023	Batch 2, Trig.
5	14.17	3664	63026	Batch 2, Trig.
6	14.88	3468	60413	Batch 2, Trig.
7	15.15	3468	70020	Batch 2, Trig.

STATIC TESTS

test #	Short. velocity	energy absorbed	Max. output load	Note
	[m/s]	at 100 mm short. [J]	[N]	
8	24.10^{-5}	3606	65760	Batch 2, Trig.
9	24.10^{-5}	3288	65280	Batch 2, Trig.
10	24.10^{-5}	4056	76051	Batch 1, Non Trig.

Table 1 Experimental results

5. DISCUSSION

The tests done on aluminium box specimens in order to analyze the structures mechanical behaviour at different velocities have shown that :

- From the observation of the strain gauges records, it results that wave propagation is the phenomenon governing the deformation and fold formation of thin sheet metal box during a crash test.
- It can be observed on the diagram load output time that each peak corresponds to a fold formation. In dynamic loading the fold formation starts from the input end on the box while by static loading the first fold is formed at different points of the box length (this concerns only the non triggered boxes).
- The folds formation is a regular repetitive phenomenon in case of aluminium with nearly equal load peaks for the triggered boxes.
- The first output bar load peak value can be checked by comparing this value to the load corresponding to the strain given by the first specimen strain gage. The load of the

first specimen strain gauge can be obtained by using the σ - ϵ material dynamic curve at the same strain rate.

The presence of trigger gives rises to a reduced value of the energy absorption both in dynamic and in static testing cases. An important point is that the trigger does not influence the first peak only but also the successive.

A direct consequence of the wave propagation is that for loads and displacements measurements the Hopkinson bar equipment gives a high level of accuracy. This can be confirmed by the following facts observed in our experiments :

-There is an accurate agreement between the folding phenomena shown by the film and the load response given by the transmission bar each peak corresponds to a fold formation [6].

- The agreement of most of the shortening values given by the film and those calculated from the measurement of the strain gages on the incident bar.

- The clear record obtained on the transmission bar which does not give an initial peak higher than the successive ones. This phenomenon also observed in the static load. confirms the low level of material strain rate sensitivity. This phenomenon is also due to the trigger effect .

- The absence of noise on the obtained strain gage records. This allows to work on a non-filtered signal allowing us to be sure not to leave out any mechanical structure response.

Finally, it is a scientific fact [1, 3, 5] that the Hopkinson bar is one of the more accurate technique to obtain a stress-strain relation at high strain rate.

This study allowed to give us a better understanding of thin sheet aluminium mechanical behaviour at impact. Some points have to be treated in more details in order to be able to make accurate Finite Element calculations [6]. One of these points should be the fold formation mechanism. This study can be done by stopping the test before the second fold formation and an other test until the second fold etc.

6. REFERENCES

- [1] DAVIES, R.M., *Critical Study of the Hopkinson's Pressure Bar*, Phil. Trans. Roy. Soc., London Ser., A. 240-375, 1984.
- [2] BIRCH, R.S., JONES, N., JOURI, W.S, *Performance Assessment of an Impact Rig*, Proc. Inst. Mech. Engrs. Vol. 202 No. C4, pp. 275-285, 1988.
- [3] LINDHOLM, U.S., *High Strain Rate Tests*, Techniques of Metals Research, Vol. 5 part 1, J. Wiley, 1971.
- [4] ALBERTINI, C., MONTAGNANI, M., *Testing Techniques Based on the Split Hopkinson's Bar*, Inst. of Physics, Conf. Ser. No. 21, London, pp. 22-31, 1974.
- [5] KOLSKI, H., *Stress Waves in Solids*, Clarendon Press, Oxford, 1953.
- [6] ALBERTINI, C., CADONI, E., CRUTZEN, Y., FRANCOCCI, P., INZAGHI, A., LABIBES, K., PETRANGELI, A., *Crash Worthiness Studies of Thin Sheet Metal Structures by Means of a Large Hopkinson bar; Benefits for Calibration of Impact Rigs and Validation of Numerical Crash Simulation*, Proceeding of International Crashworthiness and Design '95 Symposium, Valenciennes, pp. 1-14, 1995.

Testing and Modelling the dynamic behaviour of polymeric foams used in automotive industry dummies

G.Gary, L.Rota, J.J.Thomas, H.Zhao

Laboratoire de Mécanique des Solides, Ecole Polytechnique
91128 PALAISEAU CEDEX, France.

Abstract - Dummy modelling for car crash simulation using numerical implicit codes needs the knowledge of the dynamic behaviour of foam-like materials that show a strong strain rate sensitivity and can endure large strains without showing damage. In this paper, a review of recent techniques used in our Laboratory to test such materials is presented. Those techniques allow for a valuable analysis of strain-rate effects on the behaviour of soft viscous materials. A simple uniaxial model is presented for a polyurethane foam and its generalisation to a 3D model is discussed.

Introduction

To determine the response of the human body and to analyse the interaction with the inhabitant compartment, anthropomorphic dummies have been developed. The occupant protection analysis based on experimental crash dummies offers currently appreciable capabilities, but it has also limitations and, in particular, requires the need of a car prototype. Dummy modelling for car crash simulation allows for evaluation and improvement of the occupant protection in the early phases of car design and for a better understanding of biomechanical phenomena. Foam and foam-like materials are recurrent both in the crash dummies and in the occupant compartment. Modelling the dynamic behaviour of such materials is then an important goal.

Strain, stresses and strain rates observed or found in calculations for foams dynamically loaded in car crash situations are respectively in the range of 1 to 80% (nominal strain in uniaxial compression), 1 s^{-1} to 300 s^{-1} (nominal strain-rate in uniaxial compression) and less than a few MPa (Cauchy stress in uniaxial compression).

As it is commonly used for testing materials at high strain-rates (500 s^{-1}) the testing method is based on the use of Hopkinson bars. Because of low stresses, the correct testing of such media needs the use of bars made with low impedance material (such as PMMA or Nylon) which is viscoelastic. The method then takes into account the correction for wave dispersion in bars made of viscoelastic material [1]. In this method, the classical separation technique relies on the use of sufficiently long bars and a sufficiently short impulse. This, in turn, limits the measurement duration [2], [3], [4] that does not allow to obtain the simultaneously requested large strains and medium strain-rates. We present here a new method of wave separation that permits an increased time duration for measurement.

Such methods allow for measurements of forces and displacements at both ends of a specimen at various speeds of loading. A set of uniaxial stress-strain responses at various strain-rates in the requested range can be deduced and makes uniaxial modelling possible.

An example of modelling is given for a particular viscoelastic foam. It is not possible to induce the complete 3D behaviour from compression tests results only and it is difficult to make complex loadings (and furthermore associated measurements) at high strain rates. Some assumptions have then to be made, in relation with the requirements of explicit codes used for dynamic calculations.

Brief introduction to the Split Hopkinson Bar

The SHPB (Split Hopkinson Pressure Bar) system, also called Kolsky's apparatus, is a commonly used experimental technique in the study of constitutive laws of materials at high strain rates. The first use of a long thin bar to measure stresses in impact conditions has been reported by B. Hopkinson [2]. The experimental setting with two long bars widely used today is pioneered by H.Kolsky [3]. This ingenious technique for a compression test has been extended to the tensile loading by [5] and to the torsional loading by Duffy [6] with no significant changes in the concepts.

A typical SHPB test system is shown in fig. 1. It is composed of the long input and output bars with a short specimen placed between them. With the impact of a projectile at the free end of the input bar, a compressive longitudinal "incident" wave ϵ_i is created in the input bar. Once the incident wave reaches the interface specimen-bar, a part of the wave ϵ_r is reflected, whereas another part ϵ_t is transmitted to the output bar through the specimen. With gages glued on the input and output bars, these three basic waves are recorded. They allow for the measurement of forces and particle velocities at both faces of the specimen.

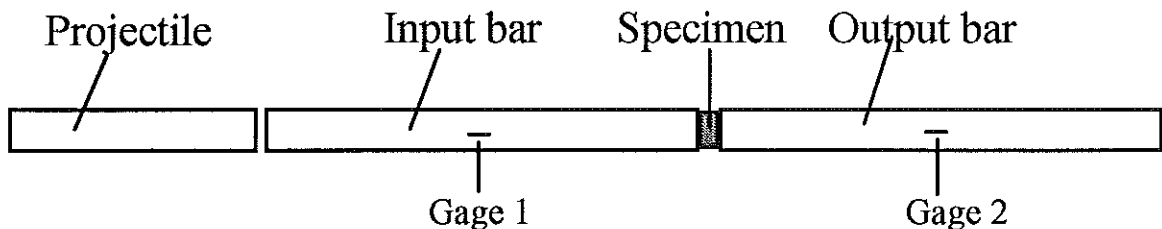


Fig. 1 SHPB test setting

The measurement is based on the knowledge of the wave propagation and on superposition principle. According to the wave propagation theory, the stress and the particle velocity associated with a wave can be accurately calculated from the associated strain easily measured by the gages. Furthermore, these values are known not only at the measuring points but everywhere in the bar because the wave can be shifted using the propagation theory. Thus, the transmitted wave is shifted to the output bar-specimen interface to obtain the output force and velocity whereas the input force and velocity are proportional to the sum of the "incident" and "reflected" waves shifted to the input bar-specimen interface.

We have then the following equations :

$$\begin{aligned} F_{input}(t) &= S_B E (\epsilon_i(t) + \epsilon_r(t)) & \text{and} & & V_{input}(t) &= C_0 (\epsilon_i(t) - \epsilon_r(t)) \\ F_{output}(t) &= S_B E \epsilon_t(t) & & & V_{output}(t) &= C_0 \epsilon_t(t) \end{aligned} \quad (1)$$

where S_B , E and C_0 are respectively the section of the bar, Young's modulus, and the speed of the waves.

Testing polymeric foams

TESTING SOFT MATERIALS

Formulas (1) show that the knowledge of output force and velocity (F_{output} and V_{output}) only needs a precise measurement of the "transmitted" wave ϵ_r . On the other hand, to have a good knowledge of input force and particle velocity, the ratio of impedance between the bar and the specimen must be in a limited range. If the impedance of the specimen is too great (compared with the impedance of the bars), ϵ_r is almost equal to ϵ_i and the value of V_{input} is not accurate. If the impedance of the specimen is too small, ϵ_r is almost equal to $-\epsilon_i$ and the value of F_{input} is not accurate. In the case of testing polymeric foams, the use of metallic bars leads to a ratio of impedance "specimen/bar" in the order of 0.001. Thus, for such specimens of weak impedance, it is indispensable to use a SHPB set-up made of weak impedance materials like PMMA or Nylon, which are unfortunately viscoelastic materials. It is then necessary to consider the wave dispersion effect in a viscoelastic bar. In the case of elastic bars this function is derived from Pochhammer and Chree's harmonic wave model [7], [8]. We have generalised this model to the case of viscoelastic bars [1] leading to a "frequency equation" similar to that of Pochhammer and Chree.

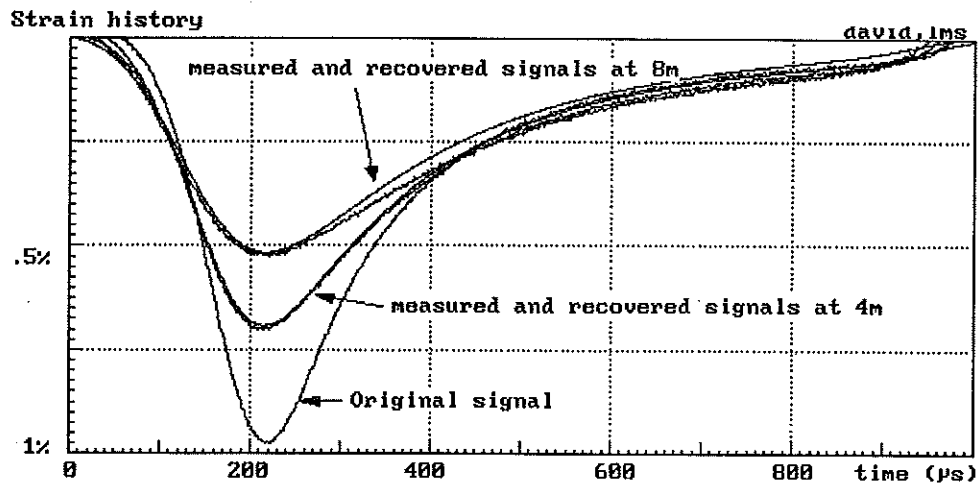


Fig. 2a Example of dispersion effects in a 40 mm diameter Nylon bar.

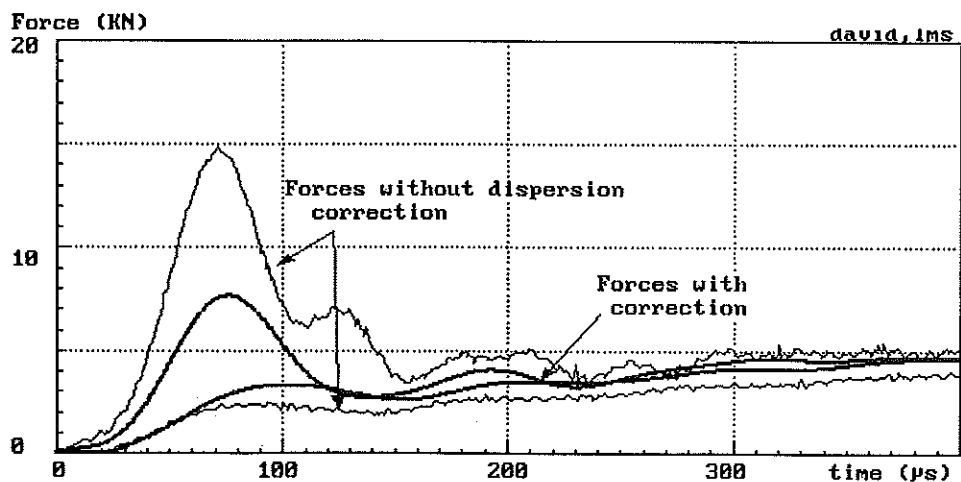


Fig. 2b Influence of dispersion correction on forces measurement

This correction is indeed more important than the correction for an equivalent purely elastic system, in particular because of a significant dumping effect. An example of the influence of this correction is shown on fig. 2a, 2b and 4c.

TESTING AT MEDIUM STRAIN RATES

LIMITS DUE TO THE CLASSICAL SEPARATION TECHNIQUE

It can be seen in Fig. 1 that the strain of the incident and the reflected waves are measured with the same strain gage (called gage 1). Those two waves are superposed at face A of the specimen and a gage situated near that place would measure their algebraic sum (which is proportional to the input force, as it appears in (1)). Calculation of the velocity (see (1)) is possible with the knowledge of the difference between those two waves but this difference cannot be determined by a direct measurement. The position of gage 1 must be chosen in such a way that the incident wave has "already gone" before the reflected wave is "coming back". The reflected wave is then again reflected at the impact end (side of the striker) of the incident bar and produces a wave that must not be superposed with the former one. Gage 1 is thus cemented to the middle of the incident bar. The duration of the incident wave (which equals to the duration of the reflected wave) is chosen to be at most equal to the time taken for a wave to reach the length of the whole incident bar (half length in a positive direction and half in the other direction). That is why the maximum length of striker is equal at most to the half of the incident bar. The time of loading applied to the specimen, proportional to the length of the striker, is then related to the length of the input bar. Consequently it can be easily shown [9] that the maximum measured strain is related to the average strain-rate by the following formula :

$$\epsilon_m \approx \alpha \tau \dot{\epsilon}, \quad \alpha \leq 1$$

where τ is the duration of the incident wave and α a coefficient depending on the specimen impedance that is close to 1 when this impedance is small in comparison of the one of the bars.

It is thus impossible to obtain significant strains for low strain rates (for an average strain rate of 100 s^{-1} , the limit of the Nylon set-up for foam testing, with a 3m long input bar, gives a maximum strain of about 10%).

AN IMPROVED SEPARATION TECHNIQUE

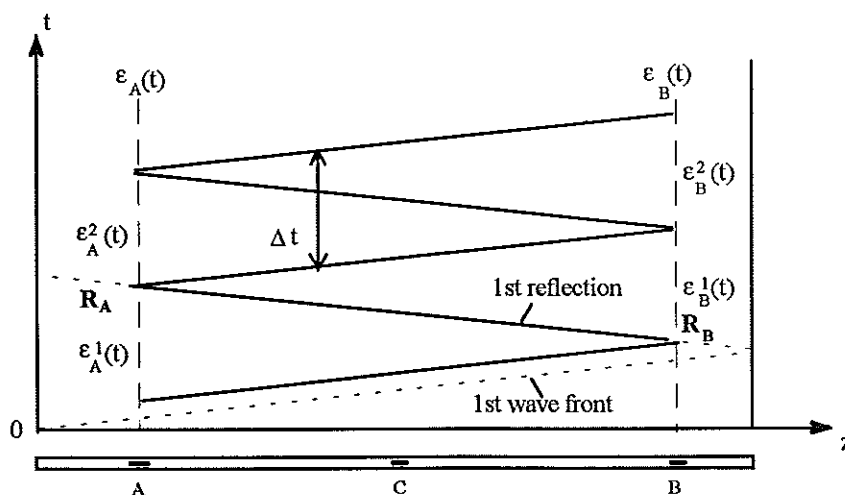


Fig. 3 Strain history analysis

The strain history in each bar is recorded by two strain gages at distinct points A and B. Since the recorded strain is the sum of the contributions of the two waves propagating in opposite directions, precise prior knowledge about one wave will allow the contribution of the other one to be calculated. Thus, from the measurement of strain associated with one wave, we can (presuming that we know precisely how the waves propagate) iteratively determine the value of the opposing wave at any instant and at any point. In practice, we decompose the two strain measurements into time intervals of finite length (fig. 3).

Let $\epsilon_A(t)$ and $\epsilon_B(t)$ be the two strains recorded at points A et B. The following functions $\epsilon_A^1(t), \epsilon_A^2(t), \dots, \epsilon_A^i(t)$ are then built in point A. Each function $\epsilon_A^i(t)$ is the product of $\epsilon_A^1(t)$ by the support function of the interval $[(j-1)\Delta t, j\Delta t]$ where Δt is the time for the wave to travel twice the distance between A et B. One then has :

$$\epsilon_A(t) = \sum_k \epsilon_A^k(t)$$

The functions $\epsilon_B^1(t), \epsilon_B^2(t), \dots, \epsilon_B^i(t)$ are built in the same way at point B, using equivalent time intervals shifted in time by $\Delta t/2$. (Fig. 3).

The propagation being known in the bar, and assuming that $\epsilon_{AI}^1(t)$ is already known at point A, the i -th contribution $\epsilon_{BI}^1(t)$ of the wave propagating towards the positive z axis ("ascending" wave) at point B is deduced of $\epsilon_{AI}^1(t)$ in the following way :

$$\epsilon_{BI}^1(t) = f_{A,B}(\epsilon_{AI}^1(t)) \quad (2)$$

where $f_{A,B}$ describes the shifting function between A and B (taking into account the wave dispersion effect). The contribution $\epsilon_{BR}^1(t)$ at point B of the wave propagating towards the negative z -axis (the "descending" wave) is the difference of the measured value $\epsilon_B^1(t)$ at point B and of the "ascending" wave $\epsilon_{BI}^1(t)$ at that point.

$$\epsilon_{BR}^1(t) = \epsilon_B^1(t) - \epsilon_{BI}^1(t) \quad (3)$$

In a similar way, $\epsilon_{AI}^{i+1}(t)$ is calculated taking into account the known value $\epsilon_{BR}^i(t)$.

The first interval at point A contains the single "ascending" (incident) wave induced at one end of the bar before it reflects at the other end. Using equations (2) and (3) we can calculate the "ascending" and the "descending" waves at point B corresponding to this interval. Continuing in this way, both the "ascending" and the "descending" waves can be calculated for all the intervals.

The shifting function, which takes into account the wave propagation dispersion and dumping effects, plays a very important role in this method. By way of example, fig. 4a shows the strain recordings at points A and B of an elastic bar. Using our separation method, we can recover the strain history at any point of the bar and, in particular, at its middle point C, where the "ascending" and "descending" waves are separate. Fig. 4b illustrates the comparison at this point between the measured value and the equivalent theoretical recovered value. In fig. 4c, the importance of having an accurate shifting function is underlined by comparing with a theoretical recovered signal, obtained by means of a shifting function within the simple one-dimensional model.

This method eliminates the time duration limitation of the classical SHPB measurement system. Indeed, the "ascending" and "descending" waves are separately know and they are used in place of the "incident" and "reflected" waves in formulas (1). The important consequence is that it enables the accurate SHPB technique to be extended to the domain of dynamic testing at medium strain rates. Until now, experimental methods in this domain have used fast hydraulic machines for which no measurement methods of equivalent accuracy exist.

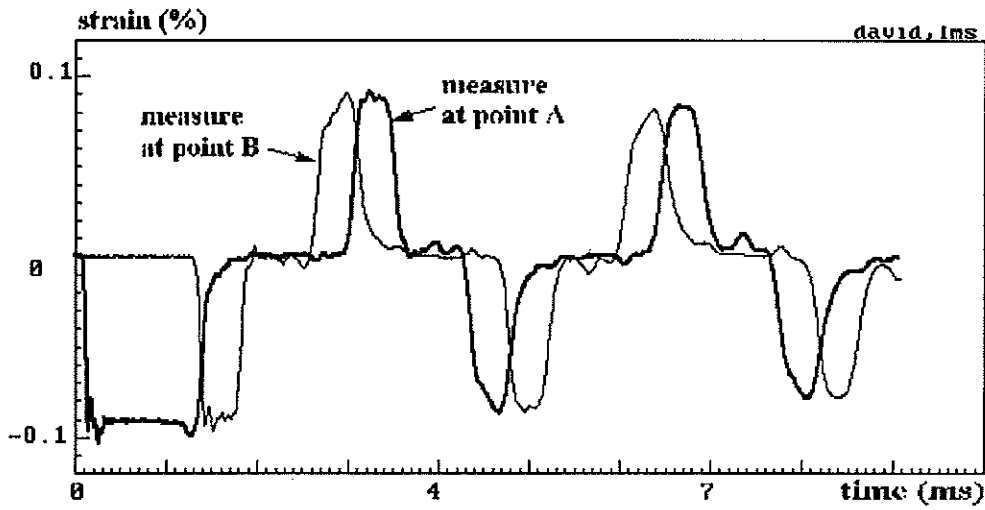
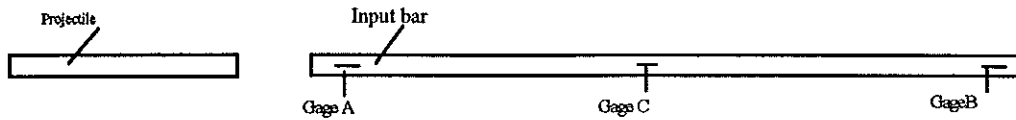


Fig. 4a Recorded signals at points A and B.

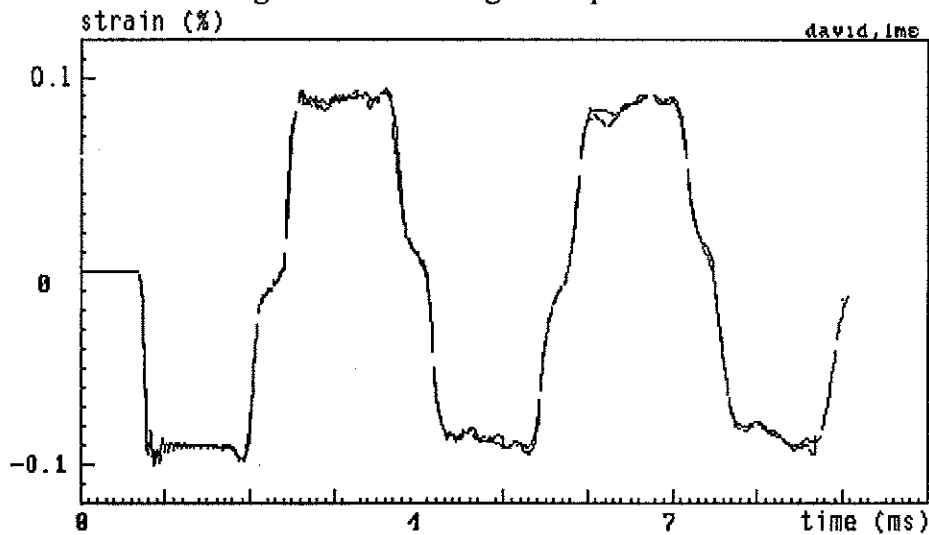


Fig. 4b Comparison between measured and 3D (complete) recovered value.

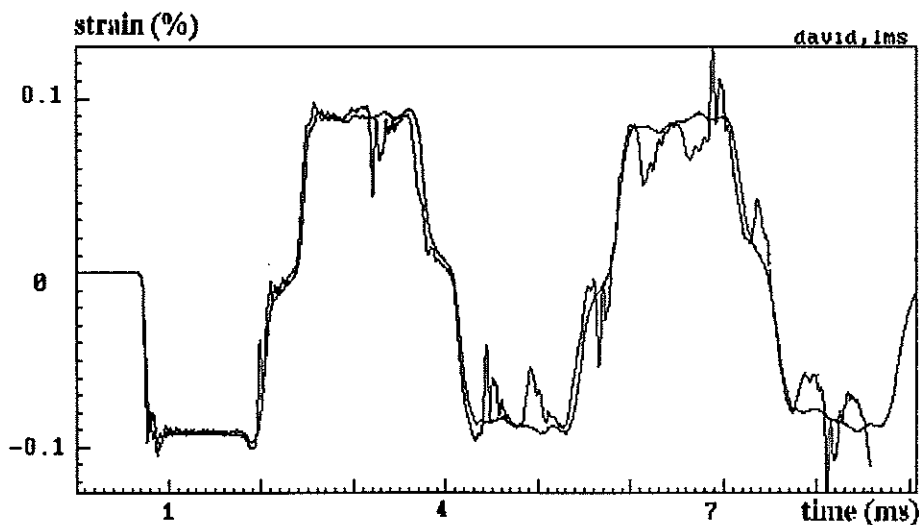


Fig. 4c Comparison between measured and 1D recovered value

TESTS RESULTS ANALYSIS

The finite value of the elastic wave speeds in materials leads to the fact that a period exists, at the beginning of the test, where the input and output forces cannot be equal. In particular, the output force is equal to zero as long as the first wave induced by the loading has not been transmitted through the specimen. This period will be short in respect to the test duration when the elastic wave speed in the material tested is high. The most ideal situation occurs for metals. The hypothesis of the homogeneity of the forces in the specimen is then reasonable and the standard analysis gives correct results even in the elastic phase of the specimen deformation [10].

However, as it appears in formulas (1), the Hopkinson bar technique allows for determination of the input and output forces (on each side of the specimen). The departure from the equality of both forces can thus be verified. When the two forces are very different, as it is often the case with foams, it has to be taken into account. In this case, the assumption of homogeneity must be discarded and inverse calculation procedure be performed [11], [12].

Application to a polyurethane foam

1D MODELLING

A set of experimental results obtained in compression in an exceptionally wide range of strain rates is used. Quasi-static tests have been done at a constant speed of loading [13] and it is then assumed that the nominal strain rate is constant in such tests (starting at $1.6 \cdot 10^{-3} \text{ s}^{-1}$, test [a] fig. 5). Results at medium strain rates are obtained using the deconvolution technique with Hopkinson bars loaded by a fast hydraulic system (10 and 60 s^{-1} [b] and [c] fig. 5). Finally, a classical Nylon Hopkinson bar provides results at fast speeds (here 210 s^{-1} , [d] fig. 5).

The tested material never shows a permanent strain enough time after the test, so that it has obviously a viscoelastic behaviour. We use then a non-linear Voigt model.

As it is described in [14] (and as it is seen on the loading part of curve [a] in fig. 5) the uniaxial response shows, in a first phase, a linear relation at small strains (less than a few percents) corresponding to the elastic response of the matrix (polymer) without micro-structural effects. This linear part is followed, in a second phase, by a long plateau (here up to more than 50%) corresponding to progressive buckling of cells and then, in the third phase, by a fast increase of the stress attributed to the densification of the material. The first phase is easily modelled. The separation between the second and the third phase being not obvious, the last two phases are described by a non-linear model in the form of (4). The coefficient k depends on the intrinsic elastic properties of the matrix and h represents an asymptotic strain supported by the material. Such materials show a very small apparent Poisson's ratio so that h could be close to the proportion of voids in the unloaded material. It also means that the stress linearly depends on the current density of the material, which gives an acceptable physical meaning to the model. For some materials, no significant damping effect is observed at quasi-static strain rates and the identification of the non-linear hypo-elastic part of the behaviour becomes obvious.

Experimental observations shows that the strain-rate effect decreases with the strain rate increase. Considering the viscous part, it is assumed that the viscosity depends on the quantity of the matrix' material involved in the deformation process (in the same way of the elastic stress and for similar reasons) and, of course, on the strain rate. The influence of the temperature, indeed important here, is not taken into account in this analysis and all the tests are done at the constant temperature of 22°C . Nevertheless, knowing that the behaviour of polymers is temperature sensitive and generally verifies the classical time-temperature relation [14], we assume, that the

viscosity of the matrix is linearly dependant, in a classical double logarithmic scale, on the strain-rate. The viscous part of the stress is then described by (5) :

$$\sigma_e = \frac{k}{h - \varepsilon} \quad (4)$$

$$\eta(\varepsilon, \dot{\varepsilon}) = \frac{\exp(a + b \cdot \ln|\dot{\varepsilon}|)}{h - \varepsilon} \quad (5)$$

Consequently, the unidimensional behaviour of the foam, is described by the following incremental relation :

$$d\sigma = \left[\frac{h}{\varepsilon_0} \frac{(h - \varepsilon_0)(\sigma_0 - B)}{(h - \varepsilon)^2} + \frac{Bd^2(d + 2\varepsilon)}{(d^2 + d\varepsilon + \varepsilon^2)^2} \right] d\varepsilon + \left[\eta + \frac{\partial \eta}{\partial \dot{\varepsilon}} \dot{\varepsilon} \right] d\dot{\varepsilon} + \left[\frac{\partial \eta}{\partial \varepsilon} \dot{\varepsilon} \right] d\varepsilon \quad (6)$$

where B and d shape the plateau and correspond to the first phase of the response. $(\varepsilon_0, \sigma_0)$ is a point of the elastic loading curve, and h the previously defined asymptotic strain. The first bracket describes the elastic part of the stress and the last two the viscous part.

As it can be observed in fig. 5, this simple model based on physical considerations gives good results for a very large range of strain-rates. It also correctly describes unloading paths.

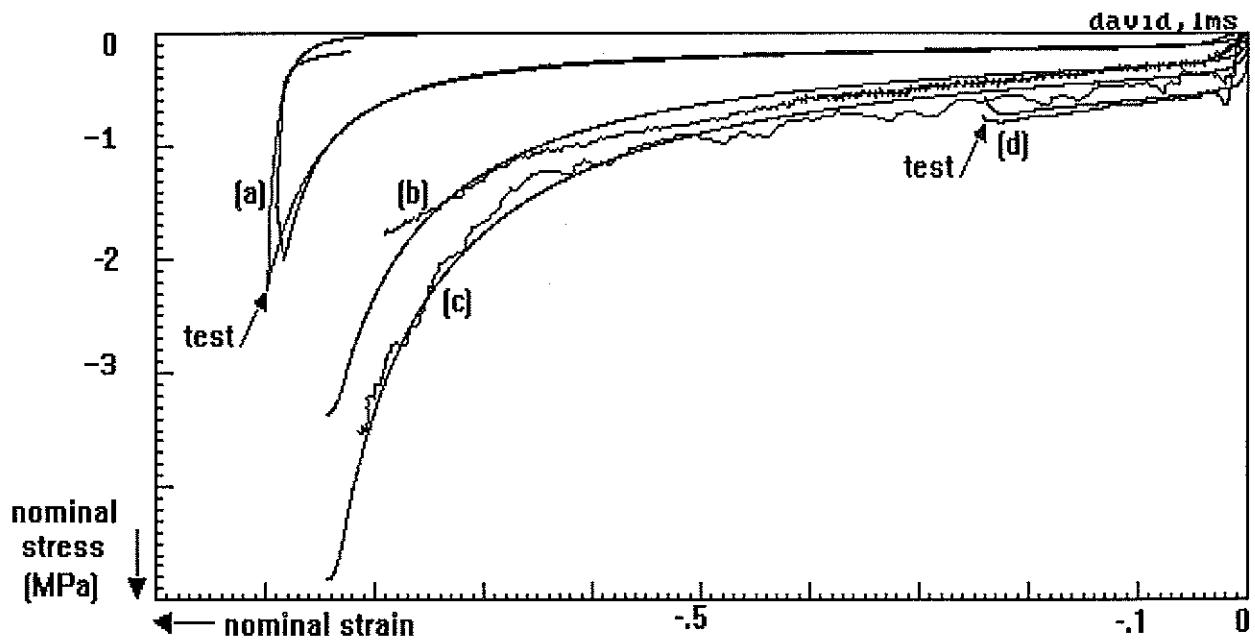


Fig. 5 Experimental results on foam. Comparison with a model.
(strain rates from $1.6 \cdot 10^{-3}$ to 210 s^{-1})

3D MODELLING

In case of 3D modelling, and especially when large strains are found, a special attention must be given to the definition of strain and stresses. Nevertheless, considering that we are in the dynamic field and that F.E.M. explicit codes are to be used, we will use the Cauchy stress (also called "true stress") and the actualised Lagrangian strain (also called "true strain"). The above formulas in the 1D situation have to be translated.

A more general form than (6) of an incremental constitutive law is expressed in the following way :

$$d\sigma = f(d\varepsilon; \varepsilon, \dot{\varepsilon}, \ddot{\varepsilon}, \dots, \alpha_i, \dots) \quad (7)$$

where α_i are internal parameters that take account of the history process. Their evolution must be simultaneously given.

In formulas such as (7) expressed in the 3D situation, stresses, strains and their derivatives are tensorial values. If it is written with scalar values, this formula will lead to a significant

number of equations. It means, in particular, that there is not one single definition of what is commonly called **the** strain rate. Because of that kind of reasons, and also because the number of simple dynamic tests available is limited, modelling in 3D needs various assumptions.

SMALL STRAINS SITUATION

An incremental stress-strain relation can always be linearised and considered as an elastic one. If the material is isotropic, it can be assumed that this incremental relation is described with only two parameters, μ and λ being given :

$$d\sigma = 2\mu d\varepsilon + \lambda \text{tr} d\varepsilon$$

Those two parameters will of course depend on the current state, the history of loading, the strain rate, the loading path (loading or unloading) and so on...

$$\lambda = \varphi(\varepsilon, \dot{\varepsilon}, \ddot{\varepsilon}, \alpha_i \dots)$$

$$\mu = \psi(\varepsilon, \dot{\varepsilon}, \ddot{\varepsilon}, \alpha_i \dots)$$

One can then think of measuring those parameters in simple tests like compression or shear tests. Considering the present stress-strain point (where the stress increment must be calculated), the problem to be solved is to relate this point to one point of a test where those parameters have been measured. The stress, the strain, the strain-rate states (and so on...) are different in the calculation and in the test so that a choice of parameters to be identified must be done. It is very common that this choice is done following the hypothesis of plasticity, assuming that the spherical and the deviatoric behaviour are uncoupled and that the non reversible behaviour is purely deviatoric. Such a choice is wrong in most cases, except for metals. For other materials, concrete for instance, the spherical and the deviatoric behaviour are also considered independently but can both show non reversible responses and coupling must be taken into account. This kind of model might give correct results when the real loading paths are simple.

Modelling in 3D on the basis of considerations of separate spherical and deviatoric behaviour is a rather easy way to generalise 1D tests' results but it needs strong hypotheses that are very difficult to check.

LARGE STRAINS SITUATIONS

In this case, even when the material is initially isotropic, it becomes at least transverse orthotropic under large strains (axial compression for example) and the number of coefficients to describe the incremental elastic behaviour increases (at least up to five). The material presented in this paper is of that kind and the evidence of the current volumic mass acting as a parameter will be taken into account in 3D modelling.

Conclusion

It is shown, in this paper, that studying the uniaxial behaviour of soft foams is possible with the Hopkinson bar technique. Low impedance bars made of a viscoelastic material, with an adapted dispersion correction method, allow for the measurement of weak forces (and then stresses - in the order of 1 MPa -). Using a special processing, based on a deconvolution method, for the signals recorded at two points of each bar, it is also possible to test foams at medium strain-rates (from 1 to 200 s⁻¹).

The knowledge of the response of a material in a wide range of strain-rates helps for a better understanding of the physics and for constitutive modelling. An example is given for a polymeric foam. Its uni-dimensional behaviour is correctly described by a rather simple constitutive model.

Physical assumptions have still to be checked by complementary observations and analysis. Some simple dynamic tests under combined loading (dynamic loading of statically pre-strained specimen, for example) will complete this knowledge and help for developing a 3D model.

References

- [1] Zhao H., Gary G. "A three dimensional analytical solution of the longitudinal wave propagation in an infinite linear viscoelastic cylindrical bar. Application to experimental techniques." J. Mech. Phys. Solids, Vol 43, n°8, pp 1335-1348, 1995, Pergamon press.
- [2] Hopkinson B., "A Method of measuring the pressure in the deformation of high explosive by impact of bullets", Phil. trans. Roy. Soc. of London, Series A.213, 1914, p. 437-452.
- [3] Kolsky H., "An investigation of mechanical properties of materials at very high rates of loading", Proc. Phys. Soc., Sec. London, Series B62, 1949, p. 676-700, 1949.
- [4] Kolsky H. , Stress Waves in Solids, Clarendon Press, Oxford, 1963.
- [5] J. Harding, E.D.Wood and J.D. Campbell, "Tensile testing of materials at impact rate of strain", J. Mech. Engng. Sci., 2, 88-96, 1960
- [6] J. Duffy, J.D. Campbell and R.H. Hawley, "On the use of a torsional split Hopkinson bar to study rate effects in 1100-0 aluminium", J. Appl. Mech. 38, 83-91, 1971
- [7] L. Pochhammer, J. für die Reine und Angewandte Mathematic, 81, 1876, p. 324.
- [8] C. Chree, Cambridge Phil. Soc., Trans. 14, 1889, p. 250.
- [9] G. Gary and H. Zhao, "Etude expérimentale du comportement dynamique des matériaux composites", Conférence AMAC (Lyon, juin 1993), Annales des composites, numéro spécial 1993, Editions AMAC Lyon.
- [10] G.Gary, J.R.Klepaczko, H.Zhao "Correction de dispersion pour l'analyse des petites déformations aux barres de Hopkinson", JOURNAL de PHYSIQUE IV, Colloque C3 (DYMAT 91), suppl. au Journal de Physique III, Vol. 1, octobre 1991, Les Editions de Physique, Avenue du Hoggar, Z.I.de Courtaboeuf, BP 112, 91944 Les Ulis Cedex A, France
- [11] G. Gary and H. Zhao, "Inverse methods for the dynamic study of non-linear materials with a Split Hopkinson Bar", Proceeding of IUTAM, Victoria, B.C. Canada, 1993
- [12] L. Rota, "An inverse approach of identification of dynamic constitutive equations", International symposium on inverse problems, Ed. Balkema, 1994
- [13] V.Kefalas, N.T.U.A., Athens, Private communication, 1995
- [14] L.J. Gibson and M.F. Ashby, Cellular Solids-Structure and Properties, Pergamon Press, 1988

gany peut faire essais semblables

COMPARISON OF CRASH RESULTS ON ALUMINIUM EXTRUSIONS AT SEVENTEEN LABORATORIES *

by

El Hadj A. HANEFI

Laboratoire de Biomécanique et de Sécurité des Usagers - INRETS
109 Avenue Salvador Allende
F-69675 Bron Cedex, France.

and

Tomasz WIERZBICKI **

Impact and Crashworthiness Laboratory, Room 5-218
Massachusetts Institute of Technology
Cambridge, MA 02139, USA.

ABSTRACT

Quasi-static and mass impact tests were performed on 60 x 60 x 400 mm extruded aluminium profiles (6063 T7) at fourteen European laboratories. The tubes had thicknesses of the adjacent walls of respectively 1.7 and 3.4 mm and a triggering dent with 2.5 mm depth.

Dynamic tests were run with two impact velocities of 8.33 m/s (30 km/h) and 13.88 m/s (50 km/h) and impacting masses ranging from 50 to 500 kg. Various definitions of a mean crushing force were introduced and a large spread (up to 15 %) of the measured force on apparently identical specimens were found.

In addition to test results, the impact problem was modelled by five laboratories using four leading numerical codes (ABAQUS, PAM-CRASH, LS-DYNA 3D and CASH CAD). Again differences up to 15 % in peak load and the mean crushing force were reported between various computer runs.

It is concluded that there are no absolute values of crashworthiness parameters. In interpreting experimental and/or numerical results one has to expect (and accept) a ± 10 % error (or spread) of data for industrial applications.

grande dispersion sur le 1^{er} pic : 70 à 210 kN

* : To be presented at the 9th DYMAT Technical Conference "Material and Structural Modelling in collision research".

** : Presently a Visiting Scientist, BMW AG, Abt. EG - 10, 80 788 Munich, Germany.

9th DYMAT Technical Conference
Material and structural modelling in collision research
TUM, Munich (Germany)
October 10-11th, 1995

Ship Collision - Experimental and Numerical Analysis of Double Hull Models

By

Solvejg Qvist, DEMEX Consulting Engineers A/S
Karl Brian Nielsen, Aalborg University
Michael H. Schmidt, Burmeister & Wain Shipyard A/S
Steen Hjelm Madsen, DEMEX Consulting Engineers A/S

Introduction

Focusing on some major grounding and collision accidents in the past few years, for example the grounding of EXXON VALDEZ in 1989 and the rock collision of the Norwegian passenger catamaran SEA CAT in 1991, there is indeed a growing attention to the safety of ships. Together with education of crew members and development of navigation systems, the improvement of the ship design is also important in order to improve the grounding and collision safety. This means that it has become relevant to seek new methods for designing ships as stated by Lord Donaldson /1/.

Today, the analysis of collision safety by crash tests and explicit finite element calculations is an integrated part of the design process in both the automobile and aircraft industry. Although the explicit finite element method is valued as a powerful tool in these fields, it is only little if at all employed in practical ship design. Compared to traditional semi-analytical methods, e.g. Minorsky /2/ and Amdahl /3/, explicit finite element calculations should have an advantage in producing more information about deformations and collapse mechanisms of the ship structure. However, before the explicit finite element method is usable for ship design, the method must be tested on geometries and materials at collision speeds, which are typical for ship structures. Some recent studies in this direction have been done by Kuroiwa /4/ and Lenselink, Thung /5/.

DEMEX Consulting Engineers A/S has in co-operation with Burmeister & Wain Shipyard A/S and Aalborg University carried out a project with the purpose of evaluating the usage of numerical methods in calculating the collision strength of ship structures. The project has been sponsored by the Danish Agency for Development of Trade and Industry.

In pursuit of this aim collision tests were performed on two different full scale models; a beam model and a stringer model (see Figure 1), each representing a part of a typical double hull shipside. Moreover, comparative calculations were made with the commercial dynamic non-linear finite element program, LS-Dyna3D /6/.

This paper describes the experiments and the numerical calculations which were carried out on the stringer model. Furthermore, some conclusions concerning the application of explicit finite element method for ship design are given.

Description of the model

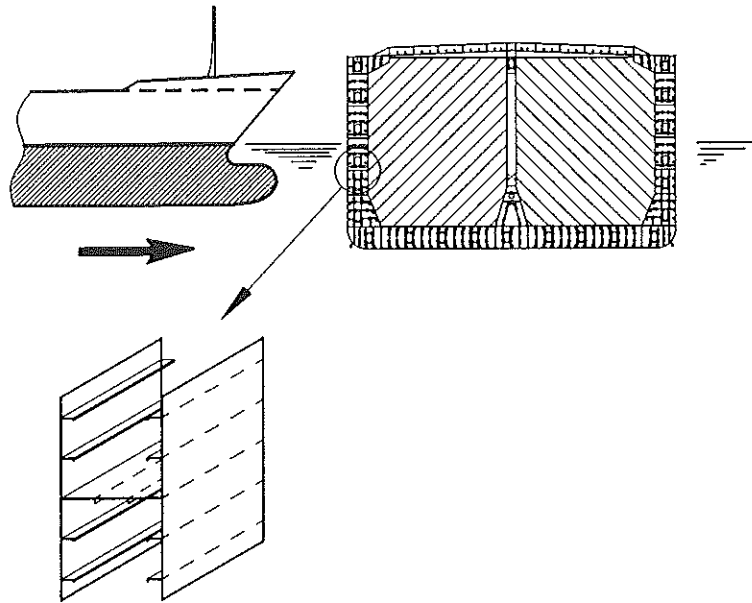


Figure 1. Double hull shipside structure.

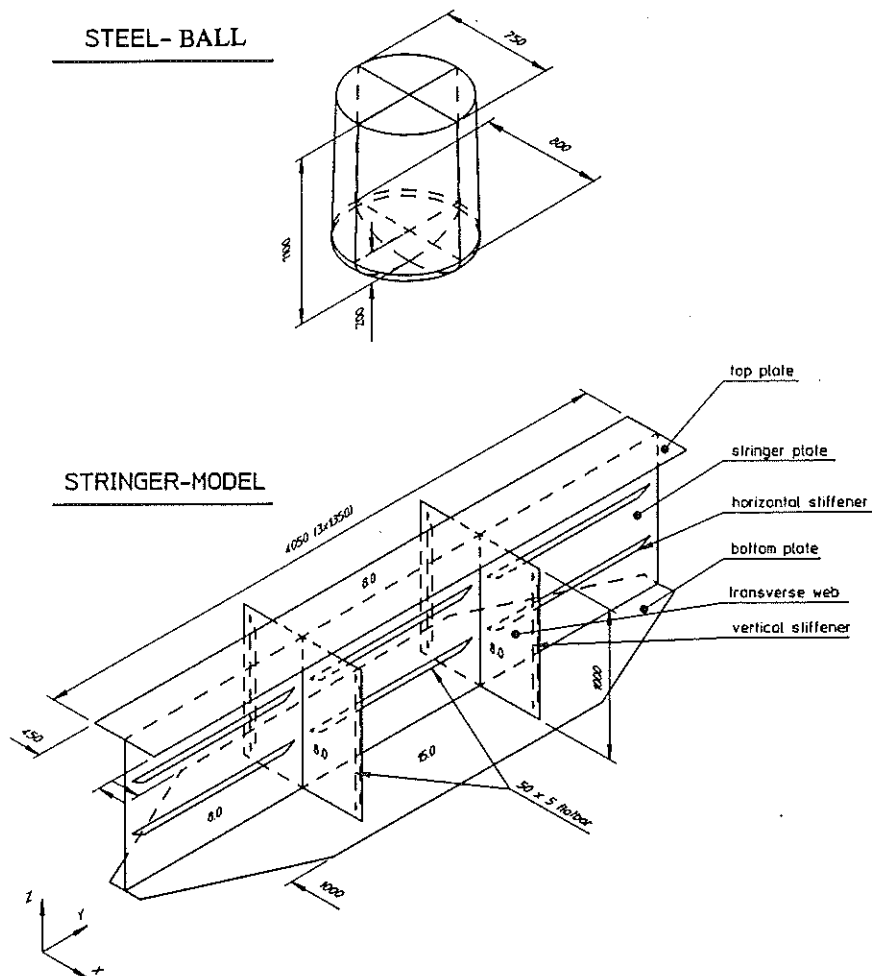


Figure 2. Stringer model and steel ball for experimental set-up.

Two identical stringer models were built of typical mild steel (classified as Norske Veritas Normal Strength with a yield stress of minimum 235 N/mm² and a tensile strength of 400 - 490 N/mm²) at B&W's shipyard in Copenhagen. The plates were joined by 3 mm fillet weldings. These structural unit models are part of side structures of a Handy Size Tanker in scale 1:1 (approximately 40,000 tonnes deadweight), which corresponds to Large Tankers (> 100,000 tonnes deadweight) in scale 1:2. The geometry of the model with overall dimensions is illustrated in Figure 2.

Compared to the side shell of the struck ship, the bow of the striking ship can be assumed rigid. Therefore a 2.75 tonnes steel demolition ball with dimensions as illustrated in Figure 2 was used to represent the bow of the striking ship.

The experimental set-up was judged to be representative for a side impact with the penetration direction perpendicular to the target side. As far as the stroke is assumed limited, the bottom plate will only be deformed to a certain degree. Compared to a real ship side structure the primary difference is the lack of longitudinal stiffening, which, to a considerable degree, would stiffen the side structure due to membrane effects. However, as the primary aim is to evaluate deformation modes, damage evolution and efficiency of the explicit finite element method, the set-up was found suitable.

Experimental analysis

The steel ball was dropped from 5 metres height, thereby having a collision speed of 10 m/sec or approximately 20 nautical knots. This speed exceeds that of conventional Bulk Carriers and Tankers, but corresponds well with the speed of for example Ferries. Because the steel ball was allowed to drop freely, it was not possible to hit the centre of the model exactly. Therefore the bottom point of the steel ball was marked with paint in order to identify the point of impact.

The model was placed on a concrete floor which in the analysis was assumed to be rigid, and four solid steel deadweights, each weighing 500 kg, were positioned on the bottom plate near the corners, see Figure 3.

Three accelerometers were mounted onto a block, which was bolted to the underside of the top plate near the point of impact, see Figure 4. Thus time dependent accelerations could be measured in three directions. By post-processing, the signals were integrated into velocities and deformations.

The experiments were recorded on high-speed-video (400 pictures per second). From these recordings, the duration of the penetration could be determined to 55 milliseconds. The recordings also showed a maximum penetration (elastic and plastic deformation) of about 240 millimetres, which corresponds to 1.3 times the residual deformation. Figure 3 illustrates the first model at the time of maximum penetration. Further the recordings show that the deadweights were thrown several centimetres up, as the ends of the model bent up.

After the experiments the models were examined and measured in order to obtain some characteristics of the damage picture. The damages - identified as buckling of the stringer plate and the horizontal stiffeners and weld failure between stringer plate and top plate - were limited to the region between the transverse webs, see Figure 4.

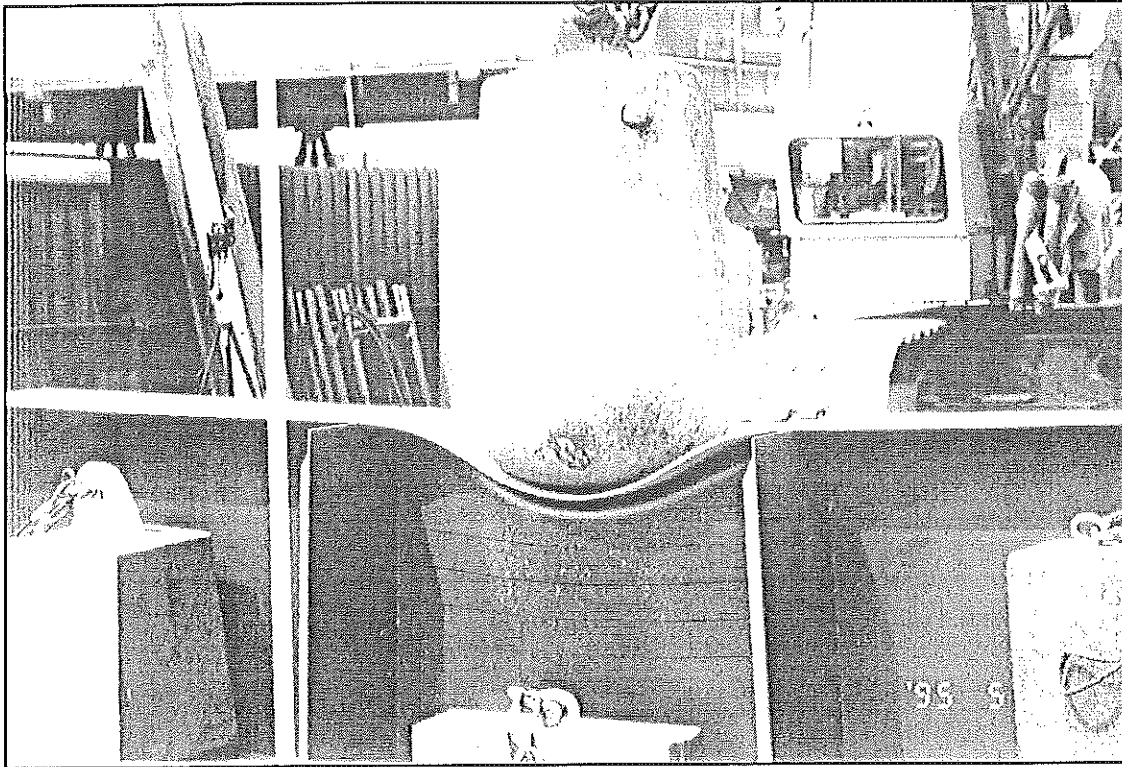


Figure 3. Showing 1st test model at time of maximum penetration.

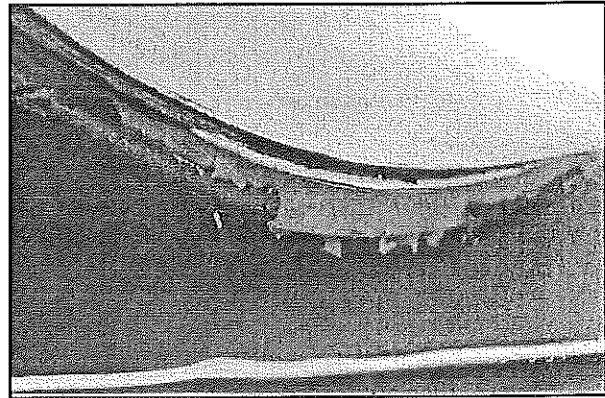
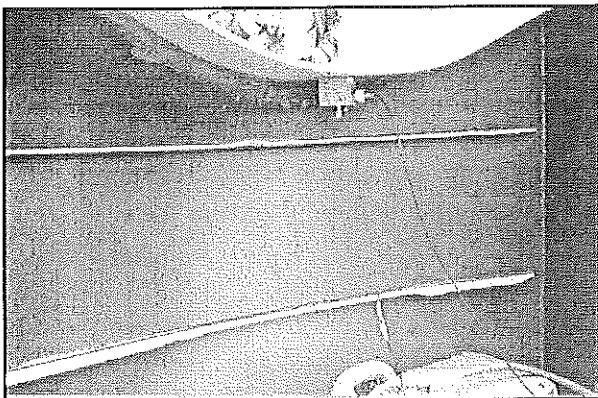


Figure 4. Damages caused by the impact are identified as buckling of stringer plate and horizontal stiffeners plus weld failure between stringer plate and top plate.

In the two tests carried out, the ball hit the model 35 and 20 millimetres from the centre line. As illustrated in Figure 8 the result was two slightly different damage pictures. By comparing the cross-sections of the models an extra fold on the stringer plate could be identified on the second test model. The residual penetration at the centre line was respectively 190 and 175 millimetres.

The weld failure can be described as tearing out the weld of the steel plate - or in other words, initial cracking of the steel plate occurred at the weld. This is in agreement with observations made in a Dutch-Japanese project on full scale ship collision tests /7/. The weld failure occurred on a total length of 350 and 200 millimetres respectively located symmetrically to the centre point.

Other characteristic measures were a decrease in distance between the transverse webs at the top plate of respectively 75 and 50 millimetres and a lifting of the bottom plate at the ends of respec-

tively 47 and 27 millimetres, see Table 1.

The differences in the experimental results indicate that some uncertainty is present and evaluation of the numerical results must be made with this aspect in mind.

Numerical analysis

The commercial dynamic non-linear finite element program LS-Dyna3D /6/ was used for the numerical analysis. The program was selected, due to its explicit formulation, which was evaluated to be most efficient for this type of problem. The code is especially suitable for problems involving many elements and extreme non-linearities at high deformation velocities. The maximum allowable timestep depends on the size of the smallest element, and the solution time (CPU-time) is proportional to the number of elements. The simulation was performed on a Silicon Graphics R4000 workstation with 43000 steps during an analysis and approximately 10 hours of CPU-time was needed in order to analyze the stringer model.

The finite element method was not only used to reproduce the experiments, but was also, to a considerable extent, involved in the test preparations. Thus, preliminary simulations were performed prior to the experiments. On behalf of these simulations the weight of the steel ball and the drop was chosen. Also the necessity of the deadweights was realized, since the simulation showed, that the ball would have penetrated straight through the model without these. The preliminary calculations, where a 3.5 tonnes ball was assumed, predicted a maximum penetration of 270 millimetres.

In the final simulations the weight and geometry of the steel ball and the geometry of the model and deadweights were adjusted. Furthermore weldings, gravity and strain rate effects were introduced and the mesh density was increased near the impact point. 4440 4-node shell elements of the Belytschko-Lin-Tsay type were used to model the ship side structure.

In the calculations it was simulated that the steel ball hit the model centrally between the transverse webs with an initial speed of 10 m/sec and stopped due to reaction force from the model. The model was placed on a rigid plate, and also the steel ball and the deadweights were modelled as rigid bodies. Plots of the model at time of maximum penetration are illustrated in Figure 5 and 6.

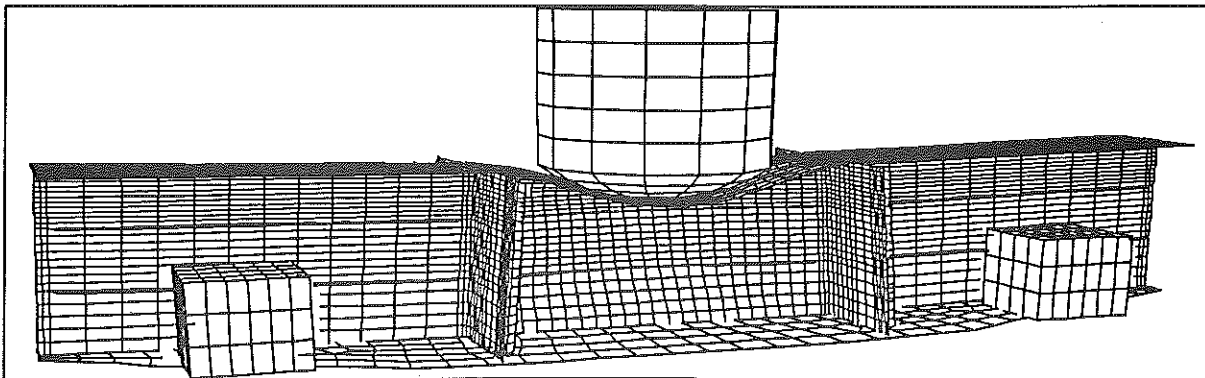


Figure 5. FE-model at time of maximum penetration.

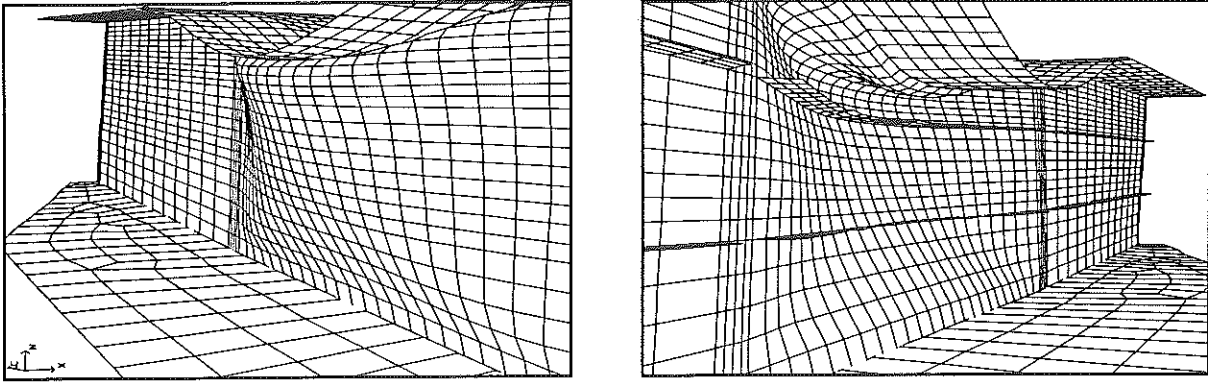


Figure 6. FE-model at time of maximum penetration from both sides.

The constitutive behaviour of the steel plate was modelled using Power Law Plasticity, where the parameters were determined by tension tests on the plate used for the models:

$$\sigma_y = k \cdot (\epsilon_e + \epsilon_p)^n$$

where σ_y = static yield stress (350 N/mm²)
 ϵ_e = elastic strain
 ϵ_p = plastic strain
 k = strength coefficient (735 N/mm²)
 n = hardening exponent (0.17)

Strain rate effects were accounted for by using a Cowper and Symonds strain rate model with empirical strain rate parameters determined experimentally on a similar steel in [4]:

$$\frac{\sigma_d}{\sigma_y} = 1 + \left(\frac{\dot{\epsilon}}{D} \right)^{1/p}$$

where σ_d = yield stress with strain rate effect
 $\dot{\epsilon}$ = strain rate
 D = strain rate parameter (2560 s⁻¹)
 p = strain rate parameter (5)

Strain rate effects turned out to have a considerable influence on the results. In simulations without strain rate effects the stringer plate bent out in an S-shape which was not observed experimentally, see Figure 7. It is therefore likely that strain rate effects are important. This shows, that although the collision speed is rather moderate in a ship collision, the problem cannot be handled satisfactorily by a quasi-static approach. Strain rate effects caused approximately 10 % decrease in penetration depth. It was also found that gravity effects should be taken into account. Including gravity in the calculations increased both the penetration depth and the residual deformation by approximately 5 %, see Figure 7.

The weldings were modelled by rigid body constraints with failure. This means that before failure the two nodes in the plate connection act as one node, and after failure they split into two independently moving nodes. As failure criterion "ductile failure", where the weld is torn out of the steel plate, was chosen. This failure mode corresponds with the experimental observations and it occurs when the nodal plastic strain exceeds ϵ_{fail}^p . The value ϵ_{fail}^p was set to 20%. A stress

criterion for weld failure was found inapplicable as long as the weld is modelled rigid till failure. Hereby no energy can be absorbed in the weld, and as the impact load is applied failure is provoked almost instantaneously.

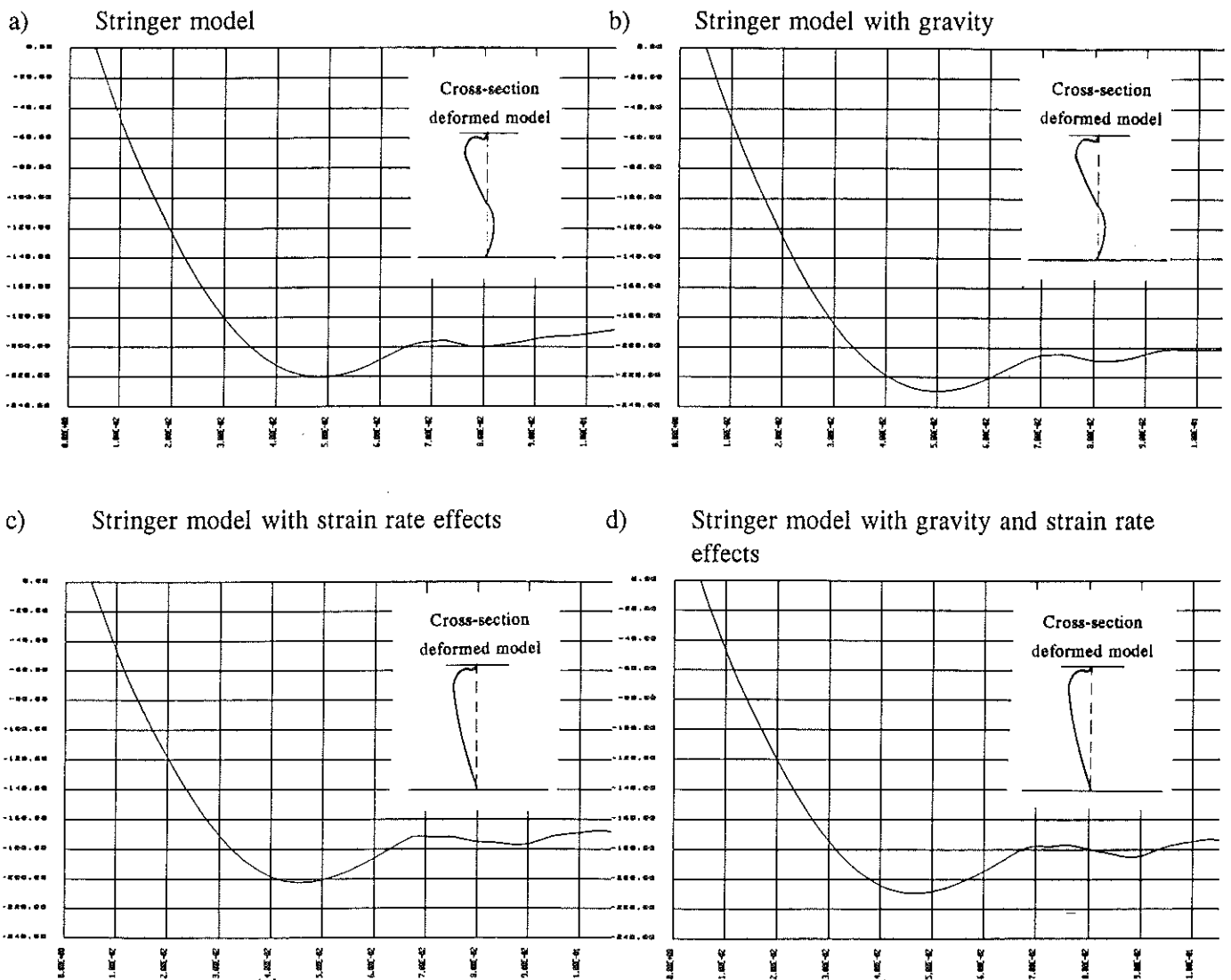


Figure 7. z-axis displacement of impact point as function of time, showing the influence of gravity and strain rate effects on the FE-model. Weld failure is not included in these simulations.

Results

The experiments showed a good reproducibility since the damage picture, except from the deflection of the stringer plate, was almost identical in the two tests. Furthermore the characteristic measures stated in the following Table 1 show only relatively minor deviations. The folding shape of the top part of the stringer plate is likely to be decided by factors like location of point of impact, quality of the fillet weld and imperfections in the stringer plate.

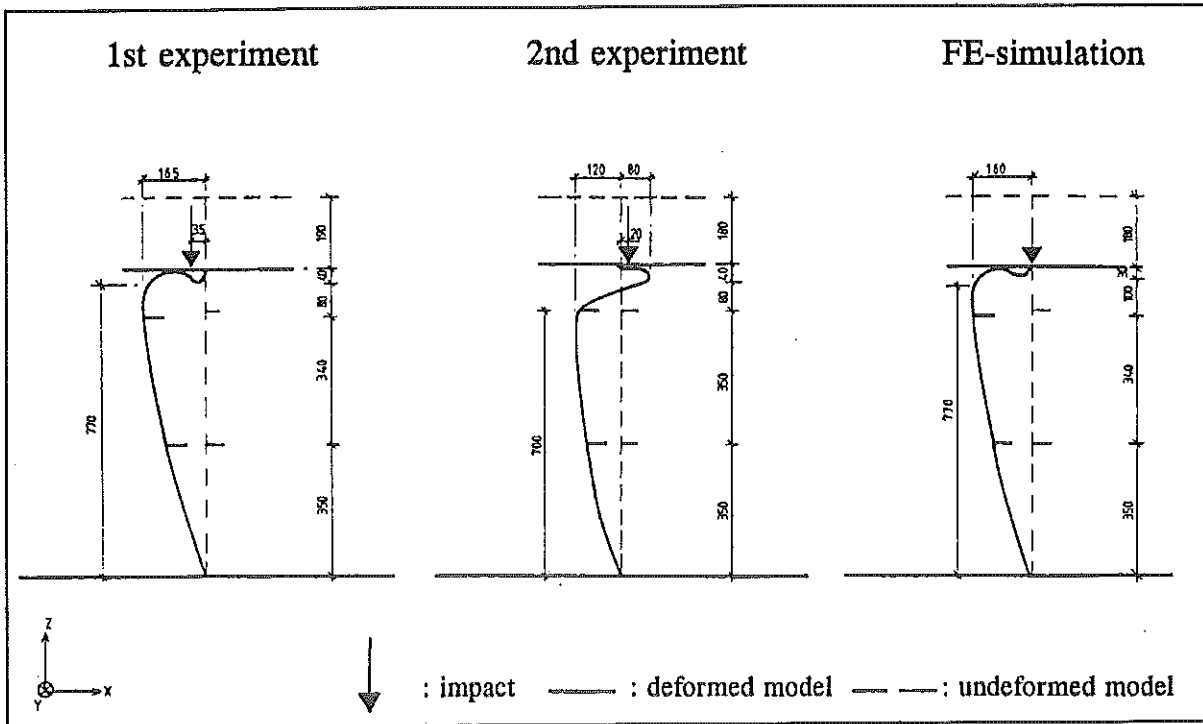


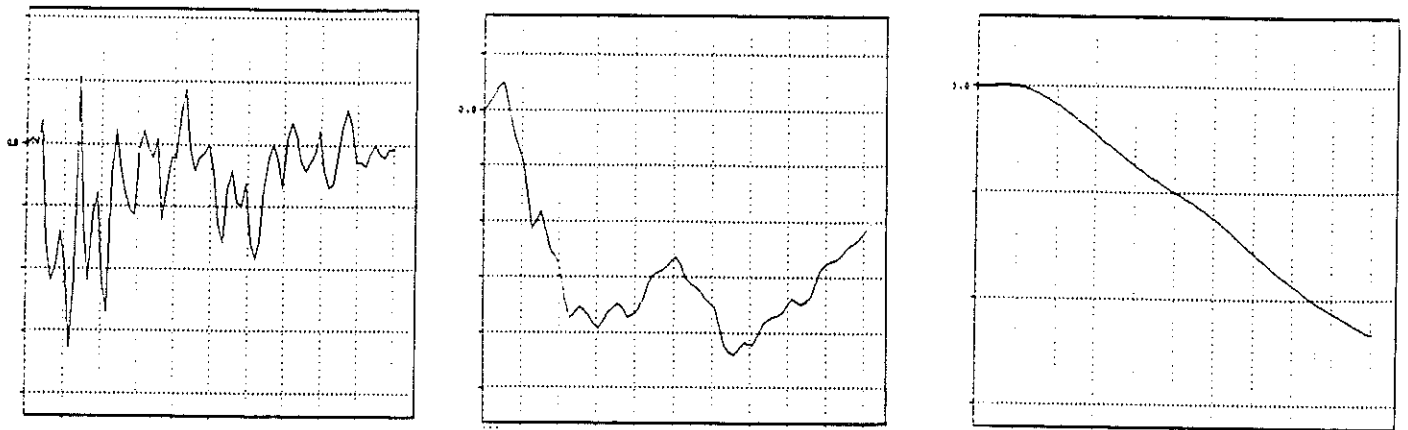
Figure 8. Cross-sections of the deformed test models and the FE-model.

	Experiment 1st model	Experiment 2nd model	FE calculation
Impact point distance from centre line	-35 mm	20 mm	0 mm
Maximum penetration	240 mm	230 mm	215 mm
Residual penetration at centre line	190 mm	175 mm	180 mm
Residual deflection of ends	47 mm	27 mm	40 mm
Residual decrease in distance between transverse webs at topplate	75 mm	45 mm	57 mm
Weld failure between stringer plate and top plate	350 mm	180 mm	250 mm

Table 1. Characteristic measures of the deformed models.

The explicit finite element calculation is in good agreement with the experimental results. As it appears from Figure 8 and Table 1, the numerical simulation provides results which in general lie between the two tests. Furthermore the curves in Figure 9 representing respectively the 2nd experiment and the FE-simulation are seemingly alike, although there could not be found agreement in the measured and the calculated magnitudes.

a) 2nd experiment



b) FE-simulation

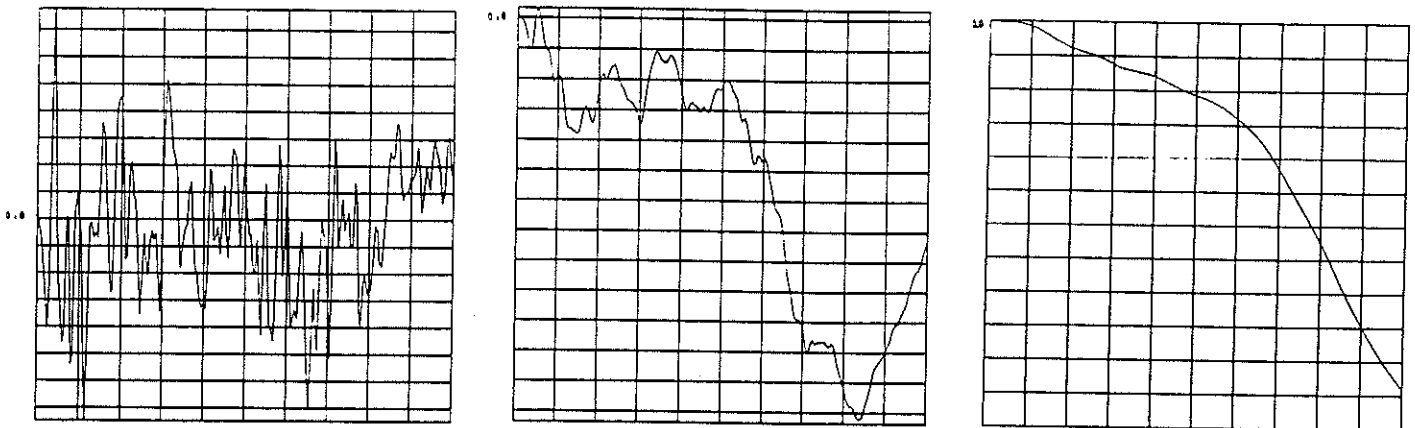


Figure 9. Time versus z-axis acceleration, time versus z-axis velocity and time versus z-axis deformation plots for the 2nd experiment and the FE-model. The Figure illustrates the first 2 milliseconds of the collision.

Conclusion

It is found that the explicit finite element method is a powerful tool to use in ship collision analysis. Already the preliminary analysis showed an overall response which was in surprisingly good accordance with the experiments when taking several minor discrepancies into account, for instance, deviation between lay-out and real geometry and neglect of strain rate effects, gravity and tearing of welds. However, the analysis also shows that omitting e.g. strain rate effects and gravity might be crucial for the overall picture. Wanting accurate results indeed raise demands for an accurate modelling.

A consequence of the results is that at a very early stage in the design phase, the choice between alternative designs can be based on a better background by employing explicit finite element analysis. Furthermore, for the final design, consequences can be checked out in a number of situations whereby the evaluation with regard to collision resistance will be of better quality. Explicit finite element analysis may also be performed on existing structures after collision in

order to evaluate how severe the structure is damaged and hereby be used as a planning tool for the repair.

For some ship types, like those of the offshore industry and high speed ferries and transport ships, it is essential to consider the collision resistance of the design. Here the explicit finite element method should be a valuable tool. The method is also applicable to the design of Navy vessels resistance to underwater explosions. However, the time to prepare the model as well as the computational effort is in a range which makes common usage of the explicit finite element method for design of conventional Tankers unlikely unless authority demands require validation of the collision resistance.

References

- /1/ Lloyd's List, Wednesday May 18 1994. Charging a course for the Uk government. From the report of Lord Donaldson's Inquiry into the prevention of pollution from merchant shipping.
- /2/ V. U. Minorsky. An Analysis of Ship Collisions With Reference to Protection of Nuclear Power Plants, Journal of Ship Research, pp. 1-4, October 1959.
- /3/ J. Amdahl. Energy Absorption in Ship-Platform Impacts, Dr. Ing. Thesis, Report No. UR-83-84, The Norwegian Institute of Technology, Trondheim (1983).
- /4/ Takao Kuroiwa, Nagasaki R&D Centre, Mitsubishi Heavy Industries, Ltd. Dynamic Experiments and Numerical Simulations of Failure of Ship's Side Structure. The conference on "Prediction Methodology of Tanker Structural Failure & Consequential Oil Spill", July 1993. Association for Structural Improvement of Shipbuilding Industry.
- /5/ H. Lenselink, K. G. Thung. Numerical Simulations of the Dutch-Japanese Full Scale Ship Collision Tests. CMO Conference on Marine Safety and Environment - Ship Production, Presentation on results project "Full-Scale Collision Tests", Thursday 4 June 1992.
- /6/ John O. Hallquist, Douglas W. Stillman, Tsung-Liang Lin. LS-Dyna3D Users Manual, January 1994. John O. Hallquist. LS-Dyna3D Theoretical Manual, May 1991.
- /7/ A. W. Vredevelt, L. J. Wevers. Full Scale Ship Collision Tests, April 1992. CMO Conference on Marine Safety and Environment - Ship Production, Presentation on results project "Full-Scale Collision Tests", Thursday 4 June 1992.

- Rupture de la soudure = prendre en compte valeur réelle - de mode prend $\bar{E} = 20\%$; est-ce la réalité?
- Vitesse de déformation? 19 m/s - c'est la vitesse du modèle -
- Y a-t-il du cisaillement dans la soudure?
- ← Important travail similaire au VOT (rapport de Wierzbicki).

*Apprecié par Wierzbicki comme
exemple de travail coopératif à
développer.*

Simulation and Enhancement of Spaceframe Vehicle Frontal Impact Crashworthiness

T D Williams, A de Pennington, D C Barton : The University of Leeds.
J R Coates and R Price: Caterham Cars Ltd

September 15, 1995

Abstract

This paper reports on the progress of a research project being conducted at the University of Leeds to investigate the frontal impact response of road vehicles utilising the spaceframe concept. Experimental testing and numerical simulations have been performed for validation and correlation purposes. A finite element vehicle model is being developed to determine the deceleration levels involved in a standard 30mph barrier test. An unconventional method of improving frontal crash behaviour is considered by the insertion of an 'add-on' energy management system.

1 Introduction and Objective

All mass produced passenger vehicles are of monocoque construction consisting of relatively large areas of sheet metal panelling incorporating major load carrying members, typically non-symmetrical closed box beam sections. Crashworthiness is 'built-in' to the structure as a form of passive safety at an early stage of the vehicle design process. During frontal crash, the structure ahead of the occupant compartment (commonly known as the crumple zone) is sacrificed and the irreversible plastic bending and folding of structural and non-structural members provide the mechanisms by which a significant amount of the impact energy is absorbed.

In contrast, the spaceframe road vehicle structure is widely used by low volume specialist car manufacturers. Caterham and TVR sports cars are examples of this category in the UK. The tubular steel framework type construction used by this type of vehicle is traditionally proven and cost effective for limited production purposes and can also be found in special purpose vehicles, tractor cabs and roll over protection [1] where passive safety and protection of survival space criteria must be met. As a result of the method of construction, such vehicles cannot rely on conventional methods of energy absorption and have insufficient energy absorbing capacity to absorb the kinetic energy of the standard 30 mph barrier test subjecting the occupants to high levels of force and momentum transfer, resulting in unacceptable passenger compartment deceleration levels. Alternative and economical methods of dissipating excess frontal impact energy must therefore be considered.

Considering the budget allowances of a small automotive manufacturer, extensive full scale test programmes are not possible. It is hoped that, through the use of computer simulation, the crash behaviour of the vehicle can be recreated and validated against experimental results and then modified to meet energy absorption/ passenger performance criteria. Although one vehicle will still require full scale testing in order to validate the results of the simulations, the savings for a manufacturer in cost and time would be enormous.

On the grounds of both economy and practicality, it is logical to seek a method of idealisation which is as simple to use and understand as possible while still providing answers which show good correlation with experiment. The complex geometry of jointed areas where many tubes both rectangular and circular in cross section converge can produce many difficulties in mesh generation for shell type elements. The finite element modelling of a spaceframe structure from beam elements is therefore a desirable option considering the complexity and expense of modelling with three dimensional elements such as shells.

Although little detailed information is available for the frontal impact behaviour of this type of vehicle, uninstrumented data show that they suffer little deformation resulting from the standard 30mph test (Figure 1). The resulting small changes in member cross section suggest that the beam element would indeed be suitable for predicting spaceframe vehicle crashworthiness.

This paper describes progress made over the last year on a research project carried out in the Department of Mechanical Engineering at the University of Leeds to study the frontal impact crash behaviour of the Caterham Seven sports car. For validation purposes, experimental impact testing has been performed upon representative spaceframe structures and compared to simulation results provided by the DYNA3D code. A finite element vehicle model currently under development for simulation of frontal barrier test conditions is then described. Finally, potential methods for improving the crashworthiness of a spaceframe vehicle are briefly discussed.

2 FE Model Validation

Due to the size and energy levels associated with full scale prototype testing, it has not been possible on the grounds of practicality and costs to produce impact results for a full size vehicle spaceframe for validation purposes. Therefore a simple representative framework has been constructed and tested at high rates of loading and the results compared with those from numerical simulations.

2.1 Experimental Testing

Dynamic impact testing is provided by a vertical impact test facility (Figure 2) known as the HERF (High Energy Rate Forming) rig. The HERF facility is capable of impacting a 111 kg steel head and piston assembly against small structures and components at velocities up to 25 m/s. A load cell centrally located in the head provides force-time histories for comparison

with DYNA3D predictions. The facility has been developed to impact pyramid type frame-work structures at a velocity of 6.6 m/s. These structures have a 0.2 m square base, are 0.3 m high and are made from 19 mm diameter 14 s.w.g mild steel seamed circular tube. They are braze welded at the joints as on the Caterham chassis.

Figure 2 also illustrates the deformed nature of the structure after impact. Each leg bends outwards and a central plastic hinge forms in the middle of the leg as the tube begins to fold. Smaller amounts of plastic deformation occur adjacent to the joints and the tube cross section at the base of each leg is squashed slightly. Structural collapse occurs at roughly 120 kN with the force level reducing thereafter as the load carrying capacity of the beam section falls.

2.2 DYNA3D Simulations

Simulation results have been gained from DYNA3D and compared with the above experiment in order to verify whether beam elements are suitable for simulation purposes of a frontal impact barrier vehicle model. Both beam and shell element models of the pyramids were constructed.

The analyses were carried out on a Silicon Graphics Power Challenge computer with four R8000 processors. Pre-processing is provided by peripheral finite element software contained within the Unigraphics solid modelling package and a combination of manual, mapped and automesh facilities are used for the generation of finite element models. The quality assured version of the DYNA3D code is used for the simulation of deformation and dynamic response. This non-linear, explicit three dimensional finite element code is distributed and fully supported by OASYS Ltd [2].

The beam element model (Figure 3) is meshed from 84 two node, Hughes-Lui beam elements with 20 elements contained in each leg. The element formulation performs one point integration along each beam axis and a uniform four point integration over the cross section.

The shell element model (Figure 4) is meshed from 1078 four node quadrilateral Belytschko-Tsay shell elements which use a default three point through thickness integration. As the pyramid structures are symmetrical, a quarter model is analysed to reduce computation time.

Provisions have been made to account for the differences in cross section and the large quantities of braze at each joint of the pyramid structure. In the beam model, element cross sections are increased to an equivalent wall thickness of 4mm for all elements sharing joint nodes. In the shell model, the elements bordering the tube intersections are also increased in thickness to 4mm. These modifications stiffen the jointed region allowing little deformation to occur as observed in the experimental test.

The basic material model used for all simulations is a simple, elastic-plastic material model with linear strain hardening with material properties as specified in Table 1. These values are in good agreement with tensile and compressive testing carried out on square and round tube samples extracted from the pyramid structures and spaceframe chassis. Strain rate sensitivity

is not currently included in the material model. It may be possible to incorporate this effect by using the Cowper and Symmonds constitutive equation which scales the material yield stress depending upon the strain rate.

Young's Modulus	Yield Stress	Poissons Ratio	Hardening Modulus
200GPa	330MPa	0.3	1.4GPa

Table 1: Material properties used for DYNA3D simulations

The impacting steel head is simulated by a 'stonewall' which has a mass and velocity equal to the experimental test. The base of the pyramid is constrained in space by a stationary stonewall. Designated nodes which are slave to the stonewall surfaces generate a reactive force if contact is made and a stick condition is assumed allowing no sliding to occur.

The impact simulations for both models were terminated after 6 ms. Table 2 gives statistical information for each model.

Model	Element formulation	Nodes	Elements	CPU time (seconds)
beam	Hughes-Lui	83	84	49
shell	Belytschko-Tsay	1009	1078	3219

Table 2: Comparison of DYNA3D beam and shell models

Figure 5 illustrates the impacting stonewall force-time histories predicted for each model and compares them to experimental test. Generally good correlation is displayed for both element formulations. As expected, the shell model offers an improvement in accuracy for the collapse load and also for the subsequent deformation. Both simulations predict the characteristic jump in load observed early in the experiment which is probably due to the arrival of a tensile stress wave caused by reflection of the initial impact compressive wave from the fixed base of the pyramid.

These simulation results suggest that beam elements are indeed suitable for modelling the collapse of a spaceframe type structure and are therefore used in the construction of the full vehicle model described below.

3 FEA Model of Spaceframe Vehicle

The Caterham Seven currently being investigated is a front engine, rear wheel drive two seater sports convertible. The vehicle weighs approximately 540 kg and is built around a single unit spaceframe. A fully independent front wishbone suspension system and a semi-independent rear de-Dion axle are connected to the chassis via bushes. The longitudinally mounted driveline is constrained to the chassis via two engine mounts and one centrally located gearbox mount and the differential is mounted centrally behind the seating position on four bushes.

A high transmission tunnel separates the occupants who are restrained by standard 3 point lap/shoulder seat belt assemblies.

Figure 6 illustrates the Caterham Seven less exterior aluminium panelling and interior fixtures. The triangulated nature of the tubular steel framework is clearly seen and is required for torsional stiffness purposes. The spaceframe is built from five square and two circular section types of tube and is braze welded at the joints. In addition to the tubing, sheet steel is used in the vehicle front end for the construction of suspension brackets, a steering rack platform and a pedal box. The wings and nose-cone of the vehicle are manufactured from glass fibre and provide little structural resistance.

A Caterham Seven has been subjected to the standard 30mph (13.4 m/s) frontal barrier test for compliance with the European frontal impact standard which limits the steering column rearward displacement to 127 mm. In a frontal crash, the leading edge of the spaceframe comes into contact with the barrier at an early stage, with only the nose-cone and radiator impacting beforehand. The front tyres contact the wall at the same time as the spaceframe. Very little overall deformation occurs in the spaceframe and there is a large amount of post impact rebound. This suggests that the passenger compartment is subjected to very high and unacceptable levels of deceleration.

A simplistic and highly idealised finite element model of this vehicle shown in figure 7 is currently under development for the purposes of performing 30mph barrier impact simulations. This model contains a crude driveline and occupant representation. The entire spaceframe is meshed from beam elements with the rear portion modelled assuming a rigid material and the front material properties consistent with those used for the pyramid structure (see Table 1). Beam element sections are increased near the joints to account for increases in cross section and the large quantities of braze. All the primary structural components in the vehicle front end are represented including the steering rack platform and aluminum panelling which are modelled with shells (panelling blanked out in figure 7). The driveline is of a rigid material and is connected to the spaceframe via discrete springs, the non-linear behaviour of which are obtained from experimental quasi-static test.

The lumped nodal mass in the driver position is a crude representation of a 65th percentile dummy and is restrained to the seat belt anchorage points via three linear elastic springs representing the seat belt assembly. The current vehicle model does not include the front or rear suspension or wheel and hub assemblies and the mass of the model is, at 328 kg, considerably less than the total vehicle weight of 540kg.

Figure 8 shows initial simulation results for the vehicle model impacted against a fixed stonewall at a velocity of 13.4 m/s. Simulation results indicate that a large amount of deformation occurs in the vehicle front end as a result of the impact. This is in conflict with experimental observations that, in a similar impact situation, there is very little structural deformation in this region. Reasons for these conflicting results are presently under investigation and include the structural contribution provided by the suspension and tyres, due to the fact that the tyres impact the barrier at the same time as the spaceframe.

4 Crashworthiness Improvement

An energy management system is proposed in order to improve the frontal impact crash performance of the Caterham by absorbing a significant amount of the vehicle kinetic energy in a controlled manner. A conventional method of crashworthiness improvement would require replacement of the front portion of the spaceframe with a structure that exhibits the required collapse characteristics. This concept carries with it obstacles and conflicting requirements for this type of vehicle including the structural integration of, and interaction with, other vehicle functions. It is a particularly difficult design problem for the Caterham car as the front suspension system is attached directly to the foremost of the spaceframe. Alternative methods of absorbing excess impact energy are under consideration and include novel propeller shaft and engine mount designs such as those investigated by Trommer [3] and Goor [4].

Yet another unconventional method of frontal crashworthiness improvement has been investigated for the Caterham Seven [5]. This involved the development of an 'add-on' energy management system through the experimental testing of energy absorbing (EA) devices. This is a desirable design option as it does not necessitate a re-design of the main spaceframe. Also, the inherent lightness of the Caterham car gives the immediate advantage that relatively low amounts of kinetic energy have to be absorbed and provides the opportunity for simple and inexpensive energy absorbers to be considered. Kuang [6] performed a similar study by the insertion of non structural EA devices in the unutilised space in series with existing load paths inside the vehicle front end.

As a result of these studies, a tube expanding design has been identified as the most suitable EA device for this application (Figure 9). Energy absorption is provided by the plastic deformation of the outer tube and the simultaneous friction at the tube interface. Quasi-static tests (Figure 10) have been conducted on both round and square tubing of varying dimensions to develop a suitable design and to characterize the energy absorption capabilities. Uninstrumented impact testing has also been performed with the HERF facility to study the effects of dynamic and off-axis loading. By choosing a particular tube geometry, devices such as these can be tailored to suit a specific energy level in order that the total vehicle crush and passenger compartment deceleration levels do not exceed their limits. For example, assuming that an energy management system consisting of four EA devices is secured forward of the main spaceframe, a mild steel tube expanding design of diameter 31.74 mm and thickness 1.65 mm compressed over 200 mm absorbs in excess of 50 percent of the kinetic energy of the Caterham moving at 30 mph. The measured force-deflection curve for this design is shown in Figure 11.

A future study will further investigate the possibility of adopting an 'add-on' energy management system. Load levels and stroke requirements will be determined by the use of conceptual EA devices using idealised rectangular force-deflection curves. Experimental testing of qualifying EA devices in the HERF facility will be supported by finite element simulations integrated with a complete vehicle model. There are also practical considerations which may include the use of non structural elements such as the radiator which could double up as part of the energy absorbing design.

5 Conclusions and Further Work

The validation of a beam element idealisation of a spaceframe structure subject to dynamic impact loading has been carried out by the experimental testing and finite element simulation of small representative framework structures. Good correlation has been achieved which suggests that the beam element formulation is suitable for the prediction of collapse loads.

A finite element vehicle model has been constructed using beam elements for the main chassis members. Initial simulation results predict uncharacteristic deformation compared to those observed in the standard 30 mph test. Reasons for this discrepancy are currently under investigation.

The development of an 'add-on' energy absorbing structure forward of the main spaceframe is a feasible and cost effective proposition for crashworthiness improvement. By combining the dynamic testing of EA components with a representative finite element vehicle model, it should be possible to develop an accurate and integrated approach to the design and development of a crashworthy vehicle structure.

6 Acknowledgements

The authors would like to thank the Keyworth Institute at the University of Leeds for providing financial support to T D Williams and Caterham Cars Ltd for their financial contribution and the provision of specimens for experimental testing.

References

- [1] Kecman D. Analysis of framework-type safety structures in road vehicles. In *Structural Crashworthiness*, chapter 13, pages 371–396. Butterworths, 1983.
- [2] Oasys Ltd. *OASYS LS-DYNA3D User Manual Version 6.0*. 13 Fitzroy Street, London W1P 6BQ, 1994.
- [3] Trommer J. Crash optimised propshafts - a new challenge for structural composites. In *Autotech '93 Congress*, 1993.
- [4] Goor D. Means of manipulating forces in the case of frontal collisions through the use of: Unique and patented engine mount concepts. *SAE*, (922081), 1992.
- [5] Williams T D. Approaches to spaceframe vehicle crashworthiness. In *CAE in Crashworthiness Seminar*. IMechE, November 1994.
- [6] Kuang H. L. Mase T. G. An assessment of add-on energy absorbing devices for vehicle crashworthiness. *ASME*, 112:406–411, October 1990.

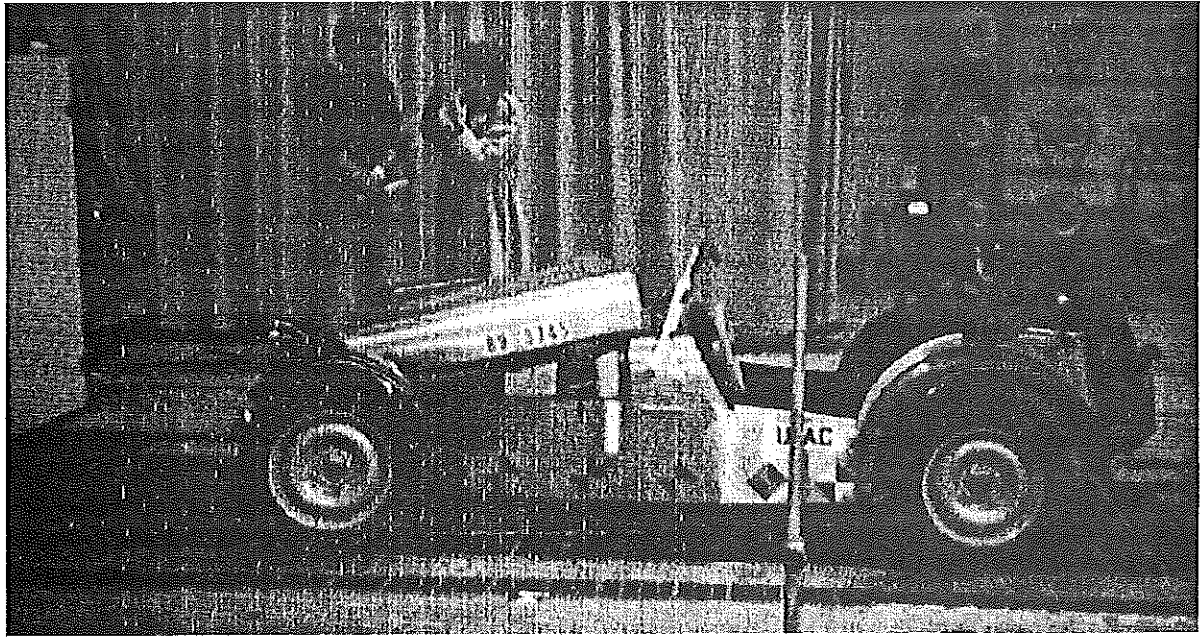


Figure 1: 30mph barrier test result

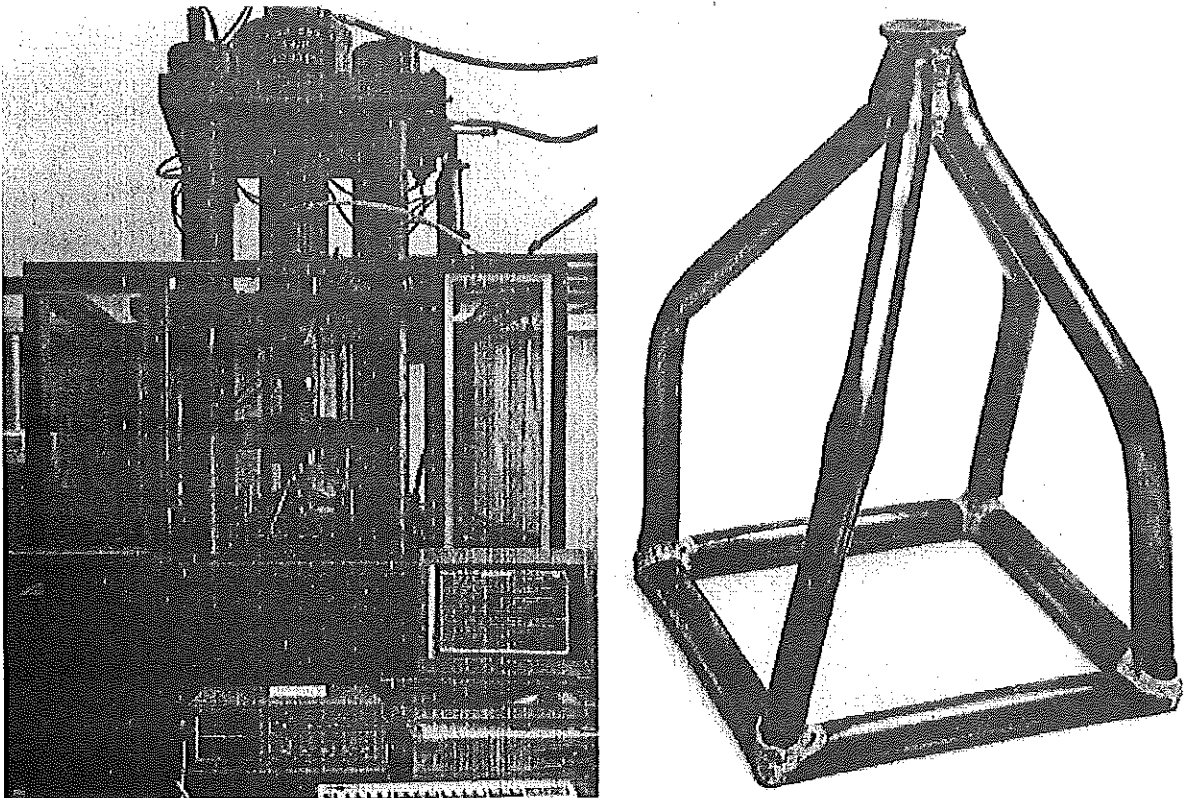


Figure 2: HERF vertical impact test facility and deformed pyramid

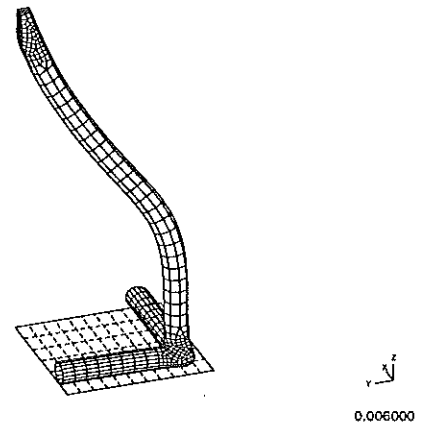
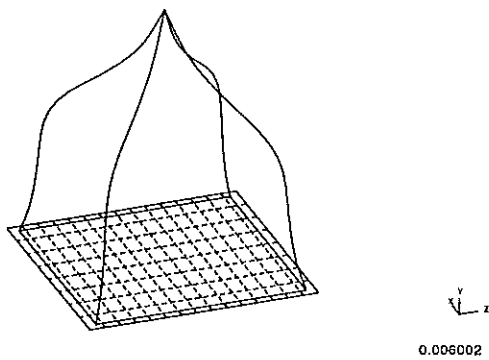
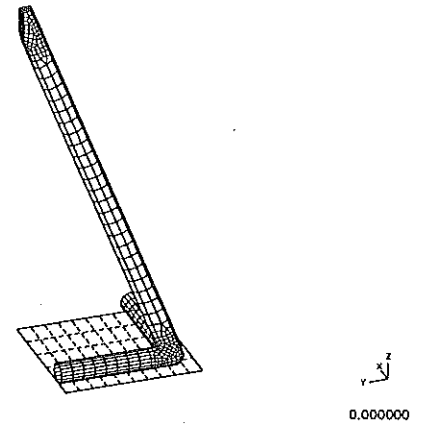
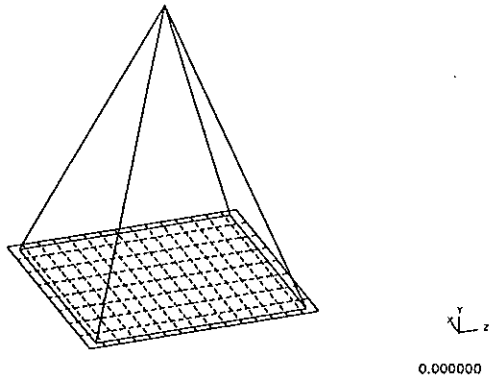


Figure 3: Beam element model

Figure 4: Shell element model

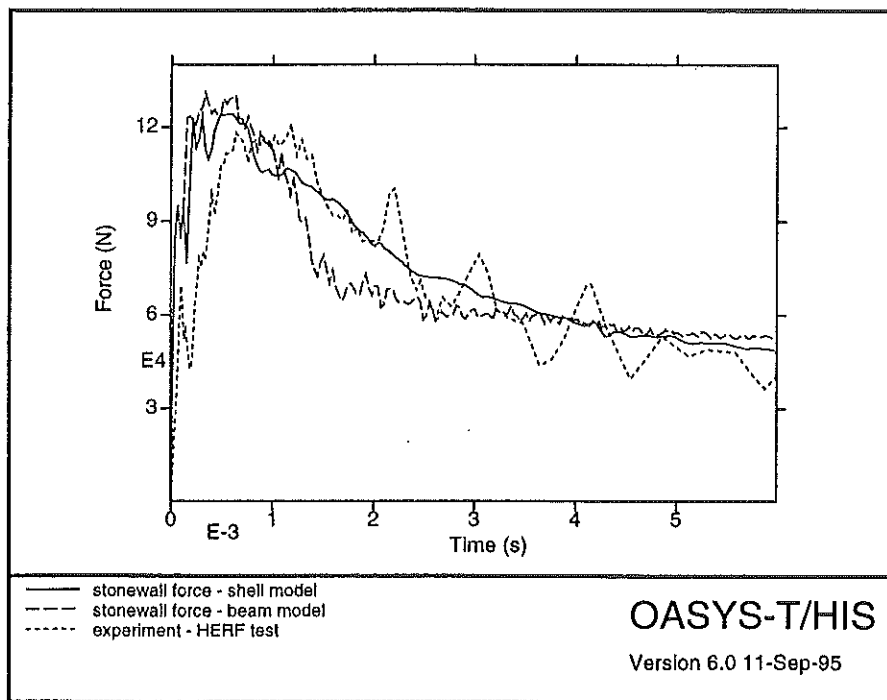


Figure 5: Force-time histories: DYNA3D beam, shell & experiment

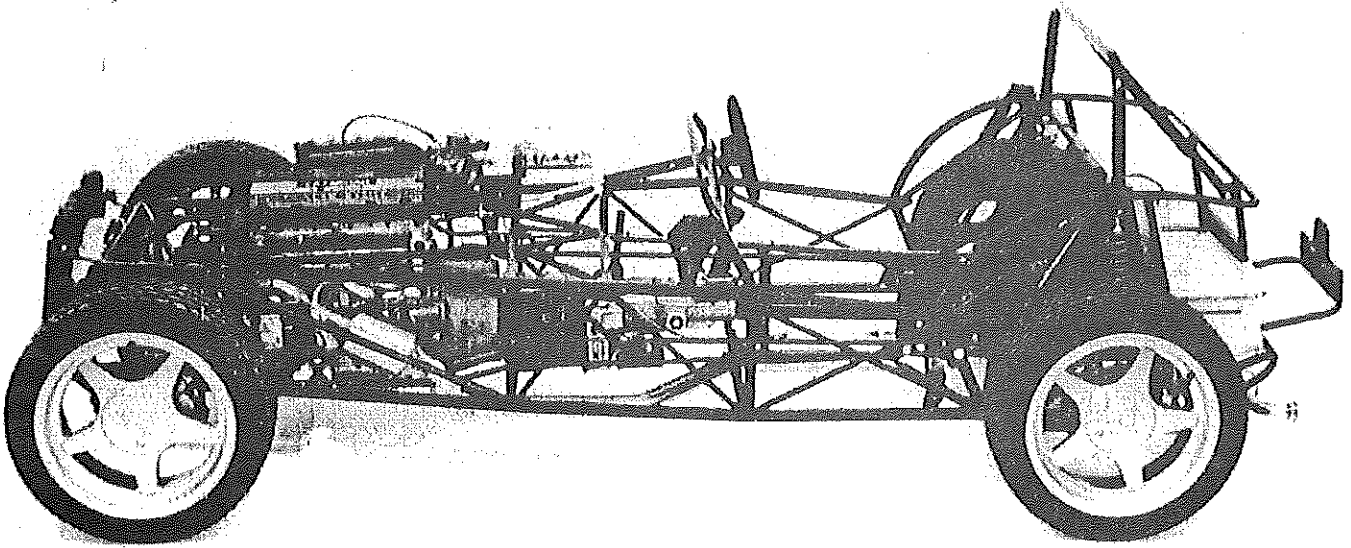


Figure 6: Spaceframe vehicle structure

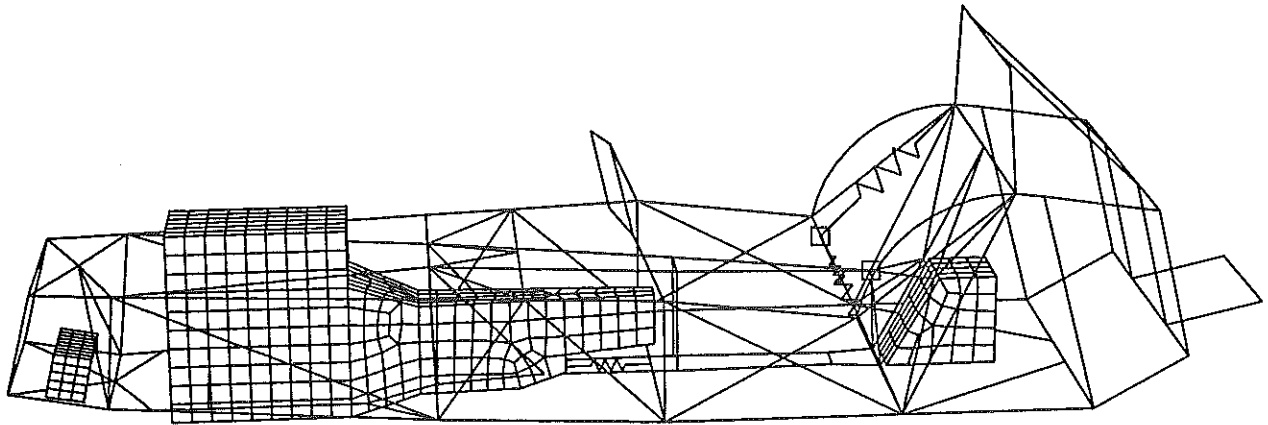


Figure 7: Developing FEA vehicle model

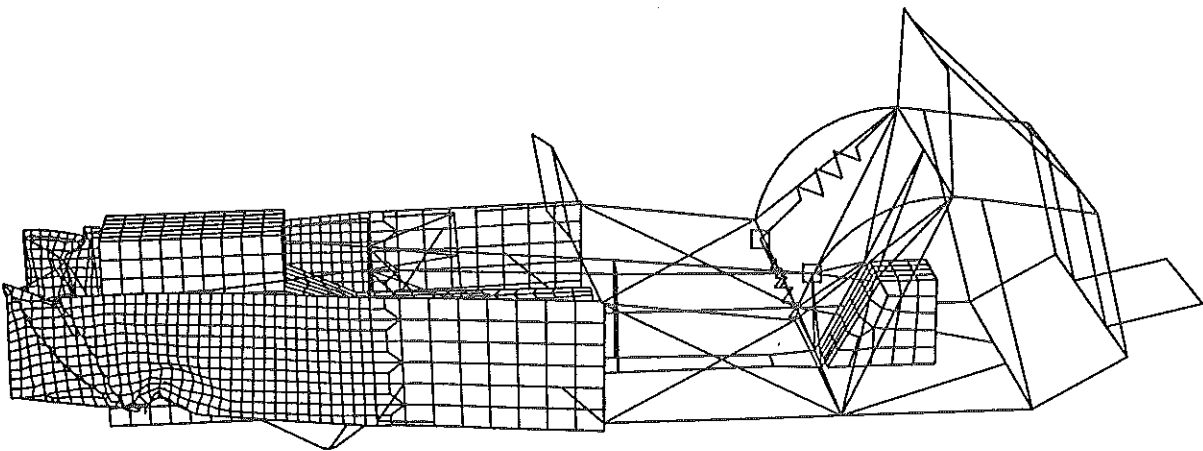


Figure 8: FEA vehicle model deformation 20 ms after impact

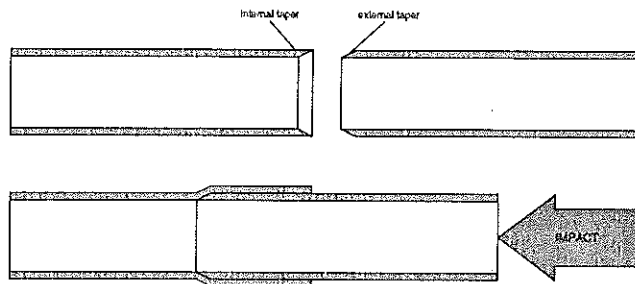


Figure 9: Tube expanding design

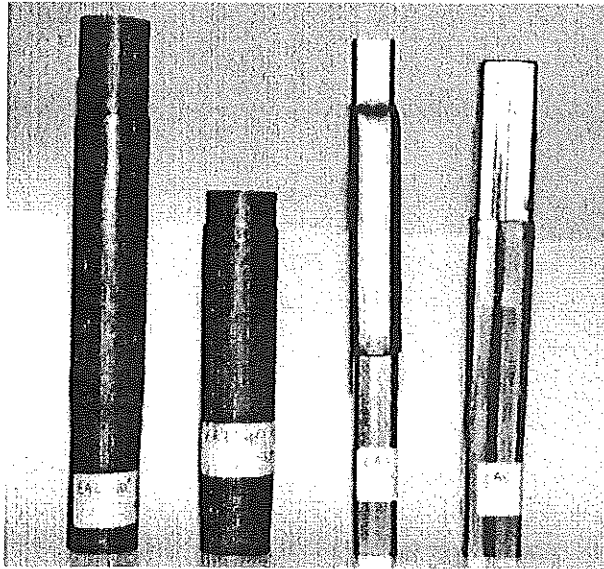


Figure 10: Results of quasi-static tests on tube expanding design

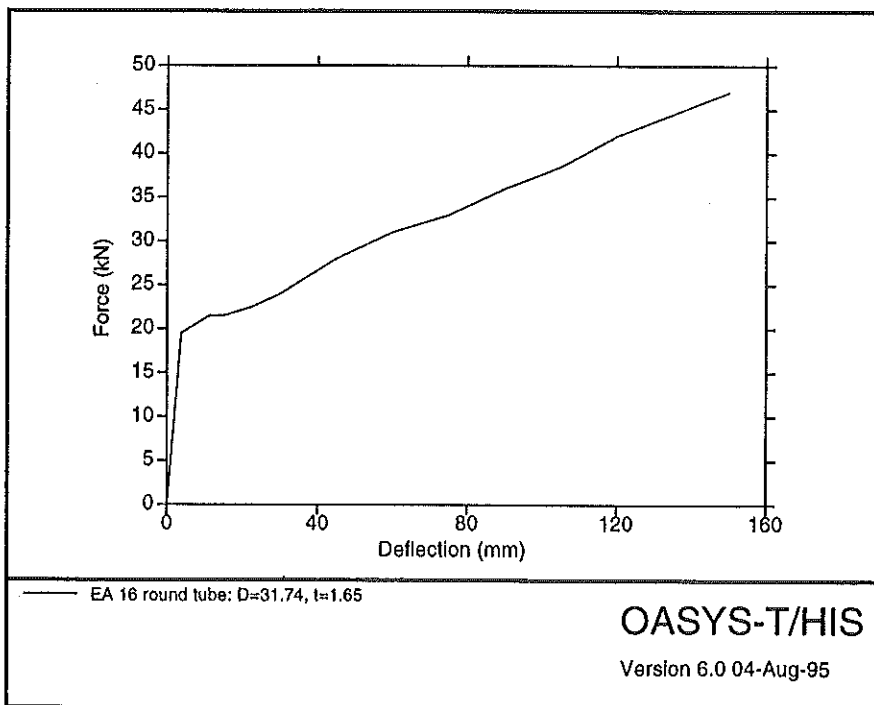


Figure 11: Quasi-static force-deflection curve for tube expanding design

DETERMINATION OF THE ESSENTIAL FRACTURE WORK OF A
POLYCARBONATE ROUND NOTCHED SPECIMEN
BY THE METHOD OF PERCENTILES

R. DEKIOUK*, Z. AZARI**, G. PLUVINAGE*

* Laboratoire de Fiabilité Mécanique, Ile du Saulcy, 57045 Metz
** INstitut Supérieur des Sciences Et Techniques, 02109 St-Quentin

SUMMARY

This report presents a study on the determination of the dynamic toughness measured on axisymmetrical bars made from polycarbonate. The criterion used for the determination of the toughness is the essential work of fracture coupled with a probabilistic approach.

Dynamic fracture tests have been realised with the help of a Hopkinson tension bar device.

INTRODUCTION

Several approaches have been used to characterise the fracture behaviour of a polymer. The most frequent are the energetic parameter J proposed by Landes and Begley [1] in 1968 and the integral J proposed by Rice [2] in 1972. Another less frequently proposed approach by Broberg [3] is used to characterise this behaviour. It is called the essential work of fracture.

$$\Gamma_e = U - \beta \cdot \left(\frac{b}{2}\right) w_{pl}^*$$

(1)

*Voir utilisation de
cette méthode.*

with U : specific fracture work
b : diameter of ligament
 β : coefficient depending on the plastic zone
 w_{pl}^* : Volumic density of plastic work

This theory allows a rather simple experimental determination of toughness and is not restricted by geometrical considerations as the J criterion.

The scattering of the toughness values, mainly in the case of polymers, is a fact of experience.

The importance of this scattering is rarely reported in the literature. Its amplitude is so large that we have been led to use a probabilistic approach for the determination of the essential work of fracture.

1. Experimental procedure

The experimental procedure requires to record the load-displacement curves from tests made on identical bars (figure 1) but with increasing crack lengths. The works of fracture U of each test is calculated as a function of the different ligament lengths.

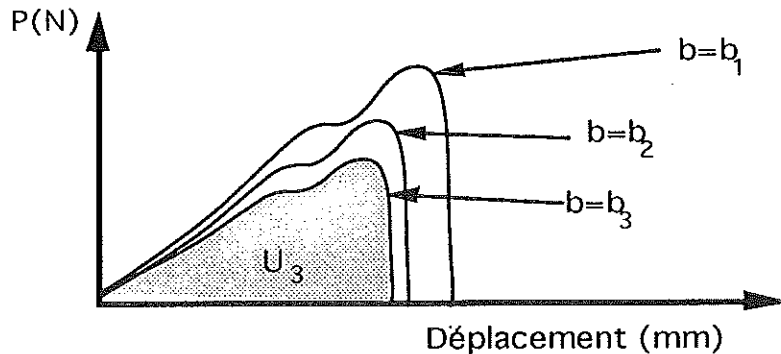


Figure 1 - Recording of load-displacement curves

The values of the fracture energy are reported on a graph as a function of the ligament length. The value of the essential work of fracture Γ_e can be determined following the linear relationship (1) between U and b . For each ligament length, a distribution of values of U is found and is characterized by the percentiles. For each percentile, it is possible to find a straight line with a least square regression. Finally, a value of the essential work of fracture Γ_e is associated with each percentile (figure 2).

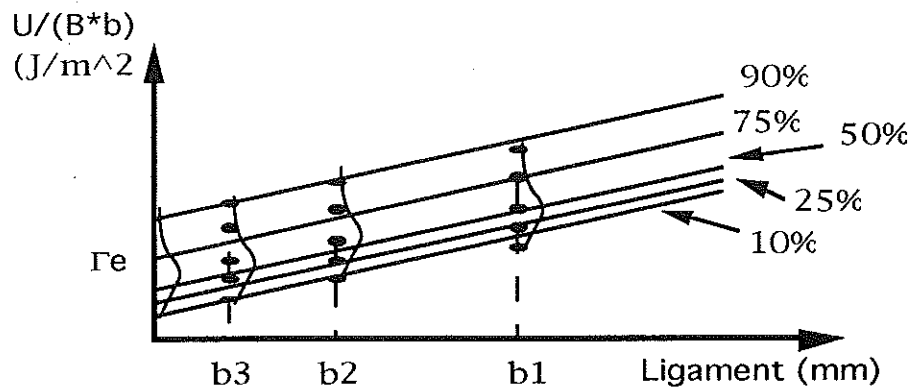


Figure 2 - Essential work of fracture

2. Experimental study

Dynamic tensile tests are conducted with the help of a Hopkinson's bars tensile device.

II.1. Experimental device.

The Hopkinson's bars device used is represented on figure 3. This device consists in a gas compression chamber, a projectile and a multiple bars inversion system. As shown on figure 3, the projectile is thrown by the air gun onto the inversion bars which in turn throws a second tubular projectile on a heel, which produces a tensile loading wave in the incident bar.

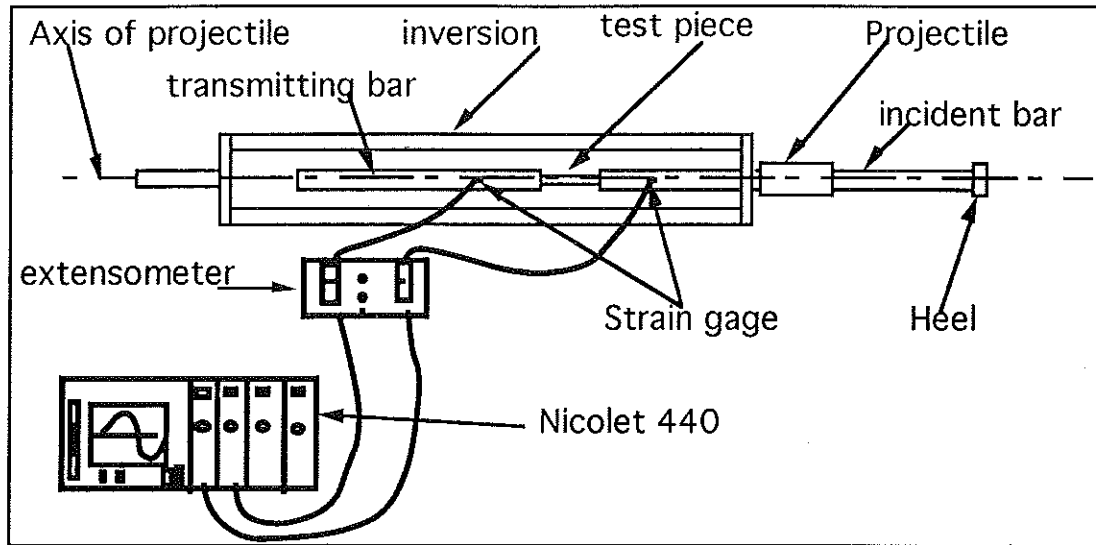


Figure 3- Dynamic Hopkinson tension bar device.

II.2. Material

The material used is a bisphénol - A polycarbonate (mechanical characteristics are listed in table 1). It is an amorphous thermoplastic, glassy polymer at room temperature. The choice of this material considered as ductile is directed :

- by the high mechanical performances which make it a frequently used technical polymer,
- by the existence of commercial grades, transparent in the visible spectrum (this characteristic may allow an easy observation of the damage mechanism),
- by the complexity of its fracture behaviour (at room temperature, the polycarbonate is in the range of ductile-brittle transition ; it shows therefore both irreversible deformation mechanisms mentioned above).

Despite its excellent mechanical characteristics, there are very few works published about the fracture toughness of this polymer.

Material	Coefficient of lineic expansion ($10^{-6} \cdot C^{-1}$)	Thermal Conductivity (W/m.C)	Specific heat to 20 °C (KJ/Kg.C)	vitreous transition temperature (C)	bending modulus (MPa)
Poly carbonate (PC)	70	0.19	1.25	143	2500

Table 1 - Mechanical characteristics.

discussion sur le fait que'il y a une partie de l'ouvrage qui est réceptionnée (vis co-)

II.3. Design of test pieces.

The test pieces have an axisymmetrical geometry (figure 4). The notches are machined with a mechanical process.

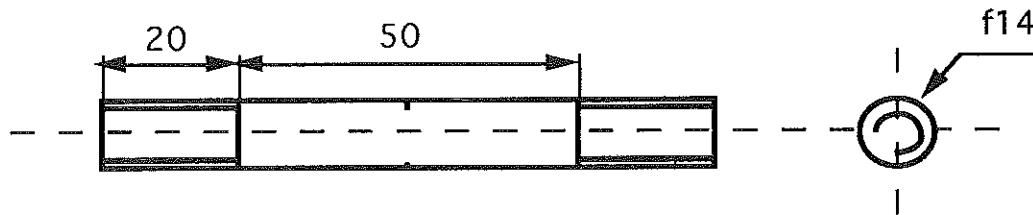


Figure 4- Axisymmetrical test piece made from polycarbonate.

III. Experimental results

III.1. Experimental protocol

Table 2 gives the ligament lengths and the number of test pieces for each length.

ligament length	Number of test pieces
4 mm	5
5 mm	5
6 mm	6
7 mm	5

Table 2 - recapitulation of the test pieces number for each ligament length

III.2. Result and discussion

The results have been examined using the percentiles method :

- a distribution of the surfacic work of fracture is reported with each ligament length and therefore the values associated with predefined percentiles (10, 25, 50, 75, 90 %) (figure 5)

- for each ligament length and for each associated percentile, we fit these points with the help of a least squares regression method.

- each intersection with the Y-axis gives the essential work of fracture Γ_e corresponding to a given percentile.

Table 3 shows the parameters of the essential work of fracture from the Weibull's distribution law.

Mean(J/m ²)	Weibull's modulus	Standard deviation
4488.65	2.86	1702.96

Table 3 - Value of the essential work of fracture Γ_e with the help of Weibull's distribution

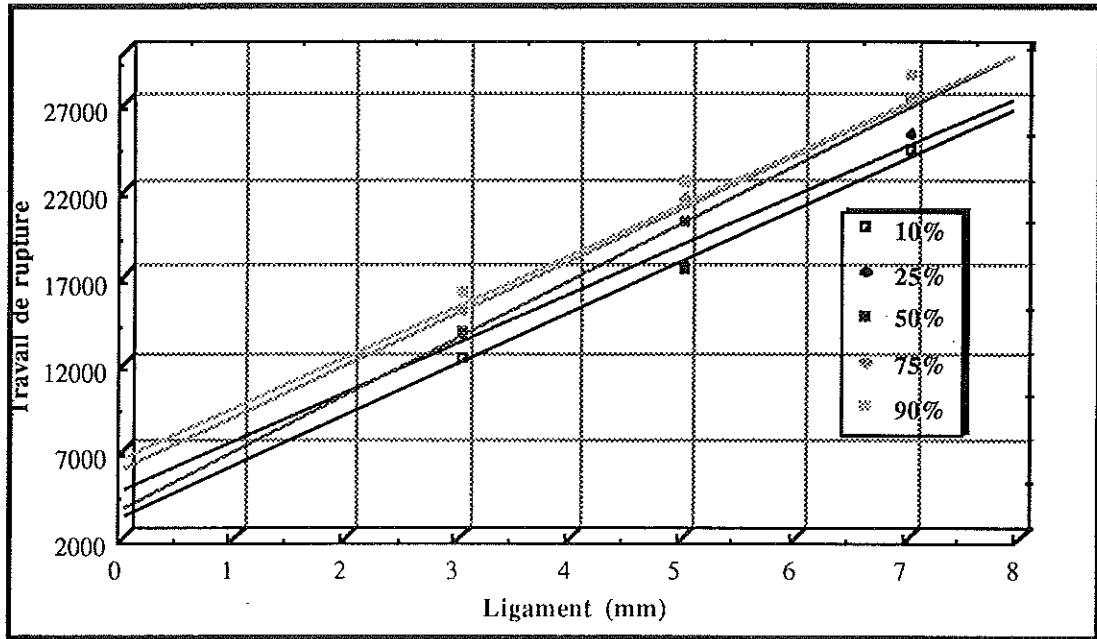


Figure 5 - The essential work of fracture with respect to the ligament length.

The mean of the essential fracture work here found is about 4.5 kJ/m^2 with a standard deviation of 1.5 kJ/m^2 . We observe a large scattering depending on the scattering itself at the different levels. This value is close to the values reported from the literature [4,5,6,7,8] in table 3.

Authors	Methode and cross head speed	Test piece	Toughness values kJ/m^2
FRASER et WARD [4]	Tension 0.1 mm/mn	Axisymmetrical	$G_{1c} = 0.37$
BERNSTEIN [5]	Tension 0.1 mm/mn	Axisymmetrical	$G_{1c} = 4.4$
KIM, JOE et OTTERSON [6]	Bending 3 points 5 mm/mn	SENT	$J_{1c} \doteq 4.3$
PATON et HASHEMI [7]	Tension 1 mm/mn	SENT	$\Gamma_e = 4.3$
SING et PARIHAR [8]	Tension 1 mm/mn	SENT	$J_{1c} = 6.13$

Table 4 - Published toughness values of the polycarbonate.

IV Conclusion

The determination of a polymer toughness can be approached using the essential fracture work together with the pertencile's method. This study has shown us the feasibility of this way.

We have observed a great scattering of results (coefficient of variation : 30 %). This is very rarely reported in the literature.

This study will be followed by :

- a study of the influence of the strain rate on the essential fracture work value
- a study of the validity of the basic assumption : a uniform energy density on the ligament which induces a linear relationship between the surfacic work and the ligament dimensions.

V Bibliographie

- [1] : **J.D. Landes and J.A. Begley**
ASTM, STP 514
pp. 24-39, (1968).
- [2] : **G.R. Rice**
"A path independant integral and the approximate analysis of strain concentration by notched cracks" Jour. of Appl. Mech., pp. 379, (1972).
- [3] : **K.B. Broberg**
Int. J. Fract.,4
pp. 11, (1974).
- [4] : **R.A. W. Fraser et I.M. Ward**
Polymer Engineering and science
Vol. 14, n°6, pp. 420-428, (1977).
- [5] : **H.L. Berstein**
"A Study of the J integral Method using Polycarbonate"
Air Force Wright Aeronautical Laboratories (US), Rapport Afwal-TR-82-4080, (1982).
- [6] : **B.H. Kim, C.R. Joe et D.M. Otterson**
"On the Determination of Fracture Toughness in Polymers"
Polymer Testing, n°8, pp. 119-130, (1989).
- [7] : **C.A. Paton et S. Hashemi**
"Plane-stress essential work of ductile fracture for polycarbonate"
Journal of materials science, n°27, pp. 2279-2290, (1992).
- [8] : **R.K. Singh et K.J. Parihar**
Journal of materials science, n°21, pp. 3921-3926, (1986).

- physical reason for using this type of model?

EVALUATION OF STRAIN-RATE DEPENDENT MODEL FOR CONCRETE UNDER TENSION-APPLICATIONS

Spiridon N. ECONOMOU
European Commission, Joint Research Centre
I-21020, Ispra (VA), ITALY

ABSTRACT: A strain-rate dependent constitutive model for the determination of stress-time-history from given monotonic strain-time-histories is presented, based on the dissertation of H. Bachmann. A series of 10 uniaxial tensile experiments carried out in the Hopkinson Bar apparatus at JRC in Ispra, form the basis for model evaluation. A comparison is done between model and experiments regarding concrete stress-strain behaviour. The model is implemented as a material model for the one-dimensional non-linear analysis of structural systems, and it is used for the simulation of Hopkinson Bar.

1. INTRODUCTION

The behaviour of concrete structures under impact or impulsive loading is of prime importance for the public safety, especially in highly developed and industrialized areas. High strain-rate dynamic phenomena take place in accidental situations¹ (such as accidents in chemical plants, liquid gas containers, nuclear power plants or collisions of vehicles, ships, or even aircrafts to civil structures), but also in cases when we have to impose this type of dynamic loading (i.e safe design of concrete foundation piles in regard to brittle failure during driving²). Moreover observations which have been evaluated from a number of experiments show that for concrete under impact loading, much more energy is absorbed in the fracture process, the tensile strength is much higher, and the strain corresponding to the maximum stress is greater than under static loading. The dynamic strength increase of concrete under tension, due to high strain-rates, arises from the heterogeneous nature of the material at the microlevel, and the inertia effects from microcracking that have been verified by experimental observation. The evaluation of the resistance of a Reinforced Concrete Structure subjected to the foresaid dynamic loadings requires, on one hand, a realistic modelling of the concrete behaviour under various loading rates and, on the other hand, the appropriate implementation of such a model into the computer codes used to analyse the structural response. A power law, is usually applied for concrete¹, to predict the tensile strength as a function of stress or strain rate. Also, it has been clearly demonstrated^{3,4,8} that in order to estimate the stress history under high strain-rates, it is the strain-history which should be taken into account and not a discrete strain value each time. The objective of this paper is the presentation of the application of a strain-rate dependent constitutive model for plain concrete, (determination of a strain-rate dependent stress-time-history, from given monotonic strain-time-histories), based on the dissertation of H. Bachmann in the University of Karlsruhe.

The present publication consists of two parts: in the first part a comparison is done between the model predictions regarding the stress-strain behaviour of plain concrete under uniaxial tension and the experimental results. The experiments on concrete specimens for different strain-rates have been done in a Hopkinson bar apparatus at the Joint Research Centre in Ispra. As input for the implementation of the model, the specimen strain history up to fracture, is given. The rest of the model parameters are used as given by Bachmann, except for those which could be adapted to the geometrical and the mechanical characteristics of the specimens (i.e. length and area of the specimen, Young modulus of elasticity etc.). For each case of strain rate (each experiment), the calculated vs. predicted values are compared for a number of parameters like the tensile strength of the specimen, the corresponding strain, the ratio of dynamic strength to the strength of the static case, the ratio of the corresponding strains, etc. In most cases the agreement between the Bachmann model and experiment appears sufficiently close and that permitted to proceed to further implementation of the model in Finite Element codes. In the second part the Bachmann model is implemented as a material model with two purposes: first for the one-dimensional non-linear dynamic analysis of structural systems, (simulation of experiments under way in the Large Dynamic Testing Facility in the framework of a program for the characterization of plain concrete by means of the Large Hopkinson Bar of JRC Ispra), and second, to be used in a F. E. code for Structural Analysis where the stress state suits to the assumptions of the model.

2. STRAIN-RATE DEPENDENT MODEL FOR CONCRETE UNDER TENSION

An interpretation and description of Bachmann model³ is attempted, together with some simple modifications we have made in order to facilitate the implementation of the model in Finite Element codes. The effect of dynamic strength increase of concrete in tension, (strain-rate effect), results from the heterogeneous nature of the material at the microlevel, hence the material cannot be treated as a homogeneous continuum with respect to wave propagation at the macrolevel⁴. A rational mechanical model, primarily based on inertia effects, has been developed by Bachmann³, in cooperation, and based, on earlier work of Eibl⁴. It consists of terms considering: a) nonlinear behavior with respect to an internal damage parameter, where the location and amount of damage are distributed stochastically; b) loading and unloading regarding internal friction and c) damage from micro-cracking inertia effects. In the context, a step-by-step determination of a strain-rate dependent stress (σ) time-history, from given monotonic strain (ϵ) time-history, for concrete subjected to uniaxial tensile stress state, is presented.

Let us say that the dynamic phenomenon takes place in time t . The response is divided into N equal time steps of length Δt . The objective is to determine stress $\sigma(t_i)$ at time-step i , where ($i \leq N$) and time t_i for known strain history $\epsilon(t)$, and also for known strain-rate history $\dot{\epsilon}(t)$, (the last can be calculated as the ratio of the difference of strain at two consecutive time points, to the time step Δt). The values of ϵ and $\dot{\epsilon}$ at time step i , are denoted by ϵ_i and $\dot{\epsilon}_i$, respectively and those at time step j , by ϵ_j and $\dot{\epsilon}_j$. The basic model assumption is that the stress $\sigma(t_i)$, to be determined comprises a time-independent part, $\sigma_o(\epsilon_i)$, (depending only on the momentary strain ϵ_i), and a time-dependent one $\sigma_\epsilon(t_i)$, (depending on the strain-history till the time t_i):

$$\sigma(t_i) = \sigma_o(\epsilon_i) + \sigma_\epsilon(t_i) \quad (1)$$

The first part the time-independent part $\sigma_o(\epsilon_i)$, is equal to the product of a linear elastic material

law $E\varepsilon_i$ times an exponential term, (regarding nonlinear behavior with respect to an internal damage parameter, where the location and amount of damage are distributed stochastically):

$$\sigma_o = E \cdot \varepsilon_i \cdot e^{-\left(\frac{\varepsilon_i - \varepsilon_o}{\delta}\right)^\gamma} \quad (2)$$

where, E : Young modulus for concrete under tension, ε_i equals $\varepsilon(t_i)$, and ε_o , δ , γ parameters related to the concrete characteristics, (for a concrete with a cubic strength 50.4 MPa, $\varepsilon_o = -1 \times 10^{-4}$, $\delta = 2.8 \times 10^{-4}$ and $\gamma=2.1$)

The second part, the time-dependent part, (which considers the internal friction and damage from microcracking inertia effects), is determined by superposition:

$$\sigma_\varepsilon(t_i) = k_m \cdot \sum_{j=1, i} \left[\Delta\alpha_j \cdot \max\left(n_j + n_{gj}, \frac{k_j \cdot S_{\beta j}}{k_m}\right) \right] \quad (3)$$

in which:

$$\Delta\alpha_j = e^{-\left(\frac{\varepsilon_j - \varepsilon_o}{\delta}\right)^\gamma} - e^{-\left(\frac{\varepsilon_{j-1} - \varepsilon_o}{\delta}\right)^\gamma} \quad (4)$$

where, j : time step index, $\varepsilon_j = \varepsilon(t_j)$ and $\varepsilon_{j-1} = \varepsilon(t_{j-1})$. In order to explain better Eq. (3), some details follow about model physical interpretation.

According to the mechanical model for the representation of the inertia effects due to microcracking, we have two phases as we can see in Fig. 1. In the first phase, the masses on each one of the two sides of the material zone around the presumed crack are not active, and the spring in between, (simulating the elastic material characterizations), follows the absolute displacement u , of the structure showing a stiffness k_f . There is a linear equation between the force S_f and the displacement u of the spring. $S_{\beta j}$ is defined, as the force required to cause cracking of the spring between the two SDOF masses. The stress that causes cracking of the spring at strain $\varepsilon(t_j)$ is equal to $E\varepsilon(t_j)$ and hence the spring force corresponding to it, is: $S_{\beta j} = (EA_i) \varepsilon(t_j)$.

When $S_f = S_{\beta}$, the second phase of crack-initiation begins, which means the breakage of the intermediate spring element of Fig. 1a. Then, the mechanical model of the two SDOF masses is activated, in order to include the energy absorption and to describe the post-cracking concrete behavior. The dashed borders of Fig. 1, represent the structural system, which has a much bigger mass in comparison to the mass (m), of the influence zone at each side of the crack; k_m is the stiffness of the spring connecting each mass (m), to the structural system; $n(\tau)$: is the mass displacement relative to the structure; and $n_g(\tau)$ is the displacement of the structural system, (see Fig. 1b).

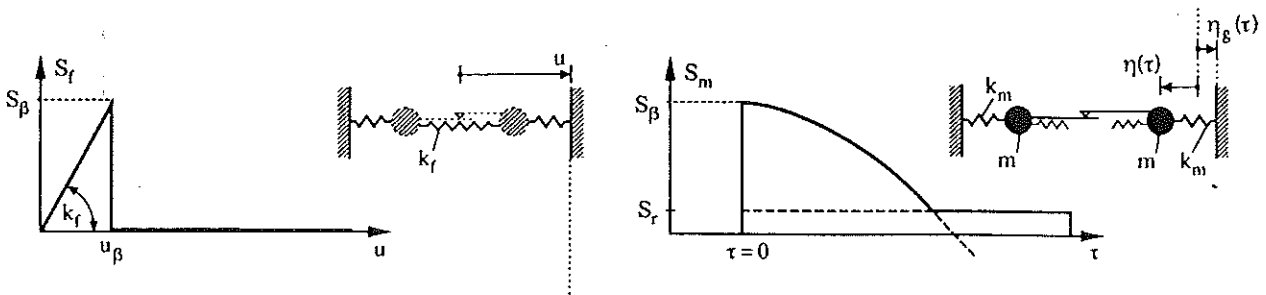


Fig. 1 Mechanical model before and after crack initiation

The Differential equation of the motion of the SDOF mass (m), is:

$$m \cdot \ddot{\eta}(\tau) + k_m \cdot \eta(\tau) = S_r(\eta) - (k_m \cdot \eta_g(\tau)) \quad (5)$$

where $S_r(n) = k_m n(\tau)$. If we denote the right-hand-side of Eq. (5) as a function of τ , $f(\tau)$, we have noticed that we can use the well-known, (for the structural dynamics continuous solution), Duhamel Integral, to express the response of the system as a function of time, $n(\tau)$, in the following way:

$$\eta(\tau) = \frac{1}{k_m} \cdot \int_0^t f(\tau) \sin \omega(t - \tau) d\tau - \eta(0) \cos(\omega t) \quad (6)$$

by integrating we take:

$$\eta_j = \eta_j(0) \cos \omega_j(t_i - t_j) + \frac{k_1 S_{\beta j}}{k_m} (1 - \cos \omega_j(t_i - t_j)) - \dot{u}_{oj} \left[t_i - t_j - \frac{\sin \omega_j(t_i - t_j)}{\omega_j} \right] + \frac{\dot{u}_{oj}}{2\tau_{1j}} \left[(t_i - t_j)^2 + \frac{2}{\omega_j^2} (1 - \cos \omega_j(t_i - t_j)) \right] \quad (7)$$

in which: $n(0)$ at the beginning of the second-phase equals S_β/k_m , and n_{gj} is given by:

$$\eta_{gj} = \begin{cases} \dot{u}_{oj}(t_i - t_j) \left(1 - \frac{t_i - t_j}{2\tau_{1j}} \right) & \text{if } (t_i - t_j) \leq \tau_{1j} \\ \dot{u}_{oj} \left(\frac{t_i - t_j}{2} \right) & \text{if } (t_i - t_j) > \tau_{1j} \end{cases} \quad (8)$$

\dot{u}_{oj} is defined as the structural velocity (m/sec), i.e. the time-derivative of the displacement excluding rigid body motion. \dot{u}_{oj} can be taken equal to the product of the strain-rate $\dot{\epsilon}$ times a reference length over which deformations are converted into nearly uniform strains, (e.g. the specimen length L). Also, the natural angular frequency, and the mass (m) are:

$$\omega = \sqrt{\frac{k_m}{m_j}} \quad \text{where} \quad m_j = A[B \cdot e^{-C\dot{\epsilon}_j} + 1] \quad (9)$$

where $A=1.5 \times 10^{-11}$, $B=470$ and $C=0.5$. For the calculation of time-dependent part of stress the integration time step Δt , should be at most equal to one-sixth of $2\pi/\omega_j$.

Since the model is valid for the case of 1-D monotonic loading, (forces in the lateral direction are not taken into account), the material characterization for the continuous element refers to a length L. Along this reference length L, a single element is applied and over the volume of the element, a number of parallel single elements are connected formulating a series of elements which represent the total material behaviour. The load-carrying capacity of the whole system can be obtained by adding the partial contributions, see Eq. (3). After the crack initiation those systems lose gradually their load-carrying capacity.

3. SPLIT - HOPKINSON BAR

For the dynamic investigation of the material properties the Split-Hopkinson Bar equipment has been proved a reliable tool,^{2,5,6,7} providing the necessary measures for verification of the constitutive model. Fig. 2 shows the Hopkinson bar apparatus which was used in a series of tensile experiments on plain concrete, at the Joint Research Centre in Ispra⁶. These experiments form the basis

4. COMPARISON BETWEEN MODEL AND EXPERIMENT

A series of 10 uniaxial tensile experiments on concrete specimens, which have been carried out in the Hopkinson Bar apparatus at the JRC in Ispra, are used for the model evaluation. The concrete specimens had a square cross-section of 6x6 cm, (the same as the cross-section of the aluminum bars of the device), the specimen lengths were varying between 3 and 15 cm. Plain concrete composition is referred in⁶. Each experiment provides the strain history $\epsilon(t)$, which together with the mechanical and geometric characteristics of the specimen, form the input for the constitutive equations. The strain history $\epsilon(t)$ of the specimen, can be determined either by using Eq. (14), or directly from the measurements of the strain-gauge which was glued to the specimen. In the last case measures of the strain were available only for the ascending part of the σ - ϵ diagram, because by the time the specimen was reaching its tensile strength, the strain-gauge broke. However, as far as there were direct measures of the strain-gauge, they were in good agreement⁶ with the calculated values of Eq. (14), finally it was decided to consider as $\epsilon(t)$ the specimen strain in the ascending part, while the formula of Eq. (14) was used for the rest of the response. The σ - ϵ diagrams for each experiment are constructed using for the calculation of the strain-history $\epsilon(t)$, and the stress-history $\sigma(t)$, Eqs. (14) and (13) respectively. These curves are shown in Fig. 3 along with informations about specimen dimensions and the average strain-rate (i.e. the mean strain-rate over the required time steps of the response). In order to make easier the comparison, in the same figure we can also see the constitutive model predictions, which consist of: a) a time-independent part of stress, $\sigma_0(\epsilon_i)$, see Eq. (2); b) a time-dependent part of stress, $\sigma_\epsilon(t_i)$, see Eq. (3); and c) the total predicted stress, $\sigma(t_i)$, see Eq. (1), vs. the input strain history $\epsilon(t_i)$ described above. In Fig. 4, the different strain-histories $\epsilon(t)$ for specimens of the same dimensions, are shown. In the model calculations, Young modulus for concrete was taken from Bachmann, as 34.000 MPa, and was not adapted to the experimentally measured E_{exp} , which was greater. This difference is obvious noticing the σ - ϵ curves in Fig. 3, and we can say that using E_{exp} in the model the overall agreement would have been better, but finally the initial value was used, since it was closer to the provisions of the relative CEB¹ committee recommendations, for concrete under tension.

Comparing experimental to model predictions we can say that in most of the cases, the two curves are quite similar regarding the σ - ϵ diagram (e.g. the tensile strength of concrete, the corresponding strain, the descending branch of the curves). Trying to quantify the agreement between experiment and model, in Fig. 3, values of the following comparison parameters are also presented:

1) Percentage of difference between model and experiment for the tensile strength, and the corresponding strain: In general this percentage for strength is less than 10% (very good agreement), while for the strain varies from 0% to 100%, (in 6 cases it is less than 20%, while the average is 38%, which is a satisfactory value).

2) Ratio of the total predicted tensile strength to the corresponding value of the time-independent part of stress (which approximates the static case): This ratio ranges from 1.7 to 2. (average 1.9). The corresponding ratio for strain ranges from 1.7 to 2.1 (average 1.95). The above average values are very close to the experimentally measured between high and low strain rates in⁶.

Concluding, in most of the cases the agreement between model predictions and experiments appears sufficiently close and that permitted to proceed to further implementation of the model into Finite Element codes.

for the evaluation of the Bachmann constitutive model, presented in the previous chapter.

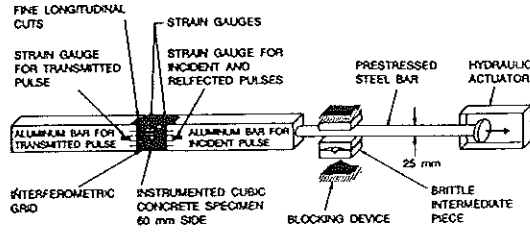


Fig. 2 Hopkinson-Bar for dynamic testing of concrete under tension

As we can see in Fig. 2 the incident pulse ϵ_I and the reflected pulse ϵ_R , were measured via strain-gauge glued on the incident aluminum bar, while a second strain-gauge glued at equal distance from the specimen, as the first one, was used for measurement of the transmitted pulse ϵ_T . The concrete specimen, with a square 6x6 cm cross-section, was sandwiched between the bars by gluing. Strain gauges were also glued to the plain concrete specimen to give direct strain measures of the concrete specimen. The average strain ϵ_s and strain-rate $\dot{\epsilon}_s$ of the specimen, are calculated from the displacements at the end of the specimen:

$$\epsilon_s = \frac{c_0}{l} \int_0^t (\epsilon_I - \epsilon_R - \epsilon_T) dt \quad (10)$$

$$\dot{\epsilon}_s = \frac{c_0}{l} (\epsilon_I - \epsilon_R - \epsilon_T) \quad (11)$$

where c_0 , is the wave propagation velocity, and l , is the specimen length. Assuming that the specimen is in equilibrium, which means uniform stress and equal forces at the specimen ends, we get:

$$\epsilon_R + \epsilon_I = \epsilon_T \quad (12)$$

$$\sigma_s = E \cdot \frac{A}{A_s} \cdot \epsilon_T \quad (13)$$

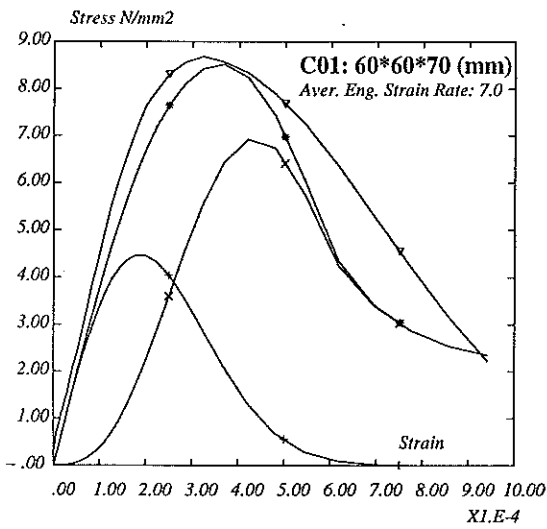
where σ_s , is the mean stress over the specimen, E and A , are Young modulus and cross-section of the aluminum bar respectively, and A_s , cross-section of the specimen. By substituting Eq. (12) into Eqs. (10) and (11), we obtain the following expressions of the average strain ϵ_s , and the average strain-rate $\dot{\epsilon}_s$, of the specimen:

$$\epsilon_s = -\frac{2c_0}{l} \int_0^t \epsilon_R dt \quad (14)$$

$$\dot{\epsilon}_s = -\frac{2c_0}{l} \epsilon_R \quad (15)$$

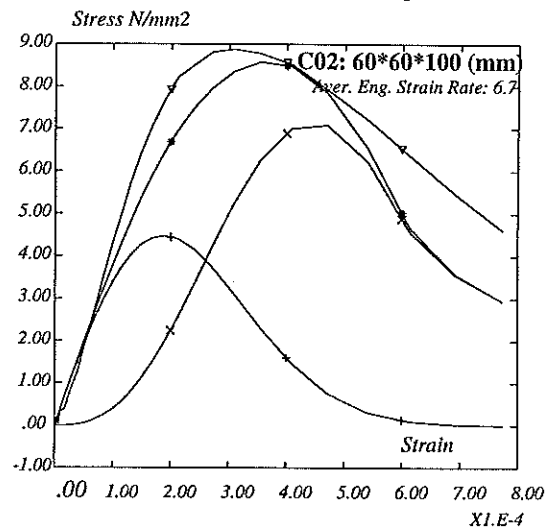
So, using the measured signals of the strain-gauge stations on the two aluminum bars near the specimen we can calculate, the strain ϵ_s , the stress σ_s , and the strain-rate $\dot{\epsilon}_s$ history of the concrete specimen.

Perc. of Diff. EXPER - MODEL for STRENGTH = 1.9(%)
 Corresp. STRAIN = 14.0(%)
 Ratio of Total Pred. to Time-Indep. Part of STRENGTH: 1.9
 Corresp. STRAIN: 2.1

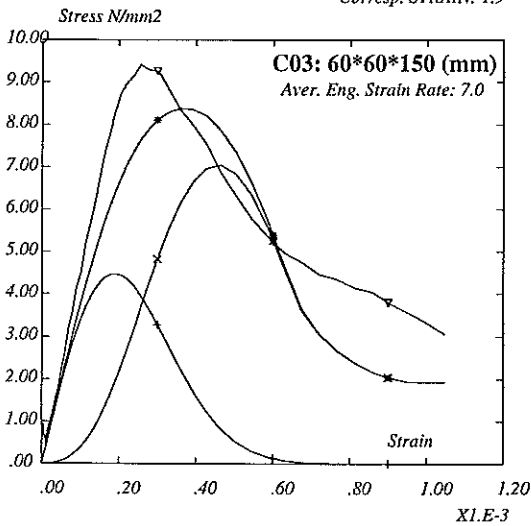


Perc. of Diff. EXPER - MODEL for STRENGTH = 3.4(%)
 Corresp. STRAIN = 14.7(%)
 Ratio of Total Pred. to Time-Indep. Part of STRENGTH: 1.9
 Corresp. STRAIN: 1.9

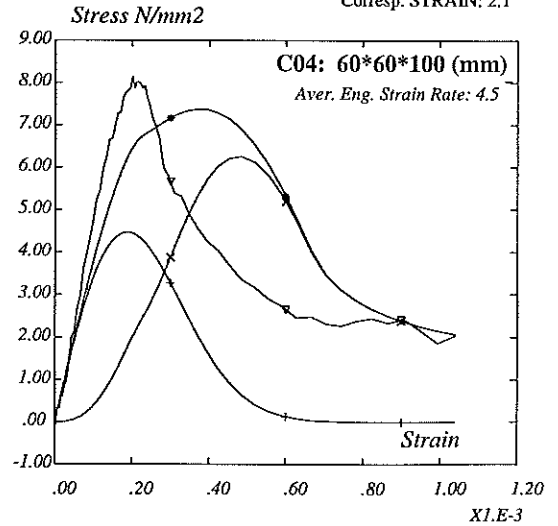
- Total
- × Time-Dep.
- + Time-Indep.
- ▽ Experiment



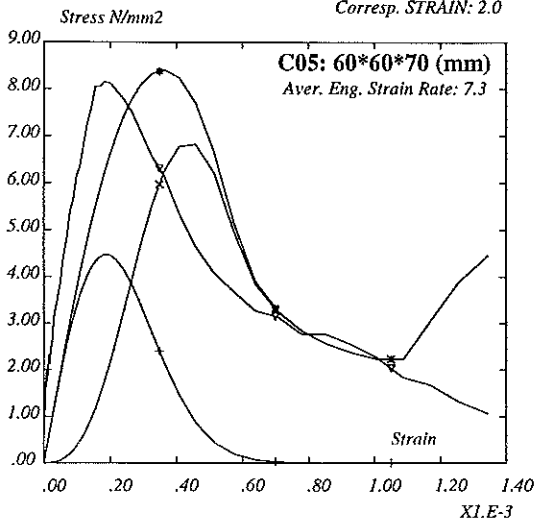
Perc. of Diff. EXPER - MODEL for STRENGTH = 10.9(%)
 Corresp. STRAIN = 39.7(%)
 Ratio of Total Pred. to Time-Indep. Part of STRENGTH: 1.9
 Corresp. STRAIN: 1.9



Perc. of Diff. EXPER - MODEL for STRENGTH = 9.0(%)
 Corresp. STRAIN = 83.9(%)
 Ratio of Total Pred. to Time-Indep. Part of STRENGTH: 1.7
 Corresp. STRAIN: 2.1



Perc. of Diff. EXPER - MODEL for STRENGTH = 3.2(%)
 Corresp. STRAIN = 99.7(%)
 Ratio of Total Pred. to Time-Indep. Part of STRENGTH: 1.9
 Corresp. STRAIN: 2.0



Perc. of Diff. EXPER - MODEL for STRENGTH = 17.8(%)
 Corresp. STRAIN = 20.1(%)
 Ratio of Total Pred. to Time-Indep. Part of STRENGTH: 1.9
 Corresp. STRAIN: 2.0

- Total
- × Time-Dep.
- + Time-Indep.
- ▽ Experiment

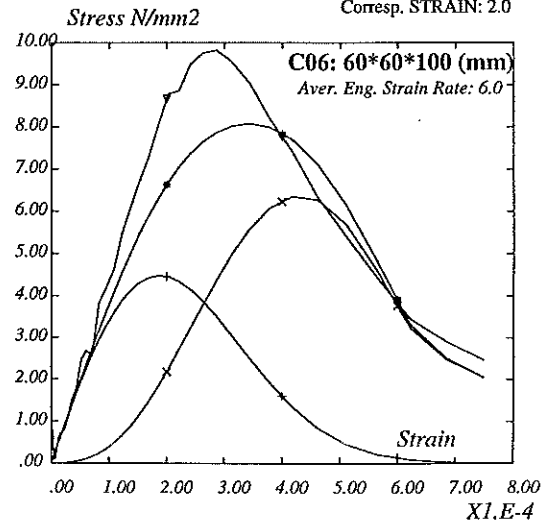
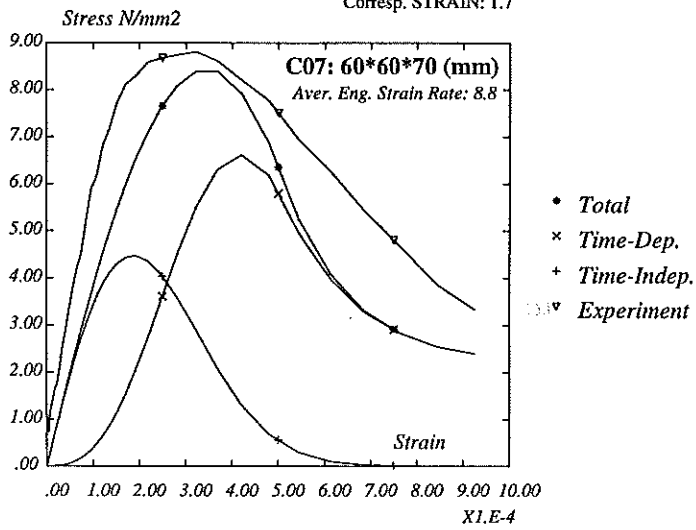
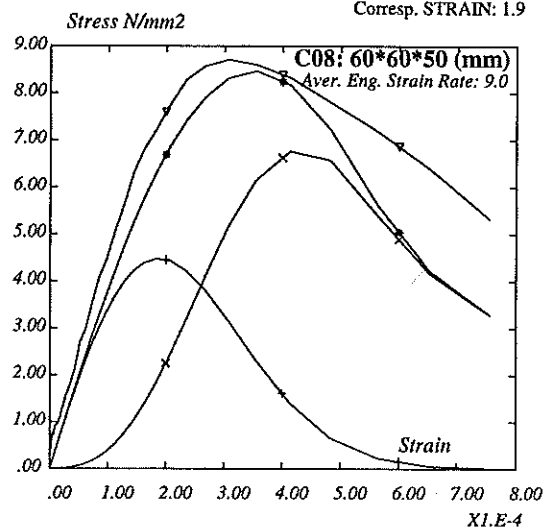


Fig. 3

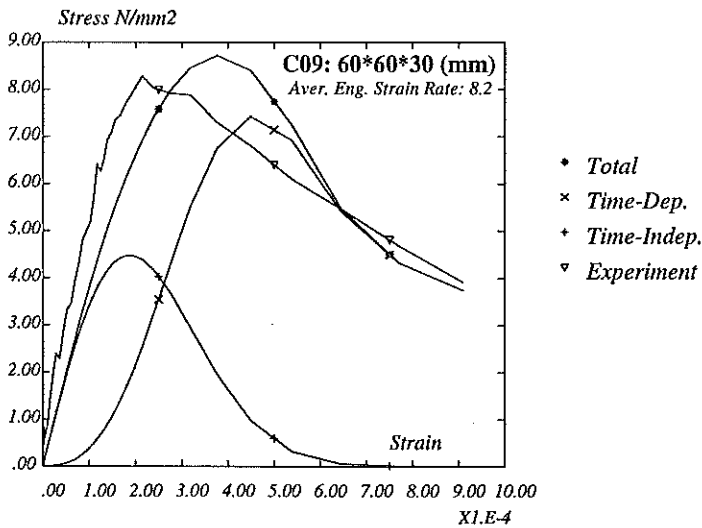
Perc. of Diff. EXPER - MODEL for STRENGTH = 4.8(%)
 Corresp. STRAIN = .0(%)
 Ratio of Total Pred. to Time-Indep. Part of STRENGTH: 1.9
 Corresp. STRAIN: 1.7



Perc. of Diff. EXPER - MODEL for STRENGTH = 2.8(%)
 Corresp. STRAIN = 15.7(%)
 Ratio of Total Pred. to Time-Indep. Part of STRENGTH: 1.9
 Corresp. STRAIN: 1.9



Perc. of Diff. EXPER - MODEL for STRENGTH = 5.3(%)
 Corresp. STRAIN = 75.3(%)
 Ratio of Total Pred. to Time-Indep. Part of STRENGTH: 2.0
 Corresp. STRAIN: 1.9



Perc. of Diff. EXPER - MODEL for STRENGTH = 7.3(%)
 Corresp. STRAIN = 15.5(%)
 Ratio of Total Pred. to Time-Indep. Part of STRENGTH: 1.9
 Corresp. STRAIN: 1.9

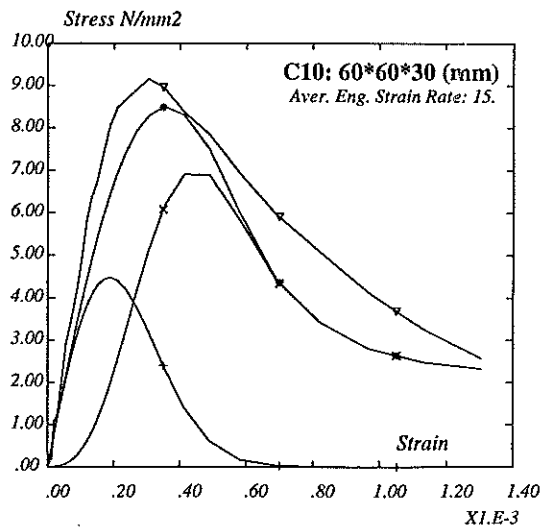


Fig. 4 Stress-strain diagrams of concrete specimens, comparison between model and experiment

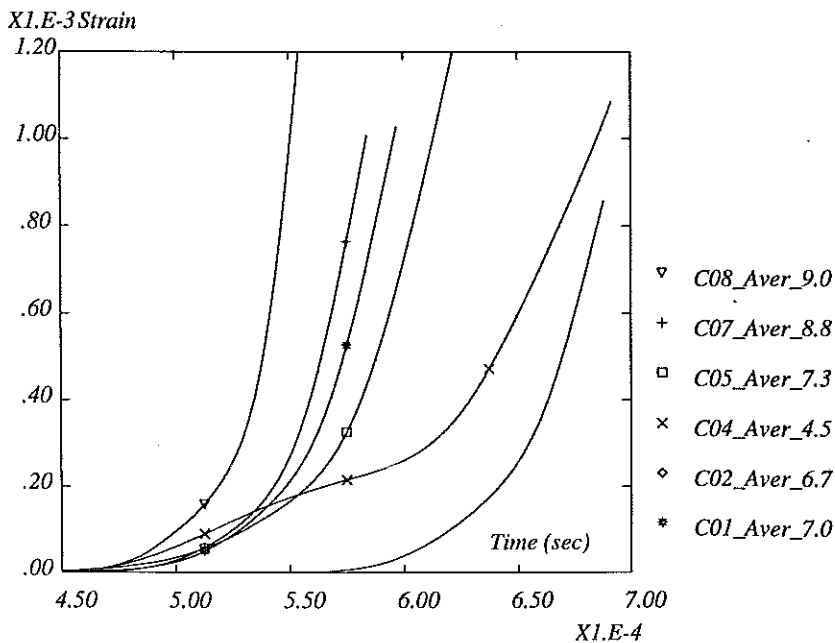


Fig. 5 Strain-histories of the concrete specimens

5. MODEL IMPLEMENTATION

Consequently the Bachmann model is implemented as an additional material model to the F. E. code, EURDYN-1D¹⁰. This code was developed at JRC in Ispra to serve as a tool for the analysis of fast transient events involving propagation of longitudinal mechanical waves (subsonic) in structures. The analysis is one-dimensional in the sense that all conditions are supposed to be uniform over the generic cross-section of the structure. Both geometrical and physical nonlinearities can be taken into account. Typical examples are impact problems, collision events, fast dynamic loading due to explosions or sudden release of initial loads due to failure, etc.

Model implementation in the foresaid code has two purposes: a) Simulation of the Hopkinson bar apparatus, where the material model will be used for the representation of specimen behaviour. This is particularly interest for the needs of a research program, currently underway in Ispra, about the study of the mechanical response of plain concrete in a large range of strain-rates; b) Material model in F. E. structural analysis, where the stress state suits to the assumptions of the model.

An application of the material model implementation is presented trying to combine both aspects referred above. A modified Hopkinson Bar is simulated for the dynamic investigation of the material properties¹⁰. The example consists of two long elastic bars, and of a specimen AB which is placed between the bars. One of the bars is prestressed and then it is released and an incident ϵ_I tension wave travels along it until it reaches the specimen, where a reflected ϵ_R and a transmitted wave ϵ_T are generated. According to the theory of elastic wave propagation ϵ_I , ϵ_R , ϵ_T are calculated as first-derivatives of the corresponding displacements, (which are functions of time). At every step of the response the material model, for calculating the new stress value needs to know not only the current value of strain, but also strain-history and strain-rate-history. The algorithm for the implementation of the time-dependent strain-rate model follows the equations written in Chapter 2, i.e. Eq. (1) to Eq. (9). In Fig. 5 we can see the σ - ϵ behaviour of the simulated specimen AB, (three nodes were selected at the beginning, middle and end of specimen discretization).

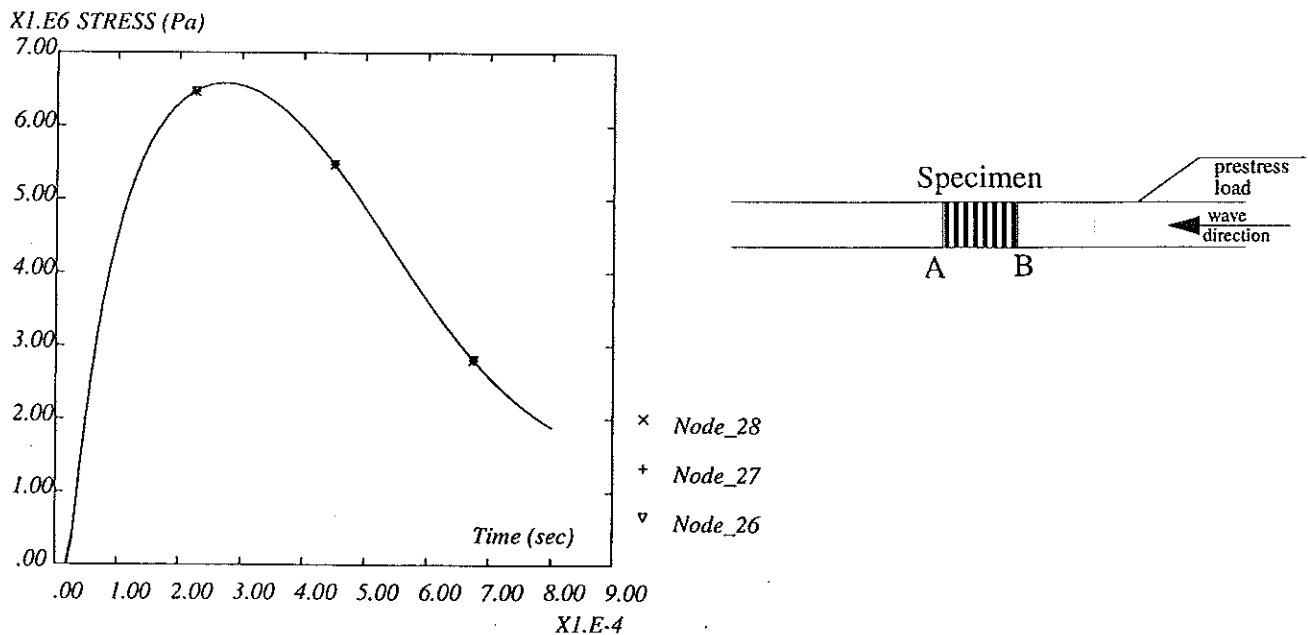


Fig. 6 Stress-Strain behaviour of the specimen

6. CONCLUSIONS

The heterogeneous nature of concrete is the dominant cause for the observed, under high rates of loading, increase: of the strength, of the corresponding strain and of the energy absorption during the fracture process. Strain-rate effects are encountered in all materials of heterogeneous nature differing only in magnitude. Bachmann mechanical model, primarily based on inertia effects, was evaluated on the basis of 10 experiments on concrete specimens under tension. Experimental strain-histories corresponding to different average strain-rates were given as input to the mechanical model, to determine the stress time-history.

The agreement between model and experiment was found satisfactory. The percentage of difference for concrete dynamic strength was less than 10%, while for the corresponding strain the average percentage was less than 40%. The mean ratio of the total predicted strength to the time-independent part, (which is near the static case), was 1.9. The mean ratio of the corresponding strains was 2.

References

- [1] CEB: "Concrete Structures under Impact and Impulsive Loading", Bulletin d' Information, No. 187, Lausanne, (1988).
- [2] Reinhardt, H. W., Kormeling, H. A., and Zielinski A. J.: "The Split Hopkinson bar, a versatile tool for the impact testing of concrete", *Materiaux et Constructions*, Vol. 19, No. 109, 55-63, (1986).
- [3] Bachmann, H.: "Die Massentragheit in einem Pseudo-Stoffgesetz für Beton bei schneller Zugbeanspruchung", *Massivbau Baustofftechnologie Karlsruhe*, Heft 19, (1993).
- [4] Eibl, J.: "Ein Strukturmodell zur Betonzugfestigkeit", Universität Dortmund, (1980).
- [5] Albertini, C., and Montagnani, M.: "Testing Techniques Based on the Split Hopkinson Bar", *Instit. of Physics, London, Conf. Ser. No. 21, 22-31*, (1974).
- [6] Albertini, C., and Montagnani, M.: "Study of the True Tensile Stress-Strain diagram of Plain Concrete with real size aggregate: Need for and Design of a Large Hopkinson Bar Bundle", *DYMAT 94*, Sept. 26-30, Oxford, U.K., (1994).
- [7] Kormeling, H. A., Zielinski A. J., and Reinhardt, H. W., Report No. 5-80-3, Delft University of Technology, Stevin Laboratory (1980).
- [8] Zielinski, A. J.: "Model for Tensile Fracture of Concrete at High Rates of Loading", *Cement & Concrete Research*, Vol. 14, 215-224, (1984).
- [9] Davies, R. M.: "A Critical Study of the Hopkinson Pressure Bar", *Phil Trans Roy Soc, London, Ser A*, 240-375, (1948).
- [10] Casadei, F., and Halleux, J.P.: "EURDYN-1D: A Computer Code for the One-Dimensional Non-Linear Dynamic Analysis of Structural Systems", Report EUR 10115 EN, European Commission, JRC, Ispra, (1985).

Comparer avec travaux de
F. Monthillet.

Dynamic Ductility of Metallic Materials

E. El-Magd

Aachen Technical University, Augustiner bach 4, 52056 Aachen, Germany

Abstract

The stabilizing effect of the strain rate sensitivity increases the ductility under impact tensile deformation. Similar to the super-plastic behaviour, high values of elongation at fractures are achieved on smooth parts. However, an increased strain rate reduces the local fracture strain leading to an increased dynamic notch sensitivity.

Introduction

In the quasi-static tension test, the strain hardening causes an increase of the force and acts stabilizing on the deformation process, while reduction of area reduces the force and acts destabilizing. Under dynamic loading, four additional factors influence the ductility of the material: The increased strain rate sensitivity leads to an increase of the local value of the flow stress in the neck zone and acts stabilizing while the adiabatic character of the deformation process reduces the flow stress and promotes instability. Mass inertia forces in the lateral direction arising in connection with the radial acceleration due to reduction of area cause the initiation of either lateral tension or lateral compression stresses depending upon the time function of the specimen elongation. And last, the local failure strain decreases with increasing strain rate which means a higher notch sensitivity under impact conditions than under quasi-static loading. With all these influencing factors, the material ductility under dynamic loading can be very different from the ductility under quasi-static conditions.

Influence of strain rate sensitivity

Neck formation and mechanical instability can be discussed in the case of tension test on the basis of the theory of imperfections. Small deviation from the ideal cylindrical form of a test bar as well as small local deviation of the yield strength of the material can be expected as a result of the production conditions within specified tolerance limits. Such imperfections are found to cause a nonuniform deformation from the beginning of the tension test. A diameter deviation grows during plastic tensile deformation leading to neck formation [1, 2]. The local

stress at the smallest cross-section is slightly higher than in other regions. Therefore, the local strain is higher and the smallest cross-section decreases more than others. This trend is promoted by the adiabatic character of the deformation processes, since higher deformed regions are even more softened by the deformation heat. On the other hand, a deformation localization is accompanied by an increased strain hardening and an increase in the local strain rate which both lead to higher local flow stresses. With increasing deformation, the maximum load condition will be fulfilled first at the smallest cross-section whereas other specimen regions are still having lower strain values and undergo a partial unloading.

The influence of strain rate can be studied considering a test bar, whose cross-sectional area is not constant along the gauge length but is given by $S_0 = S_{0\min}[1 + \alpha(x)]$, where $\alpha(x)$ can be represented by a cos-function with a maximum value of ca. 0.5 %. The material behaviour is described by

$$\sigma = [K (B + \epsilon)^n + \eta \dot{\epsilon}] \exp [-\beta (T - T_0) / T_m] \quad (1)$$

Assuming that 90% of the deformation energy is transferred to heat, the temperature increases by $dT = 0.9\sigma d\epsilon / (\rho c)$ where ρ and c are the density and the specific heat. Considering the temperature increase, the force F at an arbitrary cross-section with the current area $S_0 \exp(-\epsilon)$ is given by

$$F = S_0 \exp(-\epsilon) \frac{[K (B + \epsilon)^n + \eta \dot{\epsilon}]}{1 + a \int [K (B + \epsilon)^n + \eta \dot{\epsilon}] \dot{\epsilon} dt}$$

with $a = 0.9\beta / (T_m \rho c)$. As the force is equal for all cross-sections, the strain ϵ at an arbitrary cross-section can be determined as a function of the strain ϵ_1 at the minimum cross-section by a numerical evaluation of the relation

$$\frac{[K (B + \epsilon)^n + \eta \dot{\epsilon}] \exp(-\epsilon)}{1 + a \int [K (B + \epsilon)^n + \eta \dot{\epsilon}] \dot{\epsilon} dt} = \frac{S_{0\min}}{S_0} \frac{[K (B + \epsilon_1)^n + \eta \dot{\epsilon}_1] \exp(-\epsilon_1)}{1 + a \int [K (B + \epsilon_1)^n + \eta \dot{\epsilon}_1] \dot{\epsilon}_1 dt} \quad (2)$$

In addition, the elastic unloading of lower deformed regions after reaching the maximum load has to be considered. The total extension of the specimen is calculated by integrating $\exp(\epsilon) - 1$ over the specimen length so that the relation between Force and elongation can be calculated. **Fig 1** shows experimental results for the conventional stress strain diagram of a low alloyed steel determined in the indirect tension test by means of a split Hopkinson bar arrangement as well as a computational example showing the influence of strain rate. Specially after reaching the maximum load, the strain values corresponding to a defined value of force is increased by increasing strain rate.

Assuming that fracture takes place, as soon as an upper limit of the local strain is reached in the narrowest cross-section, the influence of strain rate on the elongation at fracture can be determined. **Fig.2** shows experimental data [3] and computation examples for this relation.

Notch sensitivity

Because ductile fracture usually starts at material regions with a high local strain and a high hydrostatic tension, the failure criterion for ductile fracture is defined by the local failure

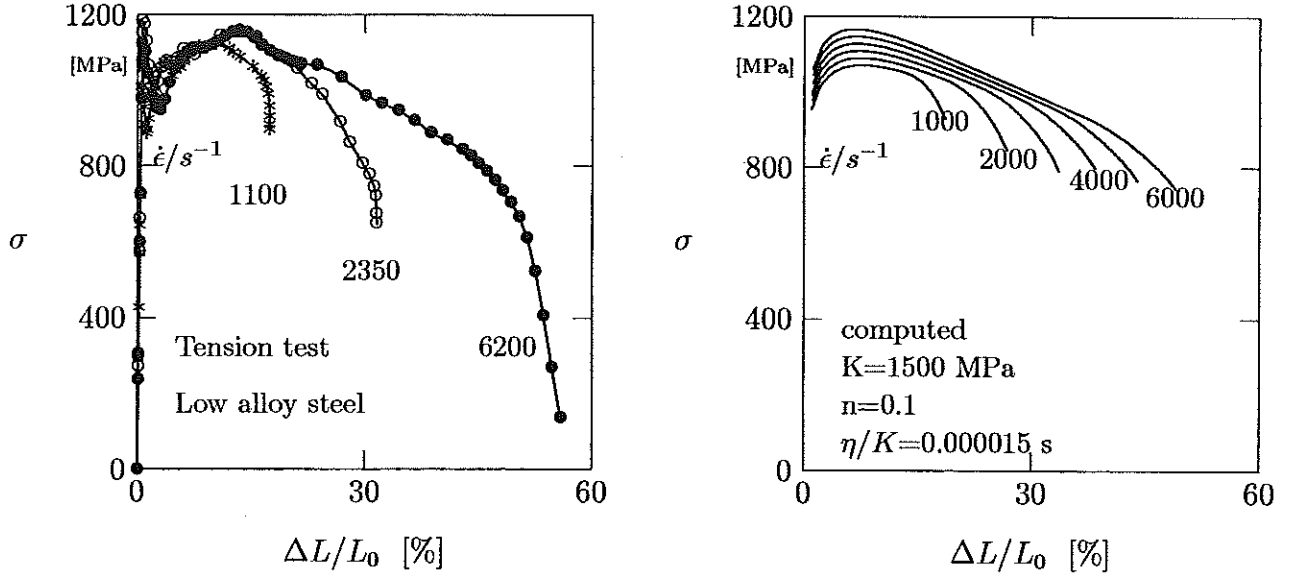


Figure 1: Influence of the strain rate on the stress strain curve a) experimental results , b) computation results

strain ϵ_f ($\sigma_m / \bar{\sigma}$) as a function of the ratio between the mean stress $\sigma_m = (\sigma_I + \sigma_{II} + \sigma_{III}) / 3$ and the equivalent stress $\bar{\sigma}$. Such a relation is deduced considering that ductile fracture occurs due to nucleation, growth and coalescence of micro-cavities. Hancock and Mackenzie [4] assumed the failure strain is given by the sum of two components: the strain up to the nucleation of voids ϵ_n which depends mainly on the purity of the material, and the strain between nucleation and fracture which is regarded to be inversely proportional to the relative rate of cavity growth with respect to strain ($d \ln R / d \bar{\epsilon}$), where R is the radius of an existing void and $\bar{\epsilon}$ is the local equivalent strain. The rate of void growth can be determined as a function of ($\sigma_m / \bar{\sigma}$) applying the theory of plasticity. McClintock et al. [5] deduced a closed-form analytical solution for the rate-of-growth of cylindrical cavities of elliptical cross-section in a strain-hardening material. A more common relation was deduced Rice and Tracy [6] for the rate-of-change of the radius of a spherical void in an ideal plastic material

$$\bar{\sigma} = \text{const.} : \quad \frac{1}{R} \frac{dR}{d\epsilon} = 0.28 \exp \left[\frac{3 \sigma_m}{2 \bar{\sigma}} \right] \quad (3)$$

With this relation, Hancock and Mackenzie [4] introduced their well known failure criterion

$$\epsilon_f = \epsilon_n + \alpha \exp \left[-\frac{3 \sigma_m}{2 \bar{\sigma}} \right] \quad (4)$$

Combined experimental and numerical investigations, such as [7], showed that the factor $3/2$ should be replaced by a material constant β having usually higher values.

Although this relation was deduced for ideal plastic materials neglecting the strain hardening and the strain rate sensitivity of the material, it was also applied to deformation conditions for which this assumption does not hold, e.g. in the case of impact loading with highly increased strain rate sensitivity. Johnson and Cook [8] applied this relation to the range of

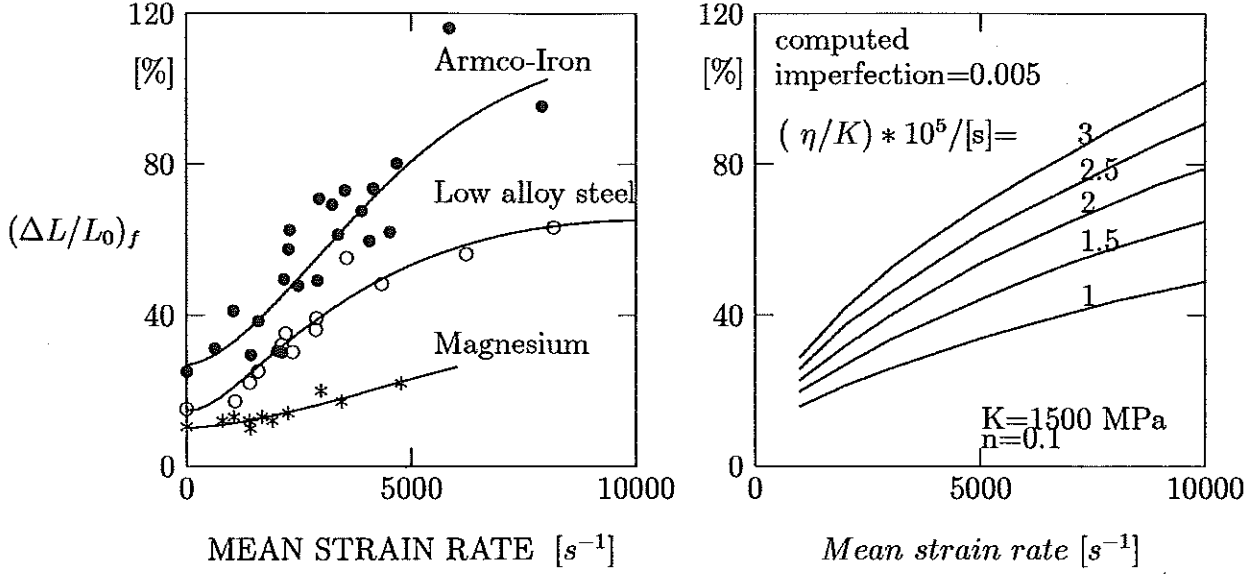


Figure 2: Influence of strain rate on the elongation at fracture: a) experimental results of the indirect impact tension test according to Weissaupt, b) coputation results.

high strain rates after introducing correction factors considering the influences of strain rate and temperature:

$$\epsilon_f = [D_1 + D_2 \exp(D_3 \sigma_m / \bar{\sigma})] [1 + D_4 \ln(\dot{\epsilon} / \dot{\epsilon}_0)] [1 + D_5 T / T_m] \quad (5)$$

It is assumed that fracture starts when a damage parameter $D = \Sigma(\Delta\epsilon / \epsilon_f)$ reaches the value of unity. As ductility usually increases with increasing temperature and the mechanical stability is increased by increasing strain rate sensitivity i.e. by increasing strain rate, it was expected, that the parameter D_4 and D_5 should be positive. In [8], this was found to be valid for relatively blunt notches. However, Barton et al. [9],[10] showed that in the case of copper no significant influence of the strain rate or temperature exists on the failure strain. On the other hand, the failure strain of Remco-iron or AQ85-iron decreased as the strain rate or temperature was increased. For this materials negative values were determined for the Parameters D_4 and D_5 . If this result is discussed in terms of the Hancock-Makenzie-condition of eq. (4), it means that the nucleation strain ϵ_n is dependent on the strain rate and temperature.

Void growth in visco-plastic materials

In order to consider the influence of the strain rate sensitivity of the material on the rate of growth of voids and on the fracture strain, following simple modell can be applied:

A spherical void of radius R is considered to exist at the center of a metallic sphere. At the outer radius L of this hollow sphere, a radial stress σ_{rL} is acting which leads to a viscoplastic deformation of the material and hence to an increase of the void volume. The material law is simply given by

$$\bar{\sigma} = \sigma_h + C \left(\bar{\dot{\epsilon}} / \dot{\epsilon}^* \right)^m \quad (6)$$

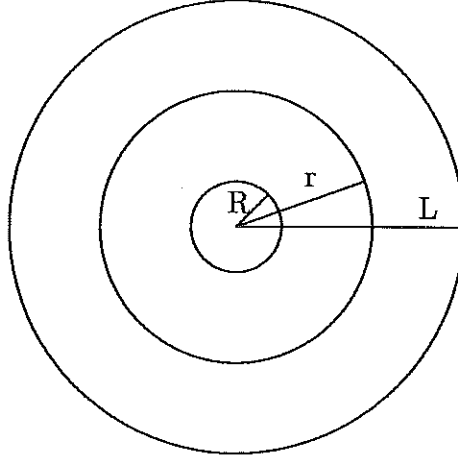


Figure 3: Modelling of the growth of voids by visco-plastic deformation of the surrounding material

For an arbitrary radius r , the tangential strain rate is given by $\dot{\epsilon}_t = \dot{r}/r$. Under consideration of the plastic volume constancy $2\dot{\epsilon}_t + \dot{\epsilon}_r = 0$, the equivalent strain rate yields

$$\bar{\dot{\epsilon}} = \sqrt{\frac{2}{3}(2\dot{\epsilon}_t^2 + \dot{\epsilon}_r^2)} = 2\frac{\dot{r}}{r} \quad (7)$$

Regarding the continuity condition $r^2 \dot{r} = R^2 \dot{R}$, the equivalent strain rate can be written in the form

$$\bar{\dot{\epsilon}} = \bar{\dot{\epsilon}}_R \left(\frac{R}{r}\right)^3 \quad (8)$$

and the corresponding equivalent stress follows considering $\bar{\sigma} = \bar{\sigma}_L$ for $\bar{\dot{\epsilon}} = \bar{\dot{\epsilon}}_L$ by

$$\bar{\sigma} = \sigma_h + (\bar{\sigma}_L - \sigma_h) \left(\frac{\bar{\dot{\epsilon}}_R}{\bar{\dot{\epsilon}}_L}\right)^m \left(\frac{R}{r}\right)^{3m} \quad (9)$$

In order to determine the distribution of the radial stress, the condition of equilibrium

$$\frac{\partial \sigma_r}{\partial r} - 2 \frac{\sigma_t - \sigma_r}{r} = 0 \quad (10)$$

is taken into consideration, where as $\sigma_t - \sigma_r = \bar{\sigma}$ according to the von Mises yield criterion. With the function $\bar{\sigma}(r)$ according to eq.(9) the following differential equation is obtained

$$\frac{\partial \sigma_r}{\partial r} = \frac{2}{r} \left[\sigma_h + (\bar{\sigma}_L - \sigma_h) \left(\frac{\bar{\dot{\epsilon}}_R}{\bar{\dot{\epsilon}}_L}\right)^m \left(\frac{R}{r}\right)^{3m} \right] \quad (11)$$

so that with the boundary condition $\sigma_r = \sigma_{rL}$ for $r = L$ a closed form analytical solution is obtained:

$$\sigma_r = \sigma_{rL} - \frac{2}{3m} \left[\left(\frac{R}{r} \right)^{3m} - \left(\frac{R}{L} \right)^{3m} \right] \left(\frac{2 \dot{R}/R}{\dot{\epsilon}_L} \right)^m (\bar{\sigma}_L - \sigma_h) - 2\sigma_h \ln(L/r) \quad (12)$$

As there is no internal pressure in the void, $\sigma_r = 0$ for $r = R$ and the relative rate of volume increase follows by

$$r = R: \quad \frac{1}{R} \frac{dR}{d\bar{\epsilon}_L} = \frac{1}{2} \left[\frac{3m}{2(1-f^m)} \frac{\sigma_{rL} - \frac{2}{3}\sigma_h \ln\left(\frac{1}{f}\right)}{\bar{\sigma}_L - \sigma_h} \right]^{(1/m)} \quad (13)$$

with $f = (R/L)^3$ which is regarded approximately equal to the volume fraction of voids in the material.

At the outer radius of the sphere $r = L$ the values σ_{rL} , $\bar{\sigma}_L$ und $\dot{\epsilon}_L$ of the radial stress, the equivalent stress and the equivalent strain rate can be regarded as equal to the values σ_m , $\bar{\sigma}$ und $\dot{\epsilon}$ of the mean stress and the equivalent stress and strain rate which are determined for the construction element geometry considering the material as a continuum either by neglecting the voids or by using a material law for porous materials.

$$\bar{\sigma} = \sigma_h + C \left(\frac{\dot{\epsilon}}{\dot{\epsilon}^*} \right)^m: \quad \frac{1}{R} \frac{dR}{d\bar{\epsilon}} = \frac{1}{2} \left[\frac{3m}{2(1-f^m)} \frac{\sigma_m - \frac{2}{3}\sigma_h \ln\left(\frac{1}{f}\right)}{\bar{\sigma} - \sigma_h} \right]^{(1/m)} \quad (14)$$

For strain hardening materials, the solution of small strains can be used as an approximation assuming that the strains are proportional to the strain rates:

$$\bar{\sigma} = K \epsilon^n \left(\frac{\dot{\epsilon}}{\dot{\epsilon}^*} \right)^m: \quad \frac{1}{R} \frac{dR}{d\bar{\epsilon}} \approx \frac{1}{2} \left[\frac{3(n+m)}{2(1-f^{n+m})} \frac{\sigma_m}{\bar{\sigma}} \right]^{\frac{1}{n+m}} \quad (15)$$

and for impact loading with very high local values of the strain rate

$$\bar{\sigma} \approx \eta \dot{\epsilon}: \quad \frac{1}{R} \frac{dR}{d\bar{\epsilon}} = \frac{3}{4(1-f)} \frac{\sigma_m}{\bar{\sigma}} \quad (16)$$

A similar relation was deduced by Seaman et. al.[11]. In analogy to the failure criterion introduced by Hancock and Mackenzie [4], the local equivalent strain at fracture ϵ_f is assumed to consist of the strain ϵ_n till nucleation of voids and an additional strain value which is inversely proportional to $d \ln R / d\bar{\epsilon}$. Assuming that the ratio $\sigma_m / \bar{\sigma}$ remains approximately constant during deformation and that $f \ll 1$, the failure criterion can be given for the different material laws by:

$$\bar{\sigma} = \sigma_h + C \left(\frac{\dot{\epsilon}}{\dot{\epsilon}^*} \right)^m: \quad \epsilon_f = \epsilon_n + \alpha \left[\frac{\sigma_m - \frac{2}{3}\sigma_h \ln\left(\frac{1}{f}\right)}{\bar{\sigma} - \sigma_h} \right]^{(-1/m)} \quad (17)$$

$$\bar{\sigma} = K \epsilon^n \left(\frac{\dot{\epsilon}}{\dot{\epsilon}^*} \right)^m: \quad \epsilon_f = \epsilon_n + \frac{\alpha}{(\sigma_m / \bar{\sigma})^{1/(n+m)}} \quad (18)$$

$$\bar{\sigma} \approx \eta \bar{\epsilon} : \quad \epsilon_f = \epsilon_n + \frac{\alpha}{(\sigma_m/\bar{\sigma})} \quad (19)$$

Experimental procedure

Indirect impact tensile tests were carried out on pure iron (Armco iron) and on the austenitic steel X2CrNiMo 18 10. A Split-Hopkinson bar arrangement is mounted in a vertical hollow cylinder and is fixed to its lower end. The cylinder stands on styropor block with negligible mechanical impedance. A falling hammer hits the upper end of the hollow cylinder and a compression wave propagates along it and is reflected at its lower end as a tensile wave, partially back in the cylinder wall and partially in the input bar. The tensile wave propagates throughout the input bar, reaches the specimen, deforms it plastically and exits to the output bar. With this arrangement, a loading period of $150 \mu\text{s}$ is achieved. The dimensions of the components are so optimized that a maximum particle velocity of 32 m/s is reached at the specimen end by wave steepening. Notched specimens with a notch radius of curvature of $\rho=0.4 \text{ mm}$ and 0.7 mm with a root diameter of $d=3 \text{ mm}$ and outer diameter of $D=4, 5$ and 6 mm were tested quasi-statically and dynamically [12]. In addition, hour-glas specimens having a circular profile line with a radius of curvature of 6 mm and 12 mm were tested. The constants of the material law $\sigma = K(B + \epsilon)^n + \eta\epsilon$ were determined by testing completely cylindrical specimens.

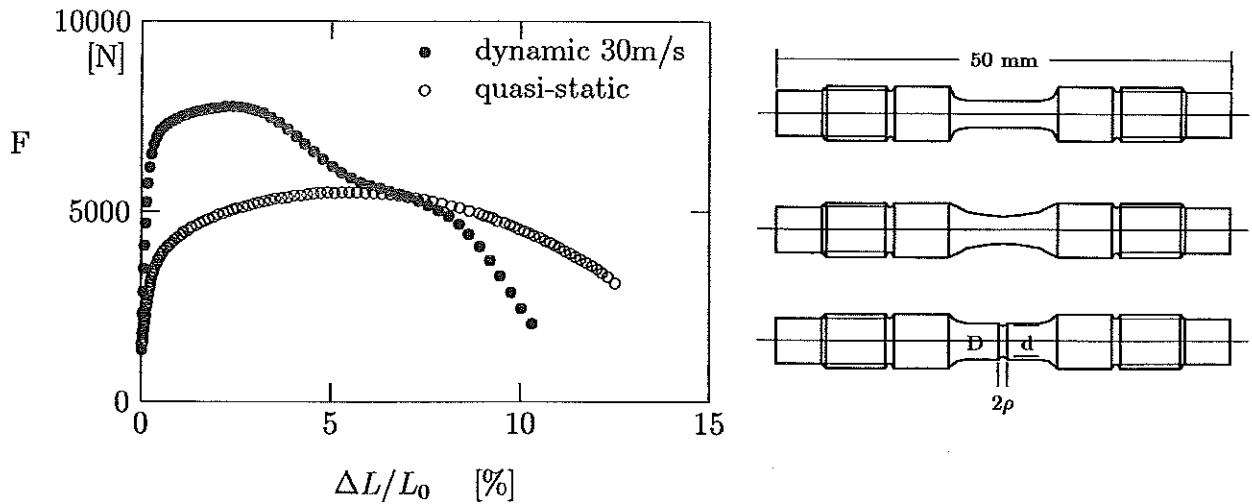


Figure 4: Comparison between the force-extension-curve of notched specimen under quasi-static and dynamic Loading; Geometry of cylindrical, hour-glas shaped and notched specimens

A comparison is shown in **Fig. 4** between the force-displacement curves of a notched bar ($D=4\text{mm}$; $d=3\text{mm}$; $\delta=0,4\text{mm}$) obtained under quasi-static and dynamic loading. In addition to typical changes in the form of the curve, it is clear that under dynamic loading, the maximum forces is increased and the elongation at fracture is reduced.

Computational results

The time function of the particle velocity determined experimentally as an input signal of the Hopkins-bar was used as a boundary condition in Finite Element computations [13] using an explicit code for dynamic loading with lumped masses . **Fig.5** presents an example for the analysis showing the current distributions of the ratio $\sigma_m/\bar{\sigma}$ and of the equivalent strain $\bar{\epsilon}$ after reaching different values for the total extension of the specimen.

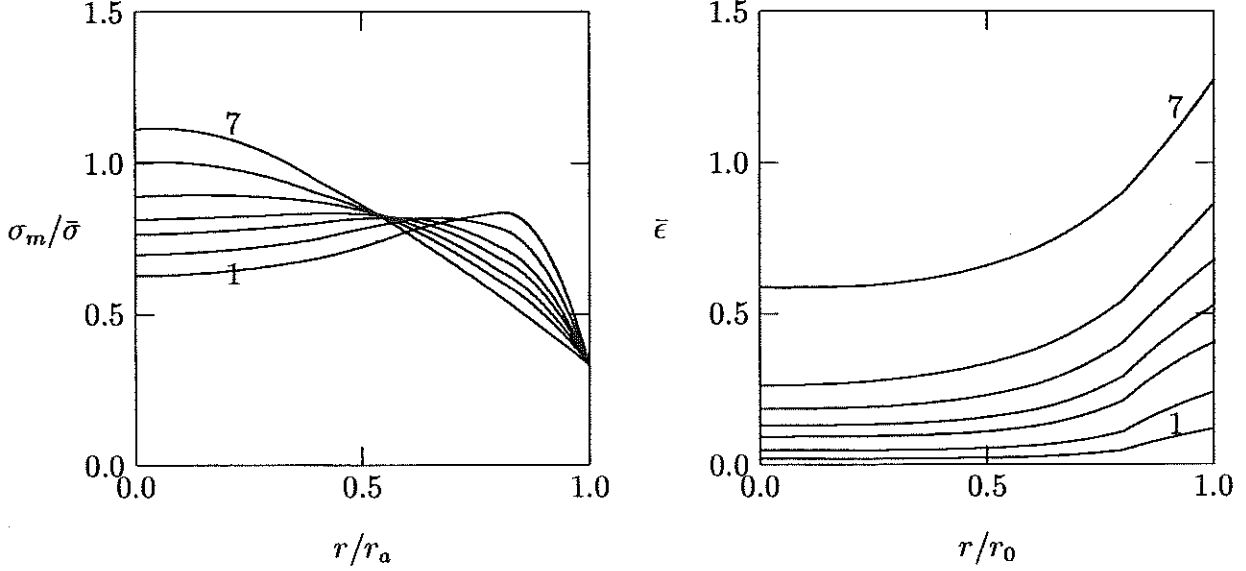


Figure 5: Destribution of the hydrostatic stress and the effective strain over the radius in the notch root cross-section after reaching differnt values of the specimen elongation: $D=4$ mm, $d=3$ mm, $\rho=0.4$ mm

Specially interesting are these distributions at fracture denoted (7) in the figure. The analysis shows that in case of notched bars the following fact can be stated: At the specimen axis ($r = 0$) the equivalent strain $\bar{\epsilon}$ is lower and the ratio $\sigma_m/\bar{\sigma}$ is higher than at the notch root ($r = d/2$). On the other hand, the analysis of hour-glas specimens with great radius of curvature showed that in this case both of $\bar{\epsilon}$ and $\sigma_m/\bar{\sigma}$ are higher at $r = 0$ than at the surface. Therefore, it can be stated that in case of hour-glas specimens as well as in the neck zone of unnotched specimens the fracture starts at the specimen axis. However, such a statement cannot be generally made for notched bars. With decreasing radius of curvature of the notch, the equivalent strain increases at the notch root much higher than at the specimen axis, so that the starting point of fracture is first unknown and cannot be located directly. Using the experimentally determined value for the total extension of the specimen at fracture, the corresponding values of $\bar{\epsilon}$ and $(\sigma_m/\bar{\sigma})$ were determined at different values of the radius in the narrowest cross-section and are represented for each specimen as a function $\bar{\epsilon}(\sigma_m/\bar{\sigma})$ in **Figs. 6 and 7**. Only one point of each curve, which is still unknown, fulfils the failure condition. All other points of the curve have an effective strain value $\bar{\epsilon}$ which is still lower than the fracture strain ϵ_f for the local value $(\sigma_m/\bar{\sigma})$. Therefore, the upper envelope of the curves $\bar{\epsilon}(\sigma_m/\bar{\sigma})$ determined for specimens with different geometries represents the failure

criterion $\epsilon_f(\sigma_m/\bar{\sigma})$. The point of contact between the envelope and the individual curve defines the location of the starting point of fracture. In case of relatively sharp notches, the envelope contacts the $\bar{\epsilon}(\sigma_m/\bar{\sigma})$ -curve at higher values of $\bar{\epsilon}$ and lower values of $(\sigma_m/\bar{\sigma})$ which means that the fracture starts at the notch root. In case of relatively mild notches the envelope contacts the $\bar{\epsilon}(\sigma_m/\bar{\sigma})$ -curve at a point with higher values of $(\sigma_m/\bar{\sigma})$ and lower values of $\bar{\epsilon}$ indicating the start of fracture at the specimen axis. For the hour-glas specimens with great radius of curvature of the profile line, high values of $\bar{\epsilon}$ coincide with high values of $(\sigma_m/\bar{\sigma})$ at the specimen axis where fracture begins.

These results are analogous to observations of Holland, Halim and Dahl [7] for quasi-static loading.

In contrary to the results obtained by Johnson and Cook [8], the fracture criterion $\epsilon_f(\sigma_m/\bar{\sigma})$ determined here for Armco-iron and for steel X2CrNiMo 18 10 under dynamic loading are much lower than that determined under quasi-static loading in agreement with the results of Barton et.al. for Remco-iron [9]

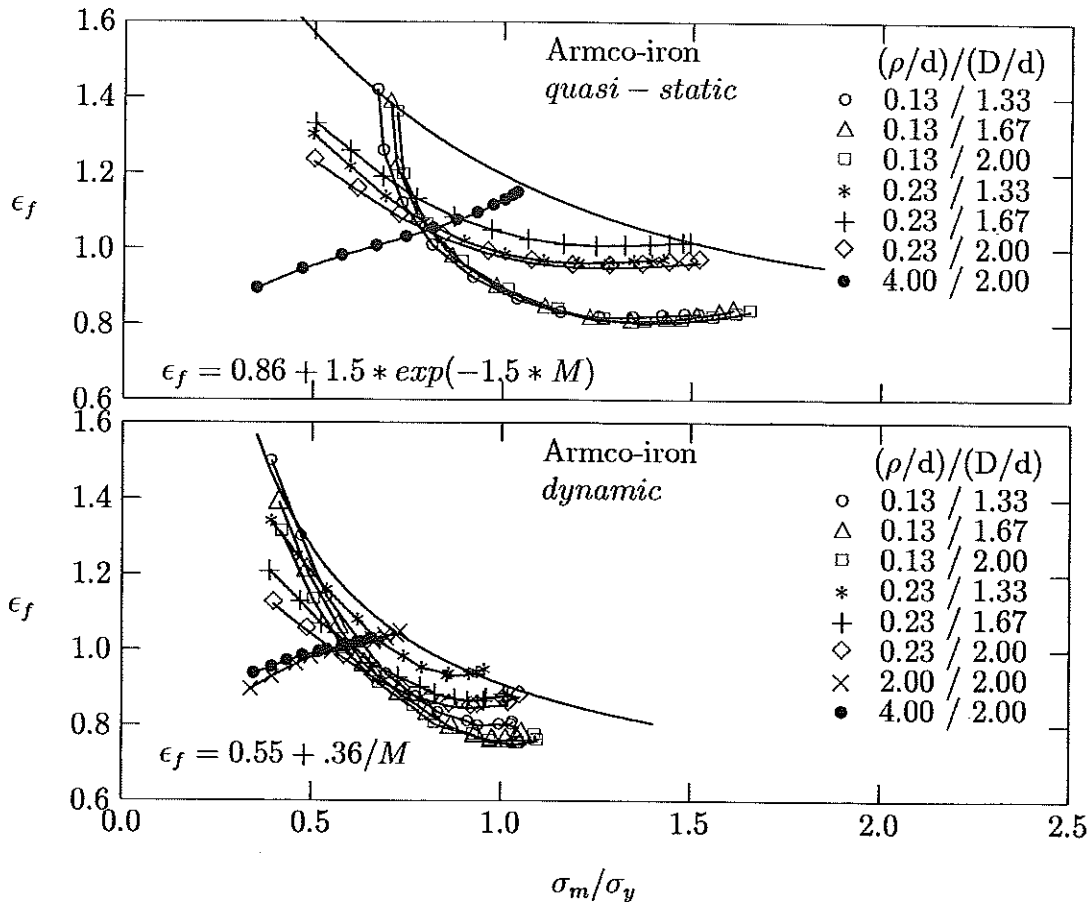


Figure 6: Local failure strain as a function of the ratio of hydrostatic stress to the flow stress for pure iron

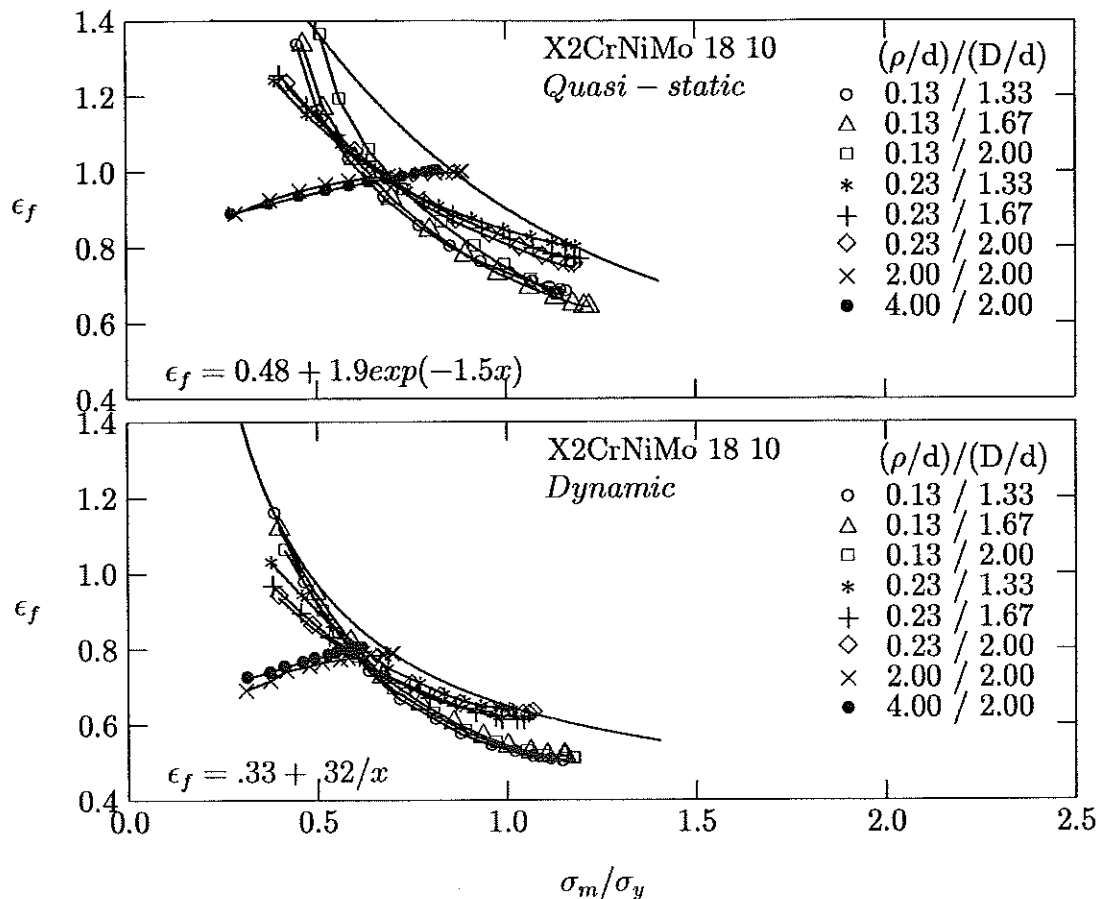


Figure 7: Local failure strain as a function of the ratio of hydrostatic stress to the flow stress for austenitic steel

References

- [1] EL-MAGD, E.: Materialprüfung 15(1973)pp. 90-95
- [2] EL-MAGD, E.: Archiv Eisenhüttenwesen 45(1974)pp.83-89
- [3] WEISSHAUPT, H.: Dr.-Ing.-Dissertaion, TH-Aachen 1995
- [4] HANCOCK, J.W. AND A.C. MACKENZIE: J. Mech. Phys. Solids, 24(1976)pp. 147-169
- [5] MCCLINTOCK, F.A.: J.appl.Mech. 35(1968)pp.363.
- [6] RICE, J.R. AND D.M. TRACY: J. Mech. Phys. Solids, 17(1969)pp. 201-217
- [7] HOLLAND, D.; A. HALIM AND W. DAHL: Steel research (1990), pp. 504-506
- [8] JOHNSON, G.R. AND W.H. COOK: Eng. Fract. Mech. 21(1985), pp. 31-48
- [9] BARTON, D.C.; J.L. STURGES; M.S. MIRZA and P. CHURCH: Journal de Physique IV, Colloque C3-931, suppl. au J. de Physique III, Vol. 1, Oct. 1991
- [10] BARTON, D.C., M.S. MIRZA, J.L. STURGES AND M. WAHEED: Journal de Physique IV, Colloque C8-659, suppl. au J. de Physique III, Vol. 4, Sept. 1994
- [11] SEAMAN, L.; D.R. CURRAN AND D.A. SHOCKEY: J. Appl. Phys. 47(1976)pp.4814-4826
- [12] TREPPMANN, C.: unpublished report, L.F.Werkstoffkunde, RWTH Aachen
- [13] ABDELAZIZ, A.: Dr.-Ing. Dissertation, RWTH Aachen, in preparation

Influence de la structure du matériau à a et bcc.

NEW EXPERIMENTAL TECHNIQUES IN TESTING OF SHEET METALS AT HIGH STRAIN RATES

J.R.Klepaczko

Laboratoire de Physique et Mécanique des Matériaux
ISGMP, Université de Metz
Ile du Saulcy, F-57045 METZ , France

ABSTRACT

Three relatively new experimental techniques which are applied for testing of sheet metals at different strain rates, from quasi-static to impact, are reviewed in this paper. Those techniques have been recently put into operation in LPMM-Metz :

- a) Inverted Split Hopkinson Bar, specially designed to test sheet metals in tension at high strain rates;
- b) Direct Impact Shear Test of sheet metals with Double Shear Specimen geometry;
- c) Direct Impact Dart Test, for testing of sheet metals in biaxial stretching and perforation.

All those experimental techniques cover a wide range of strain rates, typically from $10E-4$ 1/s to $10E4$ 1/s.

INTRODUCTION

Sheet metal is a primary material used in construction of different components of cars, coaches and other vehicles. Because of probability of collisions, cars and other vehicles must be tested at different collision velocities to evaluate their crashworthiness. Since it is much cheaper to evaluate the crashworthiness by computer simulations much effort has been put recently to improve the simulation techniques. However, the most important part of the simulation techniques is the input constitutive relation written generally in the form:

$$\text{in tension/compression } (\sigma, \varepsilon, \dot{\varepsilon}, T) = 0 \quad \text{or in shear } (\tau, \Gamma, \dot{\Gamma}, T) = 0 \quad (1)$$

In order to formulate and verify constitutive relations for sheet metals, mostly deep drawing steels, special experimental techniques have been recently developed in LPMM-Metz. Those techniques cover the whole accessible range of strain rates, for example in shear from $10E-4$ 1/s to $10E4$ 1/s, i.e. eight decimal orders. Within quasi-static range ($10E-4$ 1/s to $10E2$ 1/s), a fast, closed-loop hydraulic testing machine is employed with different special devices designed for sheet metal testing.

In the high strain rate range ($10E2$ 1/s to $10E4$ 1/s) the impact loading has been employed together with experimental techniques based on propagation of elastic waves.

Although some experimental techniques for high strain rate tension tests on cylindrical specimens are available, for example [2,7], tension tests on sheet metals are more difficult to perform. Since the deep-drawing steels exhibit relatively large plastic deformations, the uniform elongations may vary from 20% to 40%, the displacement imposed to neck specimen may be relatively large, even for a small active part of the specimen (gage length). A standard Split Hopkinson Pressure Bar converted into tension allows for only relatively small displacements of the specimen grips, usually up to ~ 3 mm. So far the two loading schemes have been proposed in the literature and used by different authors.

The first one is just a standard SHPB converted into tension by application of the split collar covering the specimen. The first incident compressive wave is transmitted through the bars, collar and specimen without imposition of plastic strain on the specimen. The first incident wave is reflected from the free end of the transmitter bar as the incident tensile wave which deforms the specimen fixed in between bars. The next part of experiment, and analysis, are analogous to the standard SHB technique, [3]. In this configuration the net displacement available in between bars is small and consequently the active gage length of the specimen must be short, typically up to 5 mm. Such characteristics of this configuration eliminate possibility of application to tensile testing of sheet metals.

The second one is based on the modified split Hopkinson bar with prestressed part in tension of the incident bar, [4]. Again the gage length must be relatively short, ~ 10 mm, and specimens used have circular geometry. A similar technique was reported more recently in [5]. In the latter case the circular tensile specimens were quite short, from 1.27 mm to 6.25 mm. A very short specimen introduces the side effect, that is the measured force is higher than for the standard-length specimen. A short specimen, however, improves to some extent the wave equilibrium and strain uniformity along the gage length.

One of the earliest experimental technique applied in impact tension was reported in [6] and later in [7]. In this method a dynamometer is used in tests made in a rotary impact testing machine with impact velocities up to ~ 60 m/s. Relatively long specimen (~ 200 mm) was loaded by impact from one side by the rotary wheel, the other side of the specimen was attached to the dynamometer. The dynamometer was fastened to the anvil of the machine as it is shown in Fig.1. This scheme of loading and force measurements are used even nowadays, for example [8]. A similar scheme was reported in [1] to test sheet metals, Fig.2.

The split Hopkinson bar arrangement (two bars and a tensile specimen in between) inherits small net displacements imposed on the specimen as it is discussed above. Consequently, it is then difficult to test specimens with a high plasticity and thus large elongations.

Another solution to test specimens with large elongations is the "block-bar" method used for the first time in compression, [9], and later converted into the so called "one bar method" in tension, for example [10] and [11]. In this scheme of loading, shown in Fig.3, one side of the tensile specimen is attached to the Hopkinson bar, typically from 2 to 3 m in length, the second side is loaded by an impact through a crossbar attached to this end. Strain gages cemented to the Hopkinson bar are used to determine the transmitted force through the specimen during its deformation. Displacement of the impact end of the specimen is usually measured by optical methods, [10,11]. This experimental technique permits for large tensile deformations up to necking and fracture. However, vibrations excited due to Hertzian contact between an impact machine and the crossbar, for example a rotary impact machine, [10], or slingshot type, [11], obscures the test. On the other hand, because application of the Hopkinson bar, the vibrations are reduced in comparison to the loading chain in the form crossbar/specimen/short dynamometer, Figs 1 and 2.

DIRECT-LOAD SPLIT HOPKINSON BAR FOR TENSILE TESTING

A very effective loading scheme which has been put recently into operation in LPMM-Metz, with a complete elimination of vibrations, is the "Inverted Split Hopkinson Bar". The function of the incident bar is completely inverted. A flat or round specimen is fixed in between two long bars, 6 meters each, and the incident bar is clamped at its active end very close to the specimen, Fig.4. The other end of the incident bar is fixed to the hydraulic jack. The incident bar is slowly preloaded by the hydraulic jack. At the desired level of stress in the incident bar the clamp is suddenly released and the *unloading* tensile incident wave which loads the specimen propagates out toward the hydraulic jack. The force carried out by the specimen is transmitted into the transmitter bar as a tensile elastic wave. Both waves, that is the *unloading* wave and transmitted one are recorded with the two-channel digital oscilloscope. A great advantage of such configuration is possibility to impose directly large displacements on the tensile specimen in the simplest way, without a collar or other wave converters. In the scheme applied in LPMM-Metz displacements imposed on the specimen can reach even 30 mm with relatively very short time ~ 1.5 ms. Because the strain gage stations are cemented very closely to the specimen ends the period of time without any disturbances from the far ends of the bars is about 2.4 ms, which is much longer than in the standard SHB configurations.

A complete theory of the test along with some technical data and preliminary results will be given elsewhere, [12].

It appears that there is no need to place a mechanical clamp in the middle of the incident bar, for example [4,5] and [13] to load specimen directly by a tensile pulse.

HIGH-STRAIN RATE TESTING OF SHEET METALS IN SHEAR

In tension tests, slow or fast, the instability occurs during plastic deformation in the form of necking, and the uniform deformation along a specimen is limited. In order to develop constitutive relations suitable for large deformations another modes of plastic deformation must be applied, for example, a very convenient scheme of loading is shear. An experimental technique for quasi-static shear test was introduced and discussed in [14]. The test uses flat, rectangular specimens whose ends are divided into three equal sections by parallel longitudinal slits, Fig. 5. The specimen is clamped in a device that prevents out-of-plane movements. The inner and outer sections are pulled in a tensile testing machine. this causes a shear deformation within the plastified regions. The rate of deformation is limited by the maximum crosshead speed of the tensile machine and the shear strain rate is thus limited to about 1.0 1/s.

A much faster scheme of loading, for a double-shear specimen geometry, has been proposed in [15]. A special device which clamps a small, flat, double-shear specimen is inserted in between Hopkinson bars. The SHPB of relatively large diameter 40 mm is charged in the standard compression arrangement. The principle of this technique is shown in Fig. 6. The order of strain rate with this technique is around $10E3$ 1/s.

A new experimental technique, specially designed to test sheet metal in a wide range of strain rates, has recently been developed in LPMM-Metz. The principle of this technique is based on already existing technique for direct-impact shear test of the Modified Double Shear specimen, [16]. The inner part of the MDS specimen with shearing zone 2.0 mm is loaded directly by a long projectile, the external parts of the specimen are supported by 3 meter Hopkinson tube. Application of a long projectiles, up to 500 mm, Hopkinson tube and the optical displacement transducer makes it possible to determine a whole history of specimen deformation, [16].

An analogous scheme of loading and measurements, but with a larger scale, that is the external diameter of the Hopkinson tube was increased from 32 mm used in [16] to 50 mm, was applied recently to test sheet specimens. Diameter of the projectiles was changed from

10mm used in testing of MDS specimens, [16], to 22 mm for sheet metal testing. Such geometry permitted for application of larger Double Shear Sheet specimen with dimensions 50 mm x 15 mm with 3.0 mm shear zone for each side, like in [14]. Specimen thickness can be varied around 1.0 mm. Configuration of experimental setup is shown in Fig. 7.

Although a complete theory of this test will be given elsewhere, here some additional informations may be important. The direct impact technique combined with a possibility to test DSS specimens with a fast closed-loop testing machine offers more flexibility in programing of the strain rate spectrum. Range of strain rates covered in LPMM for the DSS specimen is from $10E-4$ 1/s to $10E4$ 1/s, that is eight decimal orders. The range of impact velocities for flat-ended projectiles of different lengths launched from the air gun varies from 1 m/s to 100 m/s, thus the range of the nominal strain rates varies accordingly from ~ 330 1/s to $3.3E4$ 1/s. The impact velocity is measured by the setup consisting of three sources of light, fiber optic leads and three independent photodiodes, [16]. The time intervals of dark signals from the photodiodes caused by the passage of projectile are recorded by two time counters.

Axial displacement of the central part of the DSS specimen is measured as a function of time by an optical non-contact displacement transducer. The transducer reacts to the axial movements of a small black and white target cemented to the central part of the DSS specimen, Fig.7.

Axial force transmitted by the DSS specimen can be determined as a function of time from the transmitted longitudinal elastic wave $\epsilon_t(t)$ measured by the strain gages cemented on the Hopkinson tube at the distance of three external diameters from the specimen support. All electric signals are recorded by a digital oscilloscope and stored in the PC hard disk for further analyses.

Preliminary study of the rate effects on the upper yield stress as well as on saturation stress for IFHR-340 steel sheet (the microalloyed deep drawing steel) have demonstrated the usefulness of the direct impact technique, [17].

DIRECT IMPACT DART TEST

In order to test resistance of a sheet metal to perforation an experimental technique has recently been developed which permits for a dart test with a wide range of impact velocities, [18]. The target was to learn more on plastic behavior of sheet metals loaded biaxially by the hemispherical projectile. On the other hand such test results can constitute a basis for verification of numerical codes. Also, an estimation of the rate sensitivity in such conditions of loading and analysis of the mechanism of perforation was attempted. A wide range of speeds of hemispherical punch (quasi-static tests) or projectile was applied. In the case of direct impact the experimental technique for biaxial loading is again based on the experimental technique of direct impact on MDS specimen, [16]. Scheme of the experimental setup is shown in Fig.8. A circular specimen of diameter 50 mm and thickness ~ 1.0 mm, as it is shown in Fig.9, is fixed at the impact end of the Hopkinson tube of external diameter 50 mm. The specimen is impact loaded by the hemispherical projectile DIA 22.5 mm launched from the air gun. The impact velocities of different length projectiles may vary from 1 m/s to 100 m/s. The projectile velocity is measured as it is described in the previous section. Since during specimen deformation and perforation the projectile displacement is relatively large, up to 20 mm, the fringe technique was used to measure the projectile displacement as a function of time, Fig.8. This method based on the frequency coding is very efficient and error free, [19,20]. On the projectile surface a set of black and white fringes is printed with a small pitch, usually ~ 0.25 mm. During the passage of the projectile in the front of the photodiode, which is situated close by to the specimen and Hopkinson tube, the photodiode emits a series of quasi-sinusoidal voltage signals with frequency proportional to the projectile velocity. Those signals are

recorded by the digital oscilloscope together with the wave transmitted in the Hopkinson tube. Analyses of those two signals recorded as a function of time permit to determine the force vs. displacement characteristics for specimens loaded at different impact velocities. The complete theory of this test and some results are given elsewhere, [18].

CONCLUSIONS

Three experimental techniques which are reviewed in this paper offer a complete set of different tests to characterize behavior of sheet metals within wide range of strain rates from $10E-4$ 1/s to $10E4$ 1/s, both in tension, shear and biaxial loading. Since it is well known that the deep drawing steels do show relatively high strain rate sensitivity, constitutive relations used in the computer codes must take into account this feature. In addition, during tests performed at high strain rates adiabatic softening is quite important, especially in all instability problems, for example necking and perforation, so the tests of sheet metals at different temperatures may provide additional valid data.

ACKNOWLEDGEMENT

The experimental techniques reported in this review were financially supported during its different stages of development by CNRS-France and SOLLAC Industries.

REFERENCES

- [1] A.Tobota, J.R.Klepaczko and J.Gronostajski, Dynamic tensile test of metals by rotational hammer, *Theoretical and Applied Mechanics*, **18** (1980), 351 (in Polish).
- [2] K.Kussmaul and M.Shuele, Dynamic tensile tests on ferritic and austenitic steels with improved testing and measuring technique, *Proc. Conf. EURODYMAT 94, J.de Phys. IV, Coll. C8, 4* (1994), C8-23.
- [3] T.Nicholas, Tensile testing of materials at high rates of strain, *Exp. Mech.*, **21** (1981), 177.
- [4] C.Albertini and M.Montagnani, Testing techniques based on the split Hopkinson bar, *Proc. Conf. Institute of Phys., Conf. Ser. N° 21, The Institute of Physics, London*, (1974), 22.
- [5] G.H.Staab and A.Giliat, A direct-tension split Hopkinson bar for high strain-rate testing, *Exp. Mech.*, **31** (1991), 222.
- [6] M.J.Mnajoine and A.Nadai, High-speed tension tests at elevated temperatures, *Proc. ASTM*, **40** (1940), 822; also *J.Appl. Mech.*, **63** (1941), A-77.
- [7] P.E.Duvez and D.S.Clark, An experimental study of the propagation of plastic deformation under conditions of longitudinal impact, *Proc. ASTM*, **47** (1947), 502.
- [8] W.Meyer, H.D.Kunze and K.Seifert, Dynamic behavior of high strength steels under tension, in *Shock Waves and High-Strain-Rate Phenomena in Metals, Concepts and Applications*, Plenum Press, N. Y., (1981), 51.
- [9] C.K.H.Dharan and F.E.Hauser, Determination of stress-strain characteristics at very high strain rates, *Exp. Mech.*, **10** (1970), 370.
- [10] K.Kawata, S.Hashimoto, S.Sekino and N.Takeda, Macro- and micro-mechanics of high-velocity brittleness and high-velocity ductility of solids, in *Macro- and Micro-Mechanics of High-Velocity Deformation and Fracture, IUTAM Symp., Tokyo 1985, Springer-Verlag, Berlin* (1985), 1.

- [11] G.Regazzoni, Comportement et ductilité du cuivre et du tantale purs dans le domaine de vitesse de déformation, 10^{-4} - 3×10^3 s⁻¹, Thèse Docteur D'Etat Es-sciences, CEA et INP-Grenoble, (1983).
- [12] J.R.Klepaczko, A large-displacement, direct-loading split Hopkinson bar for high-strain-rate tension tests, (1995), in preparation.
- [13] C.Albertini, P.M.Boone and M.Montagnani, Development of the Hopkinson bar for testing large specimens in tension, Proc. Conf. DYMAT 85, J. de Phys. Coll. C5, 46 (1985), C5-499.
- [14] K.Miauchi, Stress-strain relationship in simple shear of in-plane deformation of various steel sheets, Proc. 13th Congress of the International Deep Drawing Research Group, Melbourne, Australia, (1984), 360.
- [15] G.Gary and W.K.Nowacki, Essai de cisaillement plan appliqué à des toles minces, Proc. Conf. EURODYMAT 94, J. de Phys. Coll. C8, 4 (1994), C8-65.
- [16] J.R.Klepaczko, An experimental technique for shear testing at high and very high strain rates, the case of mild steel, Int. J. Impact Engng., 15 (1994), 25.
- [17] J.R.Klepaczko and L.Kruszka, A preliminary study on rate sensitivity of sheet steel IFHR-340, unpublished study, (1995).
- [18] H.Boumaiz et J.R.Klepaczko, Poinçonnement par impact, cas des aciers doux, DYMAT Journal, 2 (1995), 13.
- [19] J.Garbarski and J.R.Klepaczko, Dynamic tension test of polymers, Theoretical and Applied Mechanics, 18 (1980), 265. (in Polish)
- [20] J.R.Klepaczko and A.Solecki, Effect of tempering on quasi-static and impact fracture toughness and mechanical properties for 5140 H steel, Met. Trans. A, 15A (1984),901.

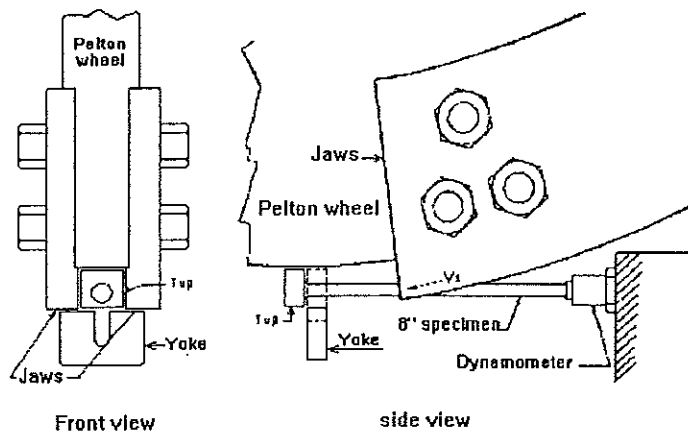


Fig. 1 Rotary impact testing machine, specimen attachment (specimen length: 203 mm) and loading, after [7].

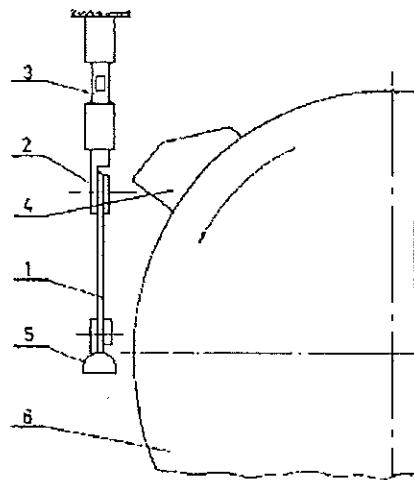


Fig. 2 Vertical rotational hammer for testing of sheet metals, 1- flat specimen; 2- upper grip; 3- dynamometer; 4- symmetric jaws (each side); 5- lower grip; 6- wheel, after [1].

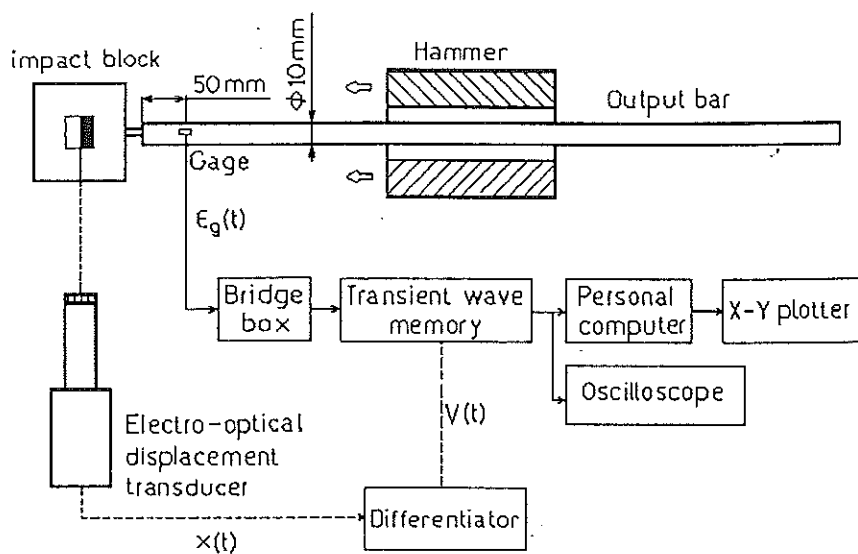


Fig.3 Scheme of "one bar method" for tension impact test (block - bar configuration), after [10].

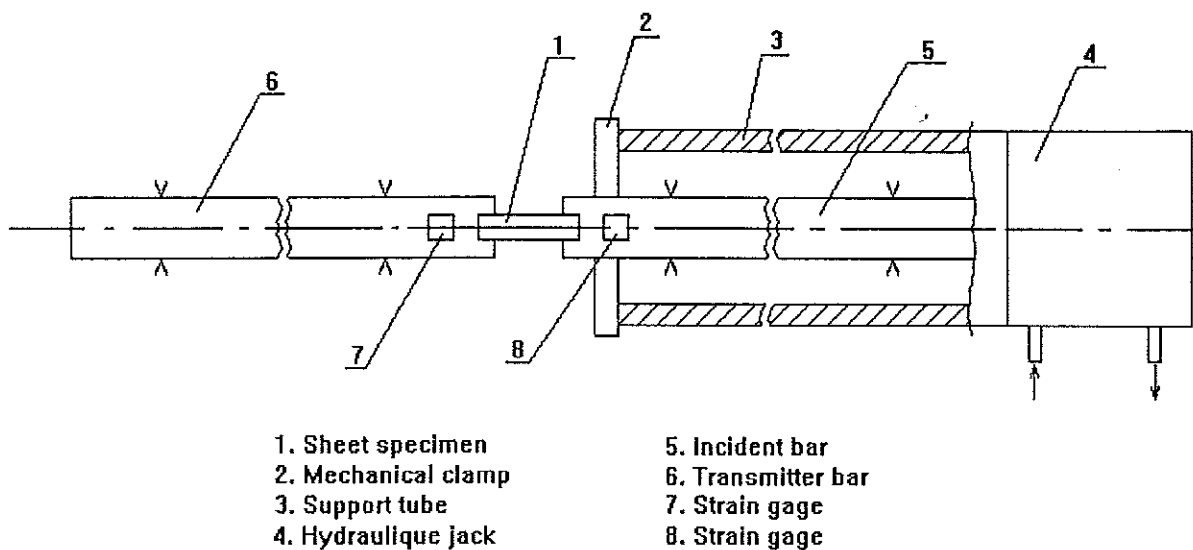


Fig.4 Scheme of the "inverted split Hopkinson bar" for direct-loading tensile test, LPMM-Metz, [12].

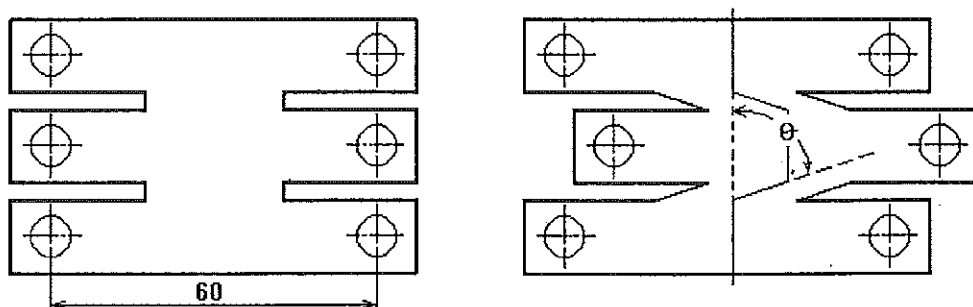


Fig.5 Specimen geometry for double-shear quasi-static test of sheet metals, after [14].

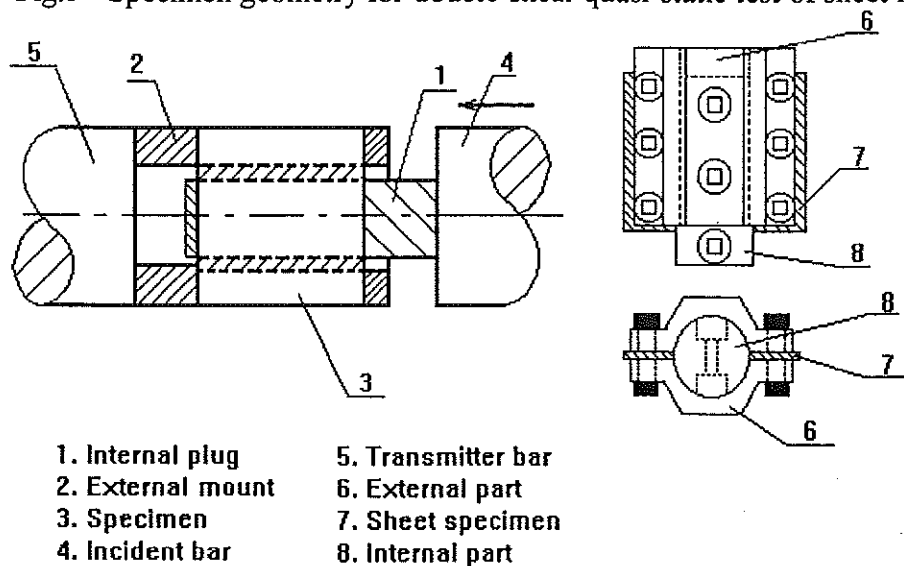


Fig.6 Device for double shear test with a standard SHPB, $\varnothing 40.0$ mm; (a) general scheme of loading; (b) details of the device, after [15].

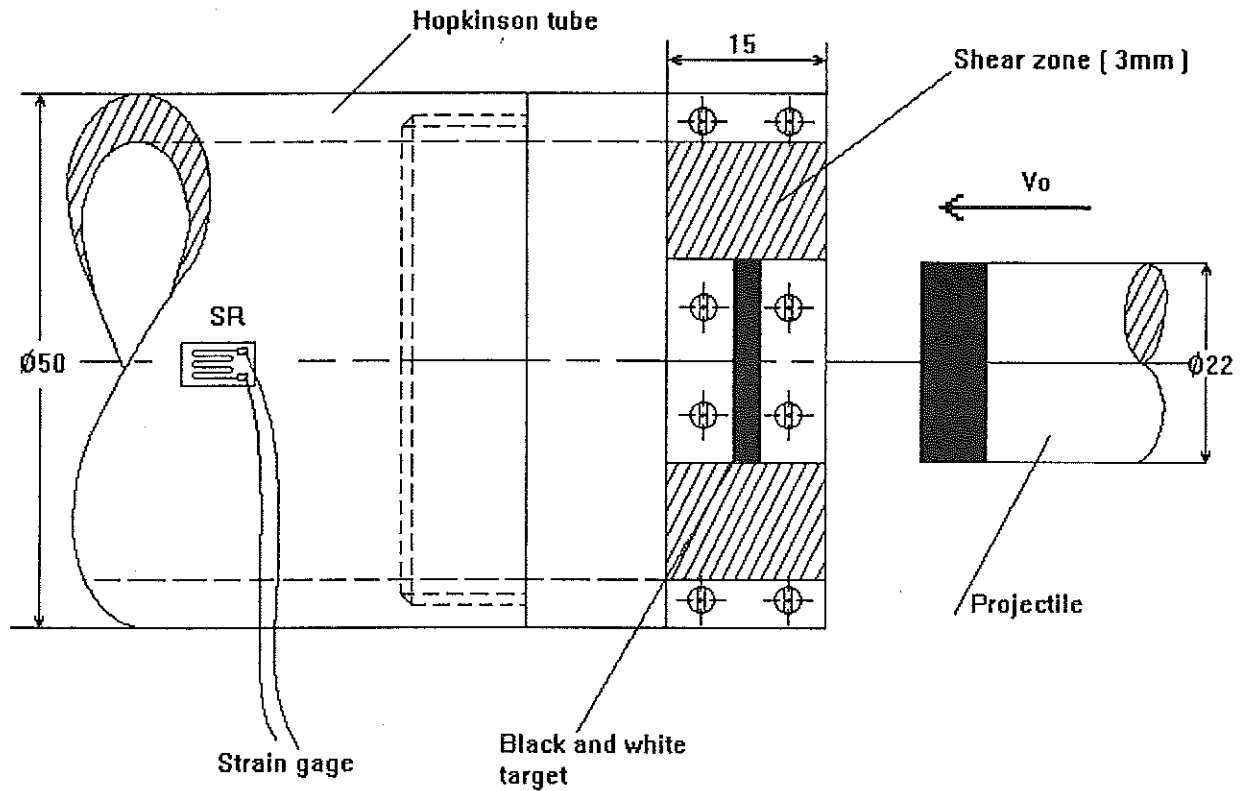


Fig7 Scheme for direct impact on double-shear sheet specimen, dimensions in mm, LPMM-Metz.

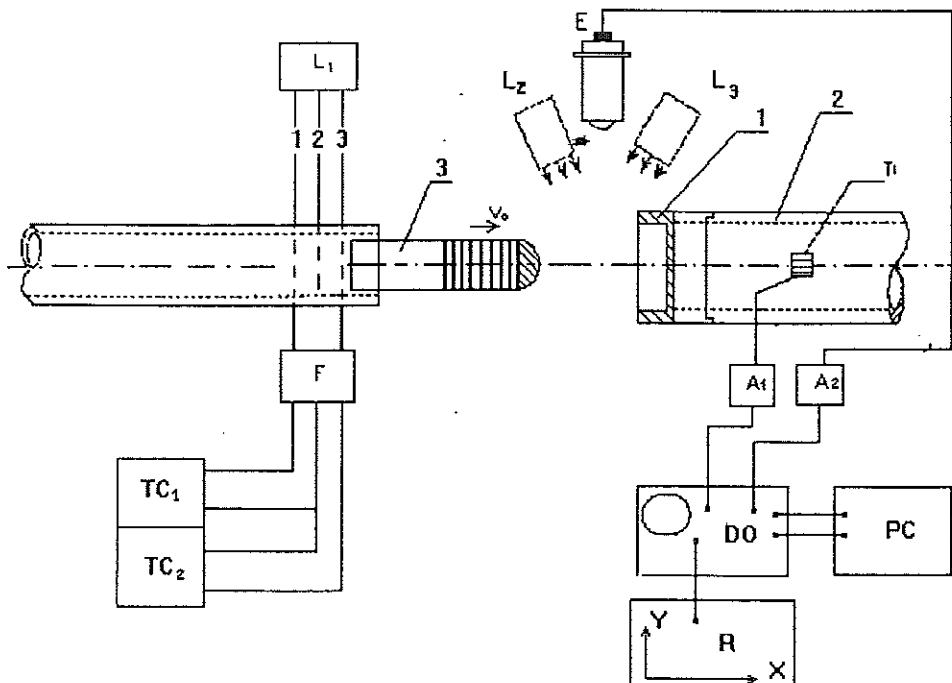


Fig.8 Scheme of experimental setup for direct-impact dart test, equibiaxial deformation and perforation; 1- specimen (see Fig.9), 2- Hopkinson tube, T1 - strain gage, A1 and A2 - amplifiers, DO - digital oscilloscope, PC - personal computer, R- x-y recorder or printer, L1(1,2,3), L2 and L3 - light sources, F and E - photodiodes, TC1 and TC2 - time counters, 3 - hemispherical projectile, [18].

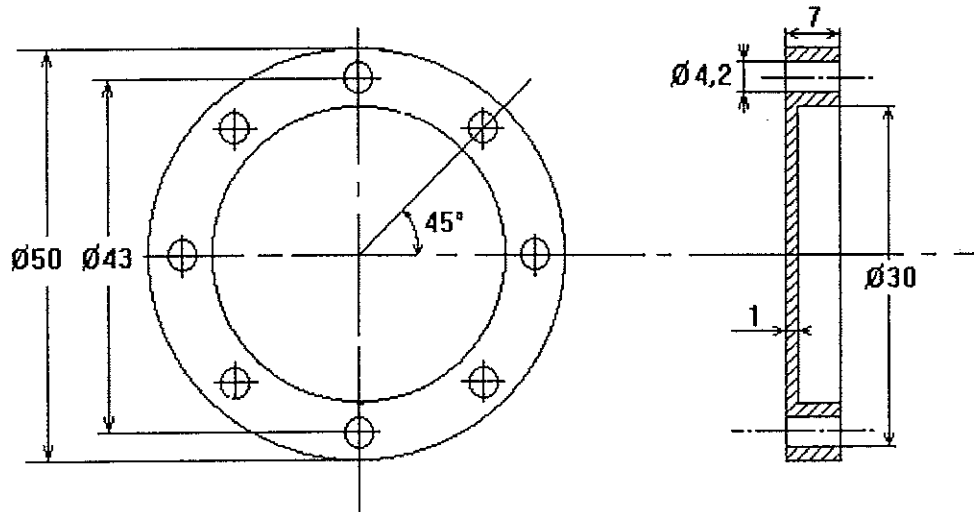


Fig.9 Geometry of flat specimen for direct-impact dart test, dimensions in mm, [18].

Spalling of alumina ceramics in uniaxial stress at elevated temperatures

Martin Mueller-Bechtel and Jerzy Najar

Department A of Mechanics, University of Technology, Munich

Introduction

At dynamic loading in plate impact experiments, uniaxial tensile strain spalling phenomenon can be attributed to excitations of very short pulse components, interacting with distributed sources of microdamage at their eigen-frequencies of some 25-50 MHz at strain rates of 10^4 s^{-1} and more, [1]. On the other hand, in dynamic experiments with thin bars at uniaxial state of stress, only strain rates of up to 10^3 s^{-1} can be achieved. The tensile mode of fracture remains prevailing in ceramics at these rates, although its mechanisms cannot be identified with dynamic source excitations, and need to be investigated yet. Having in mind applications of ceramics at dynamic and thermal exposures, attention should be paid to conducting the experiments at elevated temperatures, and to their analysis. An attempt to formulate an adequate mechanical model for spalling at uniaxial stress in elevated temperatures seems to be worth of consideration.

A brief account of extensive spalling experiments with alumina ceramic bars performed at room and elevated temperatures is given in the present paper. The results for dynamic tensile strength of bar specimens of various diameters and temperatures are discussed.

New experimental set-up and evaluation method

The split Hopkinson pressure bar (SHPB) is not fit for dynamic tensile experiments with ceramics. In this brittle material, failure develops within a single wave passage when the stress pulse is high enough, while the principle of the evaluation procedure in SHPB is based on the multiple wave reflection. Moreover, specimen grips needed in the tensile SHPB versions cause wave distortions and lead to high costs.

Also sledgehammer-type tensile devices, s. [2], have their disadvantages when applied to ceramics. They demand instrumentation of specimens and involvement in complicated wave patterns, which lead in the evaluation procedure to extensive numerical calculations. Testing at elevated temperatures above 1000 °C is here almost impossible due to the limitations on strain measurements in hot fields. The natural scatter of mechanical properties of ceramics demands long testing series, which increases substantially the cost of experiments.

Therefore, a special testing set-up was needed for tensile dynamic testing of slender ceramic bars. Specific properties of ceramics, in particular: its relatively low fracture toughness, very short fracture delay time, and high compressive - to - tensile strength ratio, have allowed to build the apparatus based on the spalling principle, and to develop an efficient and simple evaluation procedure, [3].

The set-up combines the principles of pulse initiation and its measurement, typical for SHPB, with the spalling principle of the tensile dynamic loading at the reflection of a compressive stress wave from specimen's free end. The slenderness ratio of 20 and more, and a carefully selected pulse profile result in the spall developing sufficiently far away from the reflection point to secure uniaxial stress, Fig. 1.

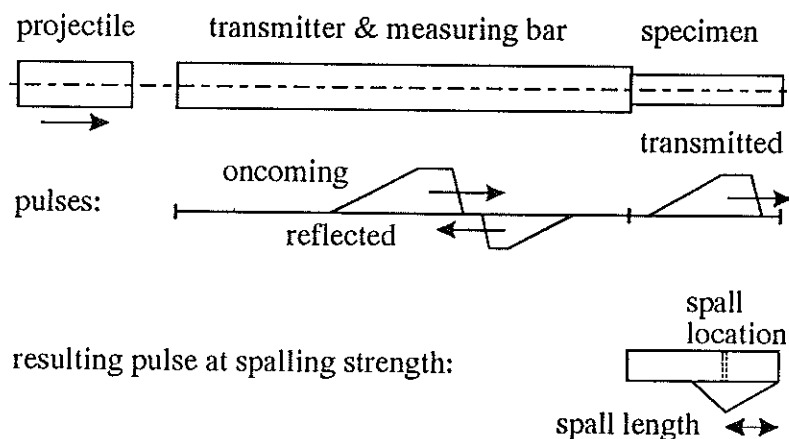


Figure 1: Experimental arrangement

The compressive pulse is induced in the transmitter bar by projectile impact. It gets registered at gauge stations of the measuring bar and stored. The same happens to the reflected pulse in the bar resulting from the difference of the impedances between the transmitter and the specimen. The transmitted compressive pulse, σ_c , propagates in the specimen basically without material damage, when its amplitude is properly chosen. Upon its arrival at the specimen's free end it gets reflected as a tensile pulse and superposed upon the still arriving compressive tail. The resulting stress distribution leads to fast growing in time tensile stresses at some distance from the free end, Fig. 2.

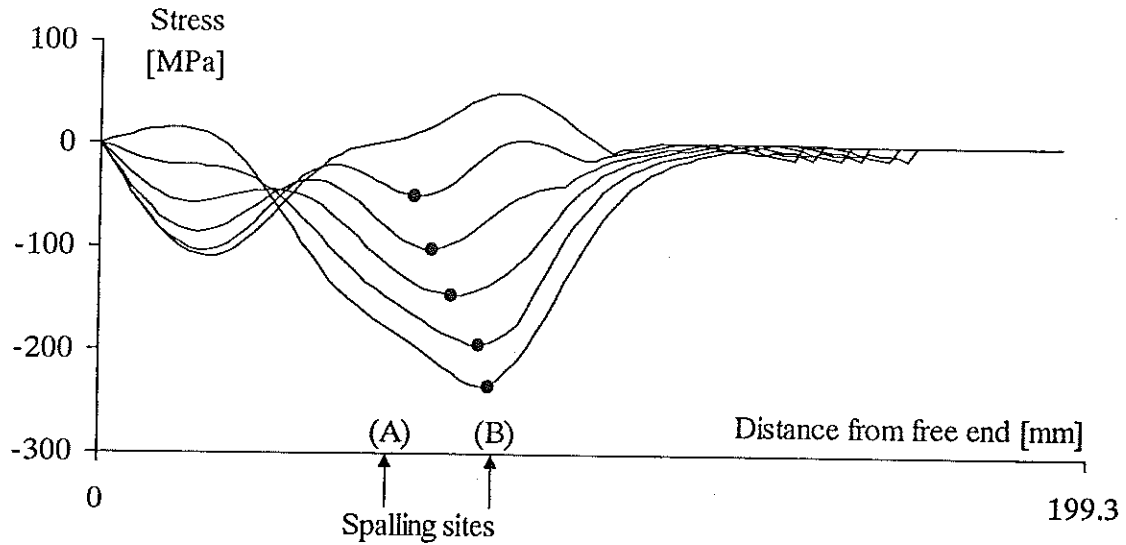


Figure 2: Resulting transient pulses in the specimen, in a time-step sequence $0,5 \mu s$

Whenever the peak value of the resulting stress distribution reaches the level of the tensile strength σ_t of the material, spalling develops immediately due to the negligible fracture activation delay in ceramics. The part of the pulse and the momentum trapped in the fragment cause in most cases secondary in-flight spalling fractures based on the same mechanism, provided sufficiently high σ_t -pulse amplitude is available.

Multiply-spalled specimen is recovered after the test from the trapping device, and the location of the spall planes is determined. Then a thorough analysis is conducted to distinguish the primary spalling fracture's location from the secondary ones. The knowledge of the site of the primary spall, when confronted with the computer-evaluated evolution sequence of the resulting tensile stress in the specimen, allows for the determination of the spalling strength of the ceramics.

Problems of adequate modelling, evaluation procedures for stress distribution, distinction between primary and secondary spalling sites, etc. called here for a thorough investigation. The evaluation procedure for stresses and determination of the spalling instance has been given in [4]. Attention has been paid to distinguishing the effects of the geometrical dispersion in the bars, to account for the effects of multiple spalling and to single out primary fractures, [5], allowing for proper assessment of the size-effect in strength, [6]. Particular care has been devoted to the development of the experimental technique at elevated temperatures up to $1500 \text{ }^\circ\text{C}$.

Spalling strength at room temperature

Some results of the spalling strength tests with alumina ceramics specimens at room temperature are presented here. Full or variously perforated round bars (2, 4 or 8 longitudinal perforations, length 1000 mm, diameter 4, 8 or 12 mm) of Frialit-Degussit AL23 ceramics were custom cut to the needed length between 200 and 330 mm, weighted in order to determine the density, marked for easier after-testing determination of the spalling position, and tested according to the above described procedure. Table 1 shows the resulting data for 9 test series, altogether 99 specimens, for details s. [6].

Table 1: Dynamic tensile strength of alumina rods at room temperature

Series no.	no. of specim.	dia. / length mm	mean strength MPa	scatter %	cross-sect. type
1	12	4 / 200	319	9.7	full
2	13	8 / 200	274	12.0	full
3	11	8 / 200	273	9.5	full
4	9	8 / 200	276	13.0	full
5	9	12 / 200	207	23.7	full
6	9	12 / 330	209	17.2	full
7	11	8 / 200	162	17.9	2 perf.
8	13	8.5 / 200	209	18.2	4 perf.
9	12	8 / 200	184	16.8	8 perf

Observe first that the mean tensile strength σ_T of full bars drops with the increase of the cross-section area A of the specimen, Fig. 3. Let's apply Weibull's two-parameter model of the failure probability P as a function of applied stress σ

$$P(\sigma) = 1 - \exp\left[-\left\{\frac{\sigma}{\sigma_0}\right\}^m\right], \quad (1)$$

where m and σ_0 are material parameters, to the cross-section activated by the spalling tensile stress and identify the failure stress with the measured fracture strength in spalling. The consequence would be the formula

$$\sigma_f A^{\frac{1}{m}} = \text{const.} \quad (2)$$

and the average value of Weibull's exponent becomes from here $m = 5.2$. This is substantially lower than the data found in the literature for static experiments on bending strength of the same material, s. [7].

On the other hand, with increasing area A systematically grows also the scatter of the strength evaluation, which cannot be attributed to the experimental method but rather related to the same probabilistic effect on which Weibull's model has been based.

These size effects can be thus well interpreted within the weakest link concept of failure probability. This is rather surprising for dynamic experiments as the concept is inherently of static nature. Moreover, also the level of the strength at spall σ_f is close to the strength values determined in static experiment, e.g. bending strength, [8].

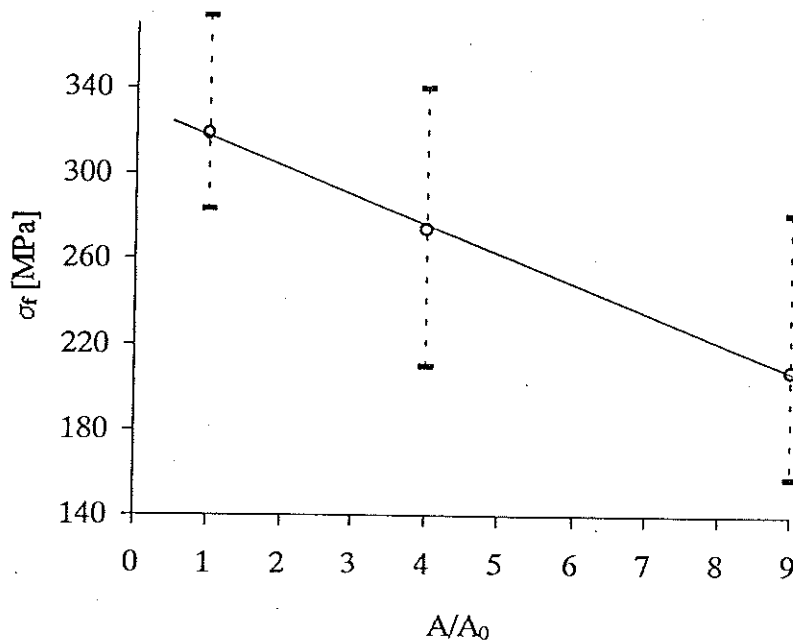


Figure 3: Tensile strength of full alumina rods vs. cross-section area

This doesn't mean, however, that the moderately high strain rates in the range of $200-500 \text{ s}^{-1}$, as observed in the tensile loading phase at the site of fracture, comp. Fig. 1, have no effect on the failure mechanism in spalling at uniaxial stress. The determination of the fracture energy density at spalling, [9], has shown that the dynamic spalling process uses up considerably more energy (by an order of magnitude) than the static fracture.

Our conclusion from the room temperature spalling tests is that it is only the failure *initiation*, where the weakest link hypothesis is still applicable. The *propagation* of the spall is, however, not at all quasi-static, and is reflected in the higher fracture energy consumption.

The influence of the cross-section geometry on the strength of rods can not be directly related to the area A alone, as the tests with axially perforated rods (holes 0.8 to 1.6 mm diameter) indicate, s. series 7-9, Tab. 1. The drop in the mean strength, as compared with full rods of the same size, s. series 2-4, and the increase of its scatter indicate rather a drop in the homogeneity of the samples due to manufacturing, and confirm the applicability of the weakest link hypothesis.

Experimental results at elevated temperatures

For the experiments at elevated temperatures, the specimen is placed in an open-ends furnace lined along the axis of the set-up. The furnace with 204 mm diameter and 356 mm length of the heating area makes possible to conduct the experiments up to 1500°C. The specimen must be shorter than the length of the furnace in order to be placed in its internal homogeneous temperature field. On the other hand, the measuring bar must not reach into the area of elevated temperature due to its limited resistance to thermal load and limited temperature range of application of the strain gauges.

An extension piece of the same material as the specimen is positioned between it and the transmitter bar, in order to bridge over the thermally inhomogeneous field at the opening of the furnace, Fig. 4. The bridging piece is glued to the specimen which ensures the proper transition of the pulse into the specimen, and at the same time makes easier the handling of the specimen within the furnace. The unit bridging piece - specimen can be lined up according to the axis of the set-up as a whole from without the furnace, which enables the proper positioning of the unit.

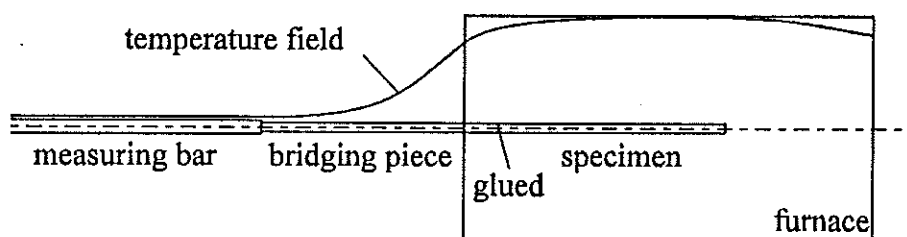


Figure 4: Experimental arrangement at elevated temperatures

The presence of the bridging piece has some influence on the transmission of the pulse into the specimen since there are some slight pulse reflections at the gluejoint. Our experience shows, however, that the proper choice of the extension piece length enables direct pulse measurements on the bridging element and thus take into account the joint reflection losses. The fracture phenomena in

the specimen itself are not influenced by the presence of the bridging piece since the reflected pulse reaches the gluejoint only some time after the primary fracture has occurred.

The evaluation of the tests at elevated temperatures is basically analogous to that at room temperature. The difference is alone in the taking into account of the changes of the wave velocity with the increase of the temperature, as the pulse travels along the bridging piece and enters the specimen placed in the homogeneous temperature field. An evaluation procedure has been worked out also for the dispersion effects at elevated temperatures.

The experimental arrangement for tests in elevated temperature has been checked in two test series of alumina ceramics made of two different batches. Cylindrical full bars of diameter 8 mm and length 200 mm have been tested in the whole range of temperatures between the room temperature and 1500°C. The tests at the room temperature were conducted within the cold furnace, in order to check the compatibility of the results with those at the room temperature in the former experimental arrangement. Altogether 28 specimens were tested, at higher temperatures the number of experiments per temperature point was diminished from six to one due to the increasing time cost. The results of the tests can be therefore treated as preliminary ones only, not representing a full sufficient statistics of the strength at elevated temperatures. They prove, however, doubtlessly the applicability of the experimental method to testing at elevated temperatures.

Table 2: Dynamic tensile strength of alumina rods at elevated temperature

Temp. °C	RT	150	330	430	720	800	890	1020	1250	1500
no. of specim	6	2	2	2	2	2	2	4	1	1
mean strength MPa	268	273	260	264	282	264	269	266	249	231

The experimental results for the spalling strength of alumina at the room temperature yield its mean value of 268 MPa. This proves that the change of the arrangement had no influence on the evaluation of the strength. With the increasing temperature, the trend of the spalling strength has not been clearly established: up to 1000°C it stays practically constant, while beyond 1000°C there has been visible only a slight drop in the strength. This differs from the response observed in experiments with very thin alumina fibres, [10], where the drop in the high temperature range was rather substantial, s. Fig. 5. The difference may be due to both scale and dynamic effects, and needs further investigations.

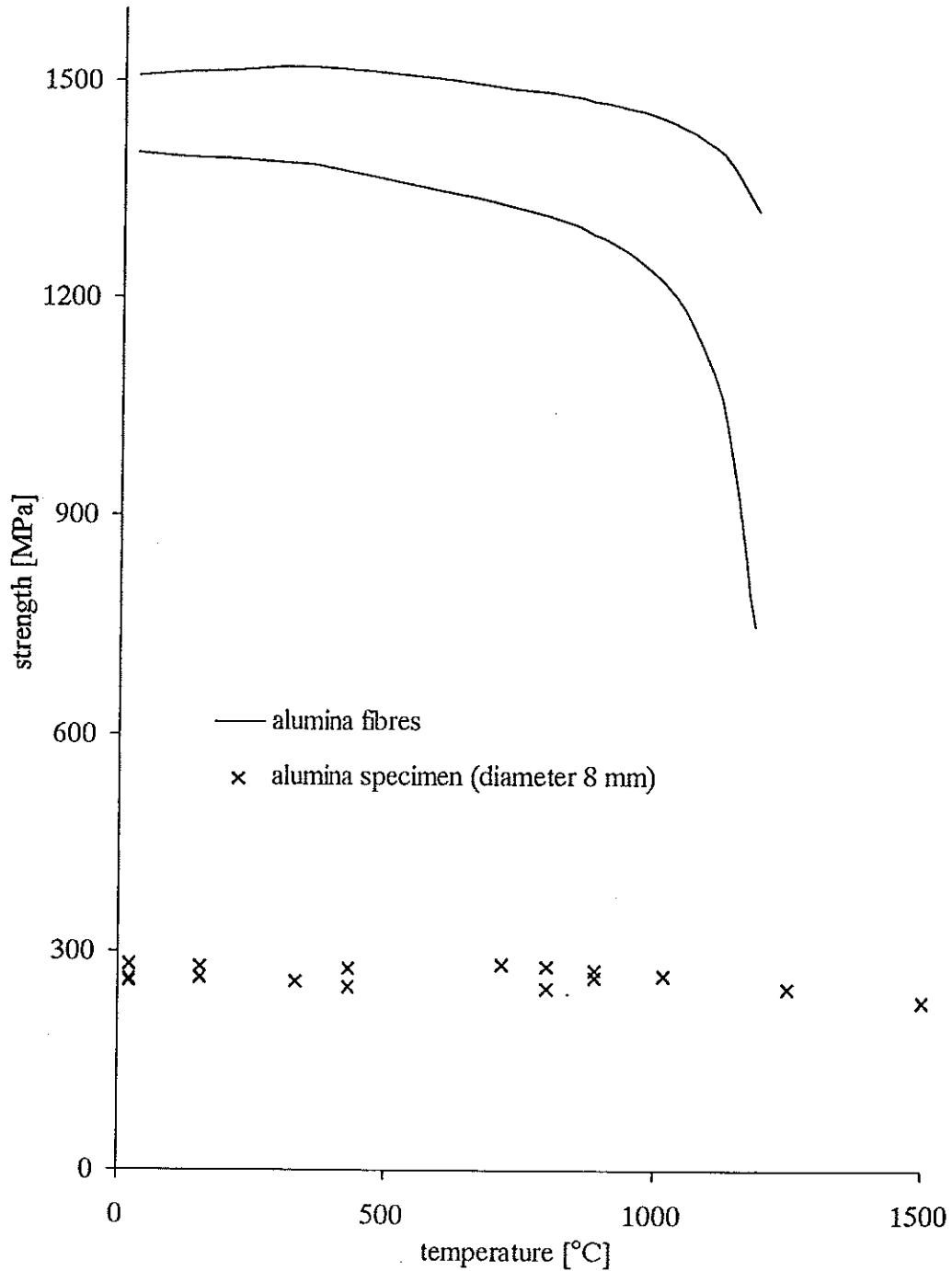


Figure 5: temperature dependence of alumina specimens and fibres

ACKNOWLEDGEMENTS

The work presented here has been performed in relation with the DFG project Na-218 on dynamic testing of high performance ceramics. Dr. S. Bierwirth and Dipl.-Ing. H.-J. Klumpp participated in the construction of the set-up and conducted part of the tests. Their input and the financial support of the German Research Foundation (DFG) is hereby gratefully acknowledged.

REFERENCES

- [1] Seaman L., Curran D. R. and Shockey D. A., *J. Appl. Phys.*, 47 (1976) 4814-4826.
- [2] Kussmaul K., Demler T. and Klenk A., *Materials at High Strain Rates*, Inst. Phys. Conf., Ser. No. 102, Sess. 4, Oxford 1989 (IOP Publ. 1989), 157-164.
- [3] Bierwirth S. and Najjar J., 13. GESA-Symp., Bremen 1990, (VDI, 1990), 403-421.
- [4] Bierwirth S. and Najjar J. 23. DVM-AK Bruchvorgaenge, Berlin 1991 (DVM, 1991) 423-432.
- [5] Najjar J. and Bierwirth S., 24. DVM-AK Bruchvorgaenge, Aachen 1992 (DVM, 1992) 439-451.
- [6] Bierwirth S., Dissertation, TU Muenchen (1993)
- [7] Munz D. and Fett T., *Mechanisches Verhalten keramischer Werkstoffe* (Springer, 1989)
- [8] Nickel H. and Steinbrech R. W. (eds.), *Mikrobruch in Al₂O₃-Keramik*, DFG, Juelich, 1990
- [9] Najjar J., *Mechanical Behaviour of Materials under Dynamic Loading*, J. de Physique IV, vol. 4, Sept. 1994 (Euro-DYMAT 94, Oxford), 647-652
- [10] Ziegler G., *Herstellung von keramischen Verbundwerkstoffen: Einstellung definierter Gefügezustände und Kontrolle des Bruchverhaltens. Gefüge und Bruch*, Bochum, 1993

DYNAMIC SIMPLE SHEAR TEST EXPERIMENT AND NUMERICAL INVESTIGATION

WOJCIECH KRZYSTOF NOWACKI and NGUYEN HUU VIEM
Institute of Fundamental Technological Research
Świętokrzyska 21, 00-049, Warsaw, POLAND

1 Introduction

Recently, a new shear device was used to perform tests sur specimens having the form of slabs such as metal sheets [1]. The loading and the displacements of this device are controlled by a Split Hopkinson Pressure Bar (SHPB) acting in compression. The special device was used to transform the compression to simple plain shear. For thin sheets in dynamic simple plain shear tests, it is the only known method to obtain a very good homogeneity of the permanent strain field over the total length of the specimen, without the localization of deformations as in the case of torsion of thin-walled tubes [2].

In this paper the test of dynamic simple plane shear is discussed. The temperature field due to plastic deformations is measured using thermovision camera. With this technique, it is possible to evaluate the stored energy due to the simple shear in the case of large deformations.

Simplified analytical solution of the boundary-value problem is provided. The analytical solution is compared with the experimental data. The performed numerical calculations enabled the evaluation of the optimal dimensions of the specimen.

2 Description of the device

Figure 1 presents the principle of the device. It consists of two coaxial cylindrical parts. The external part is tubular with inner section cylindrical and outer section hexagonal. It's height is 45mm and is reinforced to be able firmly fix the specimen. The internal part is full. It is 25.4mm in diameter and his height is 45mm. Both are composed of two symmetrical parts between them the sheet in testing is fixed using screws of high endurance (Fig.2). Two bands of the specimen between the internal and external parts of the device are in plan shear when these cylinders move axely one toward another. The width of these bands is 3mm. Each band before test is rectangle and become very near parallelogram having the length and the height constant. The specimens can have different thickness. There are two kinds of specimens: one is made from the steel XES (chemical composition: C -50, Ni -25, Cr -18, Mn -189, Cu -23, Al -57, Si -4, P-17 in 10^{-3} volume percent,

avec
l'autre
montage

thickness 0.74mm) and the other is from steel 1H18N9T (chemical composition: C -10, Mn -200, Si -80, P -5, S -3 Cr -180, Ni -80, thickness 0.5mm).

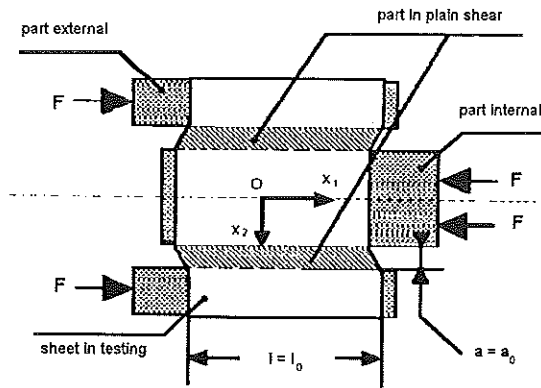


Fig 1. Principle of the arrangement

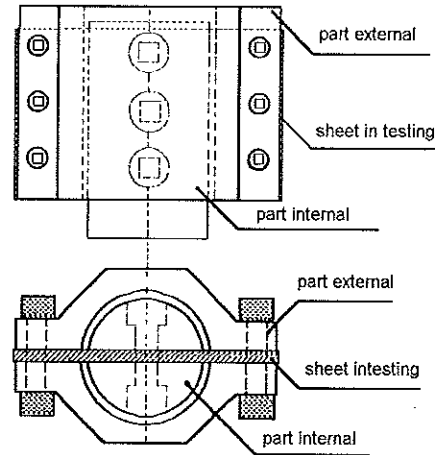


Fig 2. Arrangement in detail

First, the system is tested under quasi-static loading for verifying the effectiveness. The presence of free bounds of specimen produces the heterogeneity of stress field because the stress vector normal to the free surfaces must be zero, therefore we have assumed that the dimensions of the perturbed zone are small comparing to the dimensions of the specimen. This assumption is acceptable as shown in [1], where the mounting of the sheet is tested and the homogeneity of the field of deformation is observed. In general, we must take the ratio a_0/l_0 sufficiently small. It's shown in [8, 9] that when the ratio $a_0/l_0 \leq 1/10$, the results of test are good for both static and dynamic cases. We take in our tests $a_0/l_0 = 1/10$.

The dynamic test is similar but the loading is realized by the SHPB. The device with specimen is placed between two bars of the SHPB. Note that in this case the mechanical impedance of the shear device and the SHPB must be the same to avoid the interface parasite signal. The most more higher velocity of loading can be realized using only one bar of the SHPB. The impulse is created by the third projectile bar: the usual compression technique. We have to register the input, transmitted and reflected impulse: ε_i , ε_t and ε_r . In the axis of Fig. 1 the stress tensor has the following components: σ_{11} , σ_{22} and σ_{12} . The presence of σ_{11} , σ_{22} is due the fact that $a = a_0 = \text{const}$. The strain tensor has only non-zero component $\varepsilon_{12} = \gamma$. In this test, large deformations can be obtained, contrary to the case of torsion of thin cylindrical specimens [3]. The specimens deformed quasi-statically or dynamically to 70 – 100% observed under the optical microscope have the similar structure. The traversal lines marked on the specimens before the test remain parallel after the test.

Remarques sur l'influence de la géométrie sur la déformation initiant le cisaillement adiabatique

In the full analysis, we must take into account that the loading of the specimen isn't instantaneous. The loading compressing wave must take some time to transmit from one end to the other end of the device. However, we have in our tests very good equilibrium of forces on two sides of the shear device, see Fig.3. We observe that the input force and the output are very similar in shape neglecting the small oscillations of the input force. So, in the simplified analysis we suppose that the loading is homogeneous and proceed as the case quasi-static. Knowing the velocities on bounds of the system we can find the displacements. The force is taken to be equal to the mean value of input and output force. The sensibility on the rate of deformation in compression is presented on the Fig.4 (see [1]). The exceptional quality of the homogeneity of the residual strain field show that the simplified analysis can be used in the zone of plastic deformations.

3 Simple Shear Analysis

The simple shear in the direction e_1 of the coordinate system (e_1, e_2) is defined by the relations

$$(3.1) \quad \begin{aligned} u_1 &= \gamma(t) x_2 & u_2 &= u_3 = 0 \\ v_1 &= \dot{\gamma} x_2 & v_2 &= v_3 = 0 \end{aligned}$$

where $\gamma = \tan \varphi$ (see Fig.5) and $\dot{\gamma}$ are the plastic shear strain and shear strain rate, respectively. From the velocity field \mathbf{v} the velocity gradient \mathbf{V} , the rate of deformation \mathbf{D} and the material spin $\boldsymbol{\omega}$ can be represented in the system (e_1, e_2) as

$$(3.2) \quad \mathbf{V} \doteq \frac{\dot{\gamma}}{2} \begin{pmatrix} 0 & 1 \\ 0 & 0 \end{pmatrix} \quad \mathbf{D} \doteq \frac{\dot{\gamma}}{2} \begin{pmatrix} 0 & 1 \\ 1 & 0 \end{pmatrix} \quad \boldsymbol{\omega} \doteq \frac{\dot{\gamma}}{2} \begin{pmatrix} 0 & 1 \\ -1 & 0 \end{pmatrix}$$

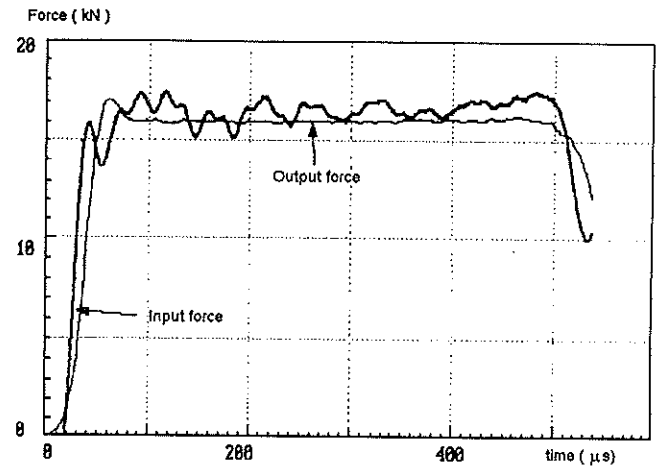


Fig 3. Measured input and output forces

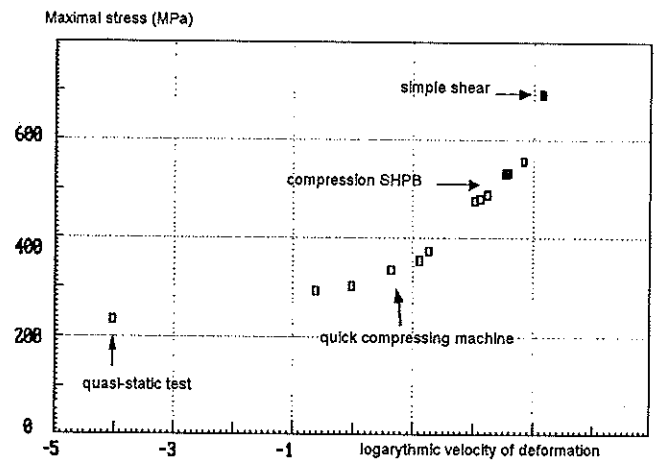


Fig 4. Comparison with the simple compression

*à 10% de déformation -
utilise Von Mises.*

The Cauchy stress tensor $\boldsymbol{\sigma}$ and the back stress $\boldsymbol{\Pi}$ have the non-zero components

$$(3.3) \quad \boldsymbol{\sigma} \doteq \begin{pmatrix} \sigma_{11} & \sigma_{12} \\ \sigma_{21} & \sigma_{22} \end{pmatrix} \quad \boldsymbol{\Pi} \doteq \begin{pmatrix} \Pi_{11} & \Pi_{12} \\ \Pi_{21} & \Pi_{22} \end{pmatrix}$$

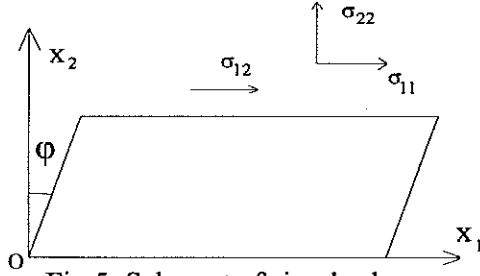


Fig 5. Schemat of simple shear

Using the constitutive relations for adiabatic process for rate-independent with combined isotropic-kinematic hardening at moderate pressures, when the thermal expansion, the heat of elastic deformation and the heat of internal rearrangement are neglected, we have the following constitutive equations [10]

$$(3.4) \quad \overset{\nabla}{\mathbf{T}} = \beta \mathbf{L} \mathbf{D} - \frac{3j\mu\beta \mathbf{D} \cdot (\bar{\mathbf{T}} - \boldsymbol{\Pi})}{\sigma_Y^2 \mathcal{H}} [(\bar{\mathbf{T}} - \boldsymbol{\Pi}) + \mathbf{P}],$$

$$j = \begin{cases} 1 & \text{if } f = 0 \text{ and } \mathbf{D} \cdot (\bar{\mathbf{T}} - \boldsymbol{\Pi}) \geq 0, \\ 0 & \text{if } f = 0 \text{ and } \mathbf{D} \cdot (\bar{\mathbf{T}} - \boldsymbol{\Pi}) < 0 \text{ or } f < 0. \end{cases}$$

where $\beta = \rho_0/\rho$ is the ratio of densities in the reference and actual configurations, $\mathbf{T} = \beta \boldsymbol{\sigma}$, $\overset{\nabla}{\mathbf{T}} = \dot{\mathbf{T}} - \boldsymbol{\omega} \mathbf{T} + \mathbf{T} \boldsymbol{\omega}$ is the Zaremba-Jaumann rate, $\bar{\mathbf{T}}$ is the deviatoric part of \mathbf{T} , \mathbf{L} is the fourth order tensor of elastic moduli, μ is the Lamé constant and f is the Huber-Mises yield criterion

$$(3.5) \quad f = \frac{3}{2} (\bar{\mathbf{T}} - \boldsymbol{\Pi}) \cdot (\bar{\mathbf{T}} - \boldsymbol{\Pi}) - \sigma_Y^2(\vartheta, \alpha) = 0$$

here σ_Y is the yield stress in simple tension, ϑ is the temperature and α corresponds to the size of the yield surface

$$(3.6) \quad \dot{\alpha} = (\bar{\mathbf{T}} - \boldsymbol{\Pi}) \cdot \mathbf{D}^p$$

The shift of the yield surface here is represented by the back stress $\boldsymbol{\Pi}$, for which the evolution law has the form of linear kinematic hardening

$$(3.7) \quad \overset{\nabla}{\boldsymbol{\Pi}} = c \mathbf{D}^p$$

where $c = \text{const}$ and \mathbf{D}^p is the plastic rate of deformation. The change in the temperature is described as

$$(3.8) \quad \rho_0 c_v \dot{\vartheta} = (1 - \pi)(\bar{\mathbf{T}} - \boldsymbol{\Pi}) \cdot \mathbf{D}^p$$

c_v is specific heat at constant volume; the first term on the right hand side of (3.8) represents the rate of energy dissipation and, therefore, $\pi < 1$. For numerous

metals π takes the value from 0.02 to 0.1 [4]. In the equation (3.4) \mathcal{H} is the hardening function

$$\mathcal{H} = 1 + \frac{c}{2\mu\beta} + \frac{1}{6\mu\beta} \frac{\partial(\sigma_Y^2)}{\partial\alpha} + \frac{(1-\pi)}{6\mu\beta\rho_0c_v} \frac{\partial(\sigma_Y^2)}{\partial\vartheta}$$

and tensor \mathbf{P} is obtained by expressing the term $(\boldsymbol{\omega}^p \mathbf{T} - \mathbf{T} \boldsymbol{\omega}^p)$ as a function of \mathbf{D}^p where $\boldsymbol{\omega}^p$ is the plastic spin. We adopt the following form for the plastic spin

$$(3.9) \quad \boldsymbol{\omega}^p = \eta \left(\boldsymbol{\Pi} \mathbf{D}^p - \mathbf{D}^p \boldsymbol{\Pi} \right)$$

where η may depend on the invariants of \mathbf{D}^p and $\boldsymbol{\Pi}$. We use here the relation for η in the work [7].

In the case of plain simple shear we have $\beta = 1$ and the equations above lead to

$$(3.10) \quad \begin{aligned} \dot{\sigma}_{11} - \dot{\gamma}\sigma_{12} &= -\frac{3j\mu}{\sigma_Y^2 \mathcal{H}} \left[\dot{\gamma}(\sigma_{12} - \Pi_{12}) \right] \left[(\sigma_{11} - \Pi_{11}) + \frac{\eta}{\mu} \mathcal{M}\sigma_{12} \right] \\ \dot{\sigma}_{12} + \dot{\gamma}\sigma_{11} &= \mu\dot{\gamma} - \frac{3j\mu}{\sigma_Y^2 \mathcal{H}} \left[\dot{\gamma}(\sigma_{12} - \Pi_{12}) \right] \left[(\sigma_{12} - \Pi_{12}) - \frac{\eta}{\mu} \mathcal{M}\sigma_{11} \right] \\ \dot{\Pi}_{11} - \dot{\gamma}\Pi_{12} &= \frac{3jc}{2\sigma_Y^2 \mathcal{H}} \left[\dot{\gamma}(\sigma_{12} - \Pi_{12}) \right] (\sigma_{11} - \Pi_{11}) \\ \dot{\Pi}_{12} + \dot{\gamma}\Pi_{11} &= \frac{3jc}{2\sigma_Y^2 \mathcal{H}} \left[\dot{\gamma}(\sigma_{12} - \Pi_{12}) \right] (\sigma_{12} - \Pi_{12}) \end{aligned}$$

here $\sigma_{11} = -\sigma_{22}$, $\Pi_{11} = -\Pi_{22}$,

$$(3.11) \quad \mathcal{M} = \left[\Pi_{11}(\sigma_{12} - \Pi_{12}) - \Pi_{12}(\sigma_{11} - \Pi_{11}) \right]$$

η is the multiplying function in the expression of plastic spin having now the form

$$(3.12) \quad \eta = \sqrt{\frac{12}{c \left(3c + 2\sqrt{3(\Pi_{11}^2 + \Pi_{12}^2)} \right)}}$$

The Huber-Mises yield criterion (3.5) is

$$(3.13) \quad \begin{aligned} f &= \frac{3}{2} (\bar{\boldsymbol{\sigma}} - \boldsymbol{\Pi}) \cdot (\bar{\boldsymbol{\sigma}} - \boldsymbol{\Pi}) - \sigma_Y^2 \\ &= 3 \left[(\sigma_{11} - \Pi_{11})^2 + (\sigma_{12} - \Pi_{12})^2 \right] - \sigma_Y^2(\alpha, \vartheta) = 0 \end{aligned}$$

and in the equations (3.10) we have

$$(3.14) \quad j = \begin{cases} 1 & \text{if } f = 0 \text{ and } \dot{\gamma}(\sigma_{12} - \Pi_{12}) \geq 0 \\ 0 & \text{if } f = 0 \text{ and } \dot{\gamma}(\sigma_{12} - \Pi_{12}) < 0 \text{ or } f < 0. \end{cases}$$

The change in the temperature ϑ is described as

$$(3.15) \quad \rho_0 c_v \dot{\vartheta} = j \frac{(1-\pi) \left[\dot{\gamma}(\sigma_{12} - \Pi_{12}) \right]}{\mathcal{H}}$$

The hardening function \mathcal{H} now is

$$(3.16) \quad \mathcal{H} = 1 + \frac{c}{2\mu} + \frac{1}{6\mu} \frac{\partial(\sigma_Y^2)}{\partial\alpha} + \frac{(1-\pi)}{6\mu\rho_0 c_v} \frac{\partial(\sigma_Y^2)}{\partial\vartheta}$$

In case of elasticity $j = 0$ and the equations (3.10) reduce to

$$(3.17) \quad \begin{aligned} \dot{\sigma}_{11} - \dot{\gamma} \sigma_{12} &= 0 \\ \dot{\sigma}_{12} + \dot{\gamma} \sigma_{11} &= \mu \dot{\gamma} \\ \dot{\Pi}_{11} - \dot{\gamma} \Pi_{12} &= 0 \\ \dot{\Pi}_{12} + \dot{\gamma} \Pi_{11} &= 0 \end{aligned}$$

with the initial conditions when $\gamma = 0$ then $\sigma_{11} = \sigma_{12} = \Pi_{11} = \Pi_{12} = 0$ we have the analytical solution:

$$(3.18) \quad \begin{aligned} \sigma_{11} &= \mu(1 - \cos \gamma) \\ \sigma_{12} &= \mu \sin \gamma \\ \Pi_{11} &= 0 \\ \Pi_{12} &= 0 \end{aligned}$$

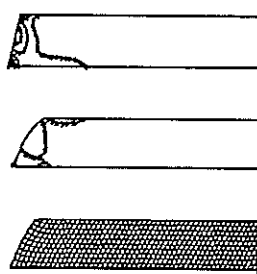


Fig 6. Simple shear of 1H18N9T

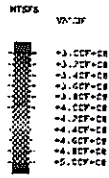
The program ABAQUS was used to do the numerical simulations of the posed problem. We see for example the heterogeneity of the strain and stress fields at the free bounds of the specimen at the distance less than 5% of the total length when the strain is 70%, exactly as in the experiments. For the steel 1H18N9T the zone of heterogeneity and the mesh are shown in the Fig 6. Fig 7 shows the Mises stress, σ_{11} , σ_{12} and the mesh at $\gamma = 0.741$.

4 Conclusions

An exceptional homogeneity of the permanent strain field at finite deformations over the total length of the specimens is observed in experiments and in the results of simulation. The proposed method is the only known test providing, in the case of a thin sheet, homogeneous stress and strain fields in both dynamic and static tests. They can be used to verify the constitutive relations proposed in [10]. The advantages of the method were discussed widely in [5]. With the technique described in [6] for simple tension, this shear device can be used to evaluate the stored energy in material.

Acknowledgments – This paper is supported by the Polish Committee for Scientific Research, KBN Project No. 7T07A02608 on “Dynamic fracture of materials”.

ABAQUS



SIMPLE SHEAR, 1N18N9T steel, v=5mm/min, MISES STRESS
TIME COMPLETED IN THIS STEP = 4.471E-01 TOTAL ACCUMULATED TIME = 4.471E-01 INCREMENT 60
ANALYSIS VERSION 5.3-1 DATE: 06-27-92 TIME: 09:48:23

ABAQUS



SIMPLE SHEAR, 1N18N9T steel, v=5mm/min, CONTOUR OF S12
TIME COMPLETED IN THIS STEP = 4.471E-01 TOTAL ACCUMULATED TIME = 4.471E-01 INCREMENT 60
ANALYSIS VERSION 5.3-1 DATE: 06-27-92 TIME: 09:48:23

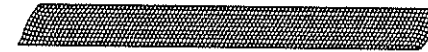
ABAQUS



SIMPLE SHEAR, 1N18N9T steel, v=5mm/min, CONTOUR OF S11
TIME COMPLETED IN THIS STEP = 4.471E-01 TOTAL ACCUMULATED TIME = 4.471E-01 INCREMENT 60
ANALYSIS VERSION 5.3-1 DATE: 06-27-92 TIME: 09:48:23

ABAQUS

NO. FACTOR = 7.4E-01



DISPLACED MESH, 1N18N9T steel, v=5mm/min, 10*100 elements
TIME COMPLETED IN THIS STEP = 4.471E-01 TOTAL ACCUMULATED TIME = 4.471E-01 INCREMENT 60
ANALYSIS VERSION 5.3-1 DATE: 06-27-92 TIME: 09:48:23

Fig. 7

References

- [1] G. Gary and W.K. Nowacki. Essai de cisaillement plan appliqué à des tôles minces. *Journal de Physics IV*, 4:65–70, 1994. Colloque C8, supplément au Journal de Physic III.
- [2] K.A. Hartley, J. Duffy, and R.H. Hawley. Measurement of the temperature profile during shear band formation in steels deforming at high strain rates. *J. Mech. Phys. Solids.*, 35(3):283–301, 1986.
- [3] A. Marchand and J. Duffy. An experimental study of the formation process of adiabatic shear bands in structural steel. *J. Mech. Phys. Solids.*, 36(3):251–283, 1988.
- [4] Z. Mróz and B. Raniecki. On the uniqueness problem in coupled thermo-plasticity. *Int. J. Engng Sci.*, 14:211–221, 1976.
- [5] W.K. Nowacki. Problèmes actuels de la dynamique des matériaux non-élastique. In *Engineering today. International Conference. Hanoi, August 5–8, 1995*.
- [6] Wiera Oliferuk, Stefan P. Gadaaj, and Maciej W. Grabski. Energy storage during the tensile deformation of armco iron and austenitic steel. *Materials Sci. and Engng*, 70:131–141, 1985.
- [7] J.E. Paulun and R. Peçcherski. On the relation for plastic spin. *Archive of Applied Mechanics*, 62:376–385, 1992.
- [8] E.F. Rauch and C. G'ssell. Flow localization induced by a change in strain path in mild steel. *Material Sci. and Eng.*, (A111):71, 1989.
- [9] A. Tourabi, B. Wack, P. Guélin, D. Favier, P. Pegon, and W.K. Nowacki. Remarks on an experimental plane shear test and on an anisotropic elastic-plastic theory. Technical report, SMIRT, 1993. Stuttgart, August 15-20,(Elsevier Sci. Publ.,1993).
- [10] Nguyen Huu Viem. Isothermal and adiabatic flow laws of metallic elastic-plastic solids at finite strains and propagation of acceleration waves. *Arch. Mech.*, 44(5-6):595–602, 1992.

The effect of the constitutive behaviour of a range of steels on adiabatic shear propensity

R N White and I M Pickup

Defence Research Agency, Chobham Lane, Chertsey, Surrey, KT16 OEE, England

Abstract

It is widely accepted that high strength steels are more susceptible to adiabatic shear. However, their constitutive behaviour ie. generally high strain hardening rate and low thermal sensitivity, would counter-indicate such behaviour. The constitutive response and propensity to adiabatically shear has been evaluated for three steels ranging in hardness from 350-730Hv. The propensity to adiabatically shear has been found to have an inverse relationship with strain rate sensitivity.

Adiabatic shear experiments indicate that steels with a strong strain rate sensitivity are less prone to adiabatic shear than steels which are insensitive to strain rate. The importance of strain rate hardening is indicated by adiabatically testing two steels with similar initial yield values but with significantly different strain rate sensitivities.

1 Introduction

The formation and evolution of adiabatic shear bands can dominate the response of structural materials to impact loading. Understanding the link between a metals constitutive mechanical behaviour and its propensity to adiabatically shear (AS) is of significant interest to wide variety of engineering applications.

This study seeks to determine the key constitutive aspects which are responsible for the initiation of AS in a range of steels. The programme evaluates the constitutive behaviour and the AS propensity of three steels; a medium hardness (MH) 350Hv steel, a high hardness (HH) 570Hv steel and an ultra-high hardness (UHH) 730Hv steel.

Continuum analyses of AS indicate that localised behaviour occurs when softening mechanisms exceed hardening mechanisms. It has been noted that materials with low work hardening, high thermal softening and low strain rate sensitivity are prone to AS¹. In contrast to this, the authors observed that the high hardness steels in this study, which had high work hardening rates and low thermal sensitivities were highly susceptible to AS.

The objective of this paper is to contrast the constitutive aspects of the steels which may influence localised shear and identify key factors which control adiabatic shear initiation. The importance of strain rate sensitivity is demonstrated in a novel strain rate hardening comparative test.

2 Experimental

2.1 Constitutive modelling

Constitutive equations have been developed for the three steels in which the strain and strain rate hardening and temperature sensitivities have been quantified.

Strain, strain rate and temperature sensitivities were determined under uniaxial stress conditions at three strain rates and over temperatures ranging from 171K to 650K. For quasi-static ($10^{-3}/s$) and intermediate rates ($10^1/s$) data was determined from tensile tests. High strain rate data ($10^3/s$) was measured in compression using the Split Hopkinson Pressure Bar (SHPB).

2.2 Quantifying the propensity to adiabatically shear

Shear data was determined at a macroscopic shear strain rate of $10^4/s$ in the SHPB using the 'tophat' shear specimen configuration² shown in figure 1. The specimens are designed to confine plastic deformation to the shear region (indicated). The rest of the specimen remains elastic. Each steel was adiabatically deformed to four different levels of macroscopic shear strain, (0.3, 0.4, 0.5 and 0.7). The target level of strain was achieved by limiting the displacement by inserting washers of an appropriate thickness over the spigot of the *tophat* specimen. Specimens deformed to each strain level were microscopically examined and their mode of deformation characterised.

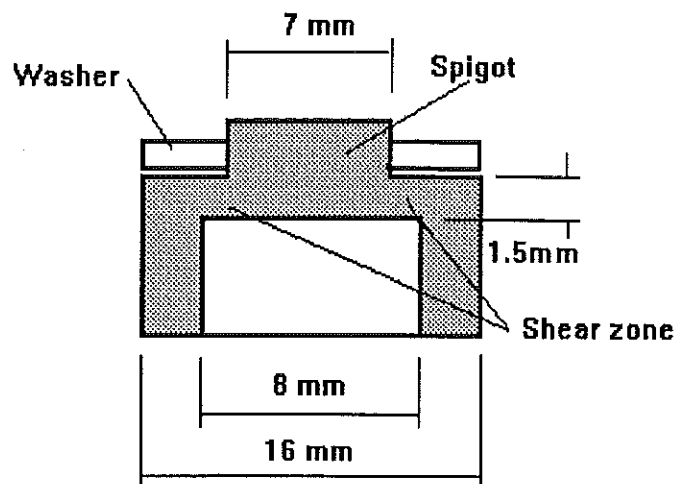


Figure 1. The cross-section of a 'tophat' shear specimen

Ne veut pas donner d'infos sur nature des aciers.

3 Results

3.1 Comparative constitutive responses

The principal constitutive components of a steels mechanical behaviour used to predict AS instability conditions are: strain and strain rate hardening and thermal softening sensitivity. These three parameters are compared for the three steels below.

3.1.1 Strain hardening

As may be expected the rate of strain hardening, $d\sigma/d\varepsilon$, significantly increases with increasing original material hardness, figure 2.

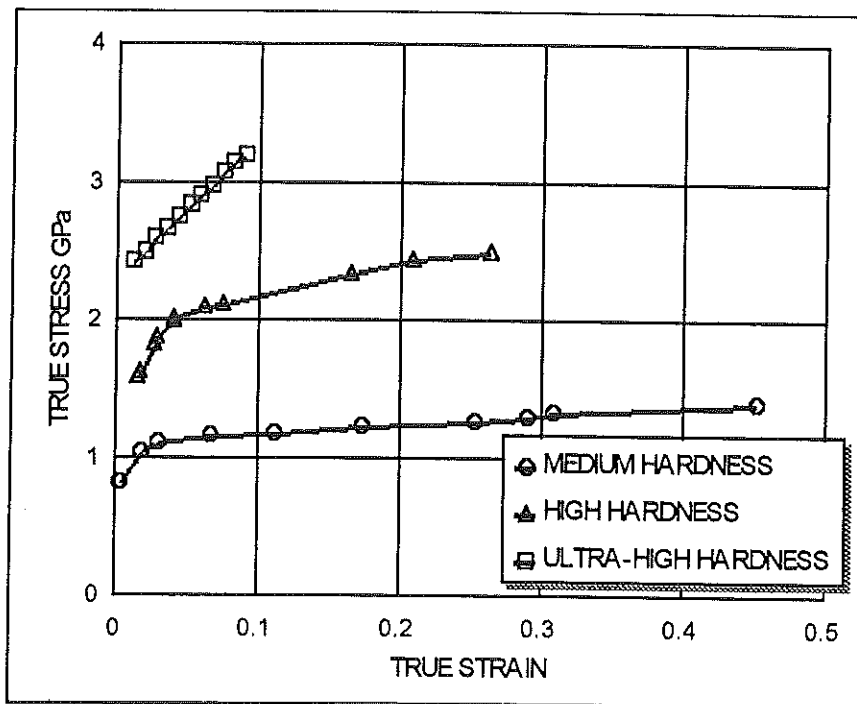


Figure 2. The strain hardening sensitivities of the three steels.

3.1.2 Strain rate hardening

The effect of strain rate on flow stress is markedly different for the three hardnesses of steel. Increasing the strain rate from quasi-static to SHPB rates ($10^3/s$) causes the flow stress of the MH (350Hv) steel to rise by $\sim 260\text{MPa}$ (figure 3a) compared to only $\sim 60\text{MPa}$ for the HH (570Hv) steel (figure 3b) and virtually zero for the UHH (730Hv) steel.

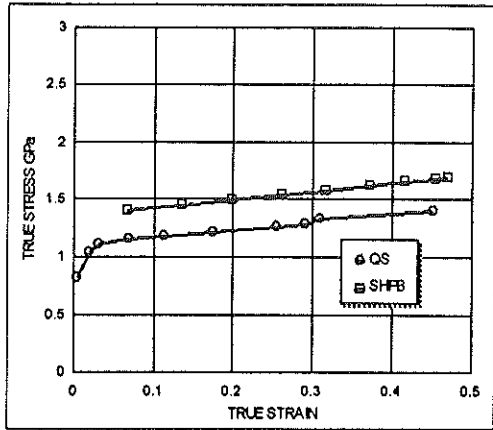


Figure 3a. The strain rate sensitivity of the medium hardness (350Hv) steel.

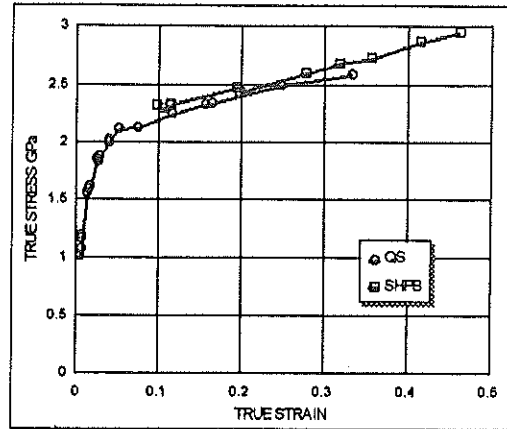


Figure 3b. Strain rate sensitivity of the high hardness (570Hv) steel.

3.1.3 Thermal softening

The thermal softening of the MH steel is much greater than the high and ultra-high hardness steels. Increasing the temperature from 193K to 473K causes the flow stress of the MH steel to reduce by 230MPa (figure 4a) compared to only ~60MPa for the HH and UHH steels (figure 4b).

The thermal response in steels is a result of two processes: thermally activated flow and elastic moduli variation with temperature. In the higher hardness steels, the thermally activated processes which are governed by microstructural features are extremely limited.

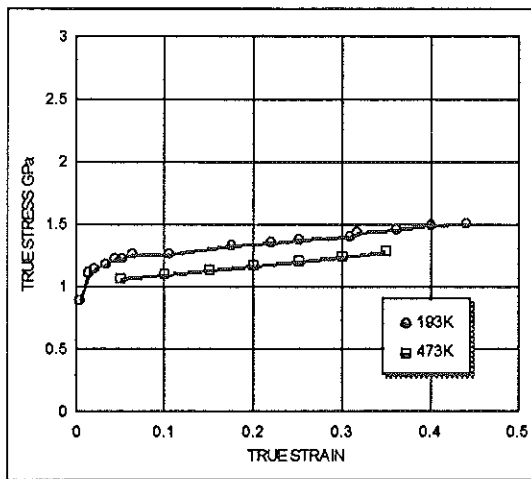


Figure 4a. Temperature sensitivity of the medium hardness (350Hv) steel.

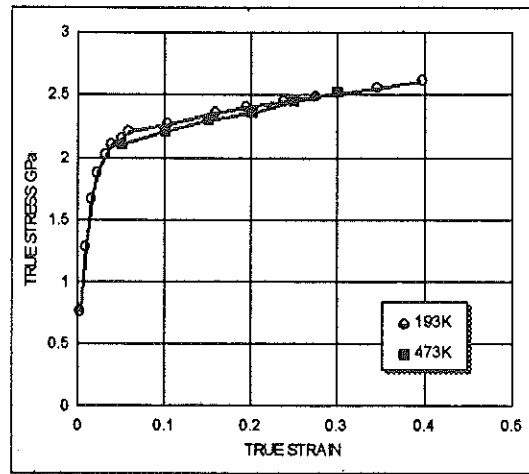


Figure 4b. Temperature sensitivity of the high hardness (570Hv) steel.

3.2 Adiabatic shear tests

Specimens deformed to each macroscopic shear strain level were microscopically examined for localised deformation. In table 1 below, the specimens are qualitatively nominated to have deformed in one of three modes:

- i) Homogeneously deformed, marked H;
- ii) Strain localised but remains intact, marked LI;
- iii) Strain localised and failed, marked LF.

Examples of the three types of behaviour (H, LI, LF) are shown in figures 5a-5c. Based on table 1, a ranking order of the propensity to AS may be established: MH (350Hv) steel being the least susceptible and UHH (730Hv) the most.

Shear strain	350Hv	570Hv	730Hv
0.3	H	H	H
0.4	H	H	LF
0.5	LI	LF	LF
0.7	LF	LF	LF
Ranking order	Low	Medium	High

Table 1

The relative propensity of the three steels to localised deformation. Shaded areas represent displacements where adiabatic localisation and failure has occurred.

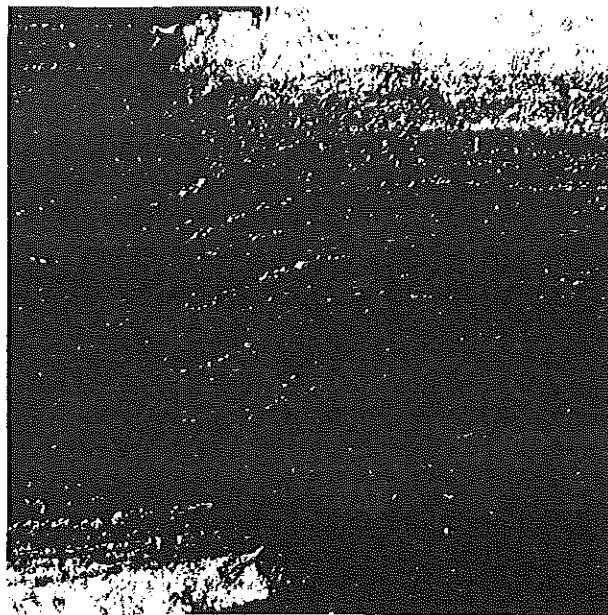


Figure 5a. Homogeneous shear strain (H) in a 350Hv steel tophat specimen subjected to 0.4 strain

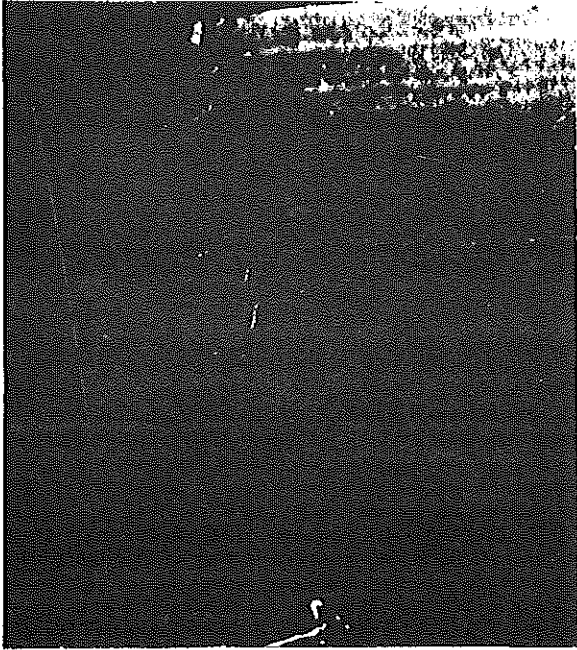


Figure 5b. Localisation (LI) of strain in the 350Hv steel at a strain of 0.5

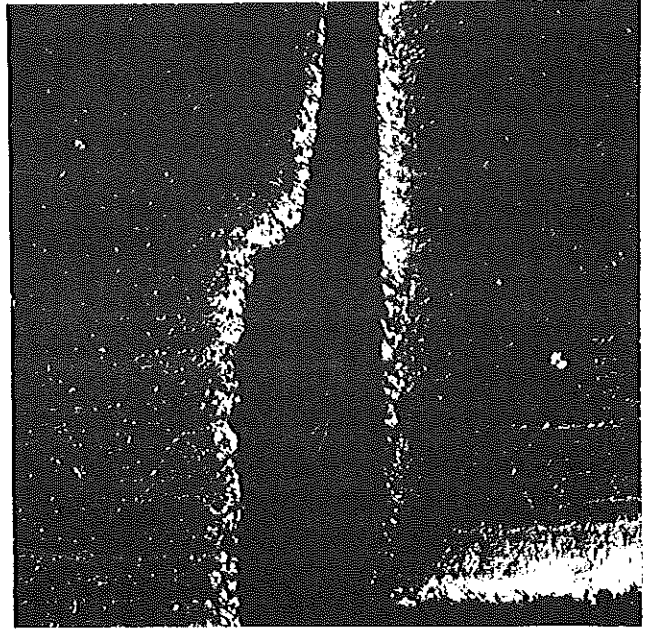


Figure 5c. Strain localisation and failure (LF) in the 350Hv steel at a strain of 0.7

4 Discussion

When shear instability is considered from a continuum material viewpoint, instability is often attributed as the condition when:

$$d\sigma = \frac{\partial\sigma}{\partial\epsilon} d\epsilon + \frac{\partial\sigma}{\partial\dot{\epsilon}} d\dot{\epsilon} + \frac{\partial\sigma}{\partial T} dT \leq 0 \quad (1)$$

However, in reality materials are heterogeneous and there is considerable evidence that AS nucleates at some microstructural feature and subsequently develops by growth and coalescence^{3,4,5}. It has also been demonstrated that shear localisation may occur prior to the macroscopic criticality condition (equ. 1). This may be due to localised initiation.

There are, however, some clear trends of structural form and constitutive behaviour which promote localisation. There is a high localisation propensity when:

- i) strain hardening rate is low;
- ii) strain rate hardening is low;
- iii) thermal softening is high.

The ranking of AS propensity is cross-correlated in table 2 with the constitutive aspects of the three steels. Each of the steels individual constitutive aspects may be ranked according to shear propensity and categorised as high, medium and low.

Propensity to AS	Strain hardening	Strain rate hardening	Thermal softening
High	MH	UHH	MH
Medium	HH	HH	HH
Low	UHH	MH	UHH

Table 2. Ranking of the three steels for AS based on each steels: strain, strain rate and thermal sensitivities.

From table 2 the MH steel has two of the three factors with the highest ranking. The UHH steel has two categories in the lowest ranking. This is the reverse order of the experimental ranked susceptibility to AS. However, the ranking according to the strain rate sensitivity and experimental localisation sensitivity are the same. This raises the question: **Is it strain rate sensitivity, or rather the lack of it, that is dominant in initiating localised shear?**

Nucleation of AS bands occurs at microstructural inhomogeneities. Upon initiation, the localised strain, strain rate and temperatures are higher than the bulk values. It is proposed that the initiation of strain localisation may be inhibited at a very early stage by **strain rate hardening**. In body centred cubic metals this hardening mechanism is operative before any substantial dislocation development occurs (strain hardening). Strain rate hardening may broaden or dissipate the localisation by relative hardening in the deformed area compared to the adjacent material.

4.1 Initiating adiabatic shear: *the role of strain rate hardening*

To demonstrate the importance of strain rate hardening, it was required to have two materials of similar initial flow stress, but with different rate hardening characteristics. The proposition being that the low strain rate sensitive material would adiabatically shear in preference to the higher rate sensitive steel.

The rate insensitive, HH steel was modified to exhibit strain rate hardening. This was done by tempering SHPB cylinders (8mm dia. x 4mm) at 550°C for 50 minutes. In figure 6, the as-received and tempered quasi-static flow curves are presented with their respective high strain rate (isothermal) flow curves. It is clear that the tempering process has modified the microstructure and in doing so has developed a thermally activated component to flow. This in turn has, as expected, produced a strain rate sensitivity.

SHPB specimens with the same initial yield strength (1600 MPa) as the as-received HH steel were produced by cold compression of the cylinders to a strain of ~0.3.

The strain rate sensitivity of the tempered steel was not affected by the strain hardening operation, figure 6. We now had two steels of similar chemical composition and initial flow strength but with different strain rate sensitivities.

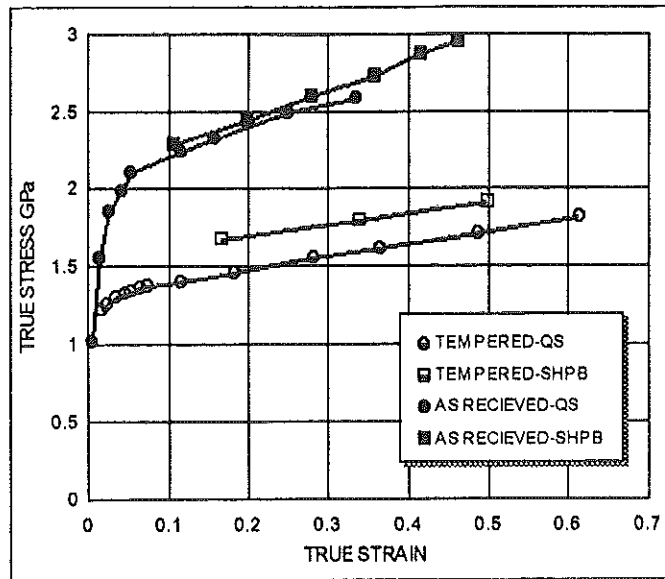


Figure 6. The strain rate and strain hardening sensitivities of the as-received and tempered high hardness steel

To test the relative susceptibility of the two forms of HH steel to AS, SHPB specimens of each were tested at a strain rate of approximately 2500/s. The as-received, rate insensitive material grossly adiabatically sheared, figure 7a, whereas the modified, rate sensitive material deformed homogeneously with no gross AS, figure 7b.



Figure 7a. The as-received, rate insensitive high hardness steel showing gross adiabatic shearing.

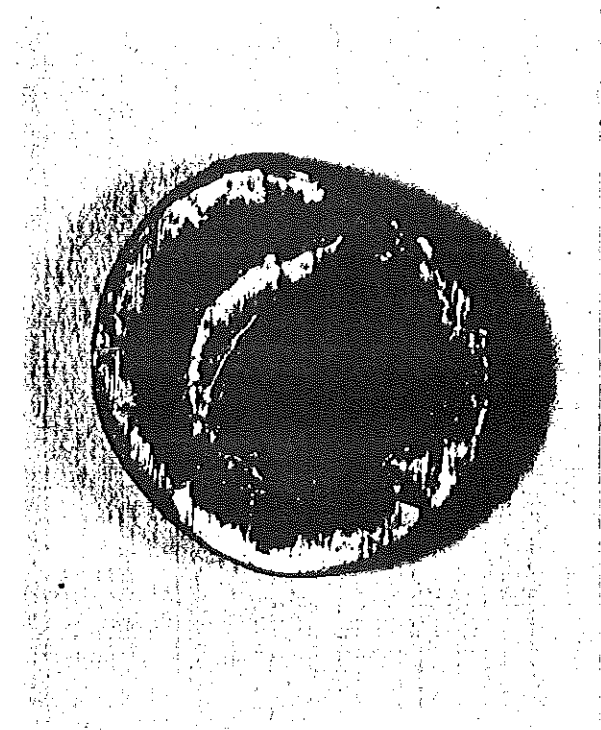


Figure 7b. The modified, rate sensitive high hardness steel deforming homogeneously with no indication of adiabatic shear.

This supports the proposition that strain rate sensitivity is an important factor in initiating adiabatic shear, ie. materials which significantly strain rate harden, inhibit AS.

In modifying the HH steel, other constitutive sensitivities were affected. It is important to examine how these may influence the test behaviour. In the tempered steel the strain hardening rate was slightly reduced and some thermal sensitivity was introduced. Both these factors would enhance the tendency to AS. However, the modified steel homogeneously deformed. This indicates the dominance of strain rate hardening in the prevention of initiation of AS bands.

Whilst the experiments suggest that the above statements are true, causality of initiation is not proven. It is possible that the microstructural differences between the various hardnesses of steel may introduce different structural inhomogeneities which may be significant.

5 Conclusions

- 5.1 The constitutive mechanical behaviour of a range of steels has been established. With increasing original hardness the rate of strain hardening $(\partial\sigma/\partial\varepsilon)_{\varepsilon_T}$ increases, the strain rate hardening $(\partial\sigma/\partial\dot{\varepsilon})_{\varepsilon_T}$ decreases, and the thermal sensitivity to flow $(\partial\sigma/\partial T)_{\varepsilon\dot{\varepsilon}}$ decreases.
- 5.2 Adiabatic shear experiments show the higher hardness steels to be more susceptible to adiabatic shear.
- 5.3 Steels with a strong strain rate sensitivity are less prone to adiabatic shear than steels which are insensitive to strain rate. The importance of strain rate hardening was demonstrated by thermo-mechanically modifying a rate insensitive steel to give it some rate sensitivity.

6 References

- 1 Hartley, K. A. and Duffy, J., "Strain Rate and Temperature History Effects During Deformation of FCC and BCC Metals," in Mechanical Properties at High Rates of Strain, Conf. Ser. No. 70, (J. Harding, Ed.), Institute of Physics, London, 21-30, (1984).
- 2 Meyer, L. W. and Manwarig, S., in "Metallurgical Applications of Shock-Wave and High-Strain-Rate Phenomena," M. Dekker, N.Y., 657, (1986).
- 3 Wright, T. W. and Batra, R. C., "The Initiation and Growth of Adiabatic Shear Bands," Int. J. Plasticity, 1, 205-212, (1985).
- 4 Clifton, R. J., Duffy, J., Hartley, K. A. and Shawki, T. G., "On Critical Conditions for Shear Band Formation at High Strain Rates," Scripta Metall., 18, 443-448, (1984).
- 5 Shockey, D. A., Curran, D. R. and Seaman, L., "Development of Improved Dynamic Failure Models," Final Technical Report for U.S. Army Research Office, Contract No. DAA-29-81K-0123, Research Triangle Park, NC, (1985).

Computational Simulation of Highvelocity Impact Situations using Smoothed Particle Hydrodynamics

S. Hiermaier⁺, K. Thoma^{*}

Universität der Bundeswehr München

⁺ *Fakultät Bauingenieur- und Vermessungswesen*

Labor für Ingenieurinformatik

^{*} *Fachbereich Maschinenbau*

Abstract:

Using hydrocodes for the simulation of high velocity impact situations often leads to severe problems at regions of high strain. A lagrangian formulation will produce large grid deformations and finally make expensive remeshing necessary. Both eulerian and mixed euler-lagrange codes need much more computing time to solve the problem. As material is flowing through the mesh geometric information about the outer shape of bodies gets lost and the solution becomes less exact at the calculated displacements.

Smooth Particle Hydrodynamics (SPH) is an alternative method. Instead of a grid this free lagrange method uses an interpolation kernel to smooth out discrete values for mass and velocity around the particles' location. There is no need to implement a contact algorithm or to remesh. Even the debris clouds resulting from impact on brittle materials may be part of a SPH simulation.

A threedimensional SPH code is currently being developed at the federal armed forces university in Munich. In this paper we demonstrate advantages and handicaps within that kind of hydrocode.

1 Introduction

Developped first to describe astrophysical problems like multi-body-systems and three-dimensional flow in the late 70s (Gingold & Monaghan, 1977) smoothed particle hydrodynamics (SPH) nowadays are used for simulations of various problems. SPH uses a lagrangian formulation of the equations of motion. The method doesn't use a distortion limiting grid and is therefore very attractive for any high velocity impact simulation. Any kind of equation of state, strength model or failure criteria may be implemented. A certain number of interpolation points called particles provide the spatial distribution of the state variables. Instead of a grid SPH uses an interpolation formula, the kernel function, to calculate a kernel estimation of the field variables at any point. The governing conservation equations, formulated as integral equations, are calculated as sums over neighboring points. An explicit central difference method is used for the time integration which delivers the field variables for time $t + \Delta t$ from the configuration at time t . The spatial derivatives of the field variables are transformed into spatial derivatives of the kernel function. Thus any vector function $f(x)$ is calculated as kernel estimation:

$$\langle f(x) \rangle = \int f(x') W(x-x', h) dx' \quad (1)$$

where $W(\mathbf{x}-\mathbf{x}', h)$ is the kernel function. Some requirements on the kernel are:

Compact support, which means that it is zero everywhere but on a finite domain. This requirement limits the influence of one particle on its neighbours to a certain region. The range of the kernel function is determined by a smoothing length h . This means that for instance the density peak of one particle i affects the calculations of new velocity, density, pressure, energy etc of all particles within the range of $2h$ around i .

The kernel has to reduce to the Dirac delta if h reduces to zero:

$$\lim_{h \rightarrow 0} W(\mathbf{x}-\mathbf{x}') = \delta(\mathbf{x}-\mathbf{x}')$$

And finally it must be normalized :

$$\int W(\mathbf{x}, h) d\mathbf{x} = 1$$

The divergence of the vector function $f(\mathbf{x})$ can be formulated in the same way as the vector function $f(\mathbf{x})$ in (1):

$$\langle \nabla \cdot f(\mathbf{x}) \rangle = \int \nabla \cdot f(\mathbf{x}') W(\mathbf{x}-\mathbf{x}', h) d\mathbf{x}' \quad (2)$$

With the integrant

$$\nabla \cdot f(\mathbf{x}) W(\mathbf{x}-\mathbf{x}') = \nabla \cdot (f(\mathbf{x}) W(\mathbf{x}-\mathbf{x}')) - f(\mathbf{x}') \cdot \nabla W(\mathbf{x}-\mathbf{x}')$$

we obtain

$$\langle \nabla \cdot f(\mathbf{x}) \rangle = \int \nabla \cdot (f(\mathbf{x}) W(\mathbf{x}-\mathbf{x}')) d\mathbf{x}' - \int f(\mathbf{x}') \cdot \nabla W(\mathbf{x}-\mathbf{x}') d\mathbf{x}'$$

The first integral on the right hand side can be transformed into a surface integral (see Swegle et al., 1994) which is zero according to the compact support requirement on the kernel function, as long as no surface with a non free boundary condition is within the range of $2h$. If only free surfaces are used the divergence $\nabla f(\mathbf{x})$ can be written as

$$\langle \nabla \cdot f(\mathbf{x}) \rangle = \int f(\mathbf{x}') \cdot \nabla W(\mathbf{x}-\mathbf{x}') d\mathbf{x}' \quad (3)$$

Equation (3) demonstrates the way SPH takes spatial derivatives of any vector function f at coordinate \mathbf{x} as the function's value at a neighbor's coordinate \mathbf{x}' times the derivative of the kernel.

As the state variables in SPH are known at discrete particle locations integrals over a continuous volume are transformed to sums over the values of neighbor particles. Every particle

represents a volume dx which is defined by the particle's mass (constant) and the current density. Thus the volume of a neighbor particle j may be written as

$$dx' = \frac{m_j}{\rho(x_j')}$$

which delivers approximations for equations (2) and (3):

$$\langle f(x) \rangle = \sum_{j=1}^N f_j W(x-x',h) \frac{m_j}{\rho_j} \quad (4)$$

$$\langle \nabla \cdot f(x) \rangle = \sum_{j=1}^N f(x_j) \cdot \nabla W(x-x_j) \frac{m_j}{\rho_j} \quad (5)$$

The sums providing the integral approximations are taken over all particles of the model. Non zero contributions can result from particles within the kernel range only. Therefore it is very useful to implement a fast search algorithm to find all particles within the $2h$ zone and take the sum over these particle values only. Otherwise the computation time for each time step would increase with N^2 . There are different theories how to sort and find the particles in space. One possibility is to generate a grid with cubic cells of $2h$ edge length. The potential neighbors of a particle in cell m,n are now to be found in the particle's own cell and in the next cells around it ($m-1,n-1 \dots m+1,n+1$).

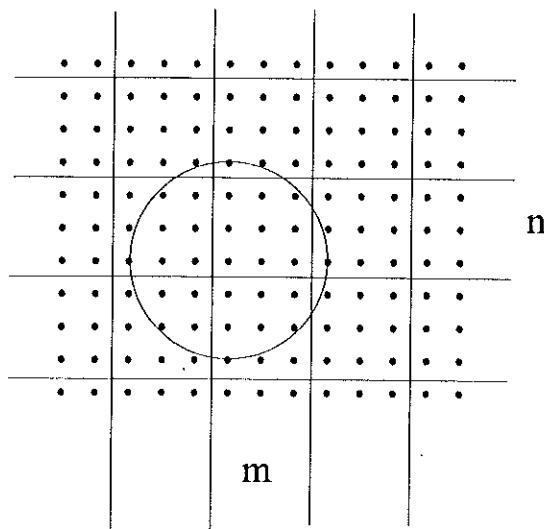


fig. 1: grid method to sort particles

Using a grid to sort and search particles will increase the computation time by $N \log N$.

The formulation of the kernel function can be done using polynomial or gaussian functions (see Monaghan, Gingold, 1983). The following polynomial kernel (Monaghan, Lattanzio, 1985) satisfies the requirements mentioned earlier:

The same equations written as sums over contributions of neighbor particles:

$$\frac{d\rho}{dt} = \rho_i \sum_j \frac{m_j}{\rho_j} (U_i^\beta - U_j^\beta) W_{ij,\beta} \quad (17)$$

$$\frac{dU_i^\alpha}{dt} = - \sum_j m_j \left(\frac{\sigma_i^{\alpha\beta}}{\rho_i^2} + \frac{\sigma_j^{\alpha\beta}}{\rho_j^2} \right) W_{ij,\beta} \quad (18)$$

$$\frac{dE_i}{dt} = \frac{\sigma_i^{\alpha\beta}}{\rho_i^2} \sum_j m_j (U_i^\alpha - U_j^\alpha) W_{ij,\beta} \quad (19)$$

represent the SPH formulation of the equations of motion, where $W_{ij,\beta}$ stands for the spatial derivative of W with regard to coordinate β .

3 Stress Calculation and Strength Model

The stress tensor can be split up into a hydrostatic pressure part and a deviatoric stress.

$$\sigma^{\alpha\beta} = S^{\alpha\beta} - P\delta^{\alpha\beta}$$

To obtain the deviatoric stresses we calculate the stress rates with the Jaumann stress rate tensor:

$$\dot{S}^{\alpha\beta} - S^{\alpha\beta} \dot{R}^{\beta\gamma} - S^{\gamma\beta} \dot{R}^{\alpha\gamma} = \mu \left(\dot{\epsilon}^{\alpha\beta} - \frac{1}{3} \delta^{\alpha\beta} \dot{\epsilon}^{\delta\delta} \right) \quad (20)$$

with the strain rate and rotation rate defined by:

$$\dot{\epsilon}^{\alpha\beta} = \frac{1}{2} \left(\frac{\partial U^\alpha}{\partial x^\beta} + \frac{\partial U^\beta}{\partial x^\alpha} \right)$$

$$\dot{R}^{\alpha\beta} = \frac{1}{2} \left(\frac{\partial U^\alpha}{\partial x^\beta} - \frac{\partial U^\beta}{\partial x^\alpha} \right)$$

The pressure part on the other hand is calculated with any common equation of state. There

are many different equations of state for ideal gases or high explosives as well as for solids. Regarding impacting solids we use the Mie-Grüneisen equation to calculate the hydrostatic pressure:

$$P = \left(1 - \frac{1}{2} \Gamma \eta\right) P_H(\rho) + \Gamma \rho E$$

$$P_H = \begin{cases} a_0 \eta + b_0 \eta^2 + c_0 \eta^3 & , \eta > 0 \\ a_0 \eta & , \eta < 0 \end{cases}$$

$$a_0 = \rho_0 C^2 \qquad \eta = \frac{\rho}{\rho_0} - 1$$

$$b_0 = a_0 [1 + 2(S-1)] \qquad U_s = C + S U_p$$

$$c_0 = a_0 [2(S-1) + 3(S-1)^2]$$

Where the Hugoniot pressure P_H is calculated as polynomial function with coefficients derived from the shock velocity parameters C (sound speed) and S .

Following the von Mises assumption that plastic flow depends on the deviatoric stresses only we use the second invariant J_H

$$J_H^2 = S^{\alpha\beta} S^{\alpha\beta}$$

as yield criterion. Libersky and Petschek (1990) were the first to implement a material strength model this way in SPH. With J_H and the yield stress $\bar{\chi}$ we limit the deviatoric stress to the von Mises yield surface.

Another strength criterion is the hydrodynamic minimum pressure (spall pressure) which is implemented in the code. If the pressure at a particle i reaches the materials negativ pressure limit then this particle loses any tensile strength. The current pressure is then reset to zero as well as the yield stress and the hydrodynamic minimum pressure for all future timesteps at particle i .

4 Artificial Viscosity

The description of shocks with the inviscid conservation equations leads to very high unphysical oscillations in the shock region. Von Neumann and Richtmeyer (1950) invented an artificial viscosity to smooth the shock over a couple of elements or particles respectively. In nature a shock wave always produces dissipation of kinetic energy into heat. The artificial viscous pressure term that is used in SPH contains a linear term in velocity that yields a shear and bulk viscosity. The

quadratic term is equivalent to the original von Neumann Richtmeyer viscosity:

$$\Pi_{ij} = \begin{cases} \frac{-\alpha \bar{c}_{ij} \mu_{ij} + \beta \mu_{ij}^2}{\bar{\rho}_{ij}} & ,if \ (\mathbf{U}_i - \mathbf{U}_j) \cdot (\mathbf{x}_i - \mathbf{x}_j) < 0 \\ 0 & ,otherwise \end{cases}$$

$$\mu_{ij} = \frac{h (\mathbf{U}_i - \mathbf{U}_j) \cdot (\mathbf{x}_i - \mathbf{x}_j)}{(\mathbf{x}_i - \mathbf{x}_j)^2 + \epsilon h^2}$$

Implementing this artificial viscosity to the SPH formulated conservation equations (17) - (19) yields the equations that are used in most of the existing SPH codes:

$$\frac{d\rho_i}{dt} = \rho_i \sum_j \frac{m_j}{\rho_j} (U_i^\beta - U_j^\beta) W_{ij,\beta} \quad (21)$$

$$\frac{dU_i^\alpha}{dt} = -\sum_j m_j \left(\frac{\sigma_i^{\alpha\beta}}{\rho_i^2} + \frac{\sigma_j^{\alpha\beta}}{\rho_j^2} + \Pi_{ij} \right) W_{ij,\beta} \quad (22)$$

$$\frac{dE_i}{dt} = \sum_j m_j (U_i^\alpha - U_j^\alpha) \left(\frac{\sigma_i^{\alpha\beta}}{\rho_i^2} + \frac{1}{2} \Pi_{ij} \right) W_{ij,\beta} \quad (23)$$

5 Time Step Method and Time Integration

The magnitude of each time step δt must be controlled with regard to spatial resolution, in this context the smoothing length h , and to the maximum velocities. A very common time step control mechanism is the Courant-Friedrichs-Levy criterion. Applied to the SPH terminology it defines the time step as:

$$\delta t = \omega \frac{h}{C + S U_p}$$

where ω is a factor most often set to 0.6, and the smoothing length h is divided by the shock

velocity expressed via the sound speed C and the particle velocity U_p .

The time integration is done using a standard leap-frog scheme which is second order accurate. That provides the new variables of state at time $t + \delta t$ as:

$$\rho^{n+1} = \rho^n \left(1 - \frac{\partial U}{\partial x} \delta t^n \right)$$

$$U_\alpha^{n+\frac{1}{2}} = U_\alpha^{n-\frac{1}{2}} + \frac{1}{2} (\delta t^n + \delta t^{n-1}) \frac{dU_\alpha}{dt}$$

$$E^{n+1} = E^n + \delta t^n \frac{dE}{dt}$$

$$S_{\alpha\beta}^{n+1} = S_{\alpha\beta}^n + \delta t^n \frac{dS}{dt}$$

$$x_\alpha^{n+1} = x_\alpha^n + U_\alpha^{n+\frac{1}{2}} \delta t^n$$

6 Example Calculation for a Plexiglas Impact

The following test was done: An oblique impact of a lead bullet onto a plexiglas plate. We measured the velocities of glass debris and lead fragments. The impact angle was 45 degrees.

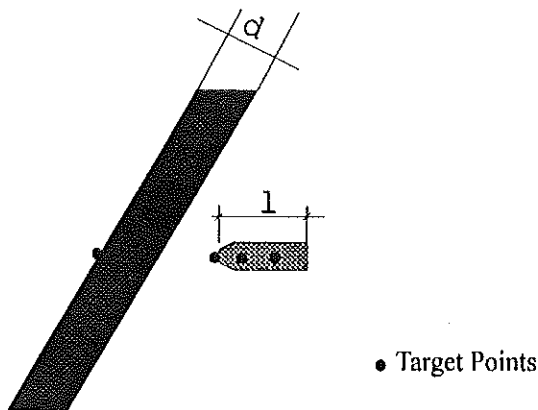


fig.2: oblique plexiglas impact

Plexiglas Plate:

$d=1.2$ cm	$\rho=1.186$ gr/cm ³
$p_{spall}=-1.5$ Kbar	$G=0.01$ Mbar
$c=0.2527$ cm/ μ s	

Lead Bullet:

$l=1.0$ cm	$\rho=11.34$ gr/cm ³
$p_{spall}=-6$ Kbar	$G=0.055$ Mbar
$c=0.2006$ cm/ μ s	$V_{Impact}=0.046$ cm/ μ s
$\sigma_Y=0.8$ Kbar	

The experiment showed us that the impact caused a debris cloud of glass material at the backside of the plate. This material is accelerated normal to the plate surface and thus at 45 degrees to the direction of the impacting lead bullet. The measured velocity of the debris particles was 151 m/s,

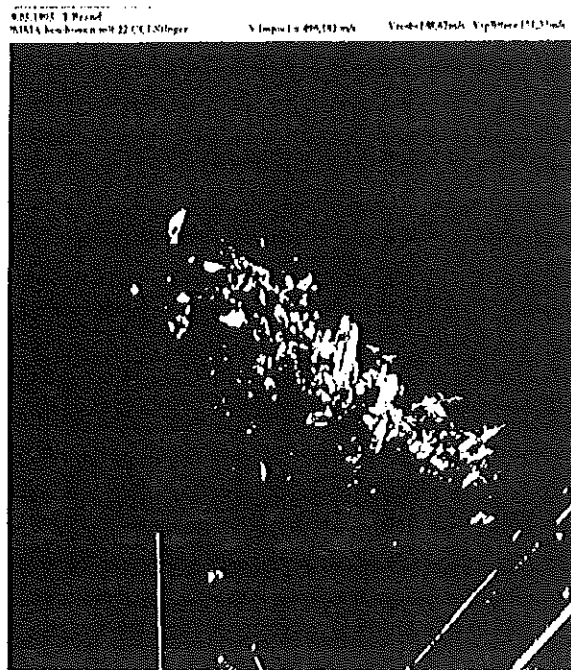
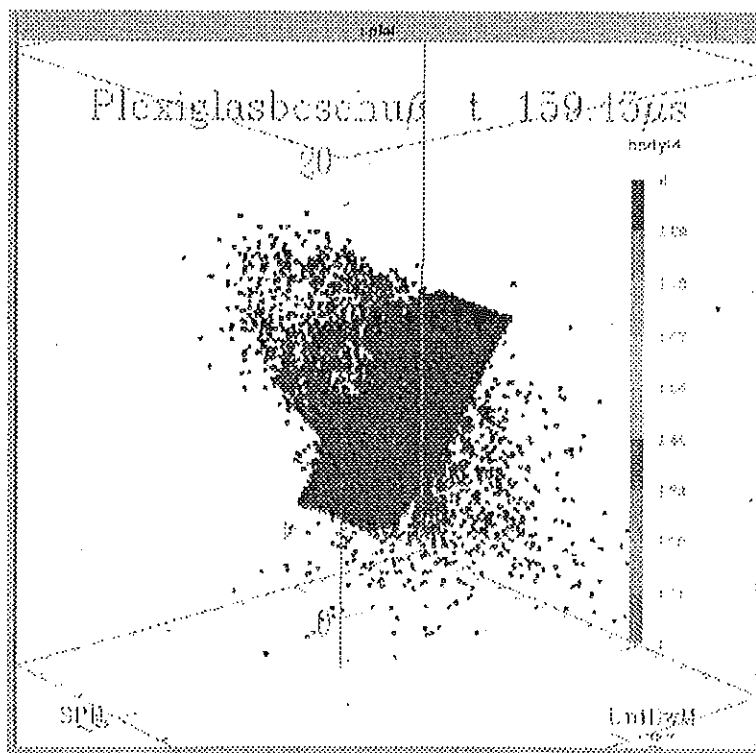


fig 3: Oblique lead plexiglas impact. Glas debris from the back side of the plate is accelerated normal to the plate surface.

the velocity of the bullet material 149 m/s. The bullet was almost completely deformed and split into some recognizable fragments and dust.

Figure 3 shows a photograph of the experiment with the plexiglas plate in the lower right corner and the debris cloud moving normal to the plate along the diagonal. Figure 4 is a plot of the three-dimensional SPH calculation. It shows a very similar debris cloud after 159 microseconds. The velocities of lead and plexiglas material vary between 120 and 170 m/s. This difference may result out of the fact that we used no damage modell for the plexiglas and a strain rate independent yield criterion for the lead material. Thus a more exact formulation of the material behaviour should improve the quality of the results. The complete energy failure of the SPH calculation was 4.9 percent after 1500 cycles.



References

- [1] Benz W., Preprint for Numerical Modelling of Stellar Pulsation, Nato Workshop, Les Arcs, France, 1989
- [2] Gingold R.A., Monaghan J.J., Monthly Notations of the Royal Astronomical Society, Nr. 181, pp. 375, 1977
- [3] Libersky L.D., Petschek A.G., *Smooth Particle Hydrodynamics with Strength of Materials*, Proceedings of the NEXT Free-Lagrange Conference, Jackson Lake Lodge, Wyoming, June 3-7, 1990
- [4] Libersky L.D., Petschek A.G., Carney T.C., Hipp J.R., Allahdadi F.A., Journal of Computational Physics, Nr. 109, pp. 67-75, 1993
- [5] Monaghan J.J., Gingold R.A., Journal of Computational Physics, Nr. 52, pp. 374, 1983
- [6] Monaghan J.J., Lattanzio J.C., Astron. Astroph., Nr. 149, p. 135, 1985
- [7] Nelson R.P., Papaloizou J.C.B., Monthly Notations of the Royal Astronomical Society, Nr. 265, pp. 905, 1993
- [8] Neumann J. von, Richtmeyer R.D., Journal of Applied Physics, Nr. 21, p. 232, 1950
- [9] Swegle J.W., Attaway S.W., Heinstein M.W., Mello F.J., Hicks D.L., *An Analysis of Smoothed Particle Hydrodynamics*, SANDIA Report SAND93-2513, 1994

ANALYTICAL CALCULATION OF BALLISTIC LIMIT VELOCITY BY WORK METHOD APPROXIMATION

Thierry FRANCOU

Centre Technique des Systèmes Navals - BP28 - 83800 Toulon Naval (FRANCE)

Summary:

Estimating the residual velocity of a projectile is conditioned by precision in determining the ballistic limit velocity. Traditional methods of analysis require a large number of calculations to find a suitable answer. We present below a method, based on a hypothesis of the profile of the force applied to the projectile in time, which allows precise determination of the ballistic limit velocity. After describing the method, we give a comparison between the theoretical and experimental values of the maximum forces and velocities of perforation, in the event that the projectile nose is longer than the thickness of the target. Despite these approximations, the over-estimations and under-estimations cancel each other out and allow a good correlation between theory and practice. However, caution is necessary as to the validity of this method when applied to targets made of armored steel.

1/ Foreword:

Man has always sought ways of protecting himself against armed aggression from outside. Though his first calculations for protection were a "binary" empirical approach (whether or not the protection would resist a given aggression), man soon looked for ways of determining with certainty the minimum thicknesses needed for his protection. Thus, nearly a century ago, the first equations were made to evaluate the depth of penetration or the residual velocity of a projectile after perforation.

Growing knowledge of the phenomena involved in perforation of protective plates gave rise to a family of analytical models. At the same time, the development of hardware led to the creation of digital tools that could solve more and more complex problems and reveal the phenomenology of the perforation.

The surface vessels of the French Navy have been designed for a "wartime" environment. They are used in areas where international tension is high and they face threats that are smaller than in wartime but that occur frequently. This is particularly true of threats from small-caliber projectiles. To evaluate the vulnerability of a ship in the face of this type of aggression it is necessary to be acquainted with the phenomena of perforation in the naval field, characterised essentially by the thickness of plate which is approximately equal to the caliber of projectiles used for assault.

2/ Aims of the study:

Traditional methods require a lot of calculation and a fairly heavy investment in electronic tools (1). Periodically, for example during feasibility or security studies, it is necessary to determine the thickness required for the protection of a vessel. In this particular context, it would be useful to have a law to evaluate, using any simple means of calculation (personal computer, calculator, etc), the thickness of the material protecting the vessel.

The purpose of this study is to present a simple method for calculating the ballistic limit velocity, that is, the minimum velocity at which a small-caliber projectile of a given shape can perforate a target of defined type and thickness. This method requires very little calculation, at the cost of lower precision. To validate our model we will compare the results obtained with those of experiments.

To limit the field of investigation of this article, we have taken the case of small-caliber, non-deformable projectiles, with a nose longer than or equal to the thickness of a representative target of a naval structure. Also, the effects of friction are neglected during perforation. To model the real projectile we have taken a conical-nose projectile, with a half-angle at summit β and with the same mass as the real bullet. The target is assumed to be ductile. Finally, we have chosen the least favorable situation from the point of view of the ship's protection, that is, the impact under zero NATO obliquity. The notations used are defined at the end of the article.

3/ Presentation of the work method (approach):

3.1/ Principle of the method:

This is an isolated target-penetrator system. By definition, we can write that the effect of the forces applied to the projectile at perforation is:

$$W = \int F \cdot dx \quad (1)$$

whereas the application of the fundamental principle of the dynamic to the projectile is written:

$$m \cdot \frac{dV}{dt} = \sum \text{Forces} = F \quad (2)$$

It results that:

$$m \cdot \frac{dV}{dt} = \frac{dW}{dx} \quad \Rightarrow \quad m \cdot V \cdot \frac{dV}{dx} = \frac{dW}{dx}$$

Or:

$$dW = d\left(\frac{1}{2} \cdot m \cdot V^2\right) \quad (3)$$

This gives the equation:

Variation of kinetic energy = Work of strength on projectile

Recht [2], showed that this variation of kinetic energy was written, assuming energy lost by elastoplastic deformation of the target constant when the impact velocity varies:

$$\begin{aligned} \frac{1}{2} \cdot m \cdot V_0^2 - \frac{1}{2} \cdot m \cdot V_r^2 &= \frac{1}{2} \cdot m \cdot V_{50}^2 \\ V_0^2 - V_r^2 &= V_{50}^2 \end{aligned} \quad (4)$$

Thus, the estimation of the effect of the forces applied to the projectile at perforation allows the calculation of the ballistic limit velocity (V_{50}) depending on the geometrical and mechanical characteristics of the projectile/target unit. We will now present a method of determining this effect by approximation of the profile of the variation of the force applied to the projectile at perforation.

3.2/ Profile of the force applied to the projectile:

In the event of perforation by ductile mechanism, the force observed has the shape given in figure 1. Three zones are clearly distinguished. We will comment on the profile obtained to understand, if the nose is longer than thickness e , what each zone corresponds to and what its limits are.

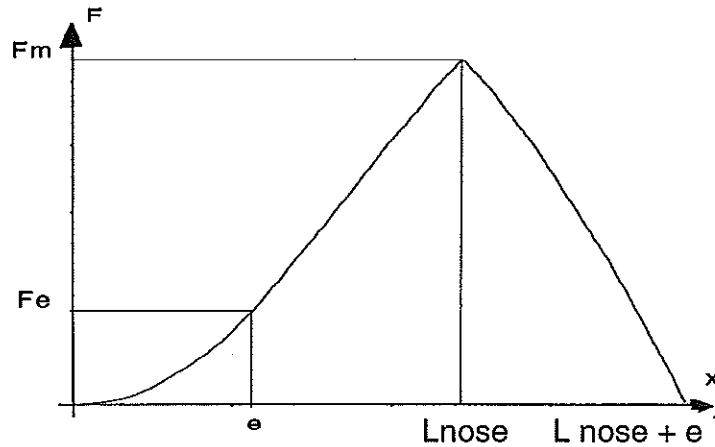


Figure 1 : Strength profil versus depth of penetration

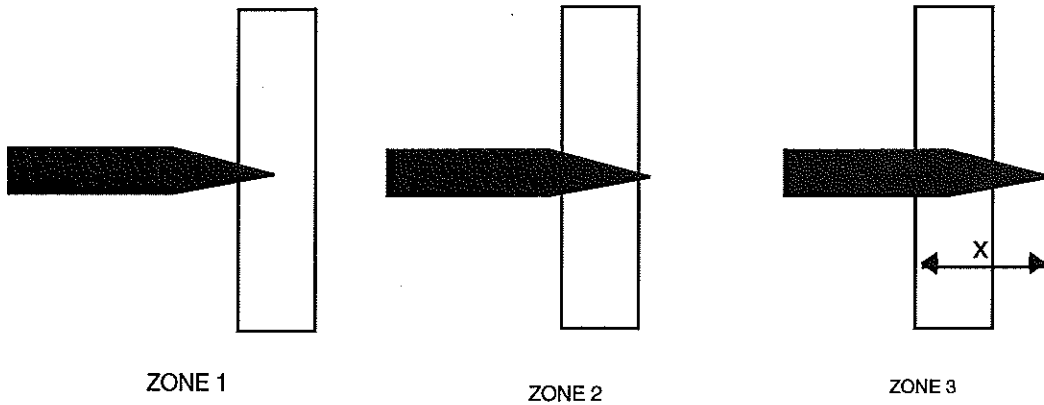


Figure 2: Distinction of three zones studied

First phase: $0 \leq x \leq e$

(x being the position of the projectile's extremity compared with the front of the target)

- The nose of the projectile penetrates the target. The contact surface, which is a cone, thus increases according to the depth of penetration, so that:

$$S(x) = \pi * \frac{\tan \beta}{\cos \beta} * x^2 \quad (5)$$

Second phase: $e \leq x \leq L_{nose}$

- The nose of the projectile reaches the back of the target and emerges. At this moment the contact surface is a cone trunk whose base radius increases with the depth of penetration. Thus:

$$S(x) = \pi * e * \frac{\tan \beta}{\cos \beta} * (2 * x - e) \quad (6)$$

Third phase: $L_{nose} \leq x \leq L_{nose} + e$

- The body of the projectile penetrates the target. As friction is neglected, only a cone trunk whose height decreases with penetration is involved in the contact.

$$S(x) = \pi * (R + (x - e) * \tan \beta) * \sqrt{(L_{nose} + e - x)^2 + (R - (x - e) * \tan \beta)^2} \quad (7)$$

3.3/ Estimation of work by approximation of force profile:

In the zones already defined, we assume that the force varies as the surface with the penetration depth. Thus, we have a parabolic variation in zone 1, and linear in zone 2. A study of function S(x) in zone 3 shows that the variation is quasi-linear. We will adopt a linear variation in this zone.

Thus, the work of strength corresponds to the area under the Force=f(x) curve. An approximation of this is provided by:

$$W = \frac{1}{3} * F(e) * e + F(e) * (L_{nose} - e) + (F_{max} - F(e)) * \frac{(L_{nose} - e)}{2} + F_{max} * \frac{e}{2}$$

Or:

$$W = (F_{max} + F(e)) * \frac{L_{nose}}{2} - F(e) * \frac{e}{6} \quad (8)$$

To be able to calculate the force effect, we now need to choose a behavior law which will give the evolution of the interface pressure and allow the calculation of F(e) and Fmax.

3.4/ Estimation of the interface pressure:

We will only consider ductile materials. Thus we will adopt a behavior law of rigid plastic type in which the dynamic pressure will depend on the static yield stress and the penetration velocity.

$$\sigma = \sigma_y + \frac{1}{2} * \rho * V_{\perp}(x)^2$$

Where V_{\perp} is normal velocity component at the contact surface,

or for a conical nose:

$$\sigma = \sigma_y + \frac{1}{2} * \rho * V(x)^2 * \sin^2 \beta \quad (9)$$

3.5/ Determination of the equation system:

We have a problem with six unknowns which are V_e , F_e , V_m , F_m , but especially V_{50} and V_r . We therefore need to find six equations to be able to solve the problem analytically. To do this we write on each zone the work theory (3). This means that:

$$\text{Zone 1:} \quad V_e^2 - V_0^2 = -\frac{2}{3} * \frac{e}{m} * F_e \quad (10)$$

$$\text{Zone 2:} \quad V_m^2 - V_e^2 = -\frac{L_{nose} - e}{m} * (F_e + F_m) \quad (11)$$

$$\text{Zone 3:} \quad V_r^2 - V_m^2 = -\frac{e}{m} * F_m \quad (12)$$

The energy conservation equation enables us to write that:

$$V_0^2 - V_r^2 = V_{50}^2 \quad (4)$$

Finally, we write that forces F_e and F_m are respectively equal to the pressure product by contact surface to the eastings and Logive, from which:

$$F_e = \pi * e^2 * \frac{\tan(\beta)}{\cos(\beta)} * (\sigma_y + \frac{1}{2} * \rho * V_e^2 * \sin^2 \beta) \quad (13)$$

$$F_m = \pi * e * (2 * L_{nose} - e) * \frac{\tan(\beta)}{\cos(\beta)} * (\sigma_y + \frac{1}{2} * \rho * V_m^2 * \sin^2 \beta) \quad (14)$$

We obtain a system of six independent equations ((4), (10), (11), (12), (13),(14)) to six unknowns, which we can solve easily. We will now try to validate this law from experimental results concerning projectiles of calibers 0.3 and 0.5.

4/ Comparison of theory and experiments:

The targets used are of four types:

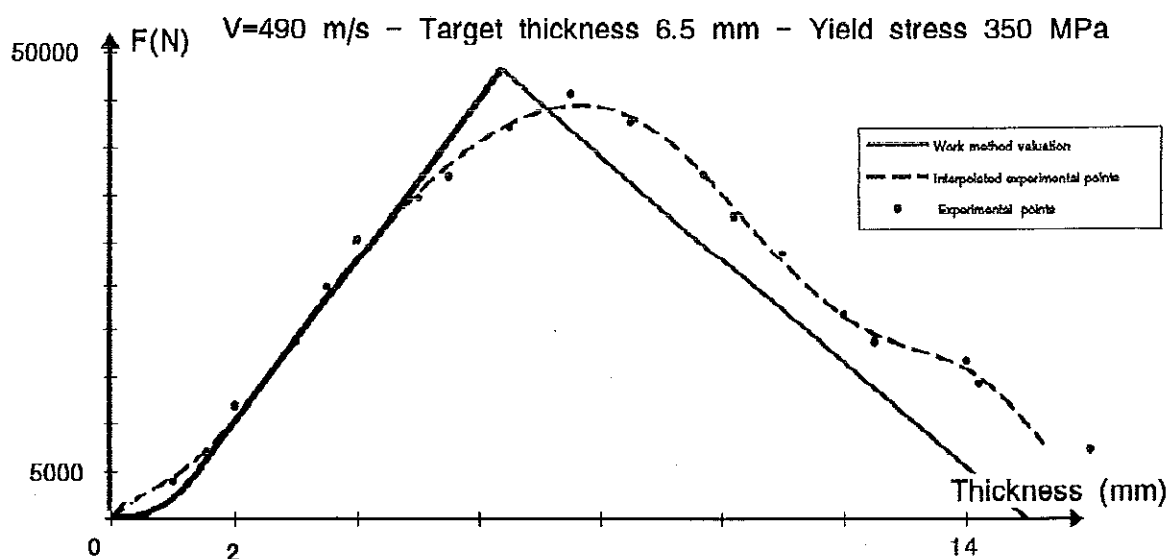
- Steel E28-4
- Soft steel with yield stress 350 MPa
- Armored steel with yield stress 850 MPa
- Armored steel with yield stress 1050 MPa

4.1/ Comparison of theoretical and experimental forces:

The curves below provide a basis for discussion concerning the validity of the work method approximation. To estimate the work of strength measured, we passed a polynome of 10 degrees through the points of measure [3], and then we calculated the area below the curve $F(x)$. From observing these results we conclude that, despite the over-estimations and under-estimations due to modeling, the errors cancel each other out to give a result on the work estimation that is lower than the measure error (estimated at 10%).

The work method approximation allows the estimation, with a good level of precision, of the work of strength applied to a projectile. However, caution is necessary in generalizing this method, as it could be possible in certain cases that the errors do not cancel each other out and that the error becomes significant.

V_0 (m/s)	W_m (N*m)	$W_{théo}$ (N*m) estimated	error (%)
230	364	375	3
330	364	343	6
490	364	385	5,4



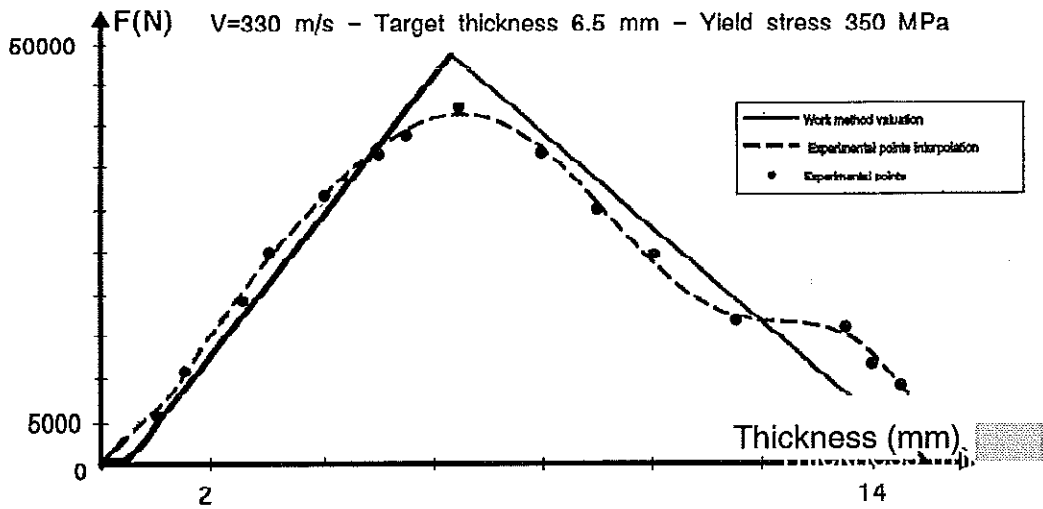
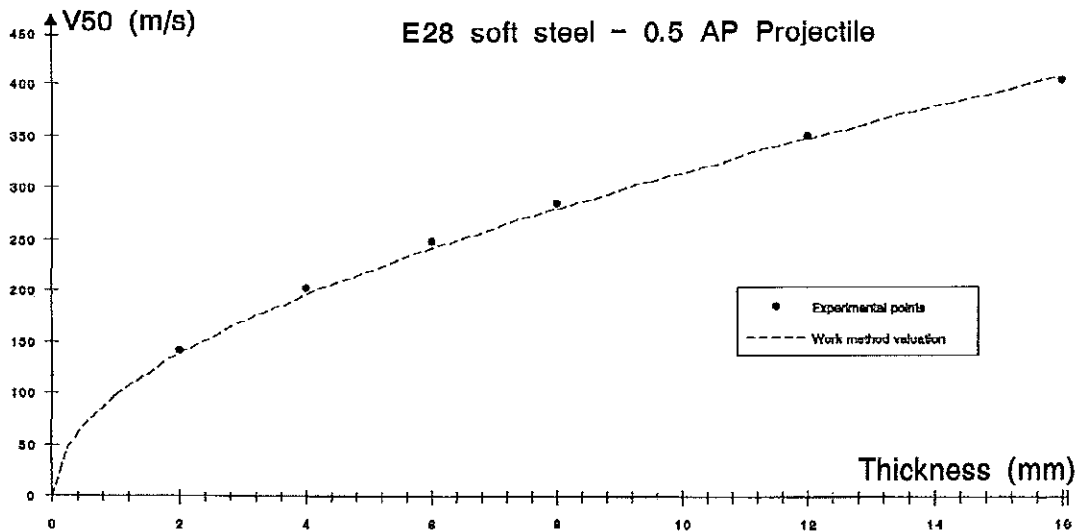


Figure 3 :Comparison of theoretical and experimental forces

4.2/ Comparison of theoretical and measured ballistic limit velocities:

We will now discuss the validity of work method approximation, applied to the determination of the ballistic limit velocity and the residual velocity of the projectile. To do that, we will work from the tests carried out on the bullet of 0.5 AP. The curves below show a comparative status between the results obtained by work method approximation and by experimentation.



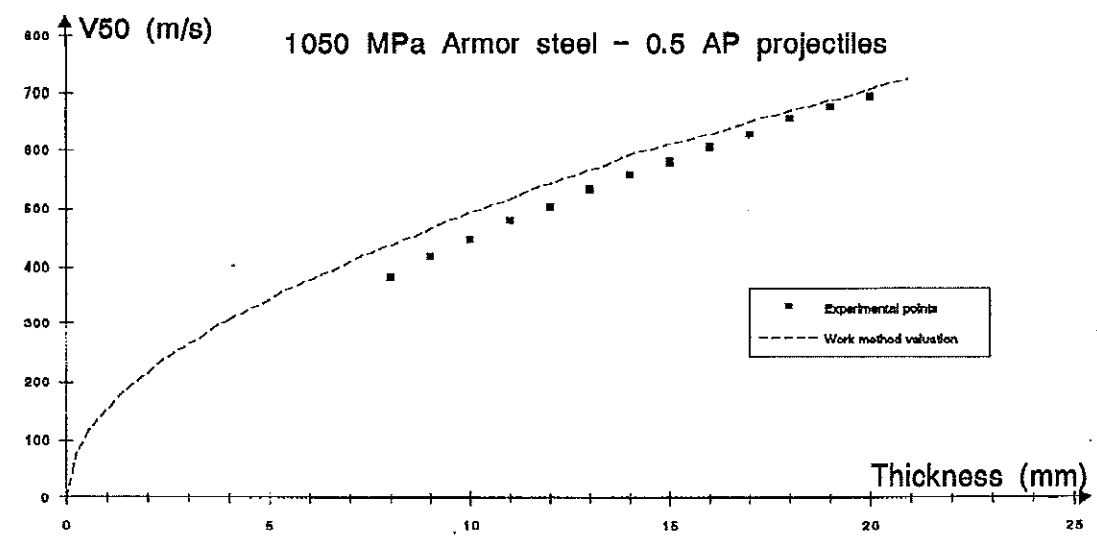
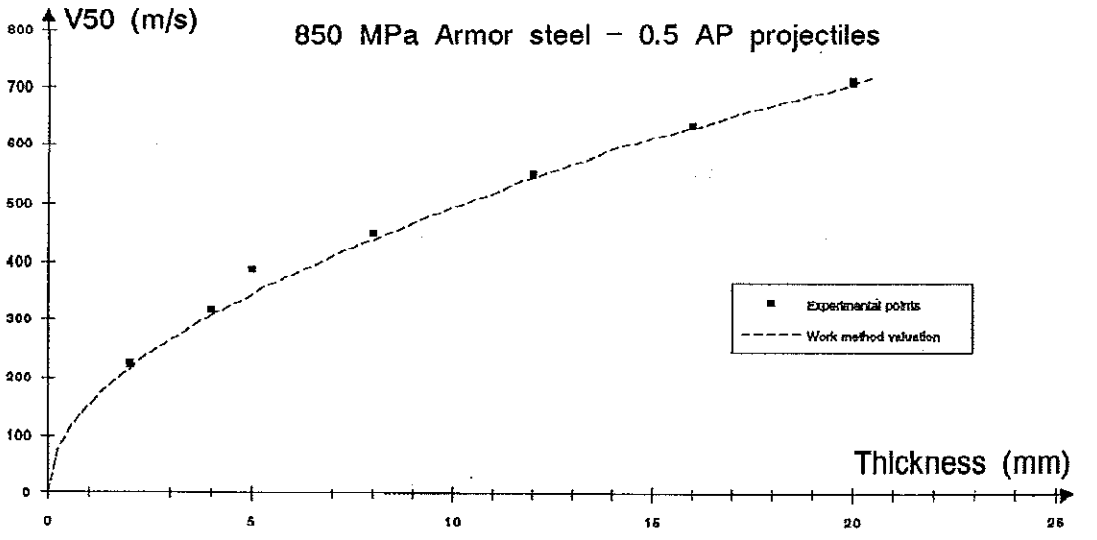
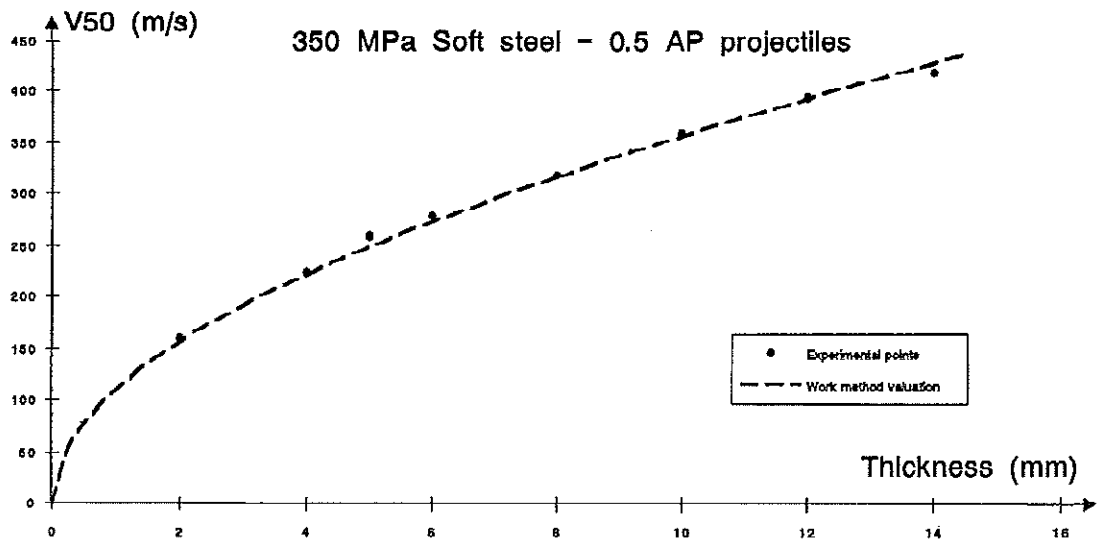


Figure 5: Comparison of theoretical and experimental ballistic limit velocities

These curves show the results for the different targets tested in the case of impact by 0.5 AP projectile. We observe a good approximation of the results for soft steels. However, in the case of armored steel, we note that the ballistic limit velocity is increased by the model. This can be explained by the fact that very hard steels do not

have ductile behavior at failure. Meunier Roux and Moureaud [4] have shown that, for these steels, the dominant mechanism is adiabatic shearing. They were then able to trace the variation of the ballistic limit velocity with the Brinel hardness of the target (figure 6) in the case of a non-hydrodynamic impact.

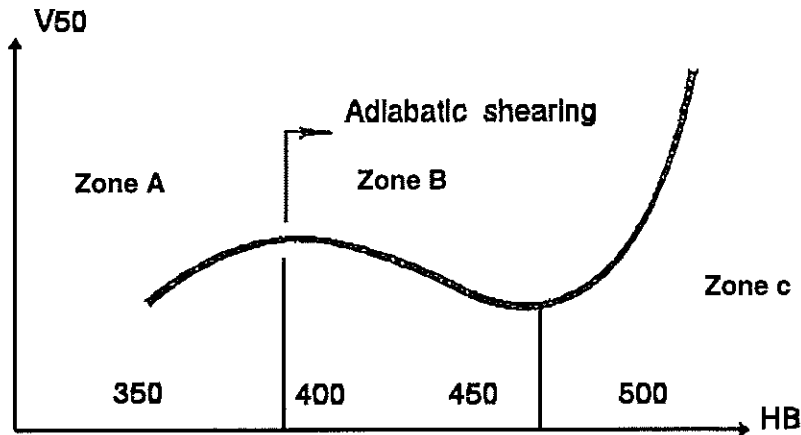


Figure 6: Variation of ballistic limit velocity with target hardness

In zone A, the dominant phenomenon is ductile failure without adiabatic shearing (case of soft steels). Zones B and C are zones where adiabatic shearing is predominant. In zone B, the increased hardness produces a reduction of the ballistic limit velocity due to greater sensitivity to the creation and propagation of cracks in the shear bands. Thus, a steel of 450 BHN hardness has very similar protective power to a steel of 350 BHN hardness. In zone C, we note the increase of the ballistic limit velocity with hardness. This is due to the fact that the projectile shatters and thus the kinetic energy of the fragments falls sharply, reducing the perforation power of the projectile.

The observation of this curve leads us to the following warning. Certainly the approximation between theory and practice is good in the case of armored steel, but the steels chosen are in zone B. We must thus be cautious as to the results obtained with armored steels, which must be validated elsewhere.

5/ Conclusion:

The method we have just developed, in a limited framework, allows a significant reduction in the number of calculations needed to obtain residual perforation parameters. It allows a reduction of answer time without major loss of precision. However, it would be complicated to try to extend this method to oblique impacts, and the use of this method must therefore be restricted to normal impacts.

In the same way, results from the use of this model with very hard steel targets must be handled with the reserves we have already expressed. On the other hand, for soft steel, as the estimation is correct, we can estimate that the dynamic approximation work method gives good results. This method therefore constitutes a useful tool, for example, for engineers looking for results for a draft.

Notations:

BHN	: Brinell hardness
D	: Projectile caliber
e	: Target thickness
F	: Strength on the projectile
L	: Total length of projectile
Logive	: Length of projectile nose
m	: Mass of projectile
R	: Radius of projectile
S	: Contact surface
V ₀	: Initial velocity
V ₅₀	: Ballistic limit velocity
V _r	: Residual velocity
W	: Work of strength
x	: Position of projectile extremity with regard to front of target

Bibliography:

- [1] FRANCOU Th. Développement d'un modèle analytique décrivant la perforation d'un matériau plastique
1995
Rapport technique
- [2] RECHT Multiple plate perforation modeling
1983
7ème Symposium de balistique
- [3] PERSSON A theoretical and experimental study of rigid projectile penetration mechanics
1976
2ème Symposium de balistique
- [4] MEUNIER-ROUX MOUREAUD Survey of AS phenomena in Armor steels with perforation
1992

Computational and Experimental Blast Shield Design in Tandem Shaped Charge Systems

N. Heider, H. Mayer

TDW, D-86523 Schrobenhausen, Germany

Tandem systems consist of two shaped charges. The initiation of the first charge creates high explosive detonation products expanding with large velocities. To assure the proper functioning of the second charge a blast shield is necessary which sustains the extremely high dynamical loads from the detonation products.

To minimize experimental testing a computational procedure was used for the design of the blast shield. A solution procedure was used which first calculates within the frame of an Eulerian simulation the time dependent dynamic pressure loads onto the blast shield. The response of the shield is analysed with the help of a Lagrange analysis. The simulations have been performed with the Hull code.

Of great importance is the material description of the blast shield. It is a reasonable way to use a simple model (for example elastic-plastic strain hardening behaviour) with a yield strength that is either a guessed value or adapted from experiments within a similar dynamical loading range.

Simulations with varying loads, blast shield designs and material parameters have been done. The numerically optimized blast shield design was tested and the results showed good agreement with the simulations especially the deformations occurring during failure are well reproduced. The presented simulation technique can thus be used with high confidence in the optimization of blast shield designs.

1. INTRODUCTION

Modern tanks show special protection systems, so called reactive armour boxes that can no longer be defeated with single shaped charge jets. The answer from the anti tank weapon development is the tandem shaped charge system. It consists of a first charge (precursor charge) that initiates and deactivates the reactive armour and a second charge (main charge, see fig. 1) that has the original task of penetrating the steel armour and destroying the tank. Both shaped charges are contained within a missile and are activated with a certain time delay.

The main problem for the functioning of the tandem system is connected with this time delay. The detonation of the precursor charge leads to highly expanding detonation products and fragments that might hit and influence the proper functioning of the main charge. To protect the main charge it is therefore necessary to develop a type of shielding which has to be optimized between the requirements of efficient protection capability and a low shield mass.

Different concepts for this protective blast shield are possible. The most successful design is the integrated barrier, where the shield between the precursor charge and the main charge is integrated into the aerodynamical missile skin (see fig. 1). This variant is analysed in detail in the following sections and has the advantages :

optimal use of available mass and volume
complete protection of main charge from the detonation products of the precursor charge
no restriction due to delay time between charge initiation.

The integrated barrier has to be optimized with respect to material selection and geometry of the design.

A very useful and successful way of doing this is by a combined computational and experimental approach. The numerical simulation with FE/FD methods allows a parametric analysis of the the problem, for example the variation of material properties and geometrical design parameters. These calculations give detailed information about failure mechanisms and their dependence on design parameters. Correlating the computational results with experiments gives sufficient confidence for further optimization loops.

2.SIMULATION TECHNIQUE

The simulation of the precursor charge detonation and its influence on the missile structure and main charge requires the description of the following phenomena :

detonation of the high explosive of the precursor charge
expansion of detonation products, shock waves, fragment impacts
interaction of the expansion products with the missile structure

The momentum and energy from the high explosive is to a significant amount transferred to the integrated barrier. The response of the the barrier to these structural loads should be as small as possible. The barrier must sustain the loads without significant plastic deformations within the required time delay interval between precursor charge and main charge initiation.

The high explosive detonation and the expansion of the detonation products are described very well with an Eulerian technique which allows to take into account the strong deformations, which the involved materials experience.

The dimensions of the complete system are very large compared with the typical thickness of the cylindrical part of the integrated barrier. It is therefore nearly impossible to create an Eulerian simulation model that includes the description of all physical phenomena mentioned at the beginning of this section. This would require a mesh size significantly lower than 1 mm to get a sufficient resolution to calculate the structural response of the barrier.

It is therefore necessary to divide the problem into the following two steps :

Eulerian FD simulation of the precursor charge detonation, interaction with the barrier and calculation of pressure loads onto the barrier

Lagrange calculation with a FE model of the barrier and the time dependent pressure loads on the barrier cap (input from the Eulerian simulation)

The Lagrange calculation allows a very detailed geometrical description of the barrier structure (up to 7 elements across the cylindrical wall) and thus gives the exact stress and strain distribution in the barrier structure.

The calculations were performed with the Hull Code which includes an Eulerian as well as a Lagrange module /ref.1/. A material library is available which contains different material models and the corresponding material data. If the user has own and better material data it is easy to add them to the library.

3.SIMULATION MODEL

3.1 Eulerian Model

The model includes about 50000 cells and has a grid resolution of 1 mm times 1 mm (see fig.4). The components of the missile that are mapped are the precursor charge, the integrated barrier, the aerodynamic missile skin and an electronic module near the charge. Station points in front of the barrier allow a detailed analysis of the pressure as a function of the time which gives the input loads for the following Lagrange calculation.

3.2 Lagrange Model

The Lagrange procedure uses a grid that is connected directly with the mapped material distribution. The geometrical model includes the integrated barrier (consists of the cap with the acting pressure loads and the cylindrical part), which has a resolution of 7 elements across the wall thickness. This is enough for a precise calculation of stress and strain distribution in the barrier structure and thus allows a precise description of the elastic and plastic behaviour and deformations of the barrier. Two types of boundary conditions at the end of the cylindrical part were used :

fixed nodes

sliding interface between barrier and nodes of a supporting mass.

There is no significant influence of the boundary condition on the results of the calculations.

3.3 Material Description

The two most important materials that should be described as well as possible are:

high explosive of precursor charge

material of integrated barrier

The high explosive and its detonation products are described by the JWL equation of state from the Hull material library.

The time dependent loading history of the barrier would require a detailed material model including strain rate effects. It should be mentioned that statical data about stress-strain relations cannot be used in this case. Thus there are two possibilities, either conducting expensive experiments in the corresponding strain rate regime, or rely on some reasonable estimate of the strength data. A typical experimental stress-strain curve at large strain rates for high strength steel is shown in fig.2. Yield strength values for this steel are therefore in the range of 15-17 kbar. For the parametric analysis we chose three simplified stress-strain curves (elastic-plastic strain hardening) with yield strength values of 15,17 and 19 kbar and corresponding ultimate stress values of 17,19 and 21 kbar at a strain of 11 % (see fig.3). These data seem to be reasonable estimates and should cover the range from medium to high strength steels. A comparison with the experimental results allows a rough correlation of these dynamical material data with the statical data of the corresponding steel. Similar material models have been used already successfully for the simulation of kinetic energy steel penetrators into concrete structures /ref.2,3/.

4.COMPARISON OF SIMULATION RESULTS WITH EXPERIMENTS

The first part of the simulation consists of the determination of the loads onto the cap of the integrated barrier. As presented in section 3 this is done by an Eulerian simulation which accounts very well for the expansion of the detonation products of the precursor charge and its interaction with the integrated barrier.

The geometrical model is shown in fig.4. The Eulerian simulation was extended over a time range of 200 μ sec. As an example the expansion of the detonation products after 50 μ sec is shown in fig.5. The high explosive is already completely detonated and the detonation products expand due to high pressure gradients.

Typical pressure values as a function of time in front of the barrier cap are shown in fig.6. The

maximum value is about 550kbar with a duration of the pressure pulse of roughly 180 μ sec. The functional shape can be approximated by piecewise linear functions as indicated in fig.7. This approximation gives the input for the following Lagrange calculation.

The structural analysis of the integrated barrier has the two aims:

- selection of barrier material (low strength or high strength steel)
- optimization of geometrical design (wall thickness of barrier)

The first three calculations were done with wall thicknesses of 1.8, 1.2 and 0.9 mm and a dynamical yield strength of 15kbar (see fig.3). The calculation was extended over a time interval of 300 μ sec, which is significantly longer than the time of the acting pressure load.

The results are summarized in fig.8, which shows the integrated barrier (deformations) at the end of calculation. The 1.8mm barrier has no deformations, the 1.2mm barrier shows only small deformations at end of the cylindrical part and the 0.9mm barrier is strongly deformed in the transition region from cap to the cylindrical part.

The three barrier designs with different wall thicknesses were tested with a high strength steel of 11kbar static yield strength and 11% maximum plastic strain. The results were very promising because no deformations occurred even for the small wall thickness of 0.9mm (see fig.9).

To optimize the material selection (reducing the requirements for a high strength steel will reduce the production costs significantly) we tried to understand the influence of the material strength on the failure mechanism. Additional calculations with varying dynamical yield strength parameters from 15 to 19 kbar have been performed.

The results for the deformation at the end of calculation are shown in fig.10. The amount of deformation near the cap increases very strongly with decreasing yield strength. The 15kbar strength material gives rise to buckling-like collapse of the barrier cap.

For experimental verification 3 additional tests with different static yield strength parameters have been performed. The selected materials have the following specifications :

material	static yield strength kbar
high strength steel	11
C60	8
St52	6

The high strength and the C60 barrier are not deformed. Only the St52 barrier shows strong deformations near the transition from barrier cap to cylindrical part (see fig.11). It is very similar to symmetrical buckling obtained with thick tubes beyond the proportional limit.

These results lead to a rough correlation between the static and dynamical strength values for this load case :

static strength kbar	dynamical strength kbar
6-7	15
8-9	17
10-11	19

Taking into account the uncertainty concerning the correlation of static and dynamical parameters the agreement between simulation and experiment is good.

The combined computational and experimental approach leads thus, with a limited number of experiments to an optimized design for the blast shield.

5.SUMMARY

A combined computational experimental approach for the design of blast shield structures is presented. The numerical simulation is based on a two step concept :

Eulerian simulation for the determination of the pressure loads
structural analysis of the barrier with the loads from the first step.

Simulations with simple models (elastic plastic strain hardening model) give already good estimates for barrier designs that can be used for experimental testing. The yield strength data have been varied parametrically within a reasonable parameter range.

Correlating the experimental results with the material description gives the basis for further optimizations of the blast shield with respect to geometry and material. With only a few numbers of experiments it was possible to develop a barrier design that is optimized with respect to mass and protection capability.

6.REFERENCES

1. D. Matuska, J. Osborn, E. Piburn, Hull Documentation, OTI, Shalimar, Florida
2. E. Rottenkolber, N. Heider, Numerical Simulation of Runway Penetration, Proc. 10th Int. Symp. Ballistics, San Diego, 1987
3. N. Heider, 3-D Finite Element Impact Simulation on Concrete Structures, Proc. ASME Winter Annual Meeting, San Francisco, 1989

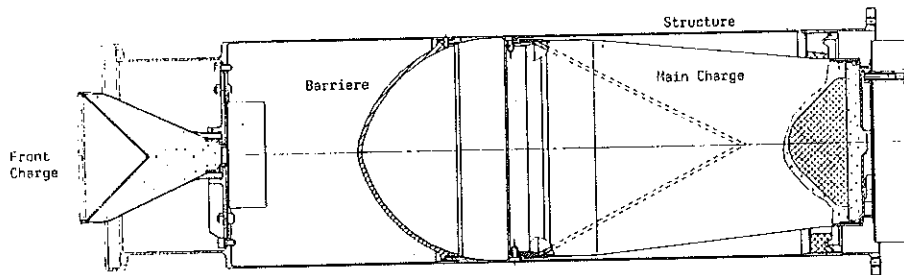


Fig. 1
Schematic Tandem System with Blast Shield

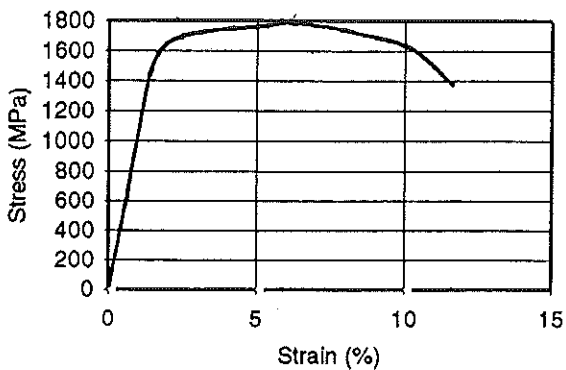


Fig. 2
Typical Experimental Stress Strain Diagram
for Dynamical Loading

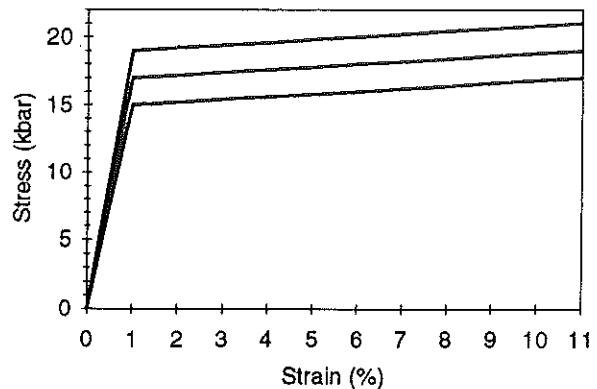


Fig. 3
Strength Parameters used for
the Structural Simulation

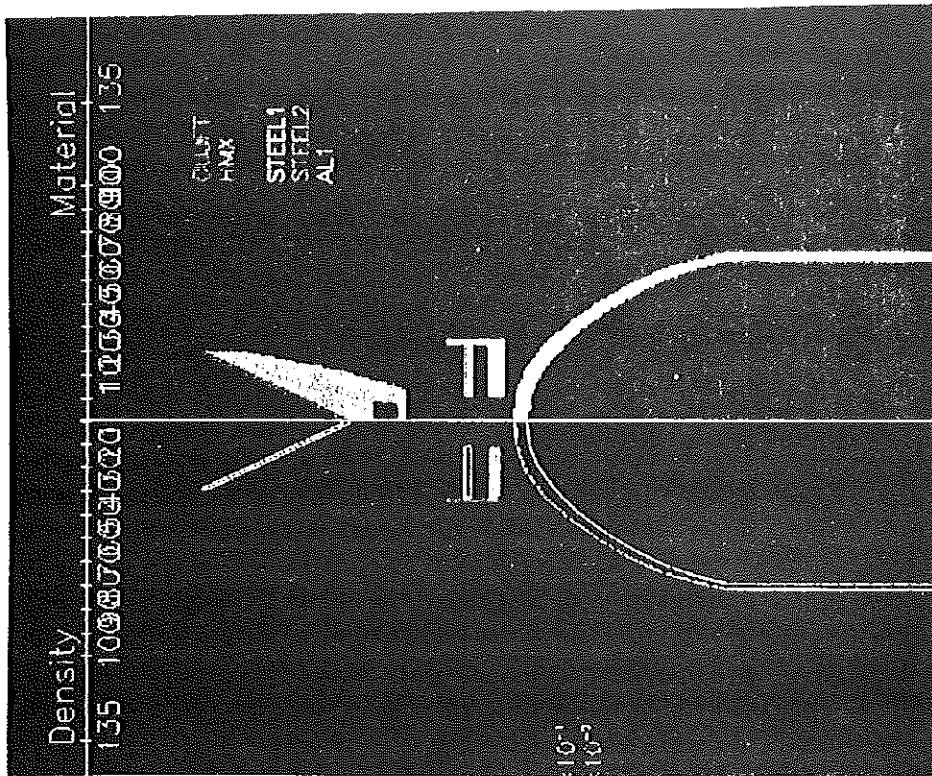


Fig. 4
Density and Pressure Plot at Time 0

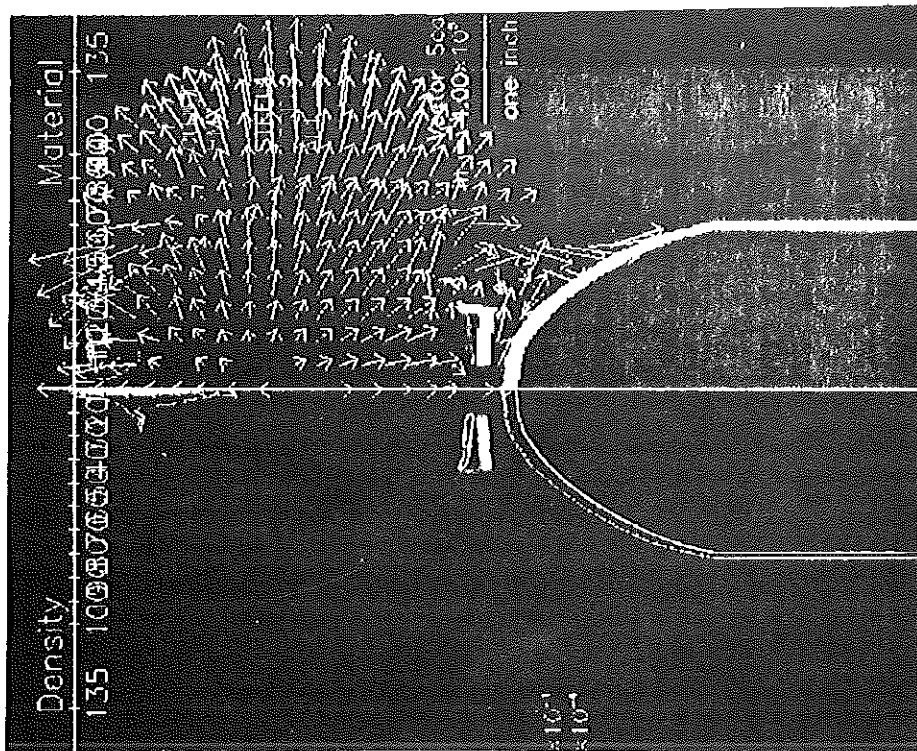


Fig. 5
Density and Pressure Plot at Time 50 us

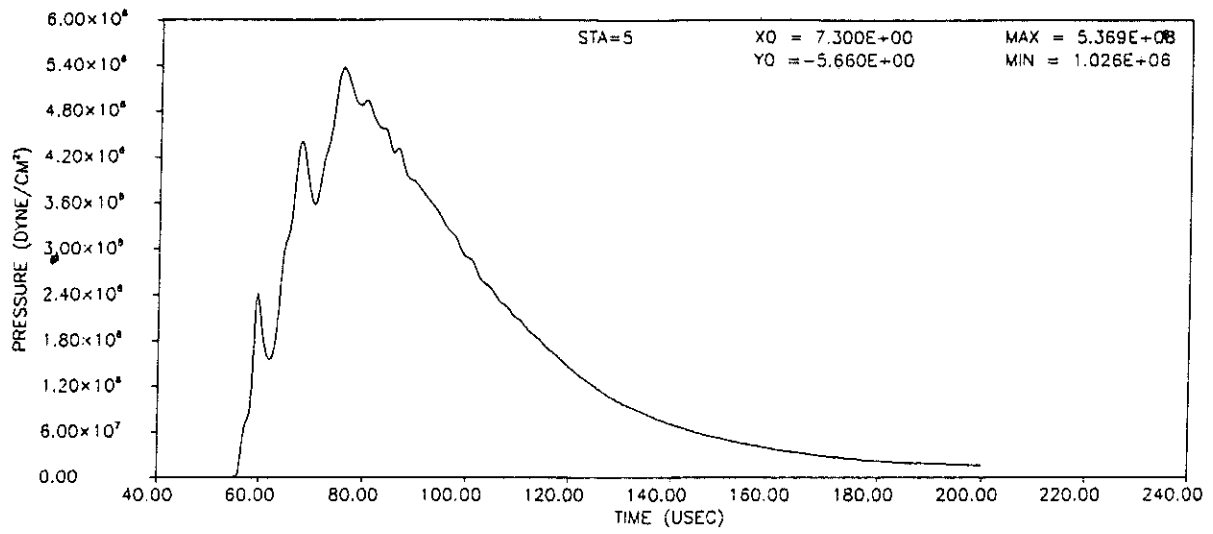


Fig. 6
 Pressure as a Function Time in Front of the Blast Shield

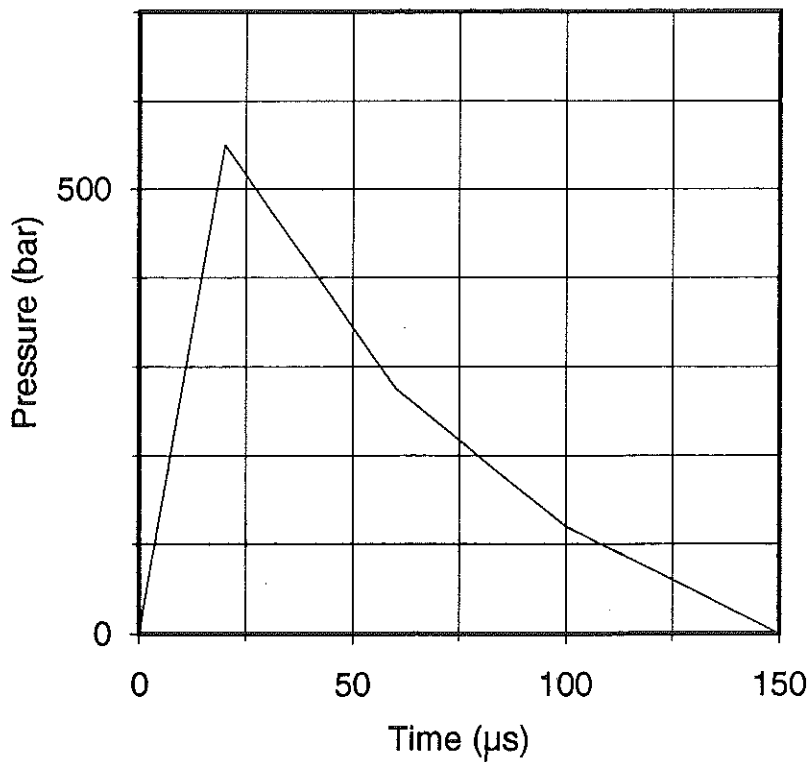


Fig. 7
 Load Case for the Structural Simulation

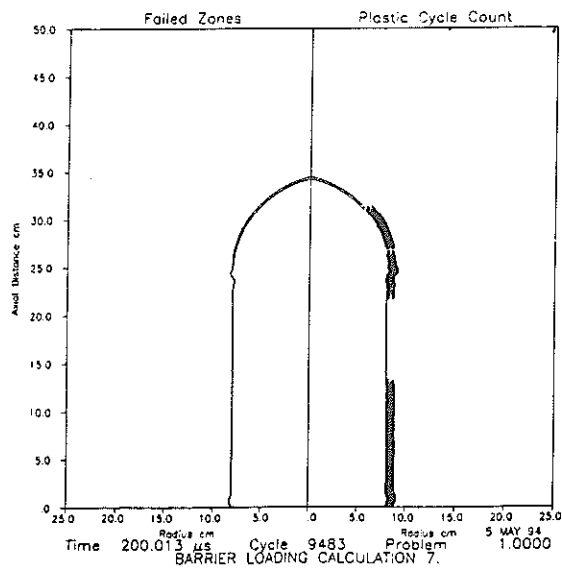
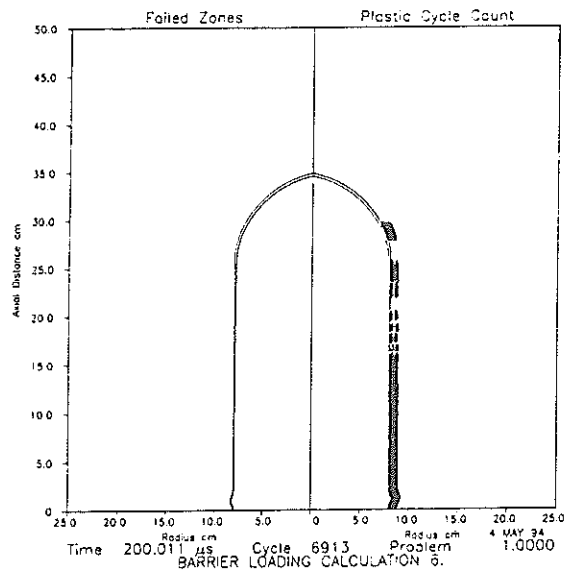
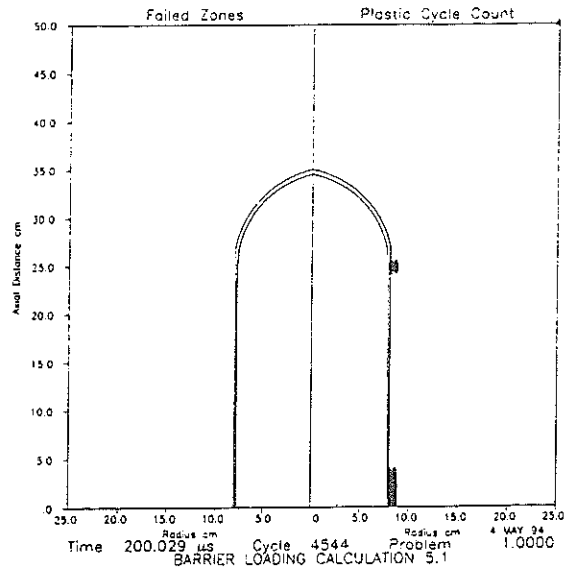


Fig. 8
Deformations of the Blast Shield (1.8mm, 1.2mm and 0.9mm Wall Thickness)

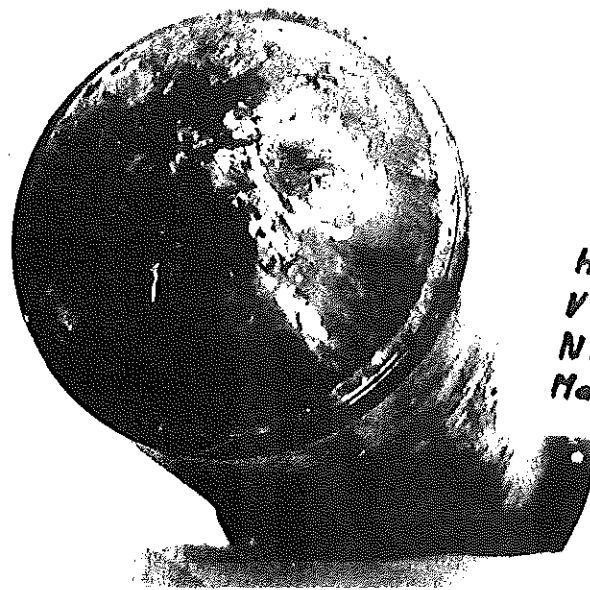
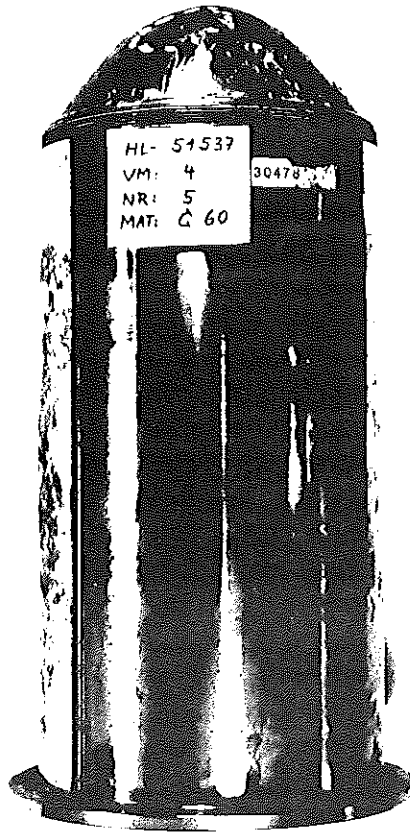


Fig. 9
Integrated Barrier after Test, Material High Strength Steel

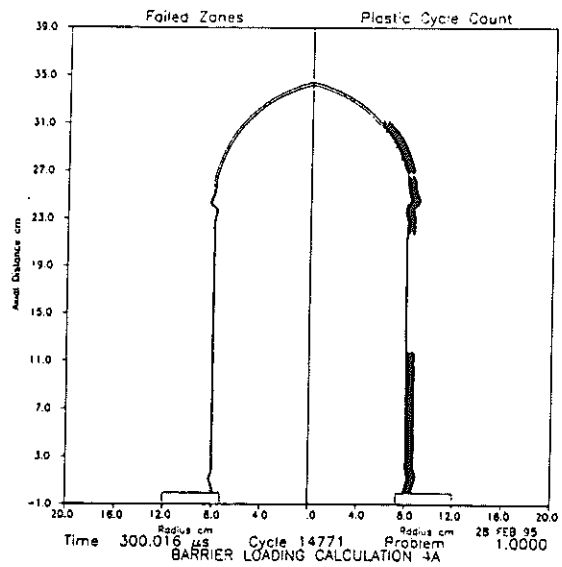
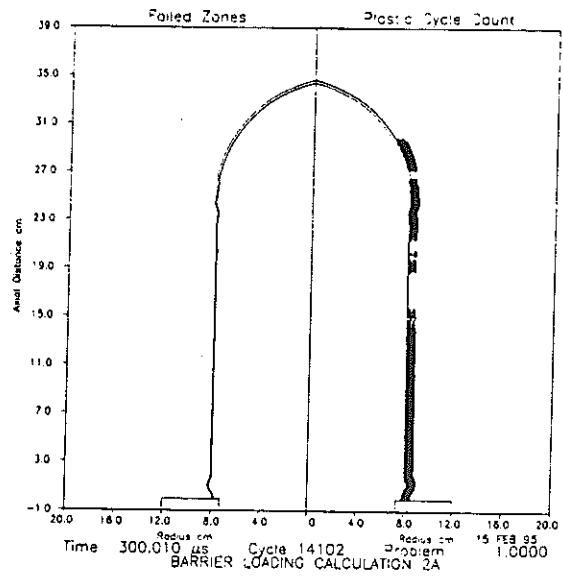
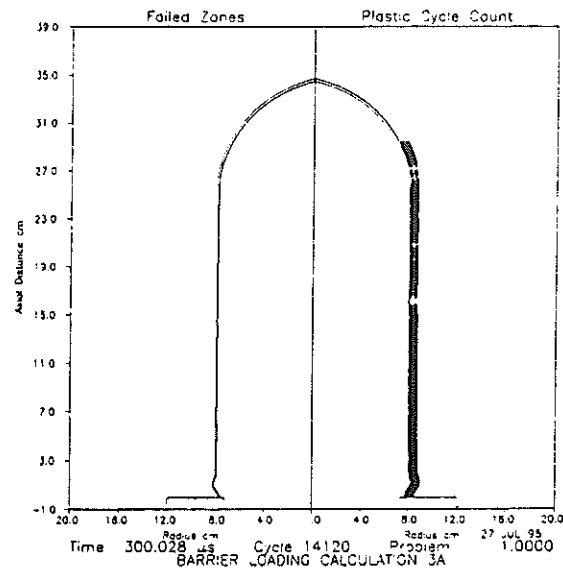


Fig. 10
Deformations of the Blast Shield (15kbar, 17kbar and 19kbar Yield Strength)

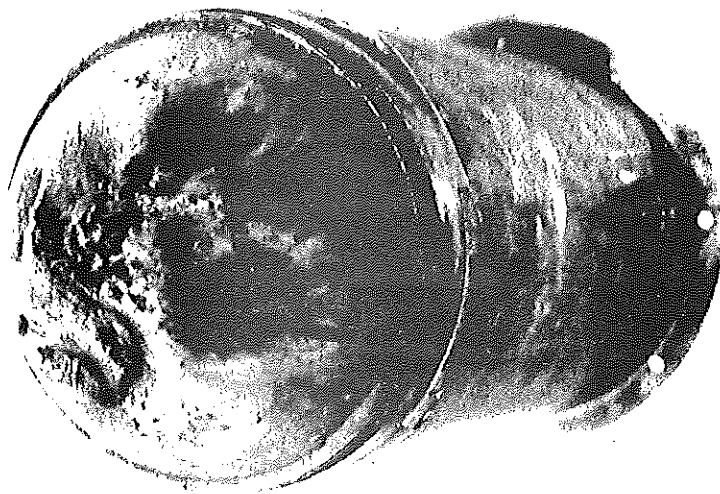
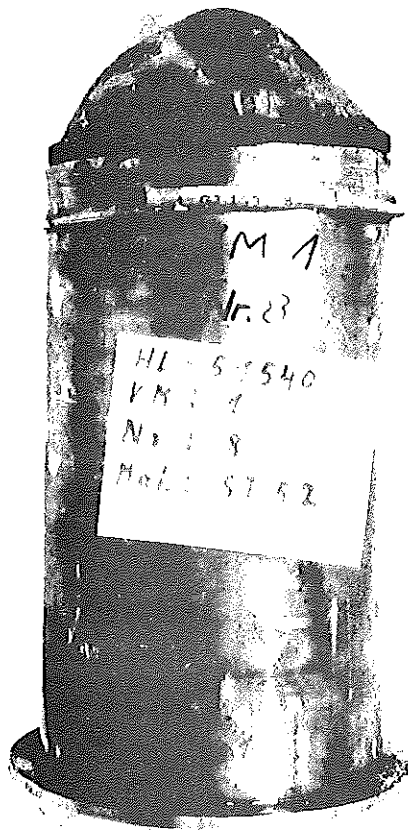


Fig. 11
Integrated Barrier after Test, Material St 52

A COMPUTATIONAL MODEL FOR CONCRETE STRUCTURES SUBJECTED TO HIGH PRESSURE AND HIGH STRAIN-RATES

Prof. Dr.-Ing. Dieter Kraus
Dipl.-Ing. Josef Roetzer

University of the Federal Armed Forces Munich
Department of Structural Engineering

Abstract:

A numerical method to calculate the behaviour of concrete structures due to high pressures and high strain rates will be presented. Stress and strain at these levels are possible by impact- or high explosive loads. For this reason the investigation of the constitutive equations had been done with fieldtests at concrete planes under contact charges. The detonation, producing a high velocity expansion of the gaseous detonation products, had been calculated in an Eulerian mesh. The concrete structure is modelled with a Lagrange mesh, which is deformed and distorted under the high instantaneous pressure pulse, produced by the detonation. Via a coupling of the Eulerian and the Lagrange mesh, the dynamic pressure pulse is imposed on the concrete. Numerical results are compared with recent executed fieldtests. The variation of fieldtests and the influence of material assumptions will be shown. For the calculations the program AUTODYN [1] was used.

1. Variation of impact velocity and behaviour of material

Form, duration and peak of an impact classifies the loading and the behaviour of the material. The impact velocity or the strain-rate often are used as criteria. The range up to 250 [m/s] is called low-velocity-regime. Those problems fall in the area of structural dynamics. Loading and response times are in the millisecond regime.

As the striking velocity increases up to 500 or 2000 [m/s] the constitutive equations become significant for the investigation of local failures.

By further increasing of the striking velocity up to 2000 or 3000 [m/s] the materials in the area of local failure behaves as a fluid. At ultra high velocities the colliding materials vaporize [7].

Experiments used for determining the dynamic material strength often are done with the Split-Hopkinson-Bar method. Thereby strain-rates due to 10^3 are reached for homogeneous materials and specimen diameters up to 20 mm. Due to the inhomogeneity of concrete greater specimen measurements are necessary [3], which are only possible for lower strain rates.

Event	Effect	Strain - Rate	
	explosive impact- colliding solids vaporized	greater 10^8	
contact charge 5000 MN/m^2 ↓ ↑ air plane collision gas explosion earth quake traffic	hydrodynamic - material compressibility not ignorable	10^8 to 10^4	lab test not possible
	fluid behavior in materials; pressures approach or exceed material strength; density a dominant parameter	10^6 to 10^4	
	viscous-material strength still significant	10^4 to 10^2	lab test possible
	primarily plastic primarily elastic some local plasticity	10^0 to 10^2 less 10^0	

Figure 1: Classification of the response of the material

In structural dynamics it is usual to consider the dynamic strength with enhancement factors. The determination of the loading normally is separated from the behaviour of the structure, this is called uncoupled calculation.

These method is not longer applicabile, because:

- the deformation and demolition of the structure influences the peak and propagation of the loading significantly
- the strain-rate reaches an order of magnitude where no enhancement factors are available
- the material description must include the variation of density.

Because of these requirements an investigation of the constitutive equations in a lab is not possible. Fieldtests with high explosive charges on concrete slabs have been done and the constitutive equations had been researched with the help of numerical calculations in combination with parametric variation.

2. Spatial and temporal representation

The used Hydrocode solves the problem setup with a coupled Euler-Lagrange formulation based on the Finite-Difference-Method. At each timestep the state of equilibrium and the conservation of mass, impulse and energy are satisfied. In the Euler formulation the mesh is unmoveable located in the space and the medium moves through it. The pressure propagation is calculated with the Jones-Wilkins-Lee equation [1]. In the Lagrange formulation the mesh, which represents the concrete structure, will be deformed and distorted under an impact. With the Euler-Lagrange-Interaction, the pressure calculated in the Euler mesh will be imposed on the structure, described by the Lagrange mesh.

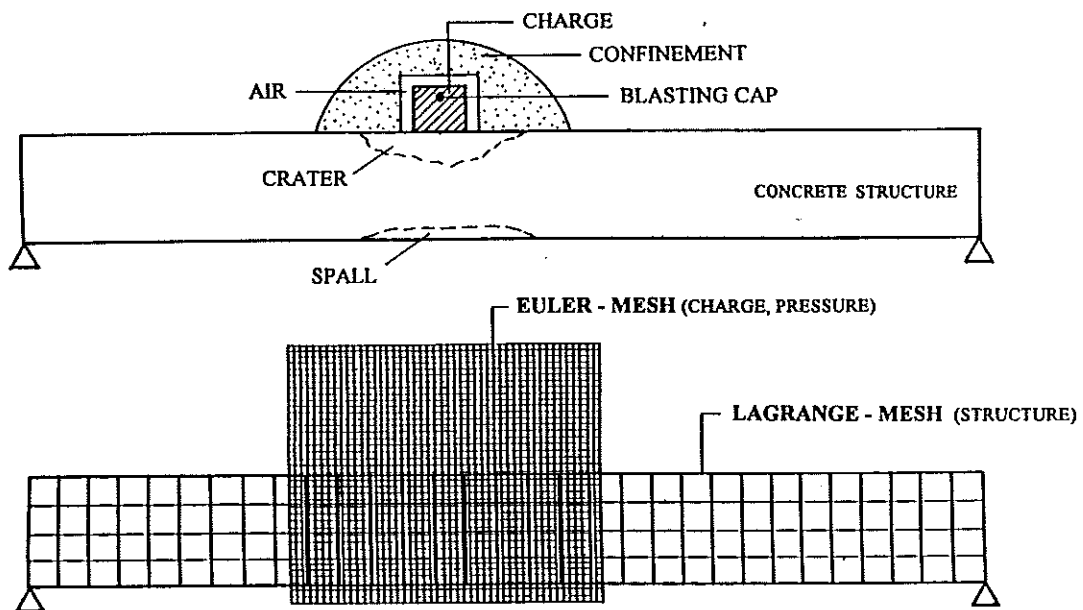


Figure 2: Testspecimen and Euler-Lagrange-Interaktion

An expanding shock wave is characterized by a great pressure gradient in a small temporal and local area. To describe these situation a very small size of the Euler-mesh becomes necessary. The size is taken so small, that the highest occurring pressure reaches at least 50 % of the Chapman-Jouquet-Pressure [1]. The size of a Lagrange element is chosen four times the size of an Euler element. With an appropriate size of the timestep numerical stability, energy conservation and the description of the wave propagation can be obtained [4].

3. Constitutive Equations

Recent calculations for concrete structures show pressures in the range of 5.0 GPa (5000 MN/m²) and strain rates up to $4.0 \cdot 10^4$ - $8.0 \cdot 10^4$ [1/s]. For this range of pressure and strain rates the classical material descriptions are not appropriate.

For an sufficient description it is necessary to divide the stresses and strains into a hydrostatic and a deviatoric part. The relation between the hydrostatic pressure and the volumetric strain is called Equation of State EOS (see fig. 3).

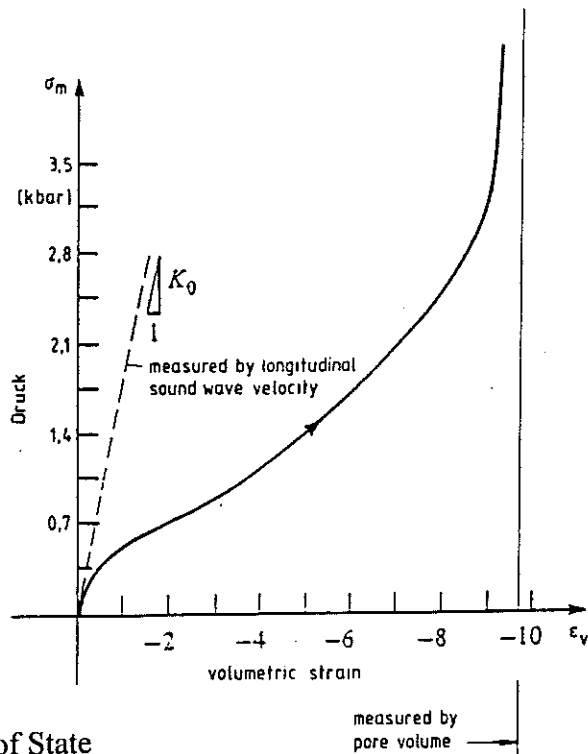


Figure 3: Equation of State

The deviatoric part is determining the strength of the materials. The failure is described by exceeding the hydrodynamic tensile limit and/or the maximum plastic distortions.

Fig. 4 and 5 show the three-dimensional failure of concrete including strain hardening. The two curves in fig. 5 show the tensile and the compressive meridian, two characteristic cross-sections through the body of fig. 4. This curves may be simplified by a modified Drucker-Prager flow condition. The results in fig 5 are obtained by static tests.

Plastic flow occurs when a certain stress combination reaches the Drucker-Prager-Limit. The calculation of the plastic deformation applies the radial-return method [6]. The stressvector is projected perpendicular to the hydrostatic axis.

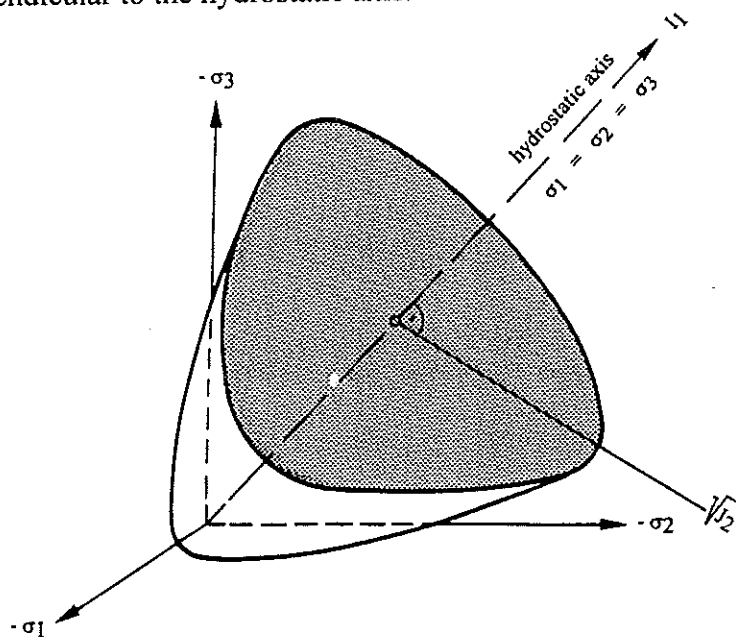


Figure 4: Threedimensional strength of concrete

This corresponds to a flow rule with constant volume. With this rule it is not possible to describe the dilatation, which is not an essential restriction for concrete.

The material failure is described by plastic distortions. The relative brittle tensile failure of concrete will be described sufficiently with the Hydrodynamic Tensile Limit (see condition 3 in figure 6). A bilinear description is used for the reinforcement.

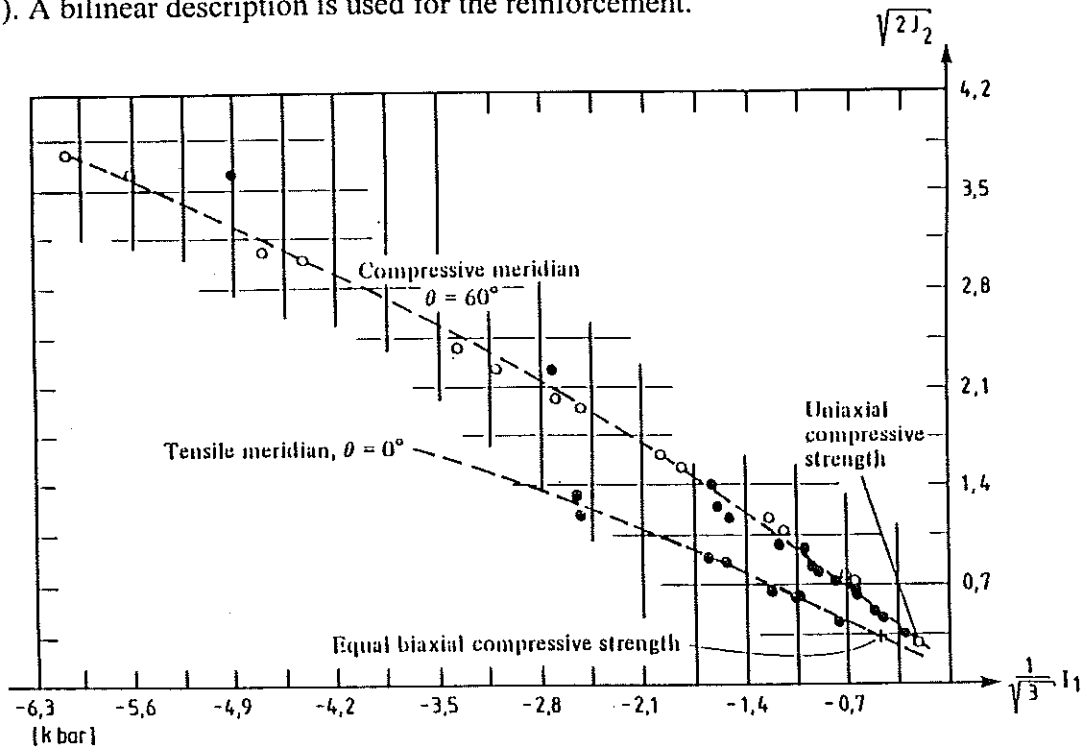


Figure 5: Threedimensional strength of concrete due to Chen [2]

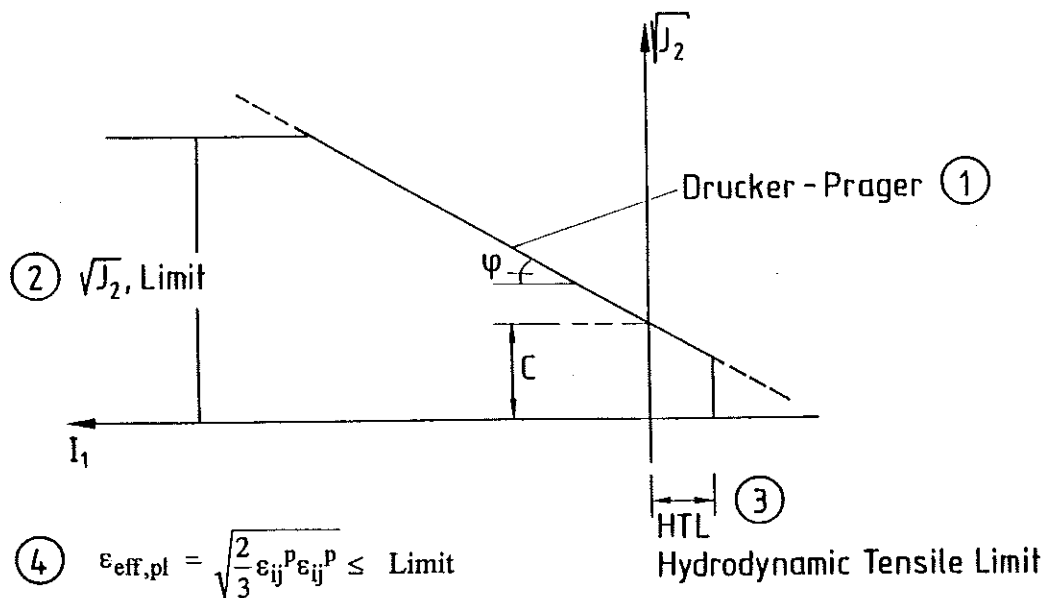


Figure 6: Criteria for elastic-plastic flow and failure

4. Comparison of calculation and fieldtests

The used constitutive equations are investigated with respect to its utility by comparison the crater volume and spall volume from calculation with fieldtests. For each series three tests under the same boundary conditions (size, strength, reinforcement, amount of high explosive, confinement) had been executed.

The test specimen consists of a slab with the dimensions 2.0 x 2.0 x 0.3 m and a concrete compressive strength of $f_{c,k} = 40 \text{ MN/m}^2$. It had a reinforcement made of 16 mm bars in a distance of 150 mm. The experimental set up is shown in fig. 7.

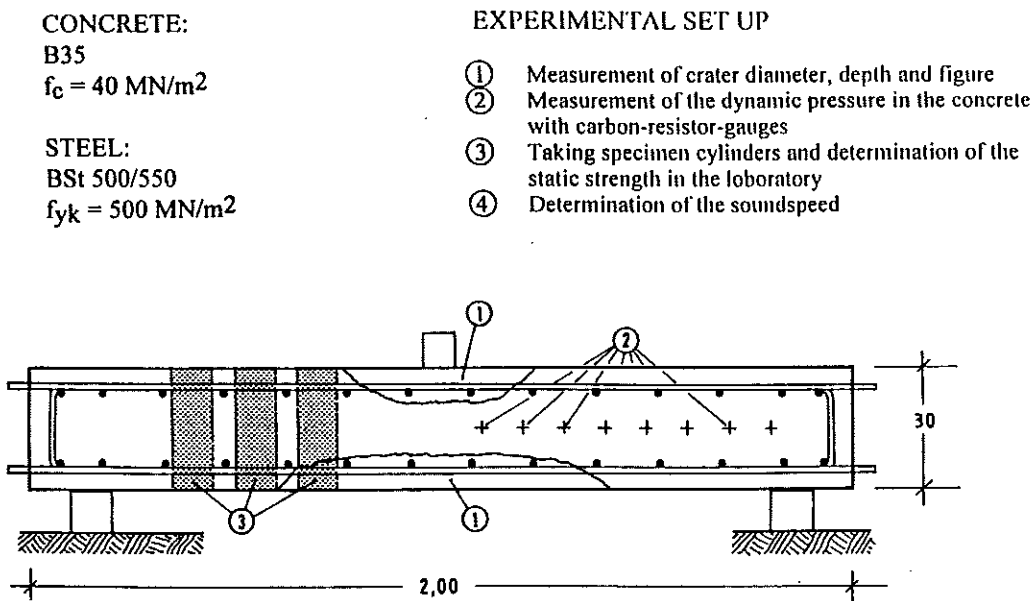


Figure 7: Experimental set up with steel reinforced concrete slab and the explosive charge positioned on the top of the slab

Explosive masses of 0.5 and 1.0 kg PETN with a density of $1.5 \text{ [g/cm}^3\text{]}$ were used. The charge was formed as a cube, positioned at the center of the slab. At two of the four testseries the explosive was covered by sand bags to simulate confined conditions.

From every concrete slab samples were taken to investigate the density, porosity, longitudinal sound wave speed and strength. The density of the concrete was $2.44 \pm 0.03 \text{ [g/cm}^3\text{]}$. The average pore content was 8.3 %, resulting in a theoretical maximum density of $2.66 \text{ [g/cm}^3\text{]}$. The measured longitudinal sound wave velocity was $4272 \pm 63 \text{ [m/s]}$, which leads to a bulk modulus $K_0 = 22200 \text{ [MN/m}^2\text{]}$. The Equation of State contains the results of these investigations.

The variation of the crater and spall for 0.5 kg PETN confined is shown in figure 8. Unconfined tests vary stronger with the spall, confined tests with the size of the crater.

Figure 9 shows the variation of the calculation results and the fieldtests.

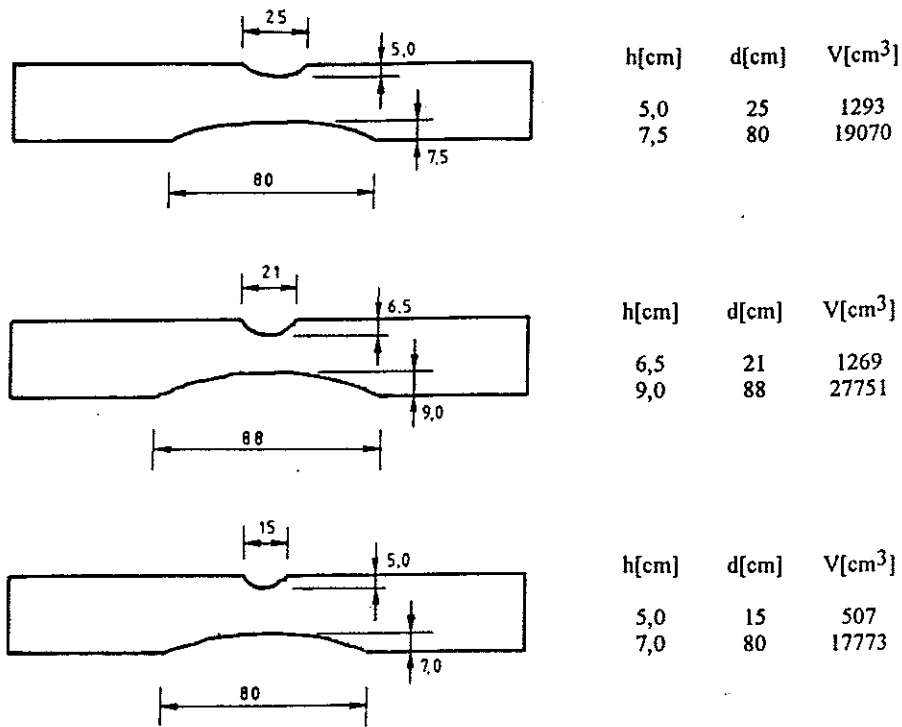


Figure 8: Variation of the crater and spall for 0.5 kg PETN confined

The following results may be concluded:

- the calculation method is suitable for investigations in the range of hydrodynamic material behaviour
- the hydrodynamic tensile limit of concrete had been found as 5 to 10 times the value of the static tensile strength

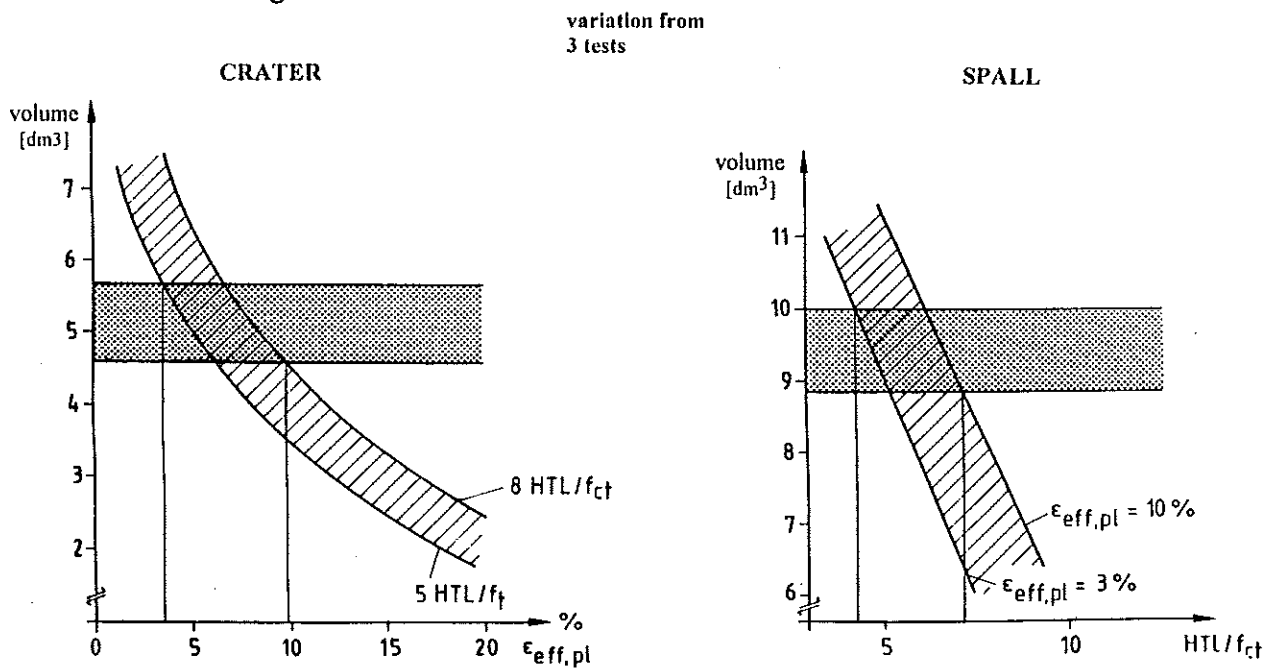


Figure 9: Results of fieldtest and calculation

- the equivalent plastic strain had been found in a range of 5 to 10 %; static values are in a range of 0.1 to 0.5 %
- with these strength parameters and significant assumptions for the EOS a good agreement between tests and calculation had been obtained.

6. References

- [1] AUTODYN TM, Software for Non-Linear Dynamics, Century Dynamics Incorporated, Users Manual, Oakland 1989.
- [2] Chen, W.F.: Plasticity in Reinforced Concrete. Mc Graw-Hill: 1982.
- [3] Eibl, J., Ivanyi G.: Studie zum Trag- und Verformungsverhalten von Stahlbeton. Heft 260 des DAfStb. Ernst & Sohn, Berlin 1976.
- [4] Kraus, D.; Roetzer, J.; Thoma, K.: The Effect of High Explosive Detonations on Concrete Structures. Post-SMIRT Impact IV Symposium, August 1993 Berlin, in Nuclear Engineering and Design 150 (1994) Seite 309 - 314.
- [5] Roetzer, J.: Stoffgesetz für Beton unter hohem Druck und hohen Dehnungsgeschwindigkeiten. Ph. D., Universität der Bundeswehr München, to be published.
- [6] Wilkins, M. L.: Calculation of elastic-plastic flow. UCRL-7322 Lawrence Livermore Laboratory 1981.
- [7] Zukas, J.A.: Impact Dynamics. John Wiley & Sons, New York: 1982.

Influence of specimen dimensions and metal density in Taylor impact tests

C.H. Nguyen

Swiss Federal Laboratories for Materials Testing and Research (EMPA),
Ueberlandstrasse 129, CH-8600 Dübendorf, Switzerland

Abstract

Reverse Taylor tests were performed at same impact velocity of about 220 m/s, with two different specimen sizes and using three pure metals of different densities, in order to study their influence in the Taylor's formulation for flow stress. The test results obtained seemed to be independent of the specimen geometry, as it is normally assumed. However, shear rupture was additionally observed, only on some specimens with the biggest size, tending to prove that the ratio of diameter to length in the Taylor specimens might be an important parameter. The cause of this shear rupture was showed, particularly in the case of titanium, to be due to adiabatic shear banding. Because of the same impact velocity for these tests, material density should play an important role; firstly as a separate term in the stress formulation and secondly in changing the ratio obtained of final to initial specimen length.

INTRODUCTION

The independancy of the specimen geometry in the results from Taylor tests is normally assumed [eg. 1], which is expressed in the well known Taylor's formulation for flow stress:

$$\sigma_{fl} = \frac{\rho_0 \cdot V_0^2}{2 \cdot \ln(L_f/L_0)} \quad (1)$$

where V_0 is the impact test velocity, ρ_0 is the initial specimen material density, L_f and L_0 are the final and initial specimen length, respectively.

From this formulation depending on three variables, it might be interesting to study the influence of the specimen dimensions and also the metal density in the impact tests. These parameters are important, not only for the tests themselves but also for any possible correlation to an impact between two structure components.

EXPERIMENTAL PROCEDURE

The Taylor tests were executed in the *reverse* manner using the apparatus at EMPA, where a rigid disk made of maraging steel was shot against the long cylindrical metal specimen, to crush its tip while reducing its length. The 30 mm in diameter disk was ballistically driven by means of an aluminum sabot. Test

specimens were manufactured in two different sizes, a 4 mm diameter, 40 mm length and a 6 mm diameter, 50 mm length. They were made of three pure metals of different densities: aluminum (99.7%), titanium (ASTM-Grade 2) and copper (OF). These tests were conducted at room temperature with the same optimized impact energy corresponding to an impact velocity of about 220 m/s, which was then taken as a *constant* in the Taylor's formulation for flow stress from Eq. (1).

EXPERIMENTAL RESULTS

Figure 1 shows typical examples of the results obtained from these reverse Taylor tests for the two specimen sizes and the three specimen materials. One can notice that the crushing of all the specimens tested was not so great, due to the relatively low impact velocity particularly for the reverse test mode.

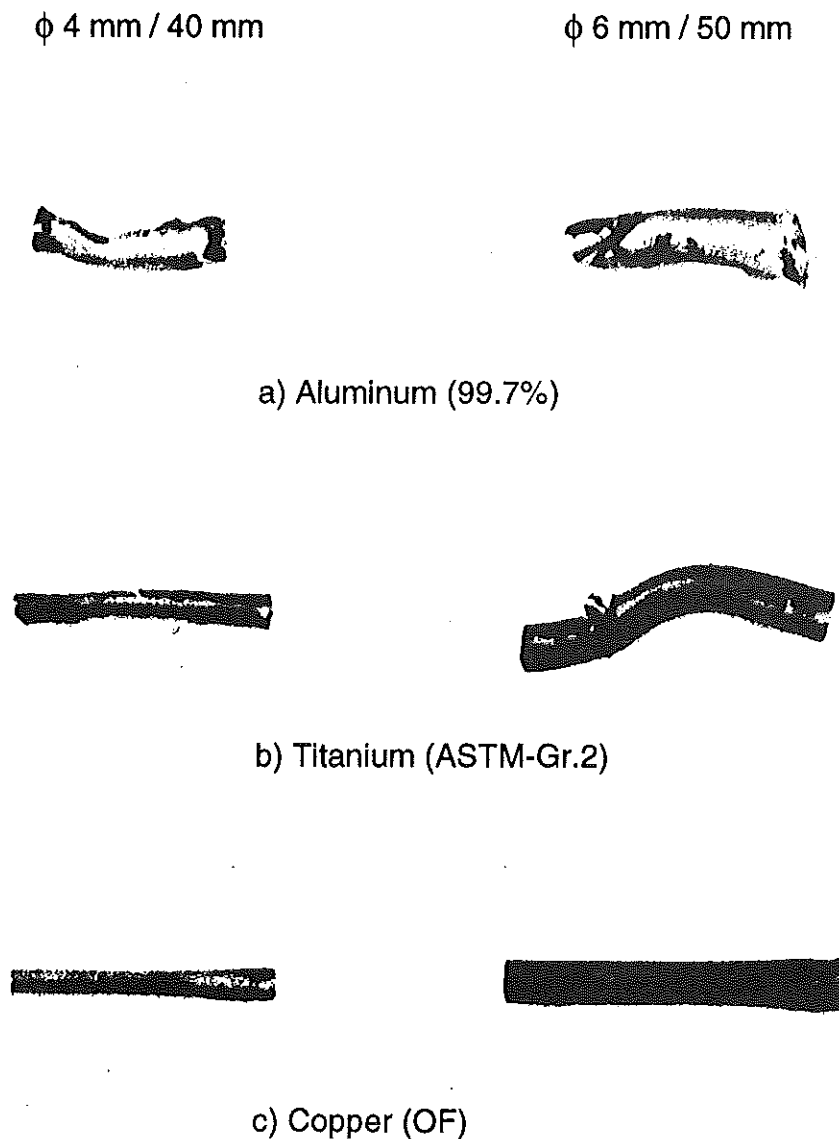


Fig. 1: Results from the reverse Taylor tests at about 220 m/s for two specimen sizes and three specimen materials.

Buckling was also observed on some tested specimens. For both the specimen sizes, the final specimen dimensions after these impact tests were measured and compared to their initial dimensions (Table 1). The corresponding flow stress values for the three specimen materials could then be calculated from these measurements using Eq. 1.

Table 1:

Comparison between initial and final dimensions obtained with the three metals and for the two specimen geometries used in reverse Taylor impact tests at about 220 m/s, together with calculated corresponding flow stress values.

Specimen dimension	Parameter	Aluminum (99.7%)	Titanium (ASTM-Gr2)	Copper (OF)
	ρ_0 (g/cm ³)	2.7	4.6	8.9
Φ4mm/40mm	L_f (mm)	(26)	36.5	36.1
	L_f / L_0 (-)	(0.65)	0.91	0.90
	σ_{fl} (MPa)	(-150)	-1180	-2050
	Φ_f (mm)	(7.1)	5.0	5.0
	Φ_f / Φ_0 (-)	(1.75)	1.25	1.25
Φ6mm/50mm	L_f (mm)	31.1*	(43)*	45.6
	L_f / L_0 (-)	0.62*	(0.86)*	0.91
	σ_{fl} (MPa)	-140*	(-740)*	-2290
	Φ_f (mm)	11.1*	7.3*	7.7
	Φ_f / Φ_0 (-)	1.85*	1.22*	1.28

() approximated values
surfaces

* associated with shear rupture

For all three metals tested, almost the same values, between the two specimen geometries, were obtained for the ratios of final to initial lengths and diameters. The length ratios were used for the calculation of the corresponding material flow stresses. These results thus supported the common assumption that the Taylor test results are independent of the specimen *length*.

However, the flow stress values, which were calculated from these dimension measurements, were different and even quite far away from the values quoted in the literature on the Taylor tests (for the same materials but with different

Furthermore, as listed in Table 1, the values obtained for ratios of final to initial specimen lengths varied with the specimen *material density*, from about 0.9 for Cu down to about 0.6 for Al (because of the same impact velocity for the tests). The material density has therefore an additional influence, in supplement to the direct effect of ρ in the calculation using Eq. 1 of the flow stress values for the three metals tested. This might be an explanation to the much higher difference in the values obtained between Cu and Al, when being compared to other impact resistance values obtained on the split Hopkinson pressure bar with the same materials [2], after correction due to differences in the strain rate levels.

CONCLUSIONS

The experimental results supported the common assumption that the Taylor test results are, for every specimen material, independent of the specimen length. However, the specimen ratio of diameter to length might be an important parameter in the Taylor test, particularly for determining if additional shear rupture occurs in the specimens. For tests executed at a same impact velocity level, the specimen material density could have a very great influence in the scattering of the test results. The Taylor's formulation for flow stress might thus be not so accurate because of its high sensitivity to the specimen parameters, particularly when compared with the split Hopkinson pressure bar method.

References

1. M.L. Wilkins and M. W. Guinan, J. Appl. Phys., 44, 3 (1973) 1200.
2. C.H. Nguyen, in: A. Bakker (ed.), Book of Abstracts ICM 7, The Hague, 1995.

FABRICATION AND CHARACTERIZATION OF QUASI-ISENTROPIC RAMP WAVE GENERATORS : A NEW GENERATION OF MIVAR

F. LLORCA, Commissariat à l'Energie Atomique, Centre d'Etudes de Vaujours-Moronvilliers, BP 7
77181 Courtry - FRANCE

F. BLEIN, Commissariat à l'Energie Atomique, Centre d'Etudes de Bruyères-Le-Châtel, BP 12
91680 Bruyères-Le-Châtel - FRANCE

ABSTRACT

A ramp wave is generated into a material when it is impacted by a graded-density material such as MIVAR. The thermodynamic loading path observed is then an off Hugoniot's curve so called quasi-isentropic compression. This particular loading can give access to a new region of Equation of State surface while other applications may concern elastoplastic behaviour of materials and damage effects. Realized since 1989, the graded density material, MIVAR, is composed of three parts : a low density front face in order to minimize the input shock state in the target, a smoothly graded density section to create the compressive ramp wave and a massive high-density substructure to hold the final pressure state. Its design has been recently redefined and improved. The first generation of MIVAR was fabricated by plasma spraying technology : a mixture of four constituents (polyethylen, Al, Cu and W) was deposited on a massive denal plate. Now, a band-casting technique for low-density organic layers (RTV) is used in conjunction with plasma spray method (mixing of only two materials Al and W). The high-density substructure is also plasma sprayed. This general process is well adapted according to the specifications given by the shock physics specialists. Dynamic experiments made on Cu-c2 and Al 6061-T6 (through particle velocity and longitudinal stress measurements) have shown up a ramp duration of several microseconds. The first input shock has also been drastically reduced by the organic layers. Negative ballistic effects, such as spalling of MIVAR, are eliminated thanks to the improved adhesive capabilities and homogeneity properties which characterize this new impactor. Furthermore, a hydrodynamic model, based on a Hopkins-Murnaghan approach, is proposed and has been validated by experiment/calculation comparisons. This model takes into account the main characteristics of the new MIVAR and particularly its initial porosity due to plasma spraying technique.

I. INTRODUCTION

Shock loading experiments give access to high pressure, temperatures and strain rate in the domain of the dynamic behaviour of materials. A classical shock wave is defined as the end state of the propagation of a thermodynamic discontinuity in a sample. When a graded density material (figure 1) is launched against a target, a ramp wave is induced by successive reflected compression waves of growing pressure amplitudes (figure 2). The most infinitesimal are these increments, the most isentropic is the loading path in the material (figure 3). So, the accumulation of low amplitude shock waves creates a quasi-isentropic shock loading.

This particular loading is generally characterised by three parameters (see figure 4):

- the amplitude of the initial shock wave P_i , governed by the impedance mismatch between the target material and the first layers of the impactor,
- the rise time T_i and the final peak of pressure P_f which are related to the thickness of the impactor, the shock impedance of its layers and the target material.

While the strain rate induced under shock-loading is controlled by the material viscosity, under quasi-isentropic loading it depends on the properties of the launched graded density impactor (thickness,

constituents...). For shock-loadings and quasi-isentropic compressions, the internal energy change in the material is the sum of the compressive energy, the plastic and viscous works. Since the strain rates are lower for quasi-isentropic loading, internal energy change due to plastic work will be similar in each case. Therefore, for high thermodynamic states, quasi-isentropic compressions allow access to domains of material dynamic behaviour that no classical shock loading experiment permits to attain (low temperature and strain rate, high compressibility). Moreover, the corresponding rise-time allows to follow the thermodynamic state of the target during its compression which is not really possible with classical shock impacts.

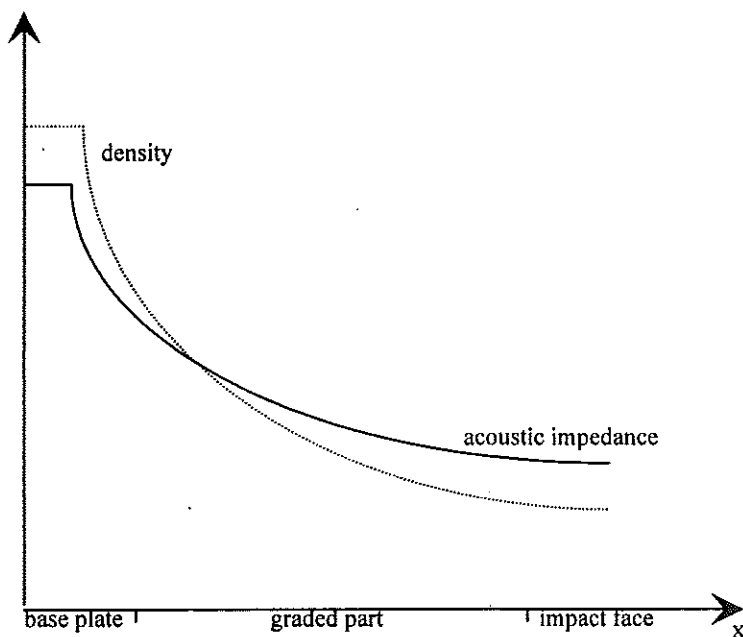


Figure 1. Density and corresponding shock impedance of a graded density impactor.

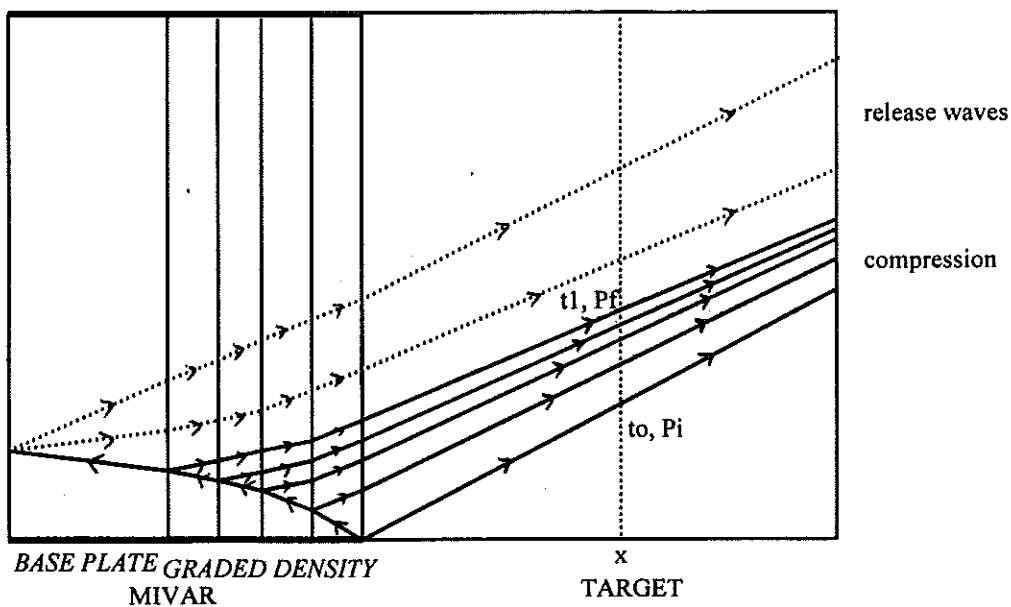


Figure 2. Distance-time diagram.

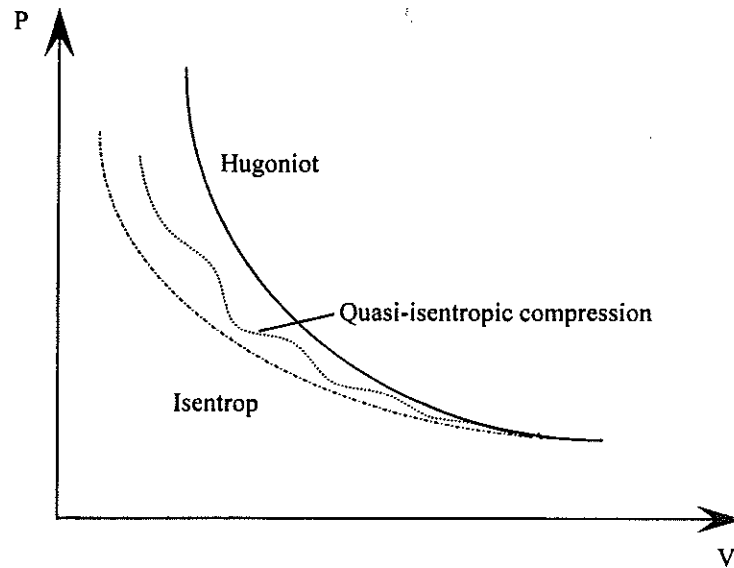


Figure 3. Hugoniot, Isentrop and quasi-isentropic compression in (P-v).

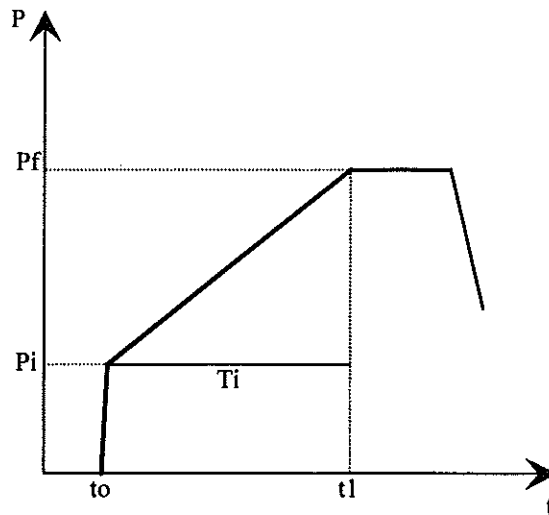


Figure 4. Stress-time history of the quasi-isentropic loading.

II. A PARTICULAR RAMP WAVE GENERATOR : THE MIVAR

Since the end of the 1970's, there has been a considerable amount of research in this field [1-2-3-4]. The MIVAR (in french *Matériau Impédance Variable*) is an optimized smooth graded density material. It has first been developed at the CEG by M. Perez and al [5-6].

The MIVAR is a composite material. Its composition is a function of the thickness ; this principle permits to create a smooth profile of density. The mixture was originally deposited on a denal or a tungsten plate by plasma spraying. This technique was invented in the 1950's and used in industry for melting and forming coatings of metals and ceramics. The process involves the introduction of powdered materials into a hot and high velocity flame of a plasma gun. The powders are melted and propelled into a target plate (see figure 5). The first generation was a four constituents (polyethylen, aluminum, copper, tungsten). With such materials, distinguished by their very different projecting characteristics, the final properties of homogeneity, isotropy and adhesion were unsatisfactory. The

aluminum, copper, tungsten). With such materials, distinguished by their very different spraying characteristics, the final properties of homogeneity, isotropy and adhesion were unsatisfactory. The principal consequences of these problems concerned the mechanical resistance to spallation during the ballistic stages of experiments. To solve these restricting effects, the design has been modified since 1992 and optimized. The present generation of MIVAR (produced at CEA) is a simplified three constituents impactor constituted of RTV (organic material), aluminum and tungsten. The figure 6 presents a schematic representation of the new configuration of MIVAR. Thank to its structure, the impactor introduces in the target a soft shock wave followed by a linear ramp of pressure. The massive substructure (called the base plate) withstands the loading generated into the material. The next table presents the principal characteristics for the three parts of the MIVAR.

	constituents	manufacturing technology	profile of density	thickness (mm)
base plate	W	plasma spraying	constant density : 17.4	2.7
graded part	Al + W	plasma spraying	parabolic : from 2.1 to 17.4	4.5
organic layers	RTV + Al	band - casting (see figure 7)	linear : from 1.01 to 2.1	1 or 2

Table 1. Characteristics of the MIVAR.

CEA has settered an original spraying process under neutral gaz at ambient atmosphere. This procedure allows to obtain high thermal flows for the plasma but also generates porosity into layers of the MIVAR. To illustrate this major influence, figure 8 shows the diagram representing the theoretical and measured profiles of density. The determination of the thickness and mass of each layer is realised comparing samples of a single layer elaborated with the same spraying parameters. The density of the base plate is that of the projected tungsten (17.4) while the first strates of the impact face has a density of 1.01. This parameter has a significant influence concerning hydrodynamic properties : at the same impact velocity, the rise time increases (the plastic wave celerity C_0 decreases) while the final pressure level decreases.

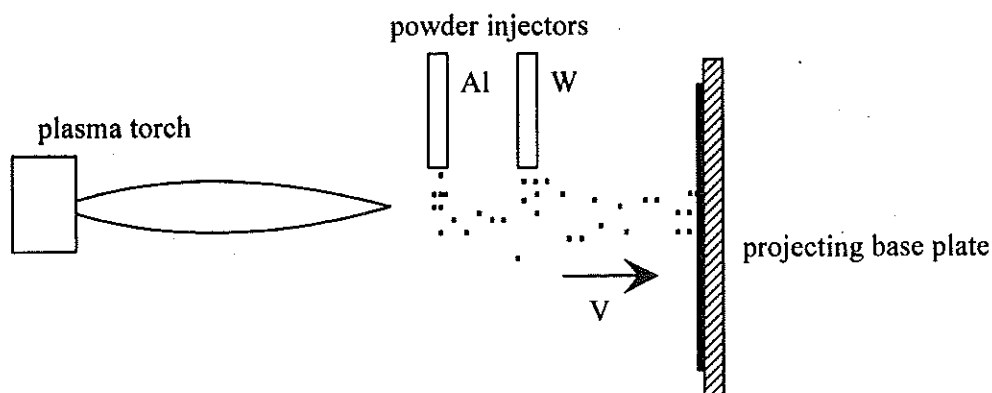


Figure 5. The plasma spray technique.

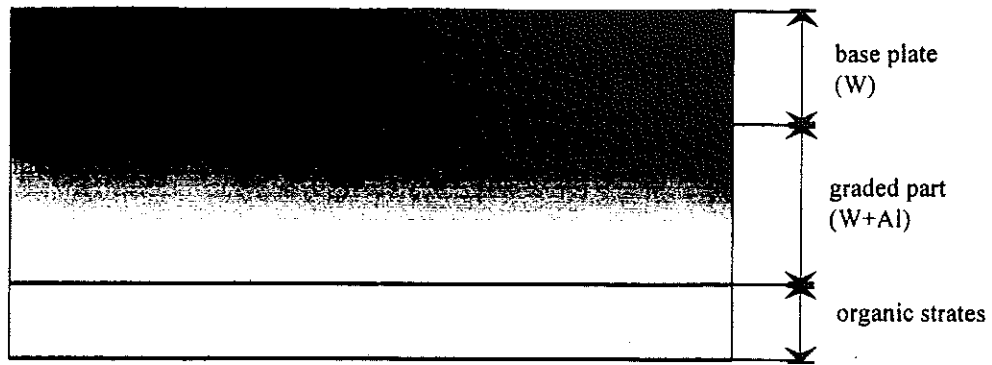


Figure 6. A schematic representation of the MIVAR.

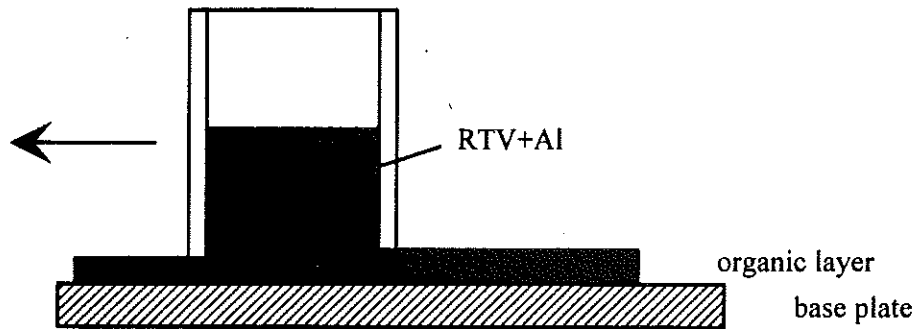


Figure 7. The band-casting technique.

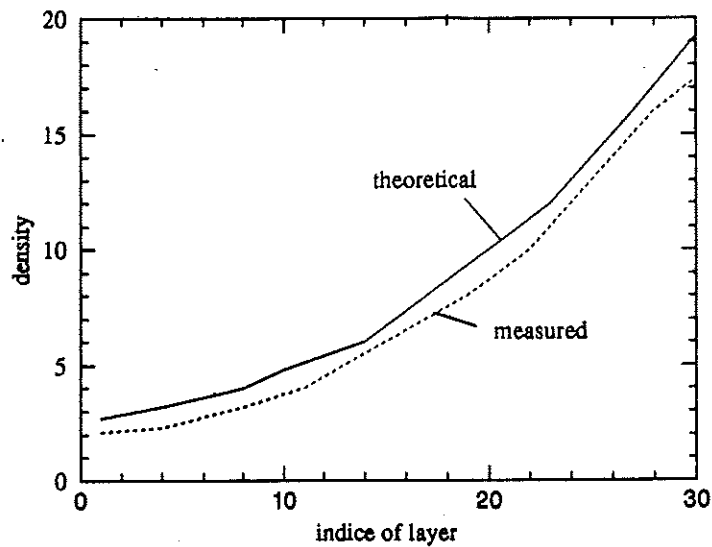


Figure 8. Diagram of the theoretical and measured profiles of density (in the graded part).

Statistical measurements show that the reproductibility and the homogeneity of the impactors are improved ; this point is very important to expect repetitive experiments and to simulate the applied shock loading with a numerical code. In conclusion, this composite material is an optimized ramp

wave generator. Its manufacturing principle permits to redefine its parameters (thickness, diameter,...) according to the requirements or constraints concerning the experimental tests.

III. DYNAMIC QUALIFICATION

In order to evaluate the dynamic capabilities of these ramp wave generators, we proceed to impact experiments. Two experimental configurations are proposed and indicated in figure 9. Two powder guns, 60 mm and 90 mm diameter, are used to launch projectiles which have a facing of a MIVAR backed by copper. When the projectile impacts a target sample, several measurements systems are involved. Pressure is measured with manganin gauges (config. 1) and the projectile and the interface LiF-sample velocities are measured by means of an Interferometric Doppler Laser system (config. 2). Next table shows the main characteristics of the four shots and the corresponding experimental results are included in figures 10 and 11.

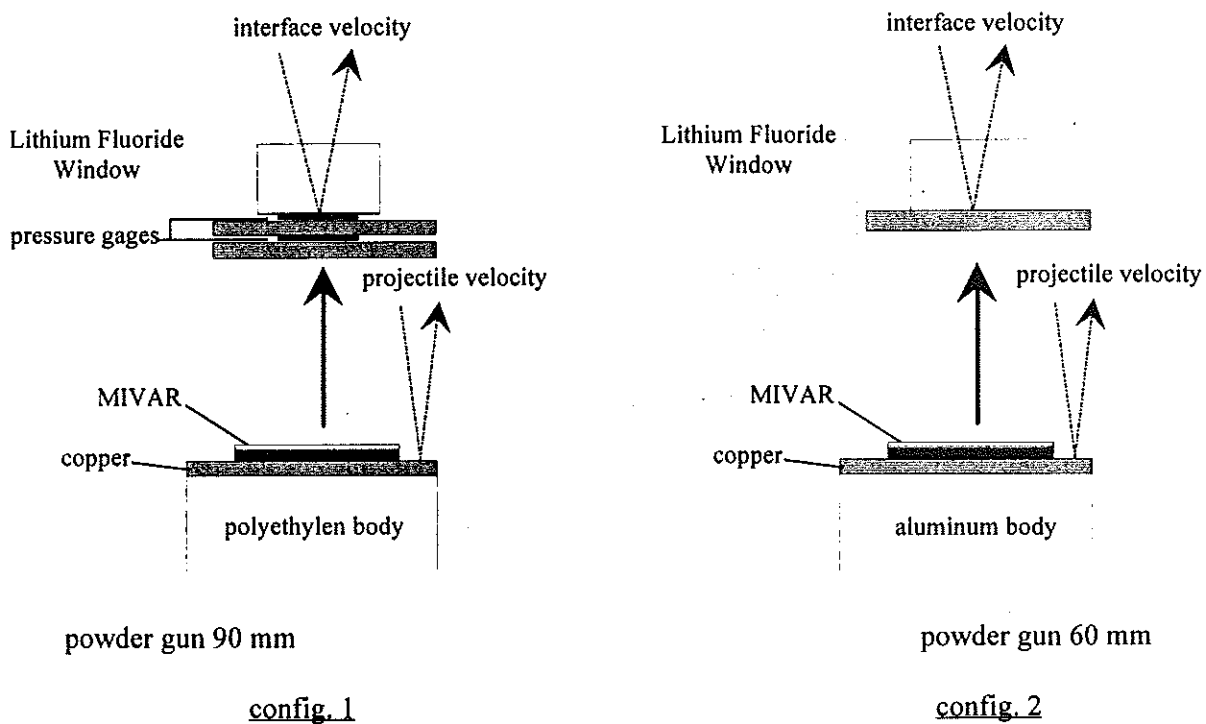


Figure 9. Experimental configurations used for impacts with MIVAR projectiles.

Shot n°	target	configuration	impact velocity (m/s)	remarks
3094	Al 6061-T6	1	864	Lithium Fluorure window
3194	Al 6061-T6	1	876	Al 6061-T6 "window"
876	Cu-c2	2	460	MIVAR without organic strates
877	Cu-c2	2	481	MIVAR with organic strates

Table 2. Characteristics of the shots.

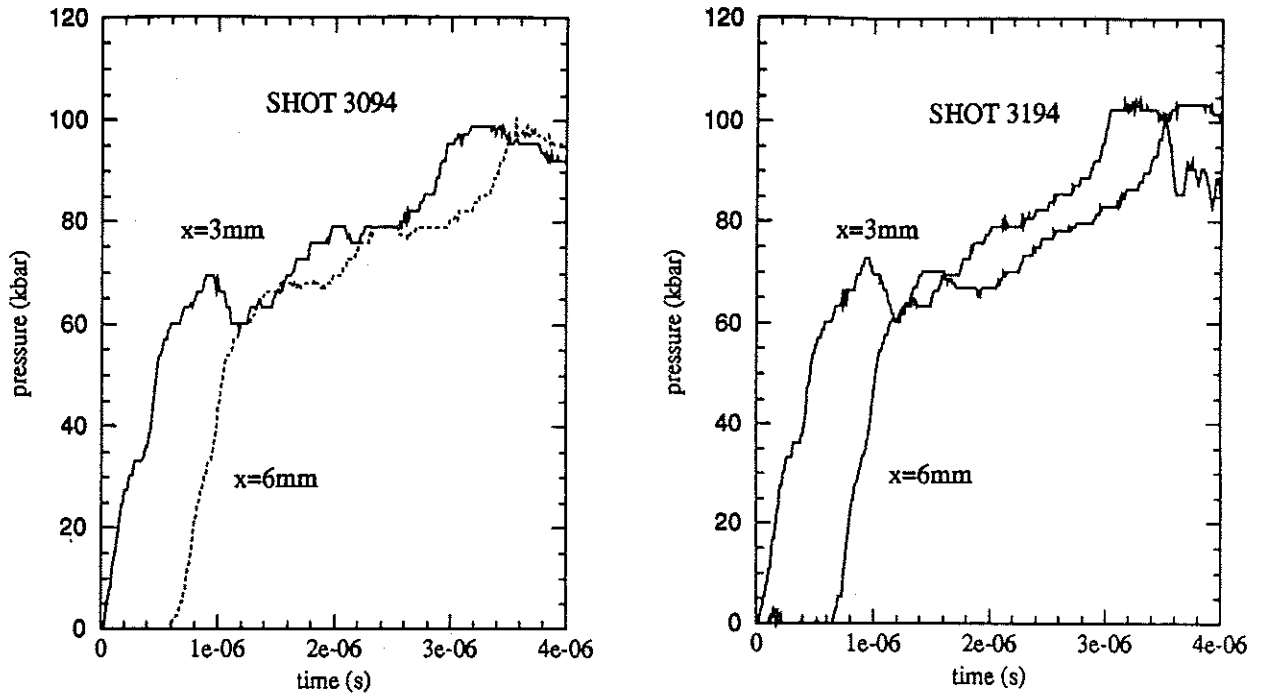


Figure 10. Pressure levels measured at two locations in configuration 1.

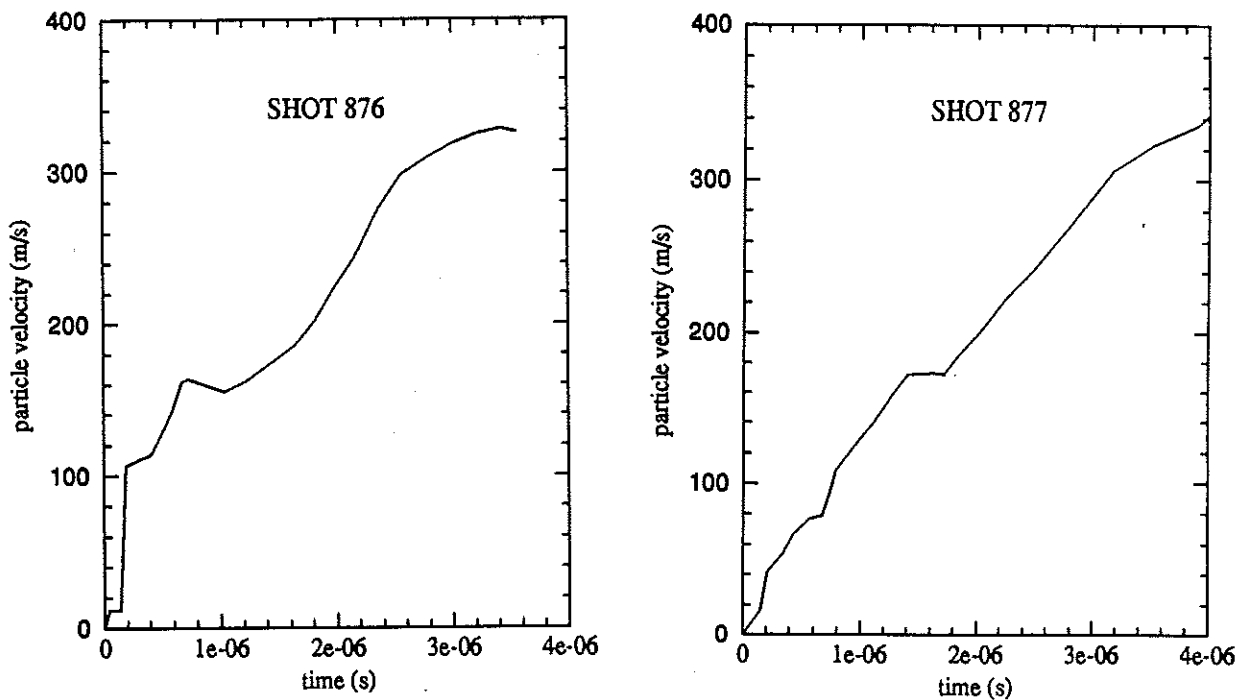


Figure 11. Interface particle velocity histories measured in configuration 2.

For shots 3094 and 3194, the experimental results reveal clean ramp waves. Comparison between the two experiments show up the perfect impedance adaptation between LiF and Al. The time rise of the loading is the same (about $3 \mu\text{s}$) and corresponds to a final pressure level of 100 kbar. During the build up of pressure, perturbation events appear. Next paragraph will show that we can relate these phenomenons to release waves generated when the compressive waves propagate through the gauges. When only interface particle velocities are observed (shots 876 and 877), the signals reveal correct ramp waves. These last ones are not entirely measured because, after $3 \mu\text{s}$ or $4 \mu\text{s}$, shock waves reach the free surface of the LiF window ; from this time, the evolution of the Doppler corrective coefficient is unknown. Influence of the organic strates upon the first shock is evident : in shot 877,

All these parameters are identified for the constituents projected by plasma spraying. Figure 12 shows the Hugoniot of each material constituent of the MIVAR. These data take into account the porosity because of the density of the studied samples ($W : 16.3, 17.4\dots$). The comparison between the experimental and numerical results obtained with a model based on an optimized mixture of the properties of the massive and porous materials is presented in figures 13 and 14. A good agreement is observed on both signals of particle velocity and pressure. One can see that the large disturbance observed at mid-amplitude of the experimental pressure signal is reproduced when pressure gauges are simulated (with polyethylen thickness). This result confirms the assumptions expressed in section III.

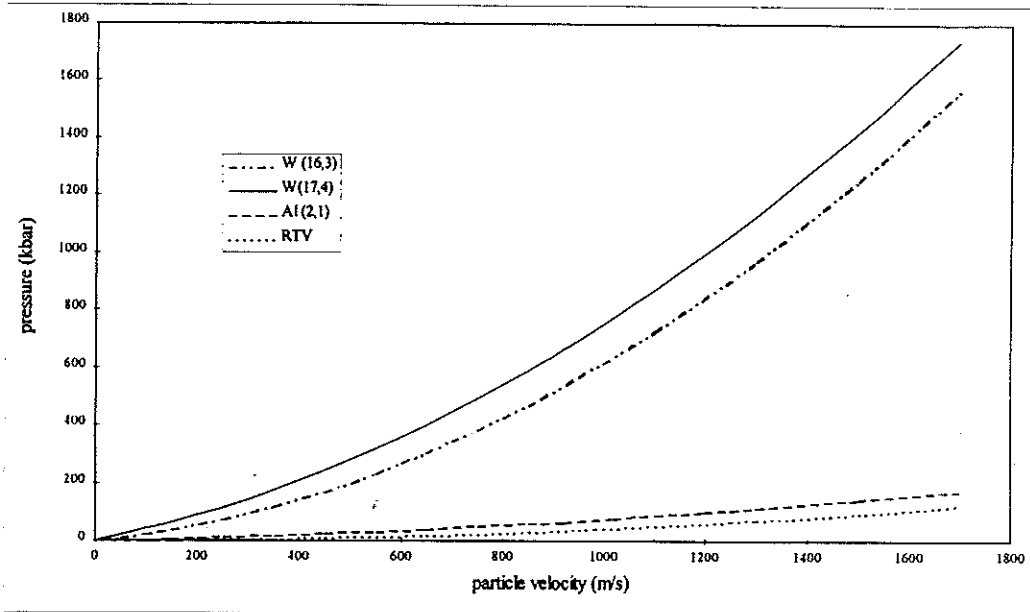


Figure 12. Hugoniot adiabat of the material constituents of MIVAR.

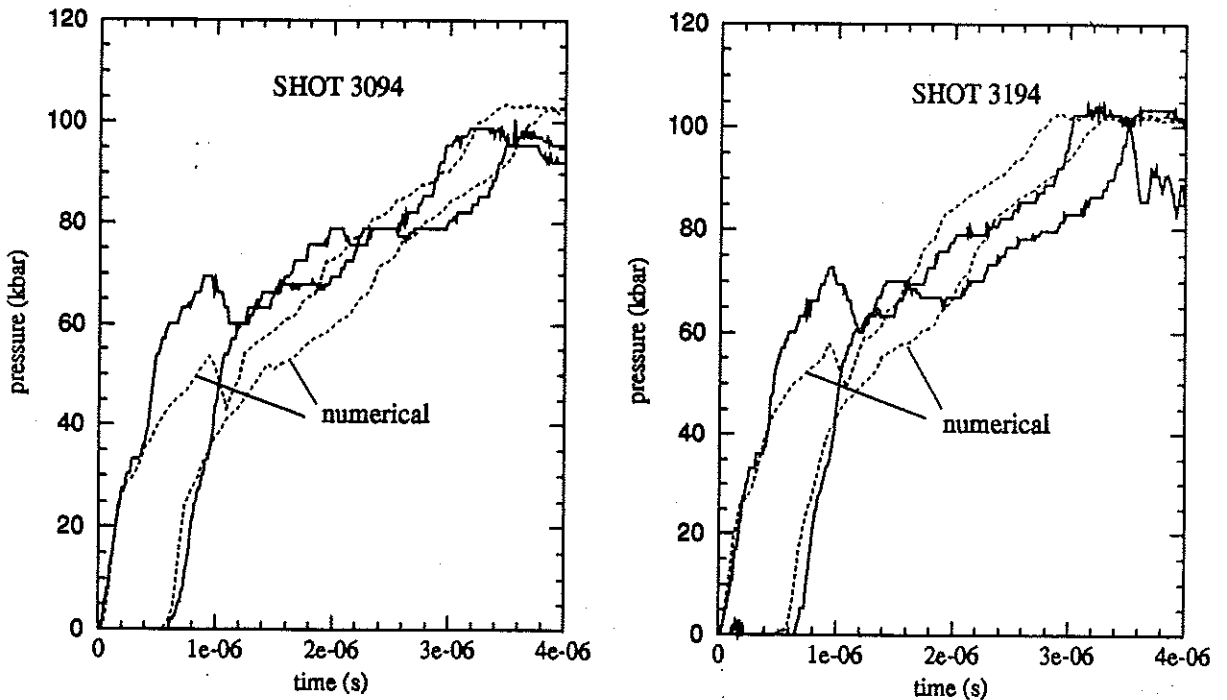


Figure 13. Comparison between numerical and experimental results. Time histories of pressure at two locations in the target.

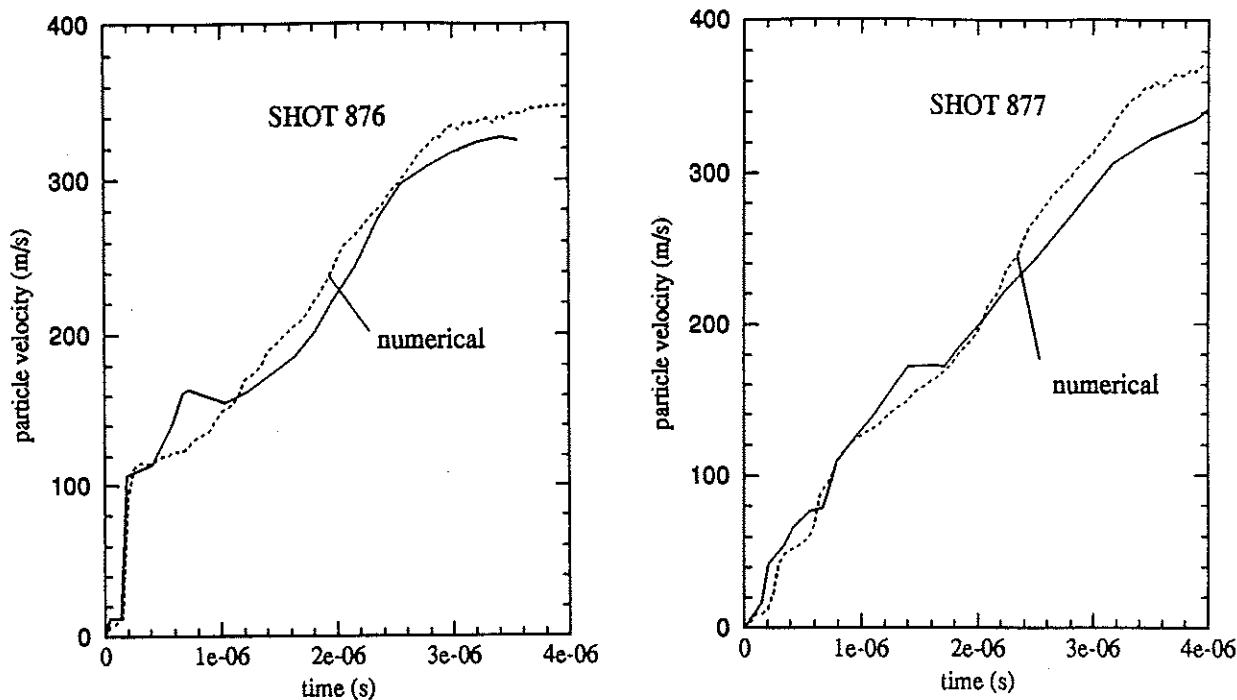


Figure 14. Comparison between numerical and experimental particle velocity profiles.

V. CONCLUSION

An optimized MIVAR has been performed using plasma spraying and band-casting technologies. This new principle allows to obtain impactors with improved properties such as homogeneity, isotropy and adhesion. The experimental data observed during impact experiments prove that integrity of these materials are conserved during the ballistic stages and the main characteristics of the generated loading are well-dimensionned. The simulation of the dynamic behaviour of these ramp wave generators, which needs the experimental evaluation of the Hugoniot of each constituent, provides an accurate representation of the shot results. All the major elements are now available to prepare further experimental investigations. That means set up original experiments to observe interesting properties of materials under quasi-isentropic compressions (off-Hugoniot dynamic behaviour, elastoplasticity for strain rates about 10^4 s^{-1} , 10^5 s^{-1} ,...).

REFERENCES

- [1] V.V. MATVEEV, V.V. PRUT, K.K. KHRABOV
"Conversion of Red Phosphorus to Black Phosphorus in Quasiisentropic Compression", *Soviet Tech. Phys. Letter*, 4, pp 221-222, 1978.
- [2] G.A. LYSENGA, T.J. AHRENS
"One-Dimensional Isentropic Compression", *Shock Waves in Condensed Matter*, pp 231-235, 1981.
- [3] M. GERMAIN-LACOUR, M. DE GLINIASTY
"Ramp-Wave Generators Studies", *Shock Waves in Condensed Matter*, pp 481-485, 1982.
- [4] L.M. BARKER
"High-Pressure Quasi-Isentropic Impact Experiments", *Shock Waves in Condensed Matter*, pp 217-224, 1984.
- [5] M. PEREZ
"Qualification of a Ramp-Wave Generator", *Journal de Physique*, 9, pp C3-713-719, 1988.
- [6] M. PEREZ
"Further Developments of the MIVAR Ramp-Wave Generator", *High Dynamic Pressure*, pp 61-68, 1989.

- utilisation de Abaqus.
- contact ponctuel? - surface? (comme de mise en forme).
- impact

NON-LINEAR DYNAMIC ANALYSIS OF FRICTIONAL CONTACT BETWEEN SHELL STRUCTURES

Denis AUBRY, Christian VAILHEN, Bernhard DRESSLER, Damien LUCAS
 LMSS-MAT, C.N.R.S. U.R.A. n° 850
 École Centrale de Paris
 Grande Voie des Vignes - F-92295 Chatenay-Malabry Cédex - FRANCE

Abstract

A formulation for dynamic frictional contact and impact problems between shell structures taking into account geometrical and material non-linearities is presented. The resulting non-linear system is consistently linearized in the framework of an implicit Newmark scheme. The elasto-plastic constitutive model is formulated entirely in stress resultants. A generalized Ivanov yield surface accounting for isotropic hardening is chosen for implementation. Friction and contact are studied in a continuum setting first. Subsequent linearization on the exact surface leads to consistent tangent operators. This behavior is then stored into symmetric interface elements. An efficient spatial contact search algorithm is also proposed.

1 Introduction

This study is part of a project for the development of an object-oriented experimental finite element code [11]. The aim is to create a flexible environment for the implementation of new mechanical and numerical models in the framework of research at our laboratory. The object-oriented approach is particularly well-suited for this purpose since it provides a maximum of modularity, reusability and reliability for a multi-programmer community.

Dynamic frictional impact of shells is one of the major problems in sheet metal forming or crash simulation. In this paper we present a total lagrangian formulation accounting for large displacements/rotations, and elasto-plastic material behavior. The implicit Newmark solution scheme allows large time steps preferably in the field of low/medium velocity applications demanding high accuracy.

In Section 2, the shell theory background is described and inserted in the dynamic principle of virtual work. Section 3 outlines the stress-resultant constitutive law, and section 4 gives an account of the mechanical model of dynamic frictional contact and its numerical implementation, in particular the contact search algorithm.

2 Principle of Virtual Work

The problem is formulated for two shells initially in Ω_{A_p} , where $A = 1, 2$, with current and reference configurations Ω_{A_x} , and Ω_{A_ξ} where $\xi = \{\xi^\alpha, \xi^3\}$, $\alpha = 1, 2$. Nevertheless, the implementation is also valid for self-contact or multibody problems. Contact occurs on parts of the exterior surfaces $\Gamma_{A_x} \subset \partial\Omega_{A_x}$. The tangent linear mapping from Ω_{A_p} to Ω_{A_x} is \mathbf{F}_A . The half

thicknesses of the shells are noted ζ_A . Assuming a Mindlin kinematic, the independent unknowns are the mid-surface displacement and the rotation vector, respectively $\mathbf{u}_{0A}(t)$ and $\boldsymbol{\theta}_A(t)$, with t the time parameter, and their first and second time derivatives $(\dot{\mathbf{u}}_{0A}, \dot{\boldsymbol{\theta}}_A)$ and $(\ddot{\mathbf{u}}_{0A}, \ddot{\boldsymbol{\theta}}_A)$. A suitable virtual displacement inspired from the real displacement structure is chosen:

$$\mathbf{w}_A = \delta \mathbf{u}_{0A} - \zeta_A \mathbf{R}_A(\boldsymbol{\theta}_A) (\mathbf{d}_{p_A} \wedge \delta \boldsymbol{\theta}_A)$$

where $\mathbf{R}_A(\boldsymbol{\theta}_A)$ is the rotation matrix of \mathbf{d}_{p_A} , the initial director at p_A . Denoting ρ_{p_A} and J_{p_A} the surface density and inertia, $(\mathbf{N}_A, \mathbf{M}_A, \mathbf{Q}_A)$ the Piola-Kirchhoff resultants and $(\mathbf{E}_{N_A}, \mathbf{E}_{B_A}, \mathbf{E}_{S_A})$ the conjugate Green-Lagrange strains, $(\mathbf{R}_{n_A}, \mathbf{M}_{n_A})$ and $(\mathbf{R}_{T_A}, \mathbf{M}_{T_A})$ the contact and friction stress resultants, the principle of virtual work is expressed on the initial configuration for each body A as:

$$G_{A,inert} + G_{A,int} = G_{A,ext} + G_{A,cn} + G_{A,cT} \quad (1)$$

where

$$\begin{aligned} G_{A,inert}(\mathbf{u}_{0A}, \boldsymbol{\theta}_A, t) &= (\rho_{p_A} \ddot{\mathbf{u}}_{0A}, \delta \mathbf{u}_{0A})_{S_{A_p}} + (J_{p_A} \ddot{\boldsymbol{\theta}}_A, \delta \boldsymbol{\theta}_A)_{S_{A_p}} \\ G_{A,int}(\mathbf{u}_{0A}, \boldsymbol{\theta}_A, t) &= (\mathbf{N}_A, \delta \mathbf{E}_{N_A})_{S_{A_p}} + (\mathbf{M}_A, \delta \mathbf{E}_{B_A})_{S_{A_p}} + (\mathbf{Q}_A, \delta \mathbf{E}_{S_A})_{S_{A_p}} \\ G_{A,cn}(\mathbf{u}_{0A}, \boldsymbol{\theta}_A, t) &= \langle \mathbf{R}_{n_A}, \delta \mathbf{u}_{0A} \rangle_{S_{A_{cp}}} + \langle \mathbf{M}_{n_A}, \delta \boldsymbol{\theta}_A \rangle_{S_{A_{cp}}} \\ G_{A,cT}(\mathbf{u}_{0A}, \boldsymbol{\theta}_A, t) &= \langle \mathbf{R}_{T_A}, \delta \mathbf{u}_{0A} \rangle_{S_{A_{cp}}} + \langle \mathbf{M}_{T_A}, \delta \boldsymbol{\theta}_A \rangle_{S_{A_{cp}}} \end{aligned}$$

Integration is performed over the initial mid-surface S_{A_p} where the restriction to contact areas is denoted $S_{A_{cp}} \subset S_{A_p}$.

In the next two sections, the stress resultants of the internal elasto-plastic work $G_{A,int}$, the contact-impact work $G_{A,cn}$, and the friction work $G_{A,cT}$ are related to the unknowns of the problem, and studied in the framework of an implicit Newmark scheme.

3 Stress-Resultant Plasticity Using Ivanov's Yield Surface

3.1 Basic Definitions and Assumptions

The starting point is plane stress J_2 flow theory where the elastic response emanates from a hyperelastic stress-strain relation. The contribution of transverse shear strains and stresses will be considered to be negligible for the evaluation of the shell yield criterion.

The developments in this section will be presented in a non-dimensional notation by introducing the following non-dimensional Green-Lagrange type *membrane* and *bending strain resultants*

$$\mathbf{e}_{(6 \times 1)} = \begin{bmatrix} e_N \\ e_B \end{bmatrix} \quad \text{where} \quad e_N = \frac{E}{\sigma_y} \{E_{N11} \ E_{N22} \ 2E_{N12}\}, \quad e_B = \frac{hE}{4\sigma_y} \{E_{B11} \ E_{B22} \ 2E_{B12}\} \quad (2)$$

where h , σ_y and E are the shell thickness, the initial uniaxial yield stress and Young's moduli, respectively.

Substituting the *Mindlin kinematic assumption* $\boldsymbol{\varepsilon}(\xi^3) = e_N + 4\xi^3 e_B$, ($\xi^3 = z/h$), into the plane stress constitutive law relating Green-Lagrange strains and Piola-Kirchhoff stresses and

integrating over the thickness yields the *resultant constitutive law*

$$\left. \begin{aligned} \mathbf{s} = \tilde{\mathbf{C}} \cdot (\mathbf{e} - \mathbf{e}^p) \quad \text{where} \quad \underset{(6 \times 1)}{\mathbf{s}} = \begin{bmatrix} \mathbf{n} \\ \mathbf{m} \end{bmatrix} = \begin{bmatrix} [n_{11} \ n_{22} \ n_{12}]^T \\ [m_{11} \ m_{22} \ m_{12}]^T \end{bmatrix}, \\ \tilde{\mathbf{C}} = \begin{bmatrix} \mathbf{C} & \cdot \\ \cdot & \frac{4}{3}\mathbf{C} \end{bmatrix}, \quad \text{and} \quad \mathbf{C} = \frac{1}{1-\nu^2} \begin{bmatrix} 1 & \nu & \cdot \\ \nu & 1 & \cdot \\ \cdot & \cdot & (1-\nu)/2 \end{bmatrix} \end{aligned} \right\} \quad (3)$$

where $\mathbf{n} = \mathbf{N}/N_L$ and $\mathbf{m} = \mathbf{M}/M_L$ are normalized resultants and $N_L = h\sigma_y$, resp. $M_L = (h^2/4)\sigma_y$ represent plastic limit loads. The factor $4/3$ comes from normalization, cf. (2).

The essential assumption made by Ilyushin [7] for the derivation of a yield surface in stress resultant space is that strain resultant increments are wholly plastic in the plastic loading case and thus normal to the yield surface. Thus the Mindlin assumption is supposed to hold for plastic flow, that is

$$\dot{\mathbf{e}}^p(\xi^3) = \dot{\mathbf{e}}_N^p + 4\xi^3 \dot{\mathbf{e}}_B^p \quad (4)$$

An *associative flow rule* and *isotropic hardening* with an equivalent plastic strain evolution are supposed to hold. For the yield function of Section 3.2 this reads

$$\dot{\mathbf{e}}^p = \dot{\lambda} \mathbf{D}_s F = \dot{\lambda} \tilde{\mathbf{D}} \cdot \mathbf{s}, \quad \text{respectively} \quad \dot{\alpha} = \dot{\lambda} \sqrt{\frac{2}{3}} \phi \quad (5)$$

3.2 Ivanov's Approximation of Ilyushin's Yield Surface

In [7] Ilyushin gives a parametric expression of a two-dimensional yield surface in the three-dimensional (Q_n, Q_{nm}, Q_m) -space (see eqs. (6), (7)) which is derived from the von Mises yield criterion in the plane stress case. This is referred to as the *exact Ilyushin yield surface*. It has been reformulated in [4] using a different set of parameters which made it suitable for numerical analysis. An approximation is due to Ivanov. In [14] it is reported to have a maximum error of 1% with respect to the exact Ilyushin surface.

Let the *stress resultant intensities* be defined by

$$\left. \begin{aligned} Q_n &= \mathbf{n}^T \cdot \mathbf{D} \cdot \mathbf{n} = \|\mathbf{n}^D\|^2 \\ Q_{nm} &= \mathbf{n}^T \cdot \mathbf{D} \cdot \mathbf{m} = \text{Tr}(\mathbf{n}^D \cdot \mathbf{m}^D) \\ Q_m &= \mathbf{m}^T \cdot \mathbf{D} \cdot \mathbf{m} = \|\mathbf{m}^D\|^2 \end{aligned} \right\} \quad \mathbf{D} = \frac{1}{3} \begin{bmatrix} 2 & -1 & \cdot \\ -1 & 2 & \cdot \\ \cdot & \cdot & 6 \end{bmatrix} \quad (6)$$

Then, given any isotropic hardening $k(\alpha)$, Ivanov's yield criterion reads

$$\begin{aligned} \phi(Q_n, Q_{nm}, Q_m) &= Q_n + \frac{Q_m}{2} + \sqrt{\frac{Q_m^2}{4} + Q_{nm}^2} - \frac{1}{4} \left(\frac{Q_n Q_m - Q_{nm}^2}{Q_n + 0.48 Q_m} \right) \\ F(Q_n, Q_{nm}, Q_m, \alpha) &= \frac{1}{2} \phi - \frac{1}{3} k(\alpha)^2 \end{aligned} \quad (7)$$

For numerical analysis the normal to the yield surface in stress resultant space is required. It is obtained from the chain rule as

$$\underset{(6 \times 1)}{\mathbf{D}_s F} = \begin{bmatrix} \mathbf{D}_n Q_n \\ \mathbf{D}_m Q_{nm} \end{bmatrix} = \tilde{\mathbf{D}} \cdot \mathbf{s}, \quad \text{where} \quad \underset{(6 \times 6)}{\tilde{\mathbf{D}}} = \begin{bmatrix} 2 \frac{\partial F}{\partial Q_n} \mathbf{D} & \frac{\partial F}{\partial Q_{nm}} \mathbf{D} \\ \text{sym.} & 2 \frac{\partial F}{\partial Q_m} \mathbf{D} \end{bmatrix} \quad (8)$$

3.3 Plastic Multiplier and Algorithmic Elasto-Plastic Tangent Moduli

In classical plasticity the multiplier $\dot{\lambda}$ is obtained by substituting the rate form of the constitutive equation and the flow rule into the consistency condition $\dot{F} = 0$. In stress resultant space authors [5, 15] usually choose the same procedure to calculate the multiplier and to derive the elastoplastic tangent moduli. Burgoyne and Brennan [4], however, argue that this is in contradiction with the basic assumption (4). That is, in case of plastic loading, the additive decomposition of total strain increments into an elastic and plastic part which is in fact the definition of the elastic strain increment is no longer valid. The rate form of the constitutive equation can no longer be related to elastic strain increments and hence elasto-plastic rigidities cannot be derived using the classical procedure.

Instead, in [4] these authors propose to integrate the continuum elasto-plastic tangent moduli obtained at any level ξ^3 from plane stress elastoplasticity over the shell thickness. They show that in the case of perfect plasticity using the exact Ilyushin yield criterion, the resulting *continuum* tangent moduli can be entirely expressed in stress resultants.

However, there is no way to generalize the method of [4] to hardening materials. Furthermore, in large displacement/rotation analysis of shells a *consistent algorithmic* tangent moduli is required to preserve quadratic convergence of the standard Newton method, cf. [13, 15]. The explicit integration of a respective plane stress algorithmic moduli is impossible and thus the consistent algorithmic rigidities cannot be expressed in stress resultants.

Therefore, in this paper, the consistent algorithmic tangent moduli is derived directly in resultant space using the classical procedure.

Starting from an equilibrium state t_n , the plastic multiplier and tangent moduli must be found for intermediate, non-equilibrated strain states e_i by a local Newton procedure at integration points. The implicit backward Euler method is chosen. The plastic strains e_n will be updated only when convergence of the global Newton procedure is achieved at t_{n+1} .

From (3) and (5)₁ the rate form of the incremental stress-strain relation at t_i follows as¹

$$\dot{s}_i = \tilde{H}_i^{-1} \cdot (\dot{e}_i - \Delta \lambda_i \tilde{D}_{i-1} \cdot s_i), \quad \tilde{H}_i^{-1} = (\tilde{C}^{-1} + \Delta \lambda_i \tilde{D}_{i-1})^{-1} \quad (9)$$

Remark. Since C and D have the same characteristic subspaces they may be diagonalized by the same orthonormal transformation matrix (cf. [15]). Thus the inversion \tilde{H}_i^{-1} is explicit.

The consistency condition for plastic flow $\dot{F} = s_i^T \cdot \tilde{D}_{i-1} \cdot \dot{s}_i = 0$ together with (5)₂ and (9) yields the multiplier increment $\Delta \lambda_i$, and substituting the latter into (9) gives the algorithmic elasto-plastic tangent moduli

$$\dot{s}_i = \tilde{C}_i^{ep} \cdot \dot{e}_i, \quad \begin{cases} \tilde{C}_i^{ep} = \tilde{H}_i^{-1} - \frac{1}{\kappa_i} (\tilde{H}_i^{-1} \cdot \tilde{D}_{i-1} \cdot s_i) \cdot (s_i \cdot \tilde{D}_{i-1} \cdot \tilde{H}_i^{-1}) & \text{for } \Delta \lambda_i > 0 \\ \kappa_i = \frac{1}{2} s_i^T \cdot \tilde{D}_{i-1} \cdot \tilde{H}_i^{-1} \cdot \tilde{D}_{i-1} \cdot s_i + \beta_i \\ \beta_i = 2 \frac{(2/3)^2 k_i'}{1 - (2/3) k_i' \Delta \lambda_i}, \quad k_i' = \left. \frac{\partial k}{\partial \Delta \alpha} \right|_i \end{cases} \quad (10)$$

Remark. The membrane-bending coupling part of the hypermatrix \tilde{C}_i^{ep} is non-symmetric and will be symmetrized for convenience in the Newton algorithm.

¹The second order derivatives $\dot{\tilde{D}}_i$ are neglected.

3.4 Return Mapping Algorithm

The plastic multiplier $\Delta\lambda_i$ is obtained from the yield criterion (7) by a local Newton procedure at integration points. The stress resultants can be obtained from the elastic predictor $\mathbf{s}_j = \tilde{\mathbf{H}}_j^{-1} \cdot (\mathbf{e}_i - \mathbf{e}_n^p)$ at any t_j , ($i - 1 \leq j \leq i$). Thus the yield criterion can be expressed as a function $\hat{F}(\Delta\lambda_j) = 0$ and the return mapping reduces to the iterative solution of the following scalar equation

$$\Delta\lambda_{j+1} = \Delta\lambda_j - \frac{\hat{F}(\Delta\lambda_j)}{\partial\hat{F}/\partial\Delta\lambda|_j}, \quad \text{where}$$

$$\left. \frac{\partial\hat{F}}{\partial\Delta\lambda} \right|_j = -\frac{1}{2} \left(1 - \frac{(2/3)^{1.5} \Delta\lambda_j k_j k'_j}{\sqrt{\phi_j}} \right) \mathbf{s}_j^T \cdot \tilde{\mathbf{D}}_{j-1} \cdot \tilde{\mathbf{H}}_j^{-1} \cdot \tilde{\mathbf{D}}_{j-1} \cdot \mathbf{s}_j - \left(\frac{2}{3} \right)^{1.5} k_j k'_j \sqrt{\phi_j} \quad (11)$$

4 Dynamic frictional contact-impact model

4.1 Mechanical model

Let \mathbf{p}_1 and \mathbf{p}_2 be two material points belonging to the respective boundaries of Ω_{1p} and Ω_{2p} , which at time t , are in contact, such that:

$$\mathbf{x}_1(\mathbf{p}_1, t) = \mathbf{x}_2(\mathbf{p}_2, t)$$

$\mathbf{n}_{x_A}(\mathbf{p}_A, t)$ is the unit outward normal at $\mathbf{x}_A \in \Gamma_{A_x}$, Ω_{A_x} being considered as a three dimensions structure. The contact force $\mathbf{R}_{c_A}(\mathbf{p}_A, t)$ applied on Γ_{A_x} at $\mathbf{x}_A(\mathbf{p}_A, t)$, and the displacement $\mathbf{u}_A(\mathbf{p}_A, t)$ of $\mathbf{p}_A \in \Gamma_{A_p}$ are written with their normal and tangent plane components:

$$\mathbf{R}_{c_A} = R_{n_A} \mathbf{n}_{x_A} + \mathbf{R}_{T_A} \quad \mathbf{u}_A = u_{n_A} \mathbf{n}_{x_A} + \mathbf{u}_{T_A}$$

On Γ_{1_x} the normal contact conditions are:

$$\left\{ \begin{array}{l} \forall \mathbf{x}_1 \in \Gamma_{x_1}, \quad ([\mathbf{x}(\mathbf{p}, t)], \mathbf{n}_{x_1}(\mathbf{p}_1, t)) < 0 \\ R_{n_1} \leq 0 \\ R_{n_1}(\mathbf{x}_2 - \mathbf{x}_1, \mathbf{n}_{x_1}) = 0 \end{array} \right. \quad (12)$$

where $[\cdot] = \cdot_1 - \cdot_2$

A penalty model is chosen to regularize (12) [3, 9], and the normal contact force applied by Ω_{x_2} on Γ_{x_1} at \mathbf{x}_1 reads:

$$\mathbf{R}_{n_1} = k_{n_1} (\mathbf{x}_2 - \mathbf{x}_1, \mathbf{n}_{x_1})^- \mathbf{n}_{x_1}$$

Where k_{n_1} is the normal penalty parameter whose value is related to the materials of Ω_{A_x} and $(\cdot)^-$ is the negative part of (\cdot) .

Denoting $\dot{\mathbf{u}}_{T_A}^p$ the plastic part of $\dot{\mathbf{u}}_A$, and μ the friction coefficient related to Γ_{A_x} , we regularize the Coulomb friction law as:

$$F = \|\mathbf{R}_{T_A}\| + \mu R_{n_A} \leq 0 \quad : \quad \text{if } \|\mathbf{R}_{T_A}\| + \mu R_{n_A} < 0 \quad \text{then } \dot{\mathbf{R}}_{T_A} = k_{T_A} [\dot{\mathbf{u}}_T - \dot{\mathbf{u}}_T^p]$$

$$\text{else } \exists \lambda \geq 0, \quad [\dot{\mathbf{u}}_T^p] = \lambda \frac{\mathbf{R}_{T_A}}{\|\mathbf{R}_{T_A}\|}$$

Where k_{T_A} is a tangent penalty parameter related to both of the current contact surfaces.

Once discretized in time, (1) is solved using an implicit Newmark scheme. In a large displacements/rotations shell theory, we consistently linearize (1) for a Newton method. The normal contact terms are differentiated with respect to time as:

$$\dot{\mathbf{R}}_{n_1} = -(\mathbf{KN} + \mathbf{NK}^T + (\text{Tr } \mathbf{L} - (\mathbf{L}\mathbf{n}_{x_1}, \mathbf{n}_{x_1}))\mathbf{I}_x)[\mathbf{x}] - \mathbf{N}[\dot{\mathbf{u}}] \quad (13)$$

with

$$\mathbf{N} = k_{n_1}(\mathbf{n}_{x_1} \otimes \mathbf{n}_{x_1}); \quad \mathbf{K} = (\mathbf{L}\mathbf{n}_{x_1}, \mathbf{n}_{x_1})\mathbf{I}_x - \mathbf{L}^T; \quad \mathbf{L} = \dot{\mathbf{F}}_1\mathbf{F}_1^{-1}$$

where all the terms emanating from the normal, the surface, and the position have been differentiated. For a shell formulation, the normal contact stiffnesses $D_{u_0}\mathbf{R}_{n_1}(\mathbf{u}_0, \boldsymbol{\theta})\Delta\mathbf{u}_0$ and $D_{\boldsymbol{\theta}}\mathbf{R}_{n_1}(\mathbf{u}_0, \boldsymbol{\theta})\Delta\boldsymbol{\theta}$ are deduced from (13) and expressed in a contravariant basis on the initial configuration. For the normal contact stress resultants \mathbf{R}_{n_1} and $\mathbf{M}_{n_1} = \zeta_1\mathbf{R}_1(\mathbf{d}_{p_1}) \wedge \mathbf{R}_{n_1}$, we can get the linearized generalized contact stress resultants from (1):

$$\begin{aligned} \Delta\mathbf{R}_{n_1} &= D_{u_0}\mathbf{R}_{n_1}(\mathbf{u}_0, \boldsymbol{\theta})\Delta\mathbf{u}_0 + D_{\boldsymbol{\theta}}\mathbf{R}_{n_1}(\mathbf{u}_0, \boldsymbol{\theta})\Delta\boldsymbol{\theta} \\ \Delta\mathbf{M}_{n_1} &= \zeta_1(\mathbf{R}_1(\boldsymbol{\theta}_1)(\mathbf{d}_{p_1} \wedge \Delta\mathbf{R}_{n_1}) - (\Delta\boldsymbol{\theta}_1 \otimes \mathbf{R}_1(\boldsymbol{\theta}_1)\mathbf{d}_{p_1})\mathbf{R}_{n_1}) \end{aligned}$$

The regularized Coulomb law provides all the elements to get the consistent tangent operators relating stress increments to displacement increments. In the elastic case, we have, on Γ_{x_1} :

$$\dot{\mathbf{R}}_{T_1} = k_{T_1}[\dot{\mathbf{u}}_T],$$

from which the elastic operator is easily deduced. For the plastic case, λ follows from the consistency condition $\dot{F} = 0$ and the relation between the stress and the displacement increments is expressed as:

$$\dot{\mathbf{R}}_{T_1} = k_{T_1}([\dot{\mathbf{u}}_T] - \lambda \frac{\mathbf{R}_{T_1}}{\|\mathbf{R}_{T_1}\|})$$

Finally, the linearized terms $D_{u_0}\mathbf{R}_{T_1}(\mathbf{u}_0, \boldsymbol{\theta})\Delta\mathbf{u}_0$ and $D_{\boldsymbol{\theta}}\mathbf{R}_{T_1}(\mathbf{u}_0, \boldsymbol{\theta})\Delta\boldsymbol{\theta}$ are obtained, and from the resultants \mathbf{R}_{T_1} and $\mathbf{M}_{T_1} = \zeta_1\mathbf{R}_1(\mathbf{d}_{p_1}) \wedge \mathbf{R}_{T_1}$:

$$\begin{aligned} \Delta\mathbf{R}_{T_1} &= D_{u_0}\mathbf{R}_{T_1}(\mathbf{u}_0, \boldsymbol{\theta})\Delta\mathbf{u}_0 + D_{\boldsymbol{\theta}}\mathbf{R}_{T_1}(\mathbf{u}_0, \boldsymbol{\theta})\Delta\boldsymbol{\theta} \\ \Delta\mathbf{M}_{T_1} &= \zeta_1(\mathbf{R}_1(\boldsymbol{\theta}_1)(\mathbf{d}_{p_1} \wedge \Delta\mathbf{R}_{T_1}) - (\Delta\boldsymbol{\theta}_1 \otimes \mathbf{R}_1(\boldsymbol{\theta}_1)\mathbf{d}_{p_1})\mathbf{R}_{T_1}) \end{aligned}$$

are deduced.

The contact non-linearity is solved by a fixed-point method with a Newton scheme: when the geometrically non-linear problem without contact is solved, we detect the contact areas and add the forces and stiffnesses in the global system. We then reiterate this work until contact areas remain constant with small interpenetrations. Between two contact iterations, new predictors are assumed, taking into account the last contact state. Once contact convergence is reached, iterations on frictional state are performed with the same strategy as for normal contact.

4.2 Numerical model

There are essentially three approaches for detecting interferences between spatial objects: "lagrangian" octrees [1], mainly for rigid body motions, analytical approaches [2] when shape structures are simple [8] or have a C.A.D. definition, and geometrical methods which linearly take into account time history [12], [16].

Impact may occur at any spatial location, a priori not belonging to any structure: thus, we choose a spatial approach, prescribing a spatial mesh. For the efficiency of the algorithm, this mesh is adaptive.

The "octree" notion is suitable for this mesh. An octree represents the space using a hierarchical cubic decomposition of the "universe space", called root. To represent an object, the root is recursively partitioned into octants until the desired resolution is reached. The terminal octants are called the leaves. While in rigid body motions the time updating process consists of applying translations and rotations to each body's octree, our updating process is a refinement-unrefinement of the single universe-space according to the current position of the shells. This is the main difference with "lagrangian" octree approaches cited above.

The leaves representing a partition of the universe-space, we only perform tests inside each leaf, thus reducing the number of tests with a suitable refinement criterion: we can prove that the number of tests n_t needed to detect all the intersections satisfies the following condition:

$$n_t \leq k.p.n$$

where n is the total number of finite elements, p is the maximum number of finite elements partially contained in an octant, and k the maximum number of octants partially containing a finite element. This yields a simple criterion for the refinement of an octant i : $k_i p_i > c$ where c is a constant, so that n_t becomes linear with respect to n . In practice if the octant size is superior to the elements size, we can check that k remains almost constant, and we apply the criterion only to p_i for each octant i . The detected intersections are stored in a graph. We get the entire contact areas by checking the shell linearized non-interpenetration condition (12)

$$([\Delta u], \mathbf{n}_{x_1}(\mathbf{p}_1, t_n)) - g \geq 0 \quad (14)$$

where:

$$\begin{cases} \Delta u = u(\mathbf{p}, t_n) - u(\mathbf{p}, t_{n-1}) \\ g = (-[\mathbf{x}(\mathbf{p}, t_{n-1})], \mathbf{n}_{x_1}(\mathbf{p}_1, t_{n-1}))^+ \\ \mathbf{n}_{x_1}(\mathbf{p}_1, t_n) = \text{sign}(-[\mathbf{x}(\mathbf{p}, t_{n-1})], \mathbf{n}_{x_1}(\mathbf{p}_1, t_n)) \quad \mathbf{n}_{x_1}(\mathbf{p}_1, t_n) \end{cases}$$

in each vertex neighborhood of the graph.

When several structures are deformable, most of the authors use master-slave surface algorithms [10]. We have developed an interface element inducing more symmetry in the treatment, and taking into account the possible geometrical "pathologies" of impact configurations.

Up to now, nothing has been assumed on the numerical modeling of the discretized contact area. The search algorithm allows to find each $\mathbf{x}_1 \in \Gamma_{x_1}$, \mathbf{x}_1 being a position of a node or a Gauss point. Once \mathbf{x}_1 is found, \mathbf{n}_{x_1} is computed and we have $\mathbf{x}_2 \in \Gamma_{x_2}$ by solving the 3x3 non-linear problem given by:

$$\mathbf{x}_2(\xi_2^\alpha, t) - \lambda \mathbf{n}_1(\xi_1^\alpha, t) = \mathbf{x}_1(\xi_1^\alpha, t)$$

Then \mathbf{n}_{x_1} , \mathbf{x}_1 , \mathbf{x}_2 and the finite elements corresponding to ξ_1 and ξ_2 are the attributes of an interface element class. An interface element can then give the frictional contact forces and stiffnesses relative to both surfaces Γ_{x_1} and Γ_{x_2} , avoiding an unsymmetric master slave treatment.

Particular attention is paid to the case where \mathbf{x}_1 is part of a shell's boundary. Thanks to our Boundary-Representation, these configurations are easily detected. Then, we change the

structure of such an interface element: if $\|\mathbf{n}_{x_1} \wedge \mathbf{n}_{x_2}\| > \epsilon$, \mathbf{n}_{x_1} is replaced by \mathbf{n}_{x_2} in the expression of \mathbf{R}_{n_1} , this force is then integrated over the one-dimensional boundary. The pathologic case of an impact between two shell boundaries still remains hard to be treated. We think of solving this problem by using a more general class of tetrahedron interface elements that would better represent the contact zone's topology.

5 Conclusion

A mechanical and numerical model for dynamic frictional contact and impact between general shell structures undergoing large displacements and rotations has been presented.

Robustness and reliability of the numerical implementation are achieved by a consistent linearization. Thus, in the framework of an implicit Newmark scheme fine frictional contact effects are accounted for. The search algorithm is based on a spatial octree decomposition with an adaptive refinement in potential contact areas. It is linear with respect to the total number of shell elements. The contact behavior is stored in interface elements which allows a computationally efficient symmetric treatment.

The use of a stress resultant constitutive law by-passes numerical through-the-thickness integration. This reduces considerably storage requirements. For isotropic materials the local iterative procedures can be made explicit and thus computationally very efficient. A generalized Ivanov yield criterion including linear isotropic hardening is chosen for implementation. It may readily be extended to more general hardening laws as has been shown in [6, 15].

References

- [1] N. Ahuja and C. Nash. Octree representation of moving objects. *Computer Vision, Graphics, and Image Processing*, 26, 207 – 216, 1984.
- [2] D. Baraff. Analytical methods for dynamic simulation of non-penetrating rigid bodies. *Computer Graphics*, 23, 223 – 232, 1989.
- [3] H. BenDhia. *Habilitation à diriger des Recherches*. École Centrale de Paris, to be published, 1995.
- [4] C.J. Burgoyne and M.G. Brennan. Calculation of elasto-plastic rigidities using the exact Ilyushin yield surface. *Int. J. Solids Structures*, 30, 1133 – 1145, 1993.
- [5] C.H. Chou, J. Pan, and S.C. Tang. Analysis of sheet metal forming operations by a stress resultant constitutive law. *Int. J. Num. Meth. Engng.*, 37, 717 – 735, 1994.
- [6] B. Dressler. PhD thesis, École Centrale de Paris CNRS URA 850, to be published, 1995.
- [7] A.A. Ilyushin. *Plasticité*. Éditions Eyrolles, Paris, 1956.
- [8] A. Kaufmann. *Algorithmes distribués pour l'intersection de courbes et surfaces de Bézier*. PhD thesis, Université Joseph Fourier, Grenoble I, 1990.
- [9] Kikuchi. and Oden. *Contact problems in elasticity: A study of variational inequalities and finite element methods*. SIAM, Studies 8, Philadelphia, 1988.

- [10] T.A. Laursen and J.C. Simo. A continuum-based finite element formulation for the implicit solution of multibody, large deformation frictional contact problems. *Int. J. Num. Meth. Eng.*, 36, 3451 – 3485, 1993.
- [11] D. Lucas. *Méthode des éléments finis et programmation orientée objet – Utilisation du langage Ada*. PhD thesis, École Centrale de Paris CNRS URA 850, 1994.
- [12] M. Oldenburg and L. Nilsson. The position code algorithm for contact searching. *Int. J. Num. Meth. Eng.*, 37, 359 – 386, 1994.
- [13] E. Ramm and A. Matzenmiller. Consistent linearization in elasto-plastic shell analysis. *Eng. Comput.*, 5, 289 – 299, 1987.
- [14] M. Robinson. A comparison of yield surfaces for thin shells. *Int. J. Mech. Sci.*, 13, 345 – 354, 1971.
- [15] J. Simo and J.G. Kennedy. On a stress resultant geometrically exact shell model. Part V: Nonlinear plasticity: formulation and integration algorithms. *Comp. Meth. Appl. Mech. Engng.*, 96, 133 – 171, 1992.
- [16] Z-H. Zhong and L. Nilsson. A contact searching algorithm for 3-d contact-impact problems. *Computers and Structures*, 33, 197 – 209, 1989.

9th DYMAT Technical Conference
Material and structural modelling in collision research
TUM Munich (Germany)
October 10-11th, 1995

ON NUMERICAL SIMULATIONS OF EXPLOSIONS ON SEALINES

K. CICHOCKI*, G. MAIER, U. PEREGO
Department of Structural Engineering, Technical University (Politecnico), Milan (Italy)

INTRODUCTION

There are several instances in engineering practice where a realistic and accurate evaluation of the loading conditions caused by an underwater explosion on a structure is of paramount importance for the assessment of the structural safety. These situations, relevant to offshore engineering applications, include underwater tunnel crossing⁴, structures for oil production and transportation and sealines in general.

Typical structural problems of this kind involve a charge located at a certain distance from a deformable (generally not plane) surface. The purpose of the analysis is generally to assess the possible structural damages produced by the charge ignition and the propagation of the consequent pressure wave which impinges against the structural surface and reflects from it.

Empirical formulae are available^{1,2} for estimating the pressure produced by the explosion of a spherical charge as a function of time and position, depending on the charge mass and distance. At a given position, the pressure history is modeled as a sudden peak followed by an exponential decay. When a structural surface is hit, wave reflection occurs. The interaction between the incident and reflected waves produces an amplification of the initial pressure peak which can be calculated analytically in the special case of a plane wave impinging on a plane rigid surface normal to the direction of propagation. This analytical solution is acceptable also in the case of a spherical wave only when the charge is sufficiently distant from the surface so that it can be assimilated to a plane wave. On the other hand, when the hit surface is deformable and curved, as in the case, e.g., of pipelines, the peak amplification can be substantially different from the analytical one. Furthermore, no information, either analytical or empirical, is available on the pressure transient at a given position after the peak has occurred.

The purpose of the present paper is to simulate the charge ignition, wave propagation and wave-structure interaction processes by finite element calculations in order to verify the available empirical formulae and to correct them for situations involving explosions near sealines. While finite element

* On leave from Technical University of Koszalin (Poland)

numerical simulations have already proved able to predict both the magnitude and form of the pressure transient in the explosive and the surrounding water^{4,5}, the reflection against a structural surface and the estimate of the consequent loading still appear to be a crucial and open issue as for engineering computations.

All numerical analyses have been carried out using the finite element code Abaqus Explicit³. This is a widely diffused commercial code based on a Lagrangian formulation and an explicit dynamic time integration.

NUMERICAL SIMULATION

As a first step, the numerical model for the propagation in water of the pressure wave generated by the explosion of a spherical charge of 100 kg of TNT is tuned by comparison with the empirical formulae proposed by Cole¹ and Henrych². The axisymmetry of the problem is exploited and the analysis is stopped before the wave reaches the mesh outer boundary so that no reflection occurs. As in^{4,5}, the behaviour of the explosive and of the water is modeled by means of Jones-Wilkins-Lee and Mie-Gruneisen equations of state, respectively. Both are available in the standard version of the code. The mesh is composed of axisymmetric four-node elements. The discretized domain is sketchily shown in figure 1. The charge is located at the centre of the sphere.

The plots in the same figure show the variation of pressure with time at four points at a distance of 1.25m, 2.25m, 3.8m and 5.35m from the source. As in the case of the analyses presented in⁵ (where the finite element code Dyna3D was used), the numerical results are in reasonably good agreement (at least qualitatively) with the empirical predictions both in terms of the peak value and of the descending exponential branch. A comparable accuracy is exhibited also at the point closest to the source (1.25m). The discrepancies are presumably due to the finite mesh size (the pressure is sampled at the centre-point of each element) and to the fact that, in the finite element analysis of figure 1, the pressure is referred to a point which moves along with the water element deformation, while in the empirical formulae the distance from the source is kept constant.

The more complex propagation and reflection problem arising when the presence of a rigid submerged pipe is considered, has been analyzed by means of the plane-strain finite element model shown in figure 2. In view of the adopted plane-strain approximation, which has been dictated by the need to limit the problem size, an infinitely long cylindrical charge of 324 kg/m has been considered. Frictionless sliding contact has been assumed at the interface between water and the pipe. The mesh shown to an enlarged scale in figure 2a refers to the charge discretization, while figure 2b shows the pipe region with the four points (denoted as 1, 2, 3 and 4) where the pressure history has been monitored. The analysis has been stopped before the propagating wave reaches the outer mesh boundary.

The results in terms of impulse (i.e. pressure integrated in time) at the four points are illustrated in figure 3. In the graph relative to points 1 and 2, two couples of curves are plotted. The first couple (lines without black dots) shows the results obtained both numerically by Abaqus and empirically by Henrych's formula for the same problem described above but without the rigid pipe. These curves are denoted by the term *incident*. When the rigid pipe is present, neither empirical or analytical estimates of the complete pressure transient are available in the literature, to the authors' knowledge. Therefore, the

second couple of curves (lines with black dots) shows the results obtained by Abaqus for the present problem and by an empirical criterion (*modified Henrych*) which is suggested in the present paper. These curves are denoted by the term *reflected*.

The conjecture which underlies the proposed criterion and which seems to be confirmed by the trend of the numerical curves, is that the total impulse (i.e. the asymptotic value of the curves in figure 3) is not modified by the presence of the pipe. At point 1, where the tangent plane to the cylinder is normal to the propagation direction, the peak value obtained according to the theoretical reflection amplification coefficient $\alpha = 2$ is assumed. The descending branch is described by Henrych's exponential curve modified imposing that the total impulse be equal to the impulse at the same point without the rigid pipe (which is easily calculated from Henrych's formula). The same criterion is adopted at point 2, with the difference that a modified peak amplification coefficient $\beta = (1 + \cos \theta)\alpha$ for $0 \leq \theta \leq \pi/2$, (θ being the angle between the outward normal to the surface and the propagation direction) is used in order to account for the deviation from normality of the incidence angle. For $\pi/2 \leq \theta \leq \pi$ (points 3 and 4), it is assumed that no reflection occurs and $\beta = \alpha = 1$ is used. Since no reflection is postulated, only three curves are shown at points 3 and 4.

The asymptotic values computed on the basis of Henrych formulae (original for incident, modified for reflected waves) turns out to be reached only accurately for the incident, not so for the reflected wave. In both cases a discrepancy is apparent in figure 3. This is due to the spurious perturbation wave reflected by the fictitious boundary. The end of the analyses visualised in figure 3 was dictated by numerical difficulties due to excessive distortion of elements near the boundary, consistent with the Lagrangian description of the kinematics implemented in the employed computer code. Hardware limitations did not allow to enlarge the problem size and to carry out the analysis for a longer time. Alternatively, in order to avoid spurious reflection effects, one could apply viscous dampers at the mesh nodes near the boundary. However, in this case the difficulty would be the correct evaluation of the damping coefficients. This approach will be pursued and discussed in a forthcoming paper.

The three-dimensional problem concerning the effects of an underwater explosion on a deformable pipe has been studied by means of three numerical simulations:

The results of these three analyses are comparatively illustrated in figure 5 and briefly commented below.

a) The complete coupled problem is tackled as shown in figure 4. The mesh is made of 8-node bricks. The pipe is discretized by means of 4-node shell elements. Exploiting the symmetries specified in figure (the artificial one with respect to plane ABFE can be reasonably accepted), only one eighth of the system is discretized. The pipe is assumed to be fully constrained at both ends. The analysis is stopped before the pressure wave reaches the pipe ends. Due to the problem size limitations, the adopted mesh is substantially coarser than the one employed for the twodimensional simulations. The contour plot of figure 5a shows the equivalent plastic strain accumulated at the end of the analyses on the midsurface of the shell.

b) The water is discretized as in (a) but the explosion and the propagation of the pressure wave are not simulated. A simplified problem is formulated, where the pressure $p(\underline{x}, t)$ on the pipe is applied as a

known function calculated by means of the modified Henrych's formula introduced above; the surrounding water is explicitly discretized using the same mesh as in (a). Rather, the pressure, considered as an assigned, known load which varies in space and time, is applied directly to the pipe. The effect of the water mass on the pipe deformation is accounted for. The contour plot of the equivalent plastic strain on the middle surface is shown in figure 5b.

c) As in (b), the load is applied directly to the pipe, but the effect of the surrounding water is not considered. The contour plot of the equivalent plastic strain is shown in figure 5c.

From figure 5, it turns out that analyses (b) and (c) produce approximately the same result in terms of equivalent plastic strain which, however is higher than the one predicted in (a). Several factors may be responsible of the discrepancy. First of all, in (b) and (c), the pressure is applied at nodes which change position during the analyses. This aspect is not taken into account and may be the source of significant errors as briefly discussed before with reference to figure 1. Furthermore, it is almost impossible to synchronize the different analyses (so that the contour plots refer to the same instant) because the wave propagation in the numerical analysis is affected by the current water pressure.

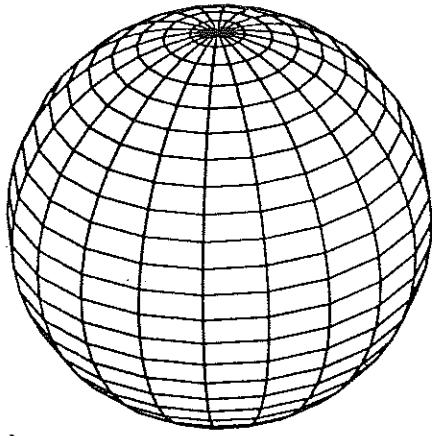
For the analyses (b) and (c) the ovalization of the pipe is shown in figure 6a and 6b respectively, as the difference between the vertical displacements of the nodes at the top and bottom, respectively, of the pipe section. While no significant difference is observed in terms of the section deformation, the time histories of the absolute vertical displacements of the two nodes appear quite different, as expected. Infact, the water mass interacts in a significant way with the pipe vibration, not with the pipe permanent deformation. However, for larger explosive charges and consequent more significant pipe motion and inelastic deformations, it is reasonably expected that the effects of water inertia would be by far more pronounced. Infact, these effects might have a crucial influence on the predicted damages in the pipe (e.g. transition from local indentation for the larger inertia effects to beam bending mechanisms for the small ones).

ACKNOWLEDGMENTS

The writers want to express their appreciation to F.Casolo, P.Monti and F.Taddei for fruitful discussions and to Snamprogetti Spa R.&D. contract with Politecnico di Milano.

REFERENCES

- [1] Cole, R.H., *Underwater Explosions*, Dover Publications Inc., N.Y., 1965
- [2] Henrych, J., *The Dynamics of Explosion and Its Use*, Elsevier, Amsterdam, 1979
- [3] Abaqus/Explicit Theory and User's manual ver. 5.4, HKS, Providence, RI, USA, 1994
- [4] Cichocki, K., Maier, G. and Perego, U., Analysis of damages due to underwater explosions on a hybrid structure, *International Journal for Engineering Analysis and Design*, 1994, **1**, pp. 341-361
- [5] Molyneaux, T.C.K., Li, L.Y. and Firth, N., Numerical simulation of underwater explosions, *Computers Fluids*, 1994, **23**, pp. 903-911



Analysis carried out exploiting axisymmetry around axis 2. Threedimensional mesh: total radius $R_t = 10$ m, spherical TNT charge 100 kg in the center.

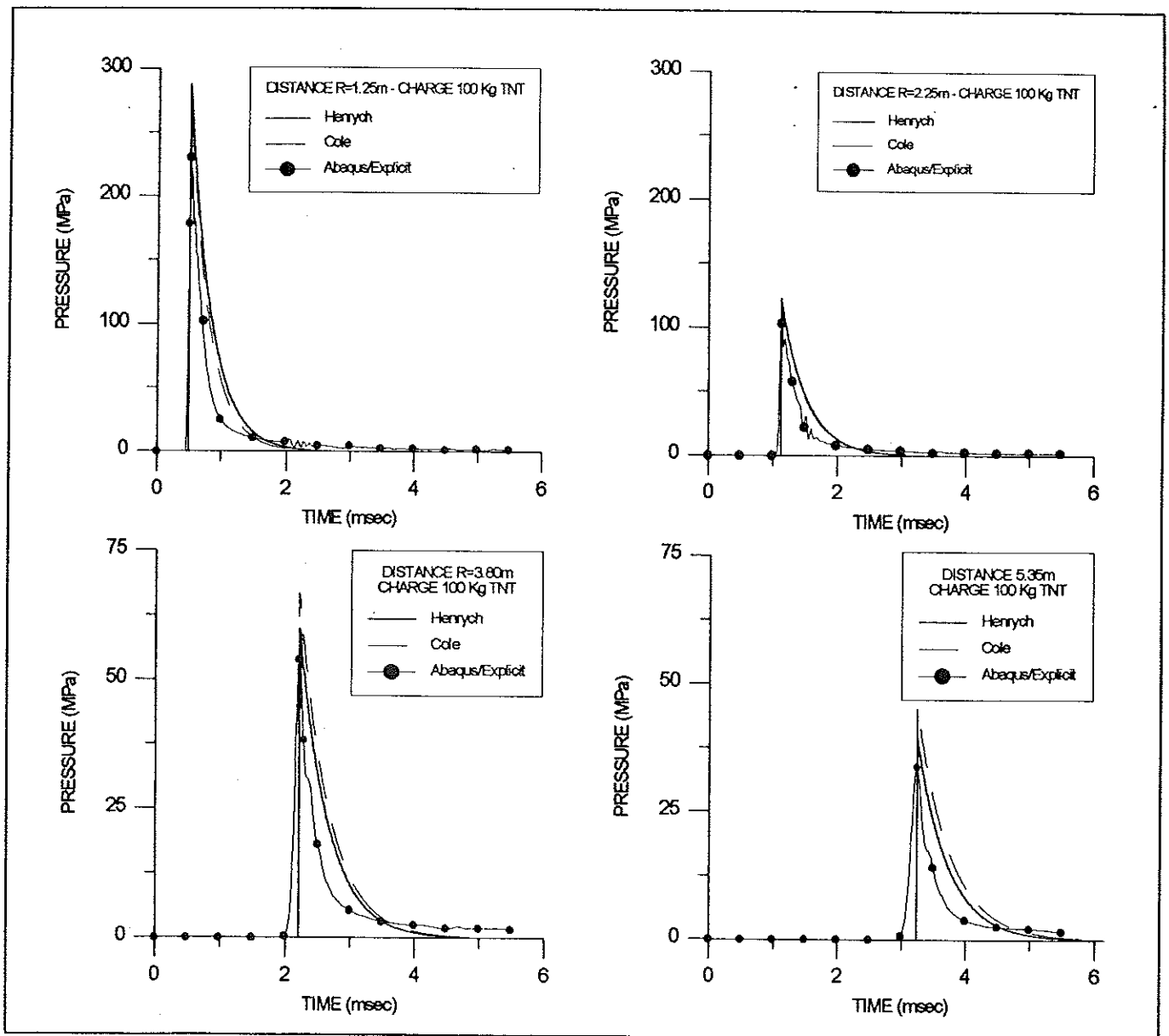
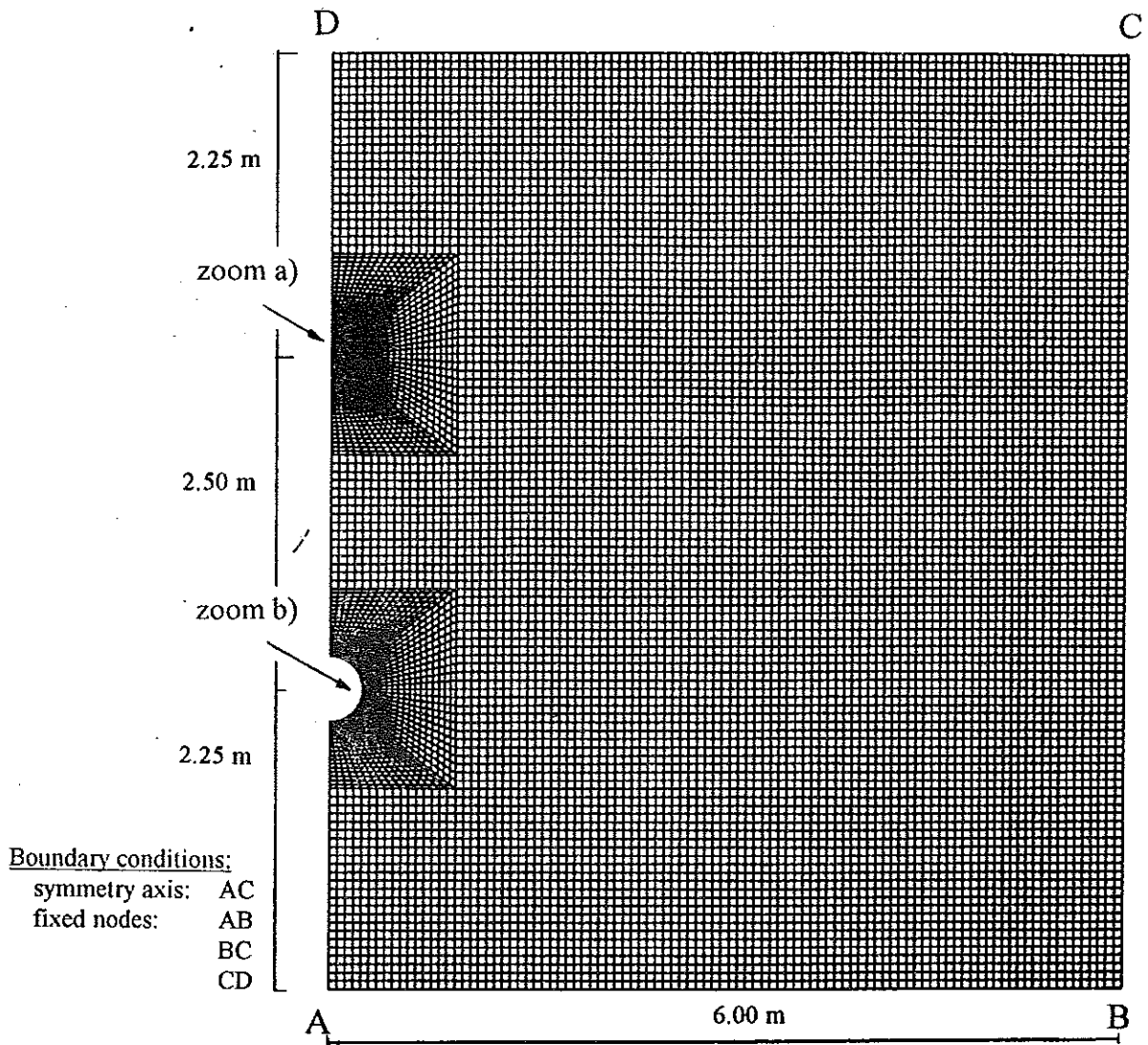


Fig. 1: Time distribution of pressure at four different distances R from the center of explosion: comparison between results of numerical simulations (dotted line) and predictions of Henrych [1] and Cole [2].



a) TNT charge (324 kg/m, diameter $D_c = 0.5$ m)

b) Rigid cylinder (radius $R_c = 0.25$ m)

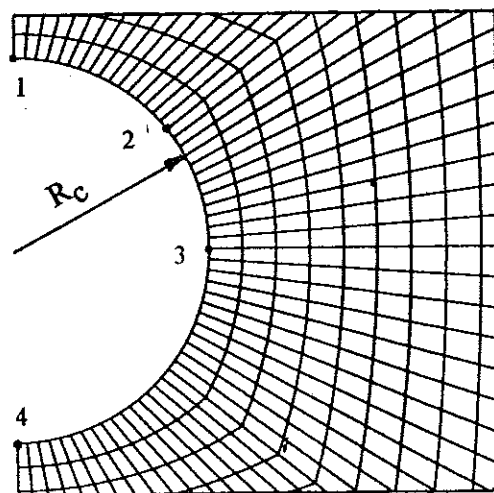
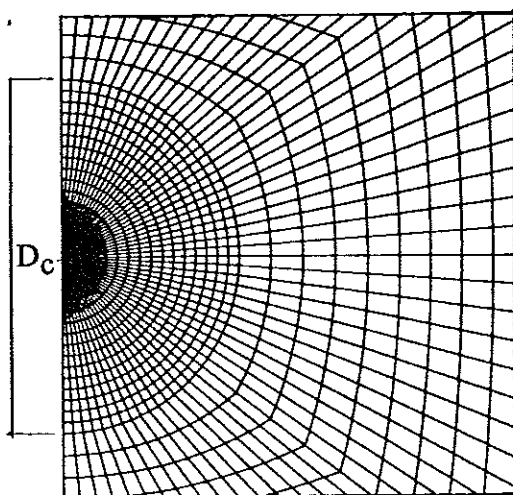


Fig. 2: Twodimensional, plane-strain mesh for the simulation of underwater explosion with explosive charge in "a". The structure is assumed as undeformable.

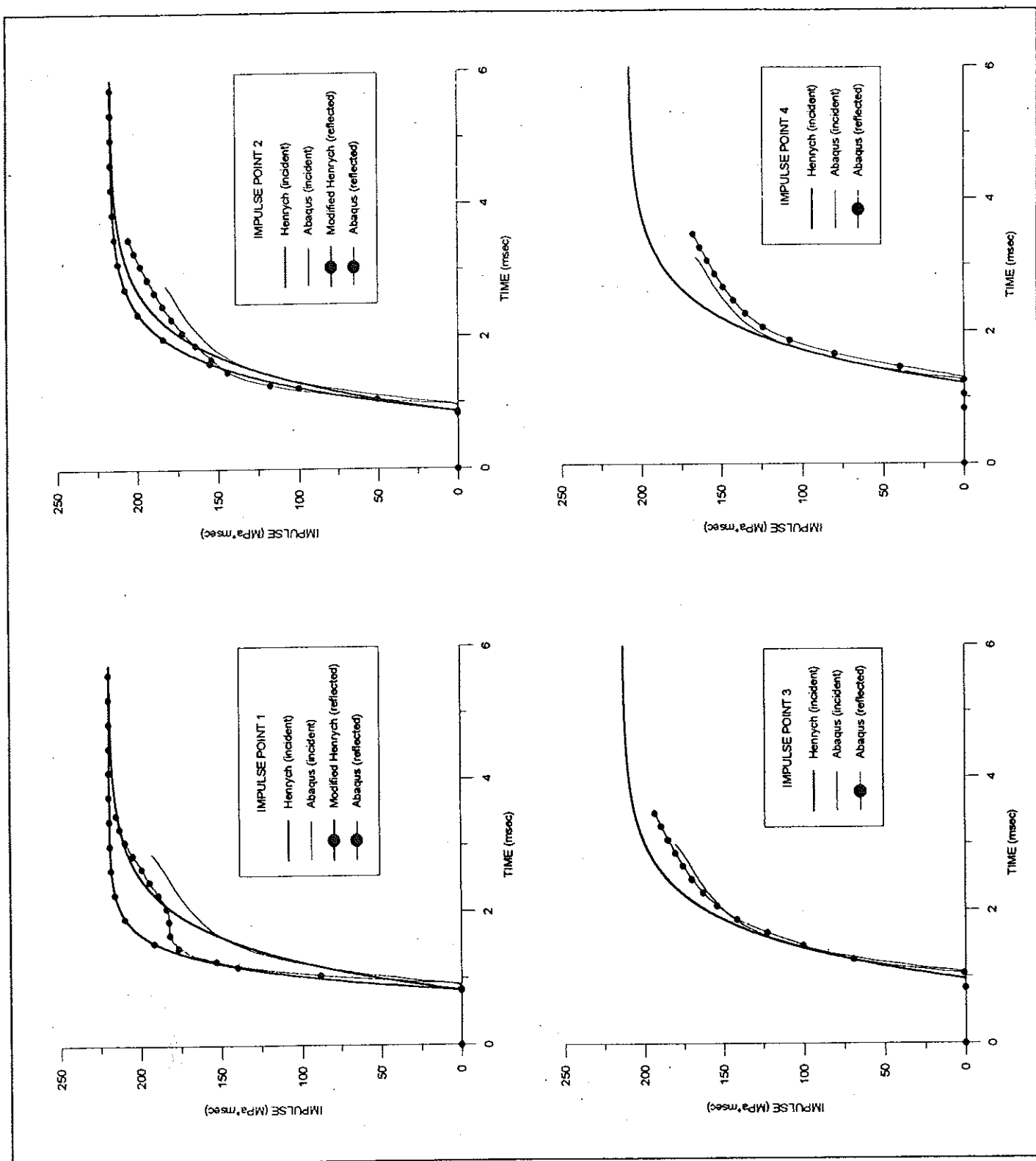
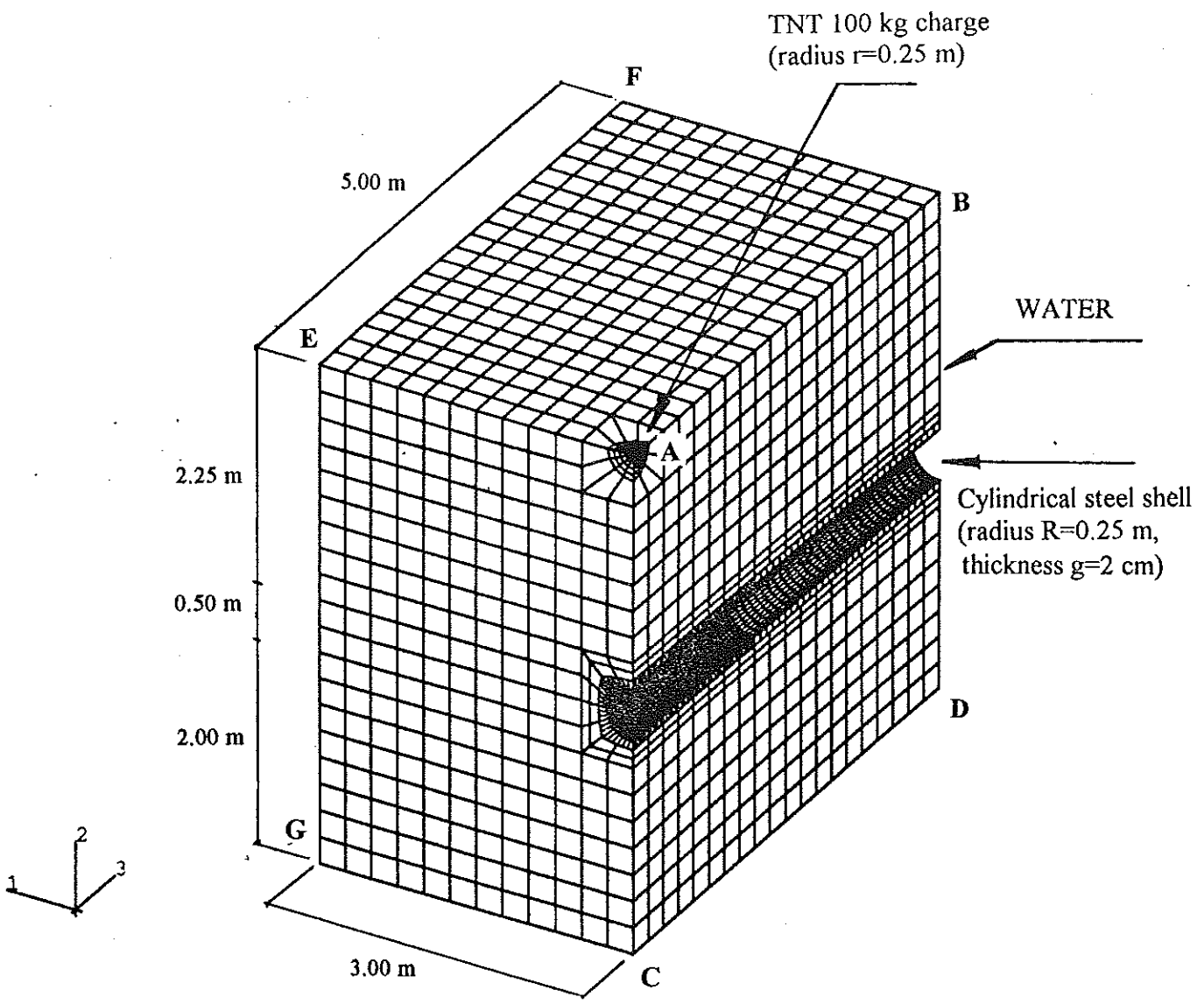


Fig. 3: Time distribution of impulse (incident and reflected pressure) versus time, at points 1 - 4 (zoom "b" in Figure 2). Numerical results are compared with Henrych's prediction.



Boundary conditions:

symmetry planes: ABDC
AEGC
ABFE

fixed nodes: EFHG (H - hidden node)
BFHD
DCGH

Fig. 4: Threedimensional mesh for the simulation of underwater explosion with explosive charge in A. Structure modelled as cylindrical deformable shell.

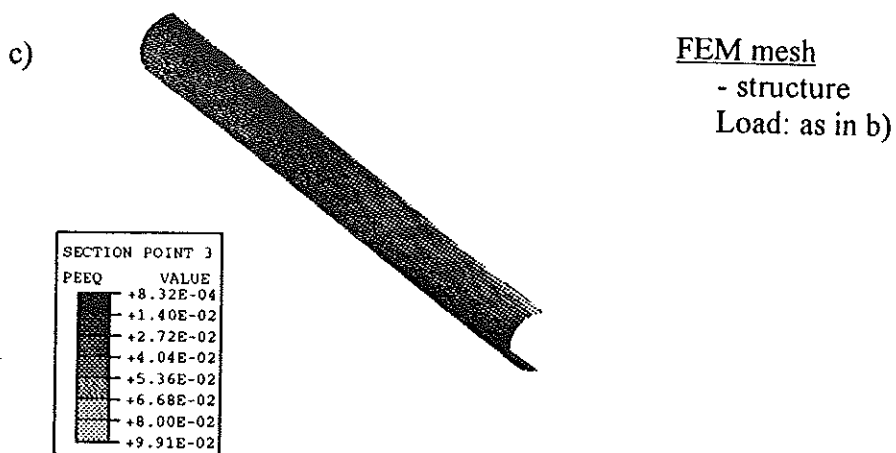
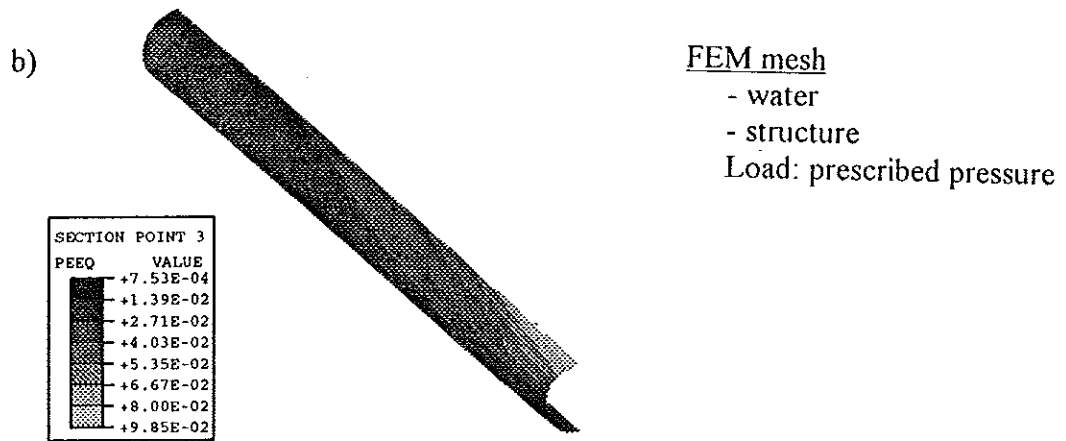
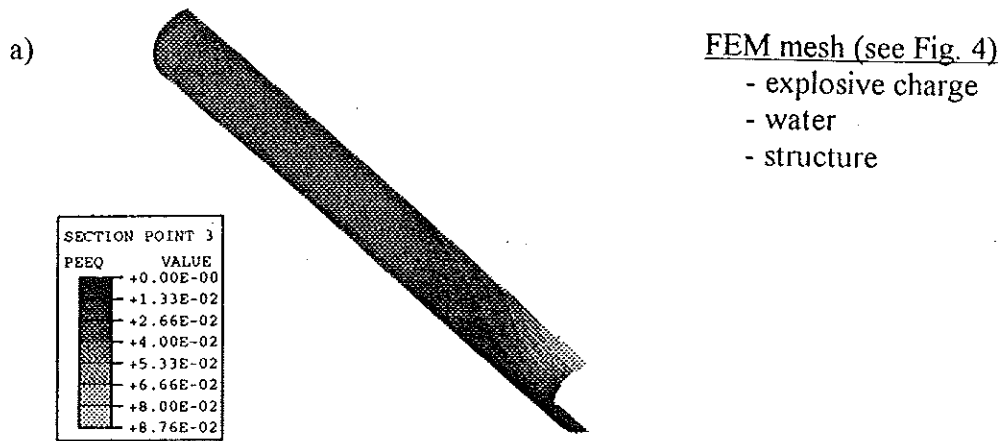


Fig. 5: Equivalent plastic strain ϵ_{eq}^p on the deformed midsurface of shell, for different finite element models of the problem.

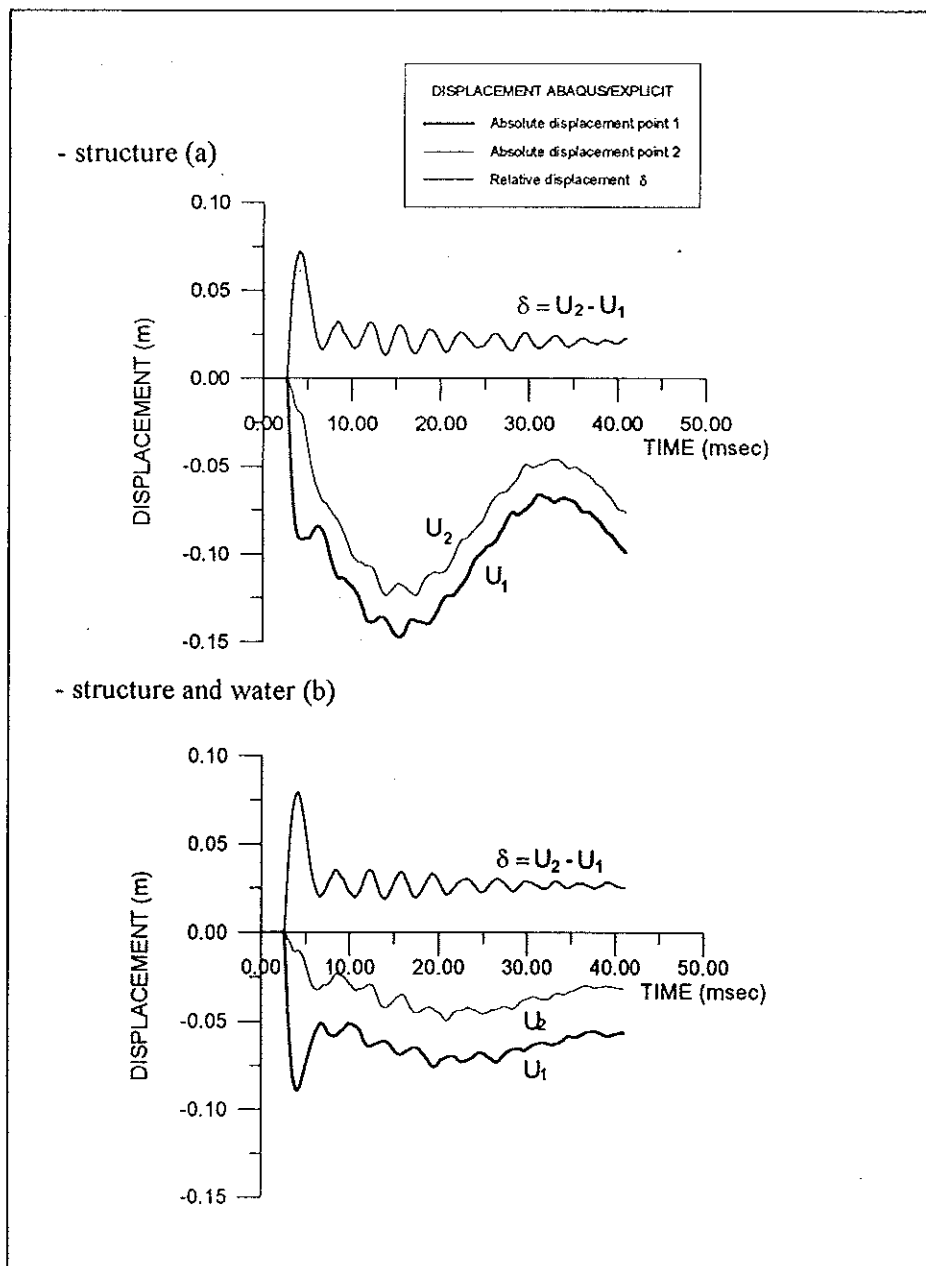
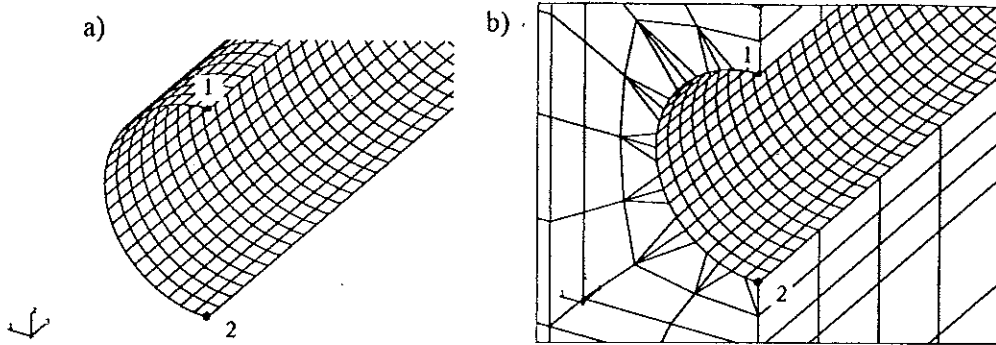


Fig. 6: Vertical displacement of two selected points for different FEM models:
 a) structure
 b) structure and surrounding water
 Load applied as prescribed pressure, varying in space and time.

A new French facility for the study of underwater explosions on naval structures.

Mohamed Mehaddi and Philippe Boyce

Centre Technique des Systèmes Navals - BP 28 - 83800 Toulon Naval (FRANCE)

SUMMARY : The new experimental pond built by the *Centre Technique des Systèmes Navals* close to Toulon (South of France) is presented in this document. The facility is devoted to the study of underwater explosions and their effects on reduced scale naval structures (nevertheless, their weight can reach 3 tons). The pond has a truncated cone shape with a 18 meter mean surface diameter, a depth of 7 meters and a 15 meter useful mean diameter at mid-depth. Charges of up to 7 kg (TNT equivalent) can be detonated ; for that, the concrete walls are protected by stones, which diffract the shock waves induced by the detonation and absorb a part of the energy.

The range of studies commonly performed in this experimental facility is quite large. To properly understand the response of naval structures subjected to shock wave loading, the analysis of bulk charge effects in water (shock wave and bubble phenomena) is frequently performed and specific measurement techniques are continuously being developed. The behaviour of shaped charges fired underwater (jet/water interaction, impacts) is also studied to predict the effects of new torpedo warheads against ships. So the deformation mechanism modeled by computers can be validated. The other types of high performance measurements deployed are transient pressure, surface stress, acceleration, local target velocity, shock wave velocity, high speed projectile (like jet-shaped charges) velocity etc. To record the signals from piezoelectric or piezoresistive gauges, a high performance 32 channels acquisition system is available near the pond.

In addition to all the gauges, high speed camera visualizations (from 1000 to 200 000 fps) can be obtained in streak or framing mode. For these kinds of visualizations, we use original high power lighting (in ombroscopy mode) in order to properly see the general physic phenomena and to accurately measure the characteristic distances (diameter of the bubble created by detonation gas products for instance).

The new French pond provides specific and complete means for assessing underwater explosive attacks and their effects : sensors and visualizations describe and quantify both the dynamic loading and the subsequent deformation mechanisms.

A- First part : general presentation of the equipment

A.1- INTRODUCTION

The Centre Technique des Systèmes Navals (CTSN) has the task of running studies on ship vulnerability on behalf of the Direction des Constructions Navales. Underwater explosions are one the different threats that have to be taken into account when designing a new ship. The CTSN thus has the responsibility of performing theoretical and experimental studies aimed at:

- increasing our knowledge of the effects of underwater detonations,
- establishing a correlation between attacks and structure responses.
- evaluating the performances of explosive compositions and warheads in an underwater environment.

In order to carry out these studies, the CTSN disposes of marine and ground test sites near Toulon.

A.2- THE CTSN TEST SITES - THE NEED FOR A DETONATION POND

A.2.1- The marine polygons and the ground sites

To detonate underwater charges, several sites are available. Such as :

- the pre-equipped polygon at Canier (south west of Toulon) : capacity up to 200 kg of TNT,
- the polygon at Carqueiranne (East of Toulon) : capacity up to 100 kg of TNT.

In the country, the Tourris test site (20 km north of Toulon) has two areas equipped with bunkers for explosions up to 10 and 250 kg respectively. These areas can accommodate all the different types of measuring equipment used for detonations: pressure measurement, rapid and ultra high-speed visualization, X rays, chronometry ...

A.2.2- The need for an underwater detonation pond

Although they are indispensable for the study of large charges, explosions at sea have a certain number of particularities that considerably increase the cost of a test:

- An experiment ship and all of its crew have to be mobilized for the day. The time it takes to travel to the site and perform the test must be taken into account,
- It is difficult to position accurately the different elements in a very rigid manner due to the effect of currents, of the surge, of the disturbances caused by the divers, etc.,
- Visualization is only possible using a fast camera (up to 3 000 pictures per second) placed in a watertight casing. Its positioning is also delicate (in particular, divers are required) and the positioning of additional lighting is almost impossible,

Performance of tests is subject to the weather and seasonal conditions (for safety reasons, it is forbidden to run this type of test during summer).

All of these reasons are sufficient to warrant the construction of a pond dedicated to the study of underwater explosions. Moreover many research tests involve very reduced-scale charges (~ 1 to few kg). This pond has been built in the Tourris site (guarded military compound north of Toulon) which will allow testing throughout the year, including during summer.

In addition, the following measurements can be taken during the detonation of a military charge (see § B.3 for details):

- transient pressure induced by propagating waves in water with tourmaline gages,
- surface stress on structures with polyvinylidene fluoride (PVDF) sensors,
- acceleration induced by shock with high frequency band width accelerometers,
- local target velocity with laser devices on structures,
- shock wave velocity and high speed projectile velocity using pin sensors.

What is more, the cinematography of the test makes possible the general understanding of the phenomena and the precise measurement of relevant distances and velocities (see § B.4).

A.3- THE TOURRIS UNDEX POND

An overall view of the pond and the associated equipment is reproduced in figure 1.

Note that:

- this pond has a truncated cone shape with a 18 meter mean surface diameter, a depth of 7 meters and a 15-meter useful mid-depth diameter,
- charges up to 7 kg (TNT equivalent) can be detonated.

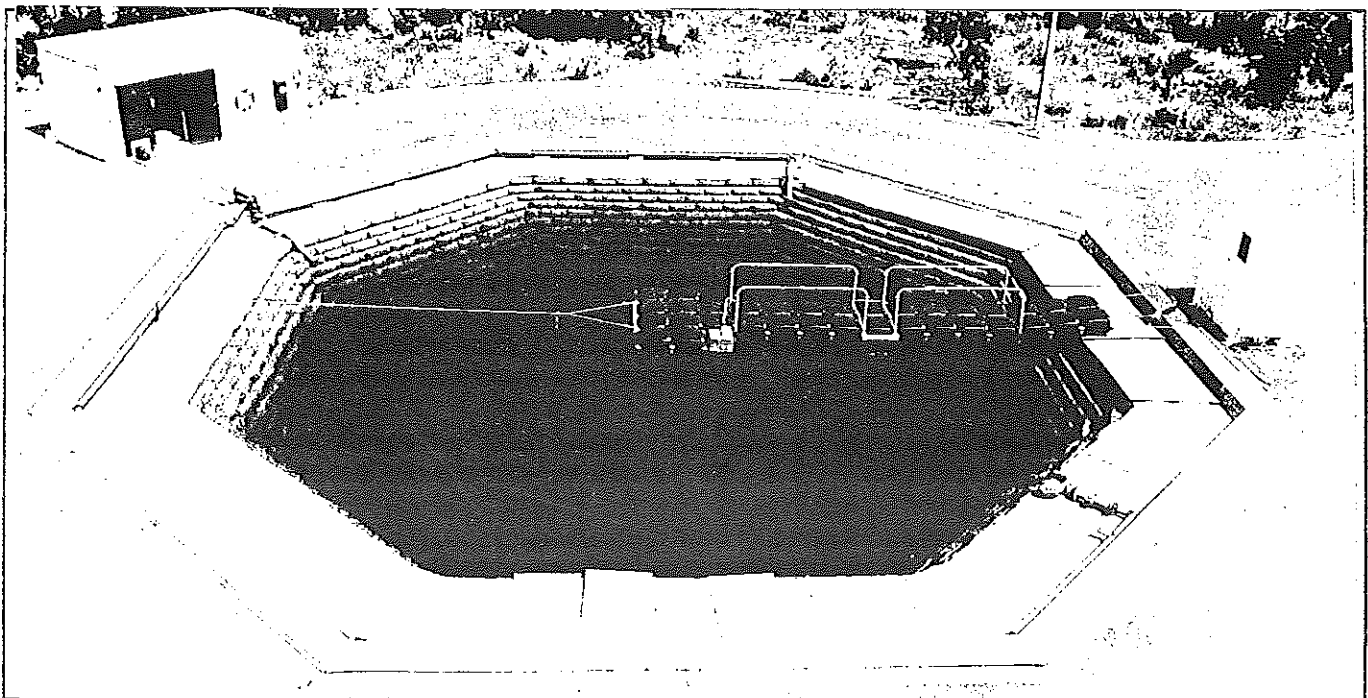


*figure 1 : General view of the site
ref : 93P109-15*

Rooms allow the preparation of the pyrotechnic charges, the protection of the personnel and the acquisition of measurements on the one hand, and the filtering and maintenance of the pond on the other.

The site is equipped with mobile telescopic crane capable of lifting 15 tons at 3 meters or 1,85 tons at 15 meters. This allows the placing of a 2 ton reduced scale target called « Méduse » in the center of the pond (see figure 2).

The "Méduse" is a rigid structure weighing two tons that contains deformable and removable zones [8]. The thickness, diameter and characteristics of the zones can be varied. So the "Méduse" allows all the extensometry, acceleration, displacement, and wall pressures measures repeatedly (see § B.3).

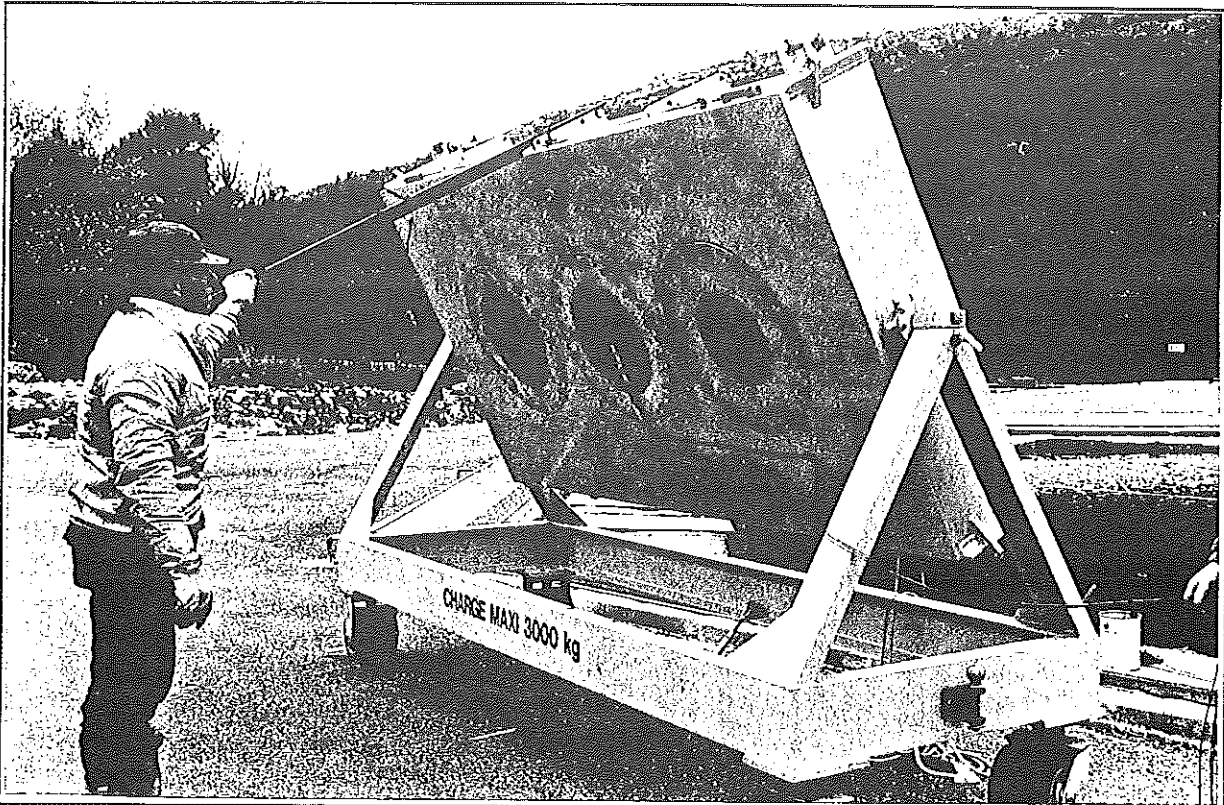


*figure 2 : « Méduse » test equipment
94P26-1*

A.4- PROTECTING THE WALLS

The framework of the pond is made up of reinforced concrete walls. It is covered by a tarred lining which ensures watertightness. It is imperative that the shock waves are diffracted as much as possible when they come into contact with the side. Water has a strong impedance which propagates high pressure waves, so the concrete sides have to be protected from the induced mechanical damages.

Two complementary solutions have been used :

- the pond has a truncated cone shape : this focalises the energy toward the free surface
- the sides are covered with "gabions". These consist of railway track ballast in felt sacks (to stop the dust from spreading) which are held in place by a wire netting framework. They diffract shock waves and prevent them from focusing.

It was decided to protect the sides with gabions after a series of tests carried out in a pond built on a 1/3 scale. In this pond, constructed to validate the different technical choices, several options for protecting the sides were tried : wooden beams, plastic material and rocks. These gabions proved to be the best energy diffractors. The two curves below show the pressure profile recorded in free water

and behind the wall respectively. A considerable reduction in the pressure can be seen, and in ideal circumstances, this reduction can reach 80%.

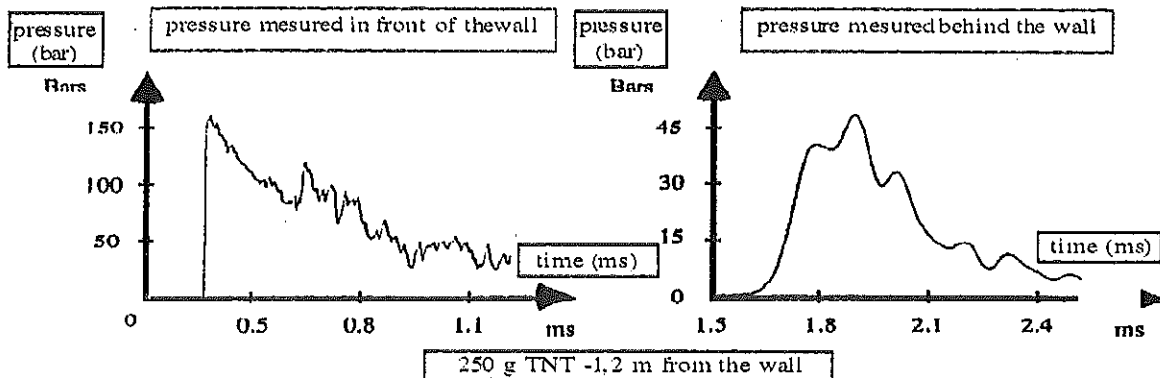


figure 3: Pressure in front of and behind the wall

B- Second Part : Associated Measuring Equipment

The second part of this document describes the physical phenomena encountered when a charge is detonated in water and then, using the CTSN detonation pond, to show how the phenomena can be reproduced. Finally, we describe the equipment (sensors, camera, periscope) which measures the values associated with these phenomena and which makes this site, as far as we know, unique in Europe.

B.1- REMINDER OF THE PHENOMENA CREATED BY AN UNDERWATER EXPLOSION

B.1.1- Free Field

An underwater explosion can be described in the following way : a detonation wave is propagating in the high explosive to transform the solid explosive into burnt gas which makes up the "gas bubble". When the detonation wave has reached the interface, it transmits a shock wave into the water. The bubble's gases have a very high pressure and temperature and under the effect of the difference in pressure between the interior of the bubble and the hydrostatic pressure and then the effect of water inertia, the bubble adopts a pulsatory behaviour characterised by the succession of cycles: initial radius - expansion - maximum radius - contraction - minimum radius. With each minimum radius value that passes, there is a secondary overpressure wave given off in the water.

As a general rule the pressure recorded near an underwater explosion shows the following characteristics :

- the shock wave induced on impact of the detonation wave with the explosive/water interface,
- secondary pressure pulse generated when the bubble containing the burnt gaz collapses.
-

The delay which separates these two events is called the pseudoperiod. It corresponds to the time the bubble takes to complete a cycle.

B.1.2- Close to a Structure

Parallel with this pulsatory movement, the bubble's center of gravity moves depending on the type of neighbouring walls. It can be noted that the bubble :

- rises to the free surface under the effect of the Archimede thrust in an infinite medium,
- sticks to the structures by hydrodynamic coupling if they are rigid.
-

The effects of the shock are modified because the target moves under the stress: the pressure on the target (called surface pressure) differs from the pressure in free water. The cavitation and the reflection phenomenon are predominant [1].

In addition, the secondary shock effects may become significant because the bubble has a tendency to draw closer more quickly to the structure during its contraction phase (which precedes the shock emission). The importance of the display of the bubble migration as well as measuring the effects on the structure are obvious.

B.1.3- Special case of Shaped Charges

Shaped charges are the subject of numerous studies in the atmosphere in order to improve their penetration performance. In water these charges exhibit a lower penetration performance (water acts as an armor). They are likely to create the same effects as a compact charge : shock waves and bubble.

The study of jet penetration in water is in itself complicated as it involves not only the water forming into a crater (and the particularity of the fluid compressibility), but also the shock waves associated with the supersonic jet and the lengthening or fragmentation of the jet in the crater being formed [2], [3].

The experiment must be highly instrumented in order to estimate the part each phenomenon takes or to separate the effects of the charge detonation and those created by the shaped charge jet. This can be done in the CTSN pond.

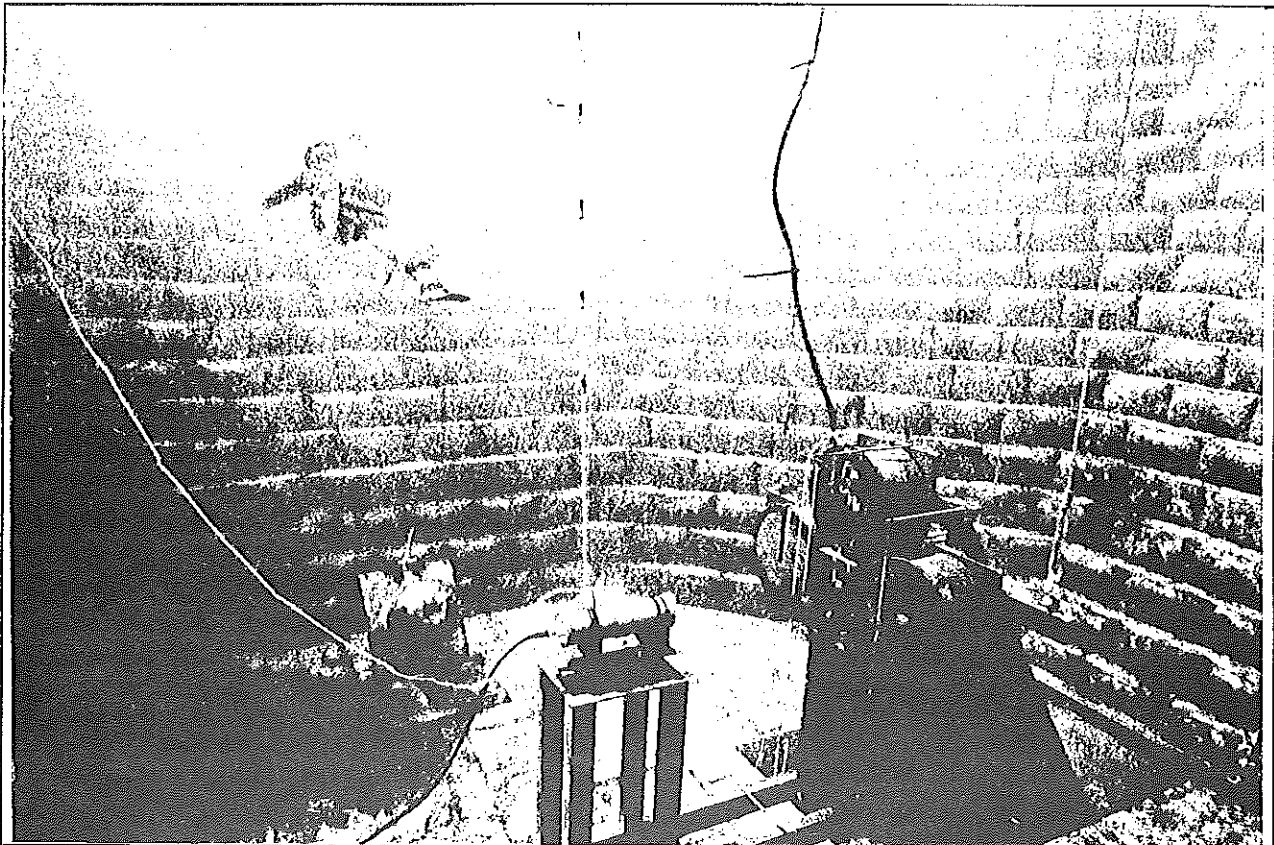


*Figure 4 :Detonation in pond of a shaped charge
93P156-9*

Figure 4 shows the detonation of a shaped charge in the pond where the following measurements were made :

- pressure in free water,
- deformation of metallic membrane on drums using extensometer gauges,
- penetration depth in armor steel plates [4],

The whole of this is completed by the rapid display (1000 images per second) of the bubble expansion using a camera placed in a shock resistant case (see § B 4).

B.2- REPRODUCING THE PHENOMENA

B.2.1- Ignition

The quality of the measurements depends on the ability to reproduce the test configurations. Ignition by exploding bridgewire ensures good reproduction of the initiation because it is not subject, as in the sea, to line lengths that are too great and which deform the leading edge of the electric pulse. In addition, during tests at sea and due to vibrations produced during transit, the recrystallised PETN pellets in the detonator may settle and reduce its sensibility [5].

The charge is detonated using an exploding bridgewire detonator (without primary explosive) and a high energy unit. This is a device which can provide the detonator with a Very High Voltage pulse from the mains power supply. There are two types :

- automatic : the very high voltage signal is provided, once the circuit is closed, at any given moment, located by the synchronous emission of a low voltage signal (a few volts) called fire top.
- controlled : the very high voltage signal is provided at a given moment. It corresponds to sending a low voltage signal to the unit. This mode is preferred to the previous, for the ultrafast display, for synchronisation reasons.

The fact it is a ground site allows a large number of tests to be carried out on the detonator only, before each detonation, in order to check the good working order and synchronisation of the firing circuits, the acquisition system and the display system. In this way as many presets as desired can be carried out, thus increasing the detonation success rate and above all the success of the measurements.

B.2.2- Standardization

The characteristic values of an underwater explosion are linked to the shock wave transmitted in the water and to the bubble behavior. They are :

- the pressure field (pressure time history),
- the time constant of the exponential decline of the pressure in a given point,
- impulse (integrale of pressure with respect to time),
- energy (integrale of the pressure squared with respect to time),
- the bubble pseudoperiod and maximum radius.

Their measurement was subject to norms set down by scientists and industrialists competent in their field. These norms establish the operating mode to be adopted by the different French laboratories so that the measurements can be compared and are homogeneous. Moreover, they require test material including at least :

- a pond with a diameter greater than 10 meters and a depth greater than 6 meters
- pressure sensors and the acquisition device used in conjunction with a pass-range greater than 2 Mhz
- a firing device
- calibrated signal generator.

The CTSN test conditions easily meets these requirements. In addition it is possible to measure the values associated :

- with the bubble movement,
- with the interaction with the structures,
- with the penetration of a shaped charge jet in water thanks to high-speed visualizations.

The main problem to be solved to record these phenomena is linked to the difference in time scales which characterise them. These differences are illustrated using the following orders of magnitude :

- formation of crater speed for a shaped charge jet : 5 mm per us.
- shock wave rising time less than 1 us,
- shock wave time constant : from 10 to 100 us,
- bubble pseudoperiod : from 10 to 100 ms (ie 10 000 to 100 000 us)
- bubble radius expansion speed in the order of 30 m/s.

B.3- SENSOR MEASUREMENTS

One of the advantages of the pool is that all of the desired measurement equipment is available on site. Thus it allows the greatest possible reduction of the constraints imposed by an underwater environment.

The sensors used are either piezoresistive, piezoelectric, or short-circuit types. They allow the measurement of:

- the pressure of the free water as a function of time: tourmaline piezoelectric sensors,
- the surface pressure (in contact with a side): polyvinylidene sensors,
- target deflection : piezoresistive extensometry gauge,
- shock induced velocity of metal membranes: laser telemeters,
- acceleration of the structures subjected to dynamic charges : large band accelerometers, chronometry of hypervelocity projectiles or shock waves. This falls in the use of the contacts or the « pin » gages.

B.3.1- Pressure measurement in free water

These measurements are taken by active piezoelectric sensors that, under the force of the pressure on a crystal, produce a signal without the need of electrical power. However, taking into consideration the small quantity of electrostatic charges given off at the terminals with an unlimited impedance, a charge amplifier must be used (requiring a power source) to produce a measurable signal.

The CTSN uses British sensors (AWE). They are equipped with a small and robust tourmaline crystal, and can thus take high dynamic pressure (more than one kilobar).

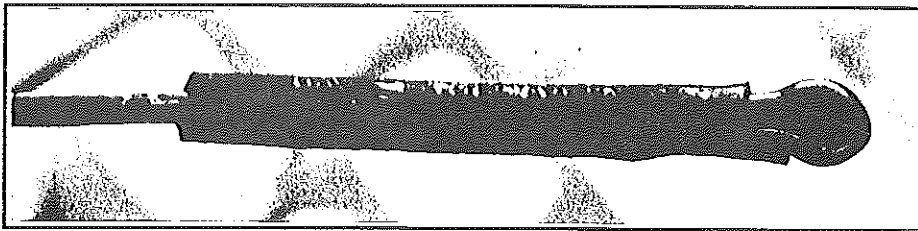


*figure 5 : tourmaline pressure sensor
95P173-9*

The charge amplifiers used (Kistler, type 5007) transform the charge into a voltage proportional to the first receptive stage, then definitely calibrate the signal according to the chosen scale.

The pressure measurements are taken in compliance with standard operating modes (§ B.2.2).

B.3.2- Surface pressure measurements

These can be taken with the tourmaline pressure gages described above, or with polyvinylidene fluoride gauges (PVDF) [6]. The PVDF gauges are composed of CH₂-CF₂ monomers placed on a stretched plastic film several microns thick. After having placed two copper electrodes on the polarized film, everything is packed between two kapton sheets.

For the measurement, the gauge is linked to a capacitor with a resistance (50 ohms). The voltage of the capacitor terminal is recorded. This voltage is proportional to the stress acting upon the gauge.

The advantage of this type of sensor is that it can take very high pressures (up to 500 kbar) but its sensibility to lateral stress distorts the measurements by producing parasite stress. This parasite stress must be estimated by adding another gauge (of constantan, alloy of copper and nickel, for example) to the structure. The gauges must be fixed with particular care, as is the case for the strain gages.

B.3.3- Deformation measurements

The sensors are extensometers with resistive wires and their purpose is to measure structure deformation. The extensions measured are in the order of microns per meter. The deformation measurement comes down to an resistance measurement that is taken using a Wheatstone bridge linked to a conditioner-amplifier (see figure 7, § B.3.7). The high shock levels are capable of

dislocating the sensors. This is why the gauges must be fixed on the structure with care (degreasing, surface grinding, pH neutralization, etc.)

B.3.4 - Acceleration measurements

The acceleration levels and the frequencies encountered are both very high in an underwater explosion: up to 10^6 g and 1 MHz. This is why the sensors used must meet given requirements :

- the sensor must remain fixed to the structure (withstand strength)
- it must have a wide pass band
- there must be a good signal - noise ratio : it is necessary to use low pass filters to limit the noise generated by the resonance of the structure to a dozen Hertz.

The CTSN has developed low pass mechanical accelerometric filters that have a high dumping coefficient. These filters have improved the signal acquisition conditions. Nonetheless, difficulties remain when the shock factor of the explosion is greater than 0,6. In this case, the acceleration measurement can be obtained by doing a double derivation of the displacement.

B.3.5 - Displacement measurements

The effects of the underwater explosions can be evaluated by measuring the indentations and the residual deformations induced on the targets. But these measurements, taken after the fact, do not allow the examination of the indentation of the structure as a function of time and the evaluation of the impact of the primary shock wave, of the secondary pressure pulse.

These arguments have caused the CTSN to conduct a study with the goal of developing non-contact optical sensors ("µe Mess Technik" type) (figure 6).

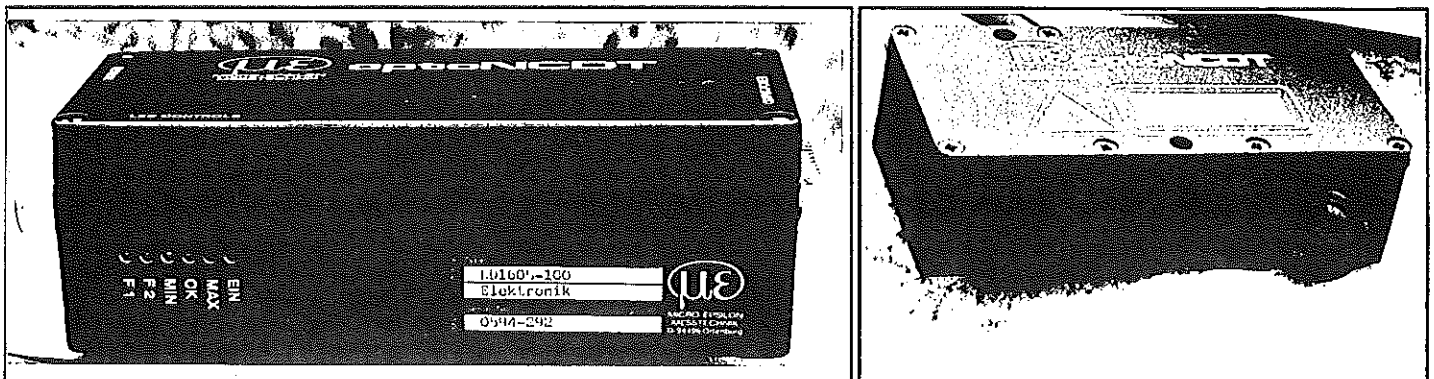


*figure 6 : laser telemeters
95P173-18*

These telemeters use the triangulation principle and their installation is precisely described in the document [7].

B.3.6- Chronometry

These measurements are taken with a contact probe or with pin sensors. The contact probes are composed of a rigid frame containing two conductive sheets (aluminum) separated by an insulator. Connected beforehand to an electric chronometer and put in contact with the passage of the projectile, they generate a measurable pulse. As for the pin sensors, they are preferably used to measure the speed of the shock wave (or the speed of detonation in the explosive) since their functioning principle rests on the ionization of the air located between two electrodes or target deflection velocity.

B.3.7- Measurement Acquisition and Processing

The short-circuit sensors (either contact or pin) are linked up to a multichronometer (32 channels available). Piezoresistive sensors are linked to a Wheatstone bridge which puts into proportion the extension, resistance and voltage variations. The tourmaline sensors are linked to a charge amplifier and the polyvinylidene sensors to an integrating circuit. The signals are finally recorded and digitized

using an acquisition system (Krenz TR6510) that has two types of measurement channels "slow" (sampling on 12 bits and at 2 MHz for 128 ms or 256 000 points), and "fast" (sampling on 12 bits and at 200 MHz for 2,5 ms or 512 000 points).

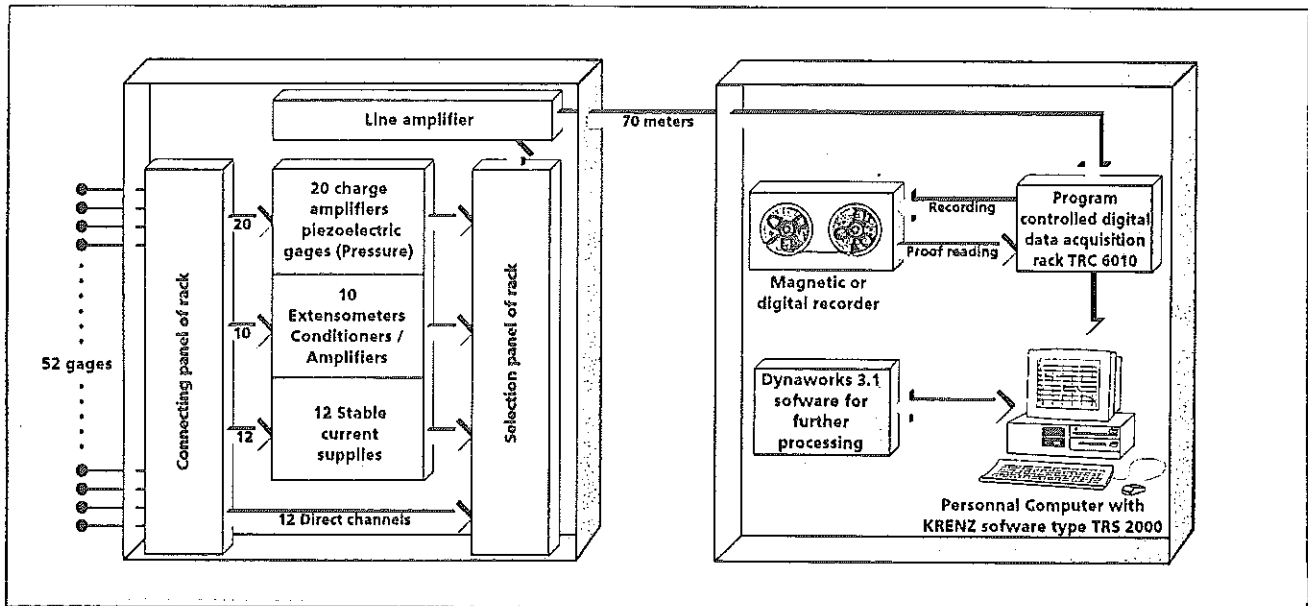


figure 7 : acquisition mimic display

In the case where this assembly is insufficient, the acquisition can be completed using 52 channels connected to a magnetic recording instrument.

The processing of these signals can be done in two ways :

- Using software in the micro-computer. Directly on site, this type of processing is very useful during the detonation of a series of explosions. The validity of the previous explosion can be quickly validated,
- Using the DYNWORKS software (designed by Intespace) located in the workplace, as a data base for experimental results.

B.4 HIGH-SPEED CINEMATOGRAPHY

To complete the information gathered by the sensors, the pond is equipped with visualization equipment. This equipment is very useful in underwater detonation, and more precisely in the analysis of the behavior of the gas bubble near a structure.

Visualization can be done in two ways:

- The camera is placed in watertight and shock resistant casing with the porthole facing the surface to take advantage of the daylight. Thus additional lighting is not required. Divers are required to adjust the optical axis. The range of rates is limited from 1000 to 3 000 pictures per second.
- The camera is installed outside of the pond, and thus is protected from the explosion. The observation is made using an optical system installed in a retractable periscope. The assembly is designed to resist a maximum of 150 bars and a shock factor equal to 0,3 (or a 2 kg explosion at 4,5 meters). It is necessary to use lighting that is appropriate for the visualization rate, which can vary from 1000 to 200 000 images per second [9]. Research in this field is progressing.

This second option has the advantage of allowing a quantitative analysis because the distance measured on the film are reliable and precise. This is possible because of the type of camera used, the type of lighting available (ombroscopy with a sight on the screen) and because adjustments can be made using the periscope. Moreover, the processing can be made by using computer image station.

Below, the diagram showing the principle of the assembly.

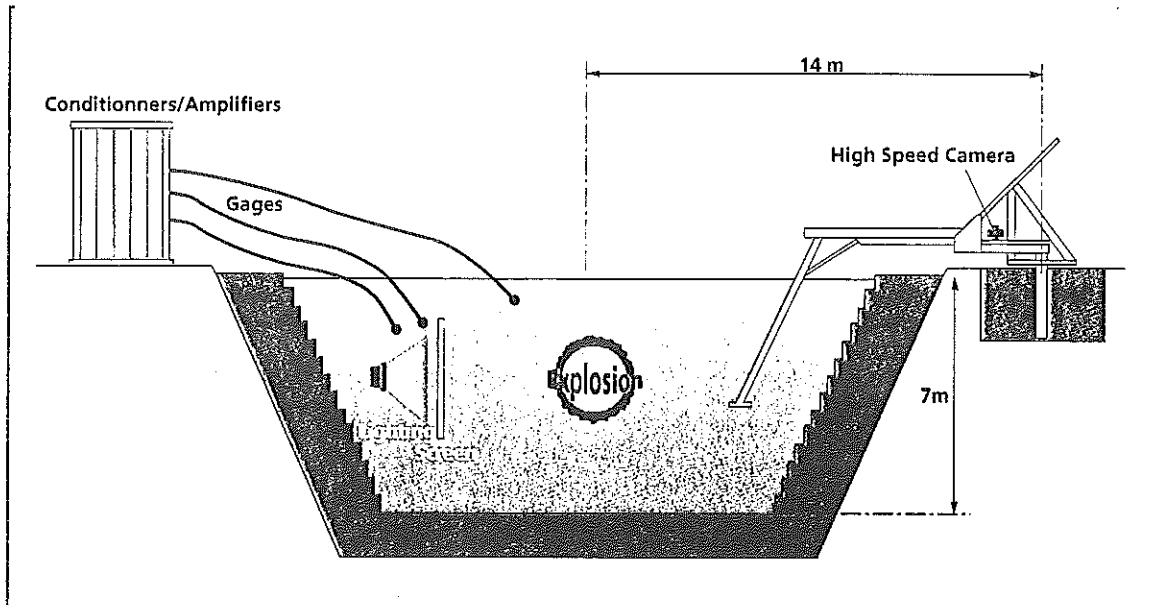


figure 8 : Periscope-camera visualization system

Note that this camera operates either in frame mode or streak mode. Its characteristics are:

- in frame mode : 500 images at a speed of 1000 to 200 000 i/s
visualization field : max : 4 m x 4 m ; min: 0.5 m x 0.5 m,
- in streak mode : Sweeping speed of 0.01 to 0.3 mm/ms
resolution of 0.25 ms.

C- Conclusion

In conclusion, it is important to retain that the CTSN has an experiment pond (depth of 7 meters, average useful diameter of 15 meters) in which can be detonated an explosive mass of up to 7 kg. It can receive a target structure weighing up to 15 tons. A total of 86 measurement channels can be simultaneously recorded: 32 digital channels (frequency of up to 2 MHz) and 54 analog channels on a magnetic recording instrument.

The pond has also "fast" and "ultrafast" visualization equipment that operates in frame and streak mode.

All of these characteristics make the Tourris pond, as far as we know, unique in Europe.

REFERENCES

[1] Auroire - « Calcul analytique de la réponse en grandes déformations de plaques soumises aux explosions sous-marines » NT 90/89 Gerpy, date: 01/12/90.

[2] Mehaddi - « Efficacité de charges creuses CCEB 62 contre des cibles comportant un module d'eau » n°23 CTSN/MDTC/DR- 95, date: 20 /02/95.

[3] Thibaudier, Tosello - « Étude de la cratérisation de l'eau par des éléments ed charges creuses » n°10 CTSN/MDTC/DR- 95, date: 27 /01/95.

[4] Mehaddi - « Tirs CCA 100 (charge creuse aluminisée 100 mm) en piscine » n°1224 CTSN/MDTC-CC/93, date: 29 /09/93.

[5] Fournier - « Méthodologie des explosions sous-marines » NT 78/89 Gerpy, date: 13/07/89.

[6] Boyce - « Réunion du groupe d'experts techniques TFG1, TFG3 et TFG4 dans le cadre des travaux du WEAG-TA 29 » n°164 CTSN/MDTC/95.

[7] Auroire - « Méthodologie de mesure de déplacement en détonique par capteurs optiques »- n°35 CTSN/MDTC/95, date: 05/04/95.

[8] Damiano - « Vulnérabilité du navire aux explosions sous-marines, exploitation du moyen d'essai Méduse » - n°56 CTSN/MDTC/94, date: 11/05/94.

[9] Mehaddi - « Visualisation des explosions sous l'eau à des cadences élevées dans le bassin du CTSN » n°86 CTSN/MDTC/NP, date: 29/09/95

- forcing function SPS
- comparer à solution analytique

Evaluation of Mesh Refinement Considerations in Finite Element Analysis of Stress Wave Propagation

Andrew Tyas (Research Associate) & Alan J. Watson (Reader)

Department of Civil and Structural Engineering
University of Sheffield, U.K.

1. ABSTRACT

Stress wave propagation is an important consideration in a range of dynamic analyses, from the local response of structures undergoing blast or high-velocity impact loading, to the use of Kolsky bar techniques to determine dynamic material properties. In the numerical analysis of such cases, it is vital that the characteristics of the stress wave are accurately portrayed as the wave passes through the solid.

It is well known that a major cause of inaccuracies in numerical analysis of wave propagation is spatial discretisation which filters out the higher frequencies associated with the wave, and induces spurious oscillations within the mesh. It is clearly important for the designer/analyst to use suitable element sizes for a particular wave propagation problem, or be aware of the loss of accuracy which choosing elements of the wrong size entails.

In order to determine the magnitude of the effect of spatial discretisation, a series of simple undamped one-dimensional wave propagation analyses has been conducted using the DYNA3D explicit finite element code. Element sizes have been varied and the effect on wave parameters assessed. Relationships between element size and quality of wave propagation are demonstrated, and recommendations are given for element size in terms of wave frequency and material properties.

2. INTRODUCTION

In many dynamic analysis problems, the response of the structure as a whole is of primary interest and detailed knowledge of stress wave propagation through the structure is unimportant. However, in a small but important number of areas, stress wave propagation is the crucial factor. For example, in high velocity impact or explosive loading of brittle materials (e.g. concrete), tensile reflections of stress waves from free surfaces can cause a tensile failure close to the surface, with the size and velocity of the fragments being dependent on the parameters of the stress wave. Similarly, in the use of a Kolsky, or split Hopkinson pressure bar, the magnitude and duration of the stress waves in the bar are required in order to calculate the dynamic properties of the material under test.

Finite element analysis of stress wave propagation is becoming increasingly common. For example, Ross *et. al* (1995) have performed finite element analyses of Kolsky bar tests using the ADINA package, whilst Barton *et. al.* (1993) and Krauthammer *et. al.* (1995) have used DYNA to study high strain rate tensile tests on steel specimens and stress wave propagation through composite materials respectively.

Finite element modelling of stress wave propagation has a major drawback, in that the effect of spatial discretisation is to cause dispersion and attenuation of the wave, and to introduce spurious oscillations (see figure 1).

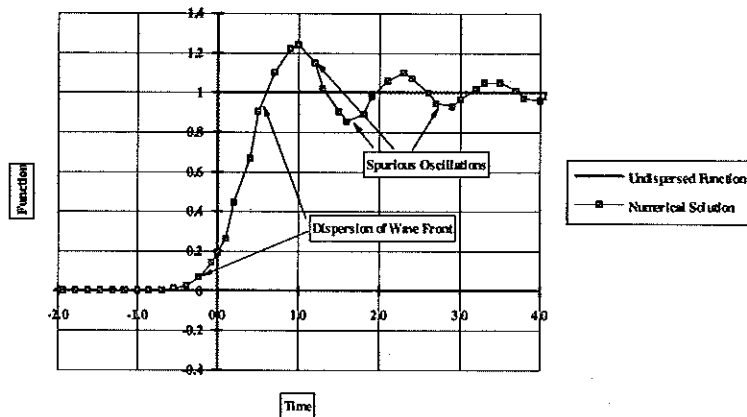


Fig 1 - Example of Dispersion and Spurious Oscillation in Finite Element Modelling of the Propagation of a Step Function.

The oscillations may be filtered during post-processing (Jiang and Rogers, 1990), but the root cause of the problem is the finite distance between integration points in the finite element mesh, and assumptions and approximations in the numerical method. It has been shown (Mackie 1992), that the use of a consistent mass matrix does not produce significant improvements over the lumped mass matrix (which is commonly used for reasons of computational cost). The same author did obtain significant improvements by using a combination of the consistent and lumped mass matrices, though this requires either that the code is written by the user, or that access to the source code of a commercial package is available, in addition to requirements of programming capability and time.

More simply, improvements in the quality of wave propagation may be achieved by reducing the element size. This method however has obvious consequences for computing cost, especially in the explicit codes frequently used for this type of analysis, where the time-step between calculation cycles is directly proportional to element size (Zienkiewicz and Taylor, 1991). It is extremely important therefore, to find an optimum element size for a given analysis.

The relationship between the wavelength (λ) of a propagating wave and the distance between integration points (Δ) has been identified as the critical parameter. Intuitive estimates of "acceptable" values of the ratio $\frac{\lambda}{\Delta}$ have been suggested, though with no indication that these figures have been

checked in actual analyses. Hitchings (1993) suggests $\frac{\lambda}{\Delta}$ between 5 and 6 as a realistic minimum and indicated that this ratio was not affected by the type of element used. The purpose of this paper is to describe a series of simple finite element analyses which have been conducted to test the validity of this assertion when applied to the widely used DYNA3D code.

3. A BRIEF OVERVIEW OF DYNA3D

DYNA3D is an explicit finite element code, which uses the central difference method to integrate the equations of motion. The code was originally devised using single point integration elements, which means that calculations are carried out at one point only for each element (at the centre of the element), rather than at each node point. As a result, at any time-step, the strain is assumed to be constant across an element, rather than varying according to a shape function. This assumption results in significant increases in computational efficiency (Hallquist 1991), but at the cost of a reduction in accuracy. Recent upgrades of the code have introduced the option of elements with

multiple integration points, but the single point integration elements are still frequently used and have been employed in this work.

4. DESCRIPTION OF THE 1-DIMENSIONAL WAVE PROPAGATION MODEL

The model analysed in this work consisted of a simple bar, 500m long and 1mm square cross-section. The finite element model of the bar was composed of shell elements 1mm wide and a nominal 1mm thick. The axial length of the elements was varied between analyses - see Table 1. Shell elements were used rather than 1-D truss elements since it is intended that this work be extended to look at two dimensional effects.

A linear elastic material model was used, loosely based on the material properties of steel ($E = 200kN / mm^2$, $\rho = 8000kg / m^3 \rightarrow c = 5000m / s$).

An axial forcing function was applied to one end of the bar, causing the velocity of the nodes at that end of the bar to vary through a half sine wave, of peak magnitude 1m/s and duration 5 μ s (see fig 2). This corresponded to a wave frequency (for the full wave cycle) of 100kHz.

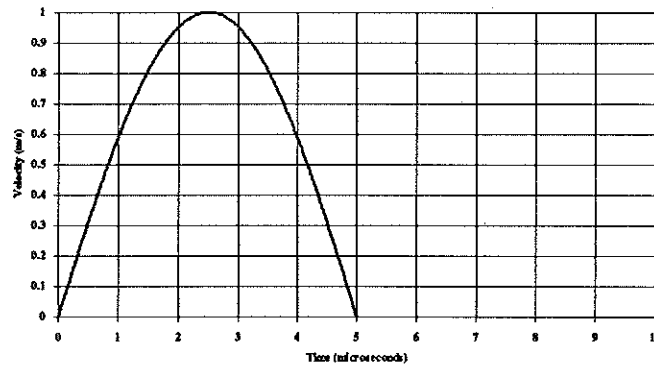


Fig 2 - Forcing function applied axially to one end of the bar

The wavelength of this wave in the steel bar is given by:

$$\lambda = \frac{c}{f} = \frac{5000}{100,000} = 0.05m$$

$$\lambda = 50mm$$

Where:

λ =Wavelength

f =Frequency

c =Elastic Wave Speed

Details of element lengths for the four analyses which were conducted are given in Table 1.

After the input pulse is applied to the end of the bar, the disturbance thus generated should ideally travel axially down the bar with velocity c (=5000m/s or 5mm/ μ s) arriving at a

<u>Run Number</u>	<u>Axial Length of Element</u>	$\frac{\lambda}{\Delta}$
1	1mm	50
2	2.5mm	20
3	5mm	20
4	10mm	5

Table 1 - Element Lengths

distance X mm along the bar after time $X/5 \mu\text{s}$. Again, ideally, the pulse should be unaffected by its propagation along the bar, so that the axial velocity imparted to each node should vary as shown in figure 2, with time zero now signalling the time of arrival of the pulse at the node. In practice, the pulse is affected by its passage along the finite element mesh which represents the bar, and the divergence of the results from the finite element analysis from this ideal is shown in the following section.

5. RESULTS OF THE NUMERICAL ANALYSIS

Figures 3 to 6 show the response to the input pulse of nodes at distance 50mm, 100mm, 200mm and 400mm (or λ , 2λ , 4λ and 8λ) from the front of the bar, with element sizes of 1mm, 2.5mm, 5mm and 10mm (or $\lambda/50$, $\lambda/20$, $\lambda/10$ and $\lambda/5$) respectively.

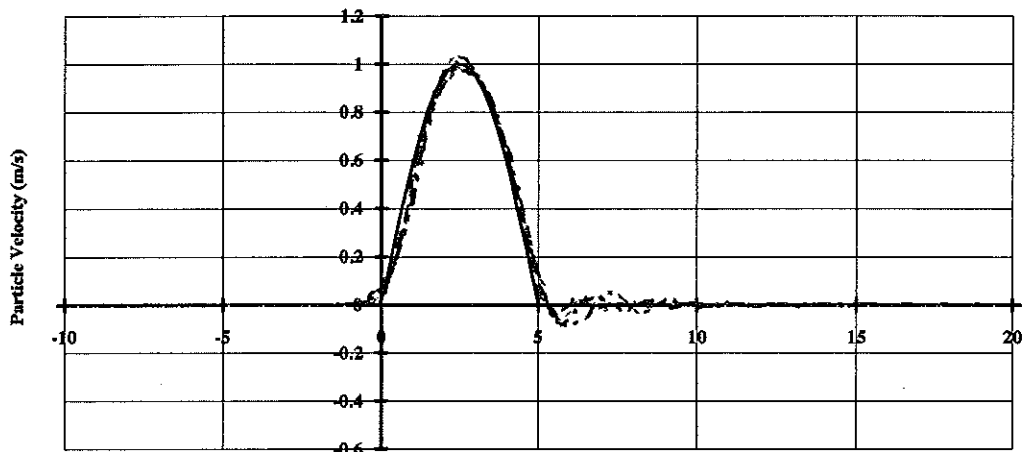
The difference between the input function and the results from the finite element analysis increases markedly with increasing element size. With $\Delta=1\text{mm}$ ($\Delta/\lambda=50$) - fig 3 - pulse appears to be virtually unaffected as it propagates along the bar, with the spurious post-pulse oscillations being of small magnitude and rapidly decaying. However, when $\Delta=10\text{mm}$ ($\Delta/\lambda=5$) - fig 6- the pulse has become highly distorted after propagating just a few wavelengths along the bar, and post-pulse oscillations are approaching the magnitude of the main pulse itself.

More detailed analysis of the magnitude of the errors in:-

- i) the arrival time of the start of the pulse
- ii) the arrival time of the peak magnitude of the particle velocity induced by the passage of the pulse
- iii) the peak value of the particle velocity
- iv) the duration of the pulse

for the different models is given in figures 7 to 10.

The percentage errors in the arrival times of both the start and the peak value of the pulse are relative to the ideal arrival times discussed in section 4 above. The "start" of the pulse is defined as the time at which the trace passes through 1% of the peak value. In the cases of errors in arrival times (figures 7 and 8), a positive value indicates that the pulse arrives earlier than the theoretical arrival time (based on wave speed and distance from the end of the bar), whilst a negative value indicates late arrival.



Re-based Time (microsec) - (Time zero corresponds to the time at which an undispersed wave would arrive at the point in question)

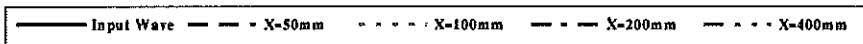
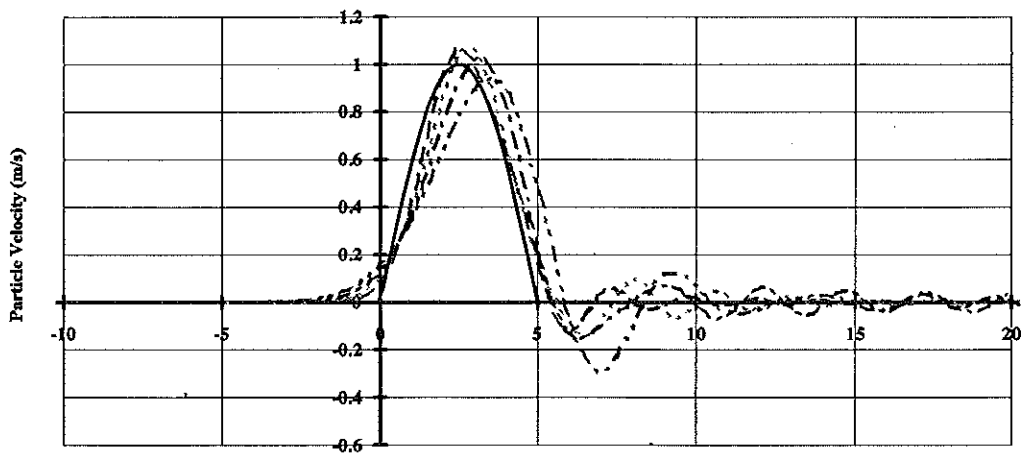


Fig 3 - Finite Element Wave Propagation Model - Element Size 1mm



Re-based Time (microsec) - (Time zero corresponds to the time at which an undispersed wave would arrive at the point in question)

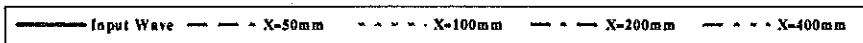
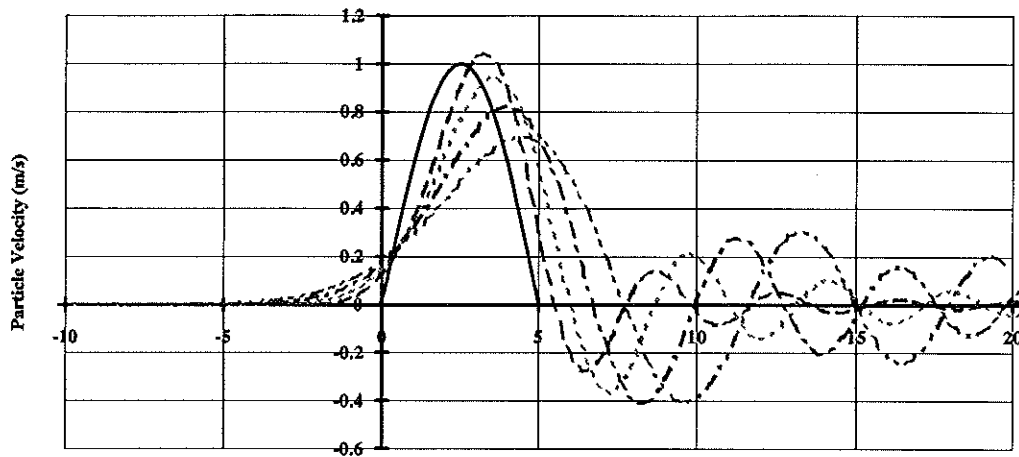


Fig 4 - Finite Element Wave Propagation Model - Element Size 2.5mm



Re-based Time (microsec) - (Time zero corresponds to the time at which an undispersed wave would arrive at the point in question)

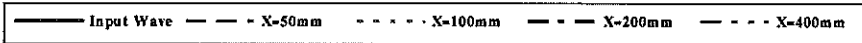
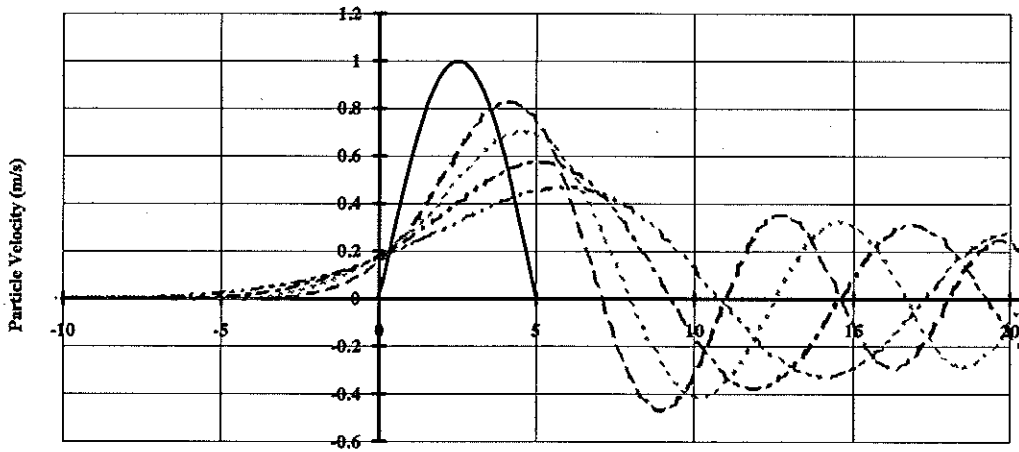


Fig 5 - Finite Element Wave Propagation Model - Element Size 5mm



Re-based Time (microsec) - (Time zero corresponds to the time at which an undispersed wave would arrive at a distance X from the front of the bar)

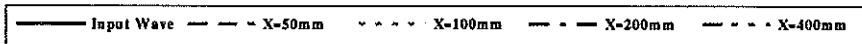


Fig 6 - Finite Element Wave Propagation Model - Element Size 10mm

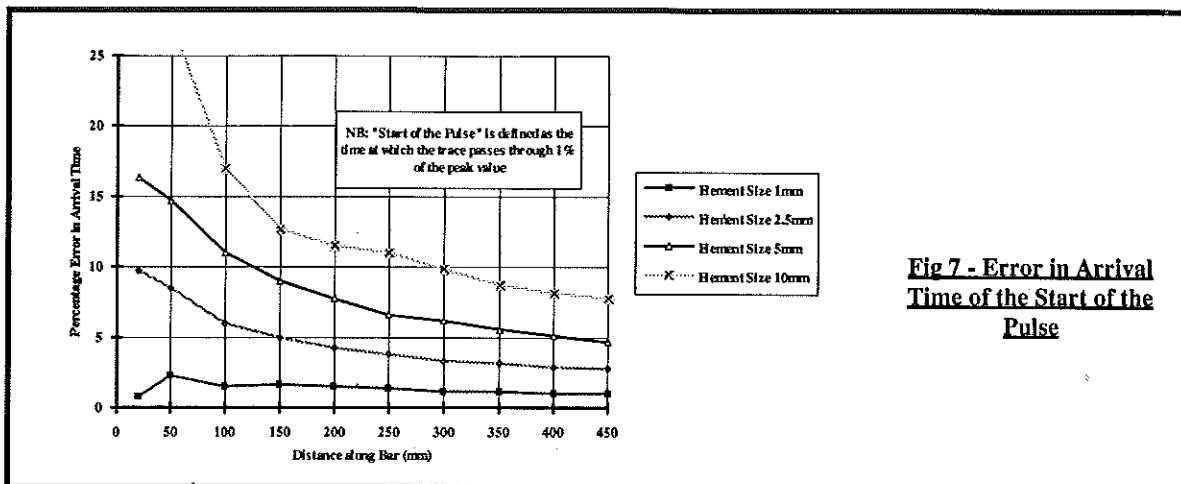


Fig 7 - Error in Arrival Time of the Start of the Pulse

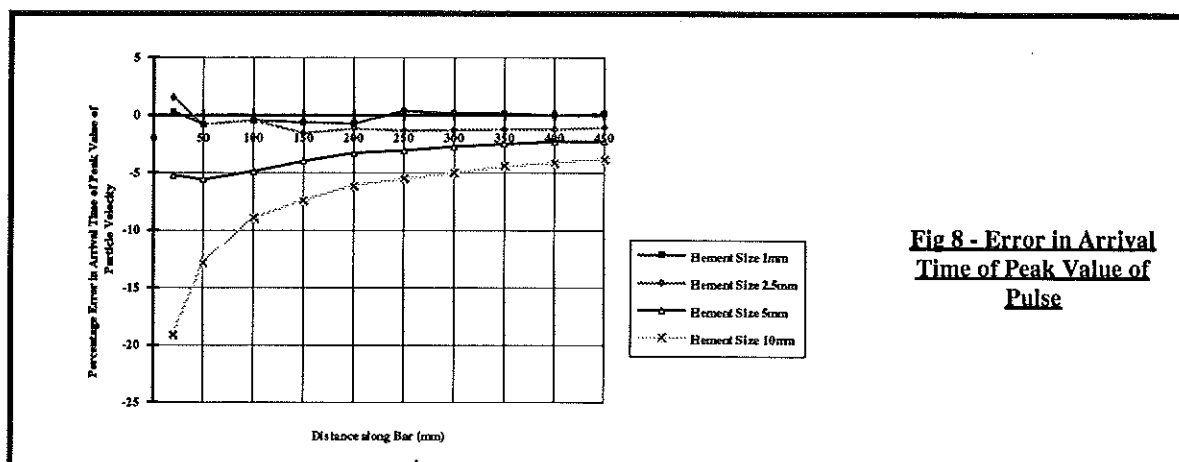


Fig 8 - Error in Arrival Time of Peak Value of Pulse

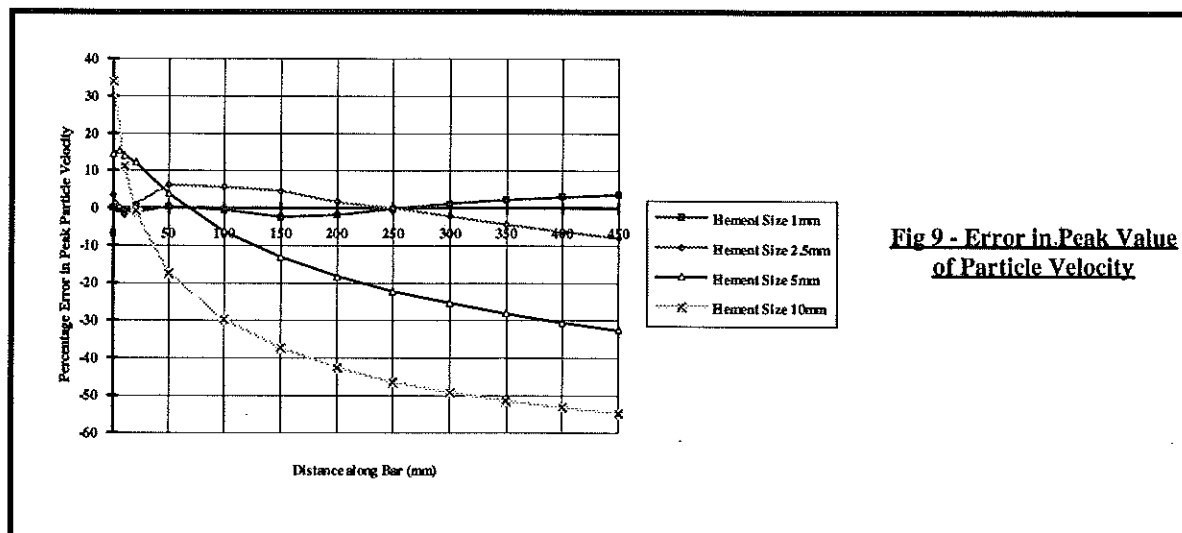


Fig 9 - Error in Peak Value of Particle Velocity

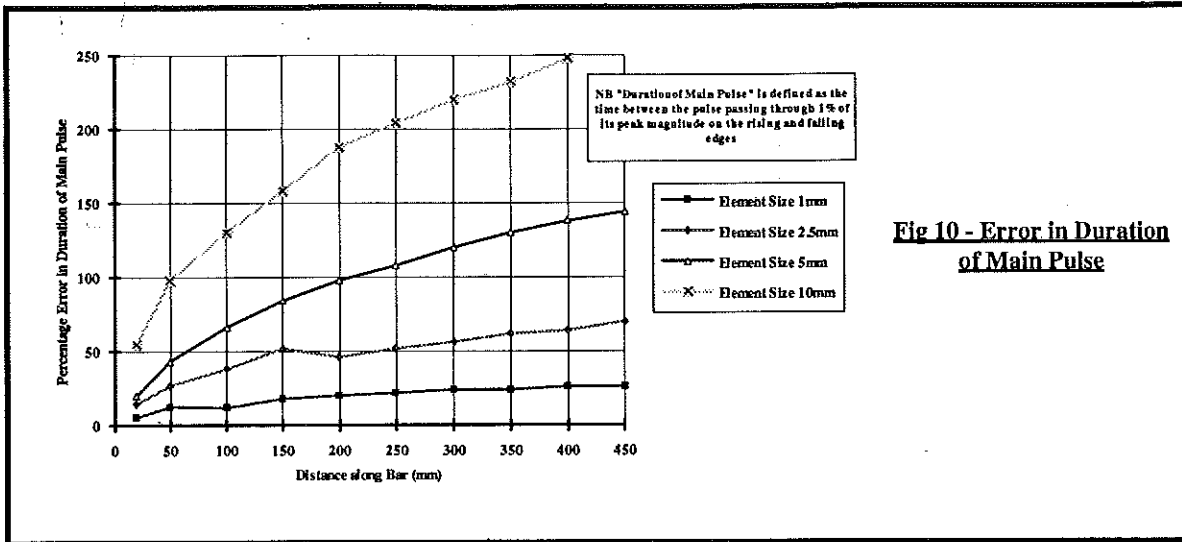


Fig 10 - Error in Duration of Main Pulse

6. DISCUSSION

The data presented in figures 3 to 10 demonstrate that in order to obtain accurate representation of wave propagation in a finite element analysis it is of crucial importance that a suitable element size is used. Clearly, the "quality" of the results from a finite element analysis is a matter of judgement for the analyst. However, in the authors' opinion, the ratio of $\frac{\lambda}{\Delta} = 5 - 6$ suggested by Hitchings (1993) would produce unacceptable errors in most wave propagation problems. It appears that, for the DYNA3D code, $\frac{\lambda}{\Delta}$ in the range 20 - 50 is more appropriate. Analyses employing multi-point integration elements should produce acceptable results at lower values of $\frac{\lambda}{\Delta}$, though, since these elements are inherently more expensive, it is unclear whether a net benefit would accrue.

The errors related to the distance which the wave has travelled require closer inspection. Errors in the pulse duration (fig 10) clearly increase with distance, the rate of increase being greater with larger element sizes. The peak particle velocity in the pulse (fig 9) generally decreases with distance propagated (as the pulse becomes longer and flatter - see figure 6 for example), though for the larger element sizes at shorter distances, the error is an *increase* in the peak magnitude. The reason for this is believed to be that, when a mis-match occurs between the frequency of the propagating wave and the element size, some of the energy associated with the wave is trapped in the element and reverberates in it rather than being passed onto the next element. At short propagation distances, the net effect of this trapped energy together with the energy from the forcing function arriving at the element for the first time may be to produce a net increase in the peak response. By the time that the wave has propagated to longer distances however, the peak value has already decayed to such an extent that even the addition of trapped energy is insufficient to produce an overall increase in peak response.

The effect of propagation distance on arrival times (figs 7 & 8) may be somewhat misleading. The *absolute* magnitude of the error actually increases with distance, though not at the same rate as the theoretical arrival times, hence the decrease in *percentage* errors.

It is suggested that an analysis such as that described in this paper could be used at an early stage in the development of a finite element model to enable the analyst to make an informed judgement on the element size to be used. This would require a knowledge of the frequency

components of the wave(s) propagating through the body under analysis. This is relatively straightforward in cases where the waves are generated by an explicitly defined loading function. In other situations, it would be necessary to perform a spectral analysis on the loading function, to determine the highest significant frequency, and base the element size on that frequency. For instance, if the wave is impact loading, it may be necessary to analyse data from preliminary analyses to gain some indication of the frequencies generated, before the final mesh size is chosen

7. CONCLUSIONS

The use of a simple model has clearly shown that the magnitude of errors which occur in a finite element analysis of wave propagation through a body are functions of the ratio of element size to wavelength and the distance which the wave has propagated.

In any finite element analysis, the analyst has to carefully balance conflicting demands of limited time and computational resources with the magnitude of error which is acceptable. The model described in this paper provides a quick and simple means by which the analyst may obtain a better understanding of the effects of mesh refinement on the accuracy of his results.

8. REFERENCES

BARTON, D., CHURCH, P., MIRZA, A., and WAHEED, M., (1993), "Further Investigations of the Tensile Test using DYNA2D", Proceedings of the 1993 DYNA3D Users Group Conference.

HALLQUIST, J.O., (1991), "LS-DYNA3D Theoretical Manual", Livermore Software Technology Corporation, CA 94550

HITCHINGS, D., (1993), "Structural dynamics in Theory and Practice - A companion to the NAFEMS Finite Element Dynamics Primer", Strucom Consulting Engineers.

JIANG, L., and ROGERS, J.R., (1990), "Effects of Spatial Discretisation on Dispersion and Spurious Oscillations in Elastic Wave Propagation", International Journal for Numerical Methods in Engineering, Vol. 29, pp 1205-1218 (1990)

KRAUTHAMMER, T., O'DANIEL, J.L., GUICE, R.L. and JENSSEN, A. (1995), "Backfill/Backpack Effects on Shelter Response", Proceedings of the 7th International Symposium on Interaction of the Effects of Munitions with Structures, 1995

MACKIE, R.I., (1992), "Improving Finite Element Predictions of Modes of Vibration", International Journal for Numerical Methods in Engineering, Vol. 33, pp 333-344, 1992

ROSS, C.A., TEDESCO, J.W. and KUENNEN, S.T. (1995), "Effects of Strain Rate on Concrete", ACI Materials Journal Vol. 92 No. 1, Jan-Feb 1995

ZIENKIEWICZ, O.C. and TAYLOR, R.L. (1991) "The Finite Element Method", McGraw-Hill, Maidenhead (1991)

The Theoretical Analysis in Explosive Reforming of Casing Pipe of Oil Well

Prof. Kai Zhang
Dalian University of Technology
Dalian 116023, CHINA.

Abstract

This paper gives the predictable formula of explosive charge used in explosive reforming of casing pipe of oil well under detonation of explosive, and the relation between the dilatation magnitude of pipe wall and explosive charge. The mechanism of rupture of pipe wall is also explicated.

Key Words: Explosive Reforming; Eccentric Explosion; Material Strengthening.

1. Introduction

The casing pipes of extracting well and water flooding well are subjected influences of statistical factors such as stagger moving of stratum and dilatation of mudstone and so on, so the partial deformations of pipe wall are always appeared, but not get ruptured, to make the internal diameter of casing pipe not to achieve deserved passage diameter, thereby the various extracting oil instruments can't reach the bottom of well, the works of extracting oil will be hindered. Through the one special explosive technology, the due explosive charge be carried to the part of deformations, after explosion, the passage diameter which has been narrowed will be expanded, but not to make rupture of casing pipe. Whether or not this special explosive reforming technology can be attained successful, depends to accurate calculation and layout of explosive charge. Secondly, we place the explosive charge in casing pipe that it can be done eccentrically only to fix up, because the two ends of explosive column are only to be fixed up to the center line of casing pipe in which part the deformations are not existed, so due to the eccentric explosion the pipe is

appeared to rupture easily; The mechanical mechanism of this rupture kind is also the theoretical problem ought to be solved.

2. The calculation formula of explosive charge for the explosive reforming of casing pipe

The deformed casing pipe is not only to have patial deformations but also to appear great longitudinal curve, so it is diffucult to set up the explosive column to the centre line of transverse section of casing pipe which is already deformed; Secondly, there are much differences for compressive resistance outside wall of well which deponds to the depth of the place where is to be deformed and the deformation degree of that pipe wall. It is not only diffucult to count on all these factors, but also unrealistic. For this reason, we'll select the mechanical model of computation; selecting the cylindrical pipe not deformed and supposing that the explosive charge is set up at the central axis of cylindrical pipe, on the basis of principle that the energy density accepted by the pipe wall is equalized to the deformation energy of cylindrical pipe^(1,2), to deduce the formula for the calculating explosive charge, at the same time, in order to count on the deformation energy of the rocks and the wall of a well just outside the pipe, the coefficient k which can be determined by a large number of land exams and practical exams underneath a well, is introduced. This formula is :

$$W = 1.343k \cdot \sigma \cdot \epsilon (D_1^2 - D^2) \sqrt{\lambda^2 + \frac{D^2}{4}} \quad (1)$$

where W — explosive charge (kg), σ — static yield stress of casing pipe material (MPa), ϵ — maximum strain of internal diameter at time of dialatating pipe, D — internal diameter of pipe before dialatation (m), D_1 — outside diameter of pipe before dialatation (m), λ — the half length of explosive column (m), k is coefficient generally taking $k = 2.5 \sim 3$. Using formula (1) to make a large number of practical exams, we have all achieved very effective predicatable value. The exams concerned shown in below Table 1.

Table 1

Number of exams	depth of well at point deformed (m)	D (m)	practical measurement of internal diametre after reforming (m)	length of explosive column (m)	weight of explosive charge (kg)	ϵ	practical measurement of strain	error (%)	indications
1 [#]	955.4	0.122	0.131	2	0.467	0.0741	0.0738	0.4	the reforming at different depth in same well, first carrying 1 [#] out, second 2 [#] and 3 [#] . At the same depth of the same well getting three explosion in order of priority 4 [#] , 5 [#] and 6 [#] .
2 [#]	846.6	0.119	0.1316	2.5	0.7716	0.1003	0.1058	5.27	
3 [#]	952.6	0.1186	0.125	1	0.309	0.1002	0.054	85.5(*)	
4 [#]	881.8	0.1014	0.1137	2	0.6173	0.1165	0.1213	3.96	
5 [#]	881.8	idem	idem	2	0.463		0(*)		
6 [#]	881.8	idem	idem	2	0.7716		0(*)		

(*) In above table, 1[#], 2[#], 3[#] are the cases of reforming at different sections deformed in same well, every reforming is all gotten on independently, where there is great error in 3[#] reached 85.5%, this is due to that the explosion point of 3[#] is close neighbour and on top of the explosion point of 1[#], 1[#] is progressed prior 3[#], the upper end of its explosive column departs from the pipe wall at 952.6M only having 1.3M, after explosion in 1[#], there is already 1mm over dilatant amount and there is a remarkable strengthening in material⁽⁴⁾, according to practical measurement, after explosion, the hardness of material of casing pipe has been raised 2.7 times, so it is attributed to that the value of σ in formula (1) will exceeds far from the static yield stress. In the same reason, the exam 5[#] is gotten on after 4[#] and the 6[#] is progressed again after 5[#] at the same place, these two explosions for dilatation are not all achieved the goal, this indicates that the explosive reforming of casing pipe must be accomplished only once for all, the multi-explosions at same place don't be carried effective result.

3. The mechanism of rupture of pipe wall at the time of eccentric explosion of explosive column in cylindrical pipe.

When the explosive column departs from the center of cylindrical pipe, if

the amount of charge is too excessive, the rupture of pipe wall will be appeared. The point of rupture is occurred in the points A and B, which is symmetrical to horizontal line and farther from charge, but not appeared in nearest point to the charge (see Fig.1), in order to indicate this phenomenon appeared in experiments, we produce the numerical analogue computation⁽³⁾. The cross-section of pipe is ellipse, the internal radius of minor axis is 46mm and the radius of major axis is 69mm, the diameter of charge column 22mm, bias distance 10mm, detonation velocity 6500m/s, from the

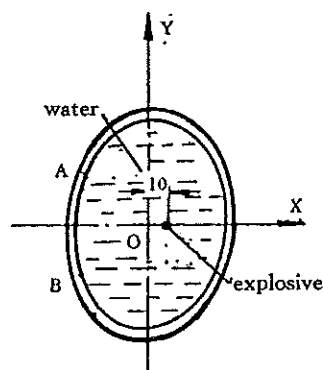


Fig. 1

computational results which indicates that at the two points A and B of $x = -44.96\text{mm}$, $y = \pm 24.03\text{mm}$ the tensile stress of 25 kbar has appeared at time of $75\mu\text{s}$, thereby, the pipe wall be ruptured in that places, from Fig. 2(b), we can see that there are two compressive stress zones of 5kbar separated inter-pipe, the compressive stresses pass through the pipe wall not only to be enhanced but transform two tensile stress zones due to the rarefaction of rocks outside, (Fig. 2c) then the tensile stress zones drew close to horizontal line, and enhanced uninterruptedly, at last reached to 25 kbar at two points A, B. From Fig. 2, it is obviously to see the mechanism for indicating how is to engender the tensile stresses. If choosing the due method to enhance the velocity of water mixed and disorderly, thereby may be the effect of zone-separating of compressive stress in pipe eliminated or alleviated greatly, therewith to eliminate the increase of tensile stress. Now, we have found the excellent method and gained successful applications in engineering.

References

- [1] Ezra A. A. principles and practice of explosive metalworking, 1973.
- [2] Cole R. H. , Underwater explosions, 1948.
- [3] Warren K. H; HEMPDS User's Manual, UCID-18075 Rev 1, 1983.
- [4] 邵丙璜, 张凯: 爆炸焊接原理及其工程应用, 1987.

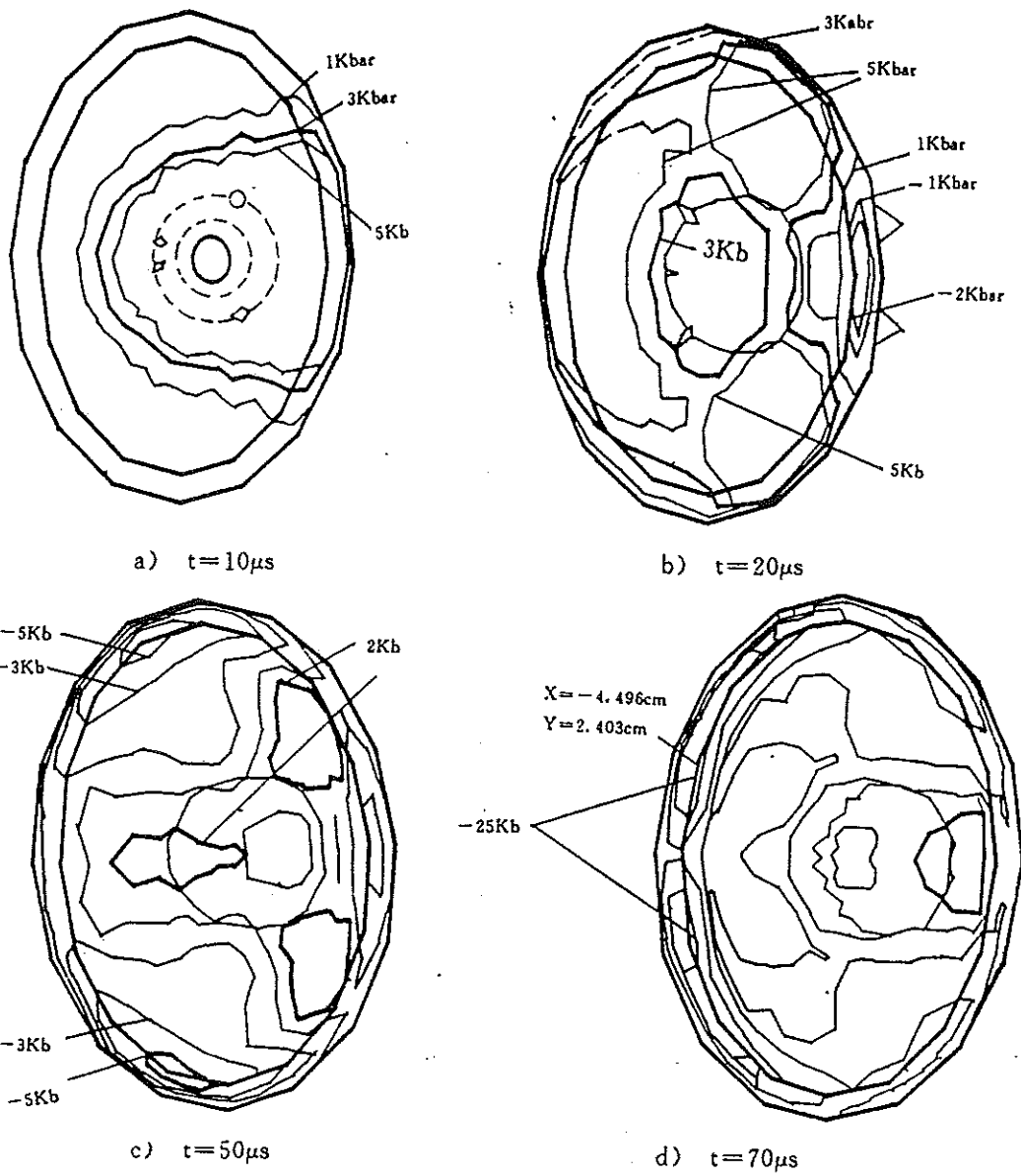


Fig. 2 The stress field after explosion of bias explosive column in eccentric pipe.